EUROPEAN ORGANIZATION FOR NUCLEAR RESEARCH
STANFORD LINEAR ACCELERATOR CENTER

CERN-EP/2002-xxx
SLAC-PUB xxxx
hep-ex/02yyxxx
DRAFT of December 18, 2001

Precision Electroweak Measurements on the Z Resonance

The ALEPH, DELPHI, L3, OPAL and SLD Collaborations,
the LEP Electroweak Working Group,* and
the SLD Electroweak and Heavy Flavour Groups†

WORKING DRAFT December 18, 2001

*some really hardworking people
†some more hardworking people

Editors' Note on DRAFT 2

This is the second draft released by the electroweak working group for review by the five collaborations. This draft is not yet in a form suitable for final approval, and its breadth of circulation within each collaboration is left to the discretion of each review board. As it is a draft, do not use the material presented here outside the five collaborations! Questions only may be addressed directly to the responsible section editors: Chapter 1: Robert Clare; 2: Günter Quast; 3: Peter Rowson; 4: Mike Roney; 5: Klaus Moenig; 6: Pippa Wells; References: Richard Kellogg; rest: Martin Grünewald. We request, however, that all comments and other feedback from each collaboration be passed on through its review board, and that the reply of each of the five review boards on this draft is sent to us by e-mail not later than **February 15th, 2002**. Of course, earlier responses are greatly appreciated!

We are most interested in comments concerning the physics presentation of the measurement results, *i.e.*, in particular up to and including Chapter 9. The numerical results in this draft are not always final but correspond to the status of summer-2001. Some later updates such as the final tau-polarisation combination procedure or new topics such as tagged light flavour results are included but not yet propagated to the subsequent analysis chapters. This draft does contain the recent b-quark forward-backward asymmetry measurements as well as (partially) the interesting final NuTeV result, and the resulting necessary discussions. Concerning the NuTeV result, however, the fits have not been updated (results on the five Standard-Model parameters change only marginally); only the new fit probability, which changes a lot, is given. No qualitative and only minor quantitative changes are expected for final results.

Comments on Draft 1 received from the experiments have been very valuable and are mostly implemented. For those which are not, our reasons are given in the following.

2001-12-18 by RC (MWG)

Chapter 1 (Introduction):
==========

ALEPH comments

- LEP vs SLD treatment:

When reading chapter 1, the description of LEP is more of a "historical" nature, focussing on the years LEP was running and the statistics accumulated. While the description of SLC is more "technical", describing in some details the parameters of the machine. I think a more homogeneous description of the two machines would be desirable. Probably we do not need to describe in much detail the machine parameters in this chapter. The relevant parameters, are described, anyway, in the description of the measurements afterwards.

Answer: this is to some extent true. Part of the problem is that the intro has been written by a LEP person. The plumbing of the SLC is somewhat different than that of LEP, so there was a natural tendency to go into a bit more detail in SLC. The SLC is, after all, the first linear collider.

2001-11-08 by GQ

Chapter 2 (Lineshape & Afb):
==========

DELPHI:
2.1 Line-shape and R_l including more (sec 2.0?) on LEP beam energy meast
difficult - what means more?
Table 2.4 shows some significant differences in the correlations for
the different experiments. It would be helpful if these were commented
on.
- there are differences, yes, but they are not "significant"; differences
at the level of a few % are normal given the small differences in
the detailed balance of statistical experimental systematic and common
errors.

Section 2.2. As mentioned above, the fit results would be better given
in a separate Section.
- no, would need general restructuring; group decided againt this.

Section 3.1 line-shape fits giving M_Z, G_Z, G_inv, N_nu, alpha_s, etc and the
upper limits on invisible and visible (cf Moenig note CERN-OPEN-97-40)
new physics BR's

Answer: added special sections in chapter 7 with this information
(in particular alpha_s andlimits on non-SM contributions
to Z decays are very SM dependent and should not appear
in this model-independent section)

L3:
L3 proposes to include in the paper:
S-matrix measurements. There would be no major problem in L3 to
deliver the results in time to be included in the paper
- some (one) other(s) have (has) difficulties!

We find unbalanced the description of the measurements themselves and the
descriptions of systematics, common uncertainties etc. At the end of
the chapter one asks oneself, but where are the results ?? We suggest
a longer introduction to the chapter stating what are the different
ingredients that go into the game, in which section they are covered,
how the different measurements finally converge to a single set of
parameters etc.
- handled by a few extra sentences saying that the unpublished parts
of the story (the combination and studies of common errors) are
naturally longer

The titles of subsections 2.3.1, 2.3.2, 2.3.3 and 2.3.4 are almost the same "Common xxx uncertainties", why not supress "Common" and "Uncertainties" ?.
- left this in for the moment.

OPAL:
(many very useful corrections, all implemented, thanks!)

o page33, figure 2.2, and caption, and related text.

'Left and Right' may be confusing. May be interpreted as left and right sides about the beam line. Any good alternative, or a way to make it clear?
- no better idea, left it for the moment

o page 38, 2.1.5, 1st para
peak+/-2 GeV --> peak+-1.8 GeV (as in 1.1.1)
- used in E_+2 and E_-2; left it for the moment

2001-11-12 by PCR

Chapter 3 (Alr & co)
====================

Please find attached the responses to the ADLO comments. I have dealt with the SLD comments internally - amd many of these overlapped with the DELPHI comments in particular (polarimeter details etc.).

Peter

****

Replies to comments on Chapter 3 :

ALEPH

A number of changes have been made to the text regarding tone and emphasis, however, the comment that the reader should not be led to believe the ALR method is more reliable than other techniques doesn't seem to be fair. A central point of this section is that the polarization technique is in fact more reliable, cleaner, simplier - etc. than other methods. I think it is important to make this point clear.

The comment on GammaZ and Mz is of course correct - the text has been modified accordingly.

The comment re the b-asymmetry systematic error being comparable to the ALR sys. error is odd - the ALR error is about 0.64% relative, compared to 0.91% relative for the b-asymmetry. This seems like a fairly sizable difference.

DELPHI

All comments have been implemented. In particular, considerbly more explanatory text has been added (along with two figures) regarding the polarimeter. Hopefully, these clarify the questions regarding "detector response functions" and the channel scanning - as well as the general level of understanding of the device : There is now a plot of predicted vs observed asymmetry in the polarimeter in each channel, a detector linearity data plot, and a plot comparing the main polarimeter with the two "cross check" polarimeter detectors (that see the Compton photon rather than the Compton electron).

L3

The general comment on how the style of chapter 3 is different than the other chapters is hard to respond to - although in the present draft chapter 3 has changed considerably compared to the draft last seen by the L3 readers. It's actually not clear if these changes move in the direction desired by the L3 reader - as more detail has been added (see the DELPHI response above). All other comments have been implemented.

OPAL

All comments have been implemented.(except the TABLE style still needs work).

2001-11-09 by JMR

Chapter 4 (Tau polarisation):
==========

DELPHI:
==========
All comments/suggestions incorporated except:
"Section4.3. Systematic erors are discussed before the reults are presented."
As this structure was that agreed to for the entire document.

L3:
==========
All comments/suggestions incorporated except:

"General comment. As mentioned at the beginning, this is one of the chapters where the presentation of results is "diluted" after the discussion in systematic errors."
As this structure was that agreed to for the entire document.

- "The paragraph "The systematic error associated ...of the signal and backgrounds" is true but it does not apply only to tau polarisation but to all results presented in this paper. This paragraph (or something similar) should be moved to the beginning of the paper and say that it applies to all measurements presented in the paper."
left as is - this is a particularly critical point for the polarisation measurements because of the fits are to MC distributions - this is not the case with all results in the paper.

"Page 91. Figure 4.6. Supress the the two chi2/dof (no lepton universality assumed and lepton universality assumed)."
The text was moved to the bottom of the figure and one chi2/dof quoted in keeping with convention of earlier section.

OPAL
=======
All comments/suggestions incorporated.

2001-11-09 by KM

Chapter 5 (Heavy flavours):
==========

DELPHI:

The Appendix would be better included in this section.

*** We think this is filling up too much space in the main text, so we prefer to keep the tables in the appendix.

Fig5.4. Remove 'preliminary'.

*** Of course in the final version we have only publications. The preliminary stuff is only to get the draft going. This answer applies also to the other comments on the same subject.

L3:

General comments:

- This chapter contains too much information, too dense and sometimes even somehow cryptic. We wander whether it would be feasible to lighten it a little bit. We find it unbalanced between experimental methods and results themselves.

*** We tried to make things clearer. However it is difficult to make it shorter. You ask for many additional things yourself.
Page 119. Subsection 5.7.2 This section should clearly state that QCD corrections are the most important corrections to the heavy flavour measurements. It should also stress tha important role of MC generator, in particular, how much are we relying in JETSET ??

In particular, isnt the estimation of C^had,T_QCD very small ?

*** Can you explain this further?

In view of the potential importance of the A^b_FB measurement, more details of the correction methods actually used and described in Ref[152] should be given in the text. This is, by far, the largest external correction applied to the measured A^b_FB.

*** You request yourself to make it lighter, we have to find some ballance.

In fact your statement the the QCD corrections are the largest effect isn't even true. THE QED corrections are larger.

It should also be pointed out that the Jet charge method is largely 'self-correcting',
unlike the lepton measurements, which are, currently, what are described in the text.

*** This is a somewhat touchy point. Much of the "self correction" is actually not a self correction but the correction is hidden in the hemisphere correlations. On the other hand especially in the modern "jetcharge" analyses where information from the vertex charge is used the correction seems to be really small.

Page 121. We propose to change equation 5.12 to:

C_ij = Sum_n s_i(n) s_j(n) delta_ij + Sum_e(e=ADLO)Sum_ij s_i(e) s_j(e) + Sum_p s_i(p) s_j(p)

where the first term is the uncorrelated errors,
the second term is the error correlated within the experiment
the third term is the error correlated between the experiments.

And add the explanatory text from the NIM paper [146] in the equation itself, by explicitly defining the different classes of systematic errors used.

*** mathematically the errors are treated completely identical, so we think it is better to keep the equation as it is

2001-12-17 by PSW

Chapter 6 - Inclusive and light quarks
==========

The chapter has been updated to reflect comments from the editorial process, including substantial rewriting of the introduction and section 6.1, fixing of typos in section 6.2, and more information on the averaged up and down type couplings from the direct photons.

Section 6.1

There are open comments from Dick K. to improve the description of the treatment of the measurement, especially the relation to sin2thetaW as a "Standard Model Parameter", and some more details of the combination procedure. The warnings about the model dependence and more specific information about when the measurement can legitimately be used could also be strengthened.

Comment from L3 on section 6.2

Pages 136 and 137. The measurements of Sqqg are affected by rather large errors, and the way they are presented (the measurement +- a collection of 5 different errors in the case of DELPHI, 3 for L3 etc.) doesn't seem very appropriate. In general we find questionable the inclusion of such old results. We propose to drop them. From "In addition, DELPHI ..." until the end of the chapter.

Answer

The results are first quoted with exactly the same error breakdown as given in each experiment's publication. I have made this more explicit in the text now. The experiments did not make the same choices of error breakdown. The paragraph following the quoted results explains the common errors that have been taken into account to make an average.

On the broader question of whether to include these results at all, I don't think their "age" should be the criterion for dropping them, since they are published. If there are known problems, that's a different question. I think it is useful that this paper should offer a complete survey of Z electroweak results, including some of these more difficult and less precise measurements, even though these have little impact on fits which impose the Standard Model structure. The weak constraints that can be made on light quark couplings should be included later in the paper, to put these results in context.

2001-12-17 by MWG

Overall structure:
==========

DELPHI requested a change in the overall structure of chapters and the presentation of measurements and results.

Answer: We (the editors) feel that the current structure of the document (chapters and their content) is adequate and reflects the way the measurements are performed and related to each other. It is already rather similar to the flow of information as advocated by DELPHI: introduction, experimental measurements, and derived parameters. The specific break-up according to physics quantities, however, would introduce artificial dependencies between chapters, notably for heavy-quark based results.

Additional topics:
==========

L3 proposes to include in the paper:
* S-matrix measurements.
* Rho measurements in case there is more than one Higgs doublet.

Answer: The S-Matrix combination is currently being pursued. Rho_tree may not be done simply due to the fact that the analytical programs do not handle this out of the box, ie, without digging into the code.

General comment:
==========

L3: As a general comment, a common style for figures (colors, fonts etc) and tables would be appreciated. In all tables giving correlation matrices quote ONLY the subdiagonal elements. In general in tables giving symmetric matrices, quote ONLY diagonal and subdiagonal elements.

Answer: Progress is being made but it's not yet completed.

Controversial comments
==========

Chapters 8 (couplings),
9 (SM analyses) and

10 (conclusions).

Chapter 8 (Couplings)
=====================

L3: Page 148. When discussing figure 8.4 (sin2teff) reference the work by Tarek Aziz who was the first to group the measurements into hadronic and leptonic ones and fit them separately.

Answer: It is unclear whether Tarik or someone else was the first to observe this. If we cite someone, we would need to cite all papers discussing this point. However, we do not feel that there is too much to the leptonic versus hadronic difference, as its significance is mainly driven by Alr versus Afb0b.

L3: Section 8.5. When saying "... only g_Rb shows a significant deviation". Make the statement more quantitative and reference the first one who did it, J.H. Field, Phys Rev D 058 093010-1.

Answer: For the citation, the same applies here as for the previous comment. In particular, the editor recalls a comment on g_Rb in a talk by W.Hollik already more than 6 years ago...

L3: Last paragraph. The sentence "Thus the effect is either a sign for new physics ... or a fluctuation ...", quantify the fluctuation (how many sigmas) and in which input measurements.

Answer: At this point for sin2teff, it is the _relative_ discrepancy of two measurements, and we cannot say yet which one is off. The joint chi2 is quoted in the previous section. Only with the help of additional measurements, such as MW, or the SM (ie going to a model), can we assign which measurement is likely to be off/fluctuating. The SM analysis is performed later, and the pull of Afb0b w.r.t. the SM fit is given there.

OPAL: uds couplings: In chapter 8, we would like (at least to try) to include the couplings for light quarks extracted from the available data.

Answer: This is foreseen; some issues in the parameter transformation of these numbers to extract uds couplings are currently being studied.

OPAL: The relationship of the fermion couplings to the experimentally measured quantities is complicated by the non-orthogonality of sin^2 and rho, which is highly significant for down-type quarks. We feel this could be clarified by:

1) adding a "text book" plot of g_v vs g_a to fig. 8.2, covering the whole plane, and showing the error contours (at high CL) for all fermion species

2) adding arrows to the error contours of fig 8.3 showing how they would shift in response to changes in A_f and R_f

Answer: Concerning 1) we feel the information is more adequatly presented by Figure 8.3, as in this figure the trivial differences between g_v and g_a for the different fermion species due to T_3 and q_f are taken out. Concerning 2) the corresponding information is currently added to the caption.

Chapter 9 (MSM)
==========

ALEPH: Choice of theory-driven hadronic vaccuum polarisation

Answer: As soon as it is published, we'll change to use the hadronic vacuum polarisation of Troconiz and Yndurain, hep-ph/0111258, as the theory-driven result. Their result is currently the most precise one, with an error of 0.00012 (factor three on the experimental result).

ALEPH: MW's sensitivity to radiative corrections

Answer: Section 9.6 concerns Z-pole results only, ie, not MW. The sensitivity of MW is mentioned explicitely in Section 9.7.2.

ALEPH: Sensitivity of the W mass to Higgs

Answer: The width of the MT-error band relative to the alpha-error band is larger for MW than for the Z-Pole observables, esp. sin2teff and thus all asymmetries. In this sense MW is an ideal observable.

ALEPH:
I think it could be quite useful to have the Higgs mass prediction separated in: Asymmetries, Mw and leptonic width, and the uncertainties splitted as: statistics + Dalpha + Dmtop + Dalphas.

This will make apparent the limitations of each determination, and will give a hint on what the future measurements will bring to this game.

Answer: We are afraid that something like this would yield too long a description of the additional fits and too many numbers. On the other hand, we think most of the info requested is already contained in the big summary Table and in the three sets of Higgs sensitivity plots. A plot showing the Higgs mass derived from each observable X through a 5-parameter MSM fit to (alpha,alpha_s,MZ,MT,X) is added.

ALEPH: Pulls and Higgs:

Pulls are defined as pulls and thus the sign of the pull is not correlated to whether the observable in question wants a higher or lower Higgs boson mass. We have added a sign to the Higgs sensitivity of each observable, telling whether the observable in question wants a higher or lower Higgs mass compared to the result of the global fit.

ALEPH: Treatment of systematic theory errrors: Gaussian versus box

Answer: Because of the method of chi2 minimisation, systematics must be treated as Gaussians throughout. For a box of full width d=2sigma, the equivalent sigma would be smaller by sqrt(3). Thus we are, if anything, conservative.

DELPHI: Eq.9.1 should be given much earlier, in a revised Chapter1 as suggested above.

Answer: The generic discussion of the running alpha and the contributions to Delta-alpha are now given in the Introduction. The specific point of having two classes of evaluations with different precision is so specific that we feel it is better presented in the SM section.

DELPHI:
3 Fits and interpretations (assuming that this is the publication of the combined final LEP1 data but that at publication time m_W is still not final, don’t introduce M_W from the beginning at the same level as the final LEP1 data and final Run 1 m_t value but add it only from time to time as an "after-thought" to show what its future impact would be if the value and error don’t change)

Answer: This is already done: we first present the fit to the Z-pole data only, and add in only later external measurements incl. MW. On the other hand we want to avoid to present complete results from too many different fits.

DELPHI:
3.n Finally, present the running couplings (using alpha_s from these data) not meeting (as they should in a GUT) if there is a desert to m_Planck, implying GUT needs (eg) SUSY (or something else? - Z's? or whatever?)

Answer: We would need some computer code for Q^2 evolution in SM and MSSM (just couplings evolution or full SUSY fits?).

DELPHI: Section9.9. We feel it is unwise to drop the A_FB results from the fits. It implies you think they are wrong.

Answer: The two sentences on removing Afb0b constitute a compromise between two extreme positions: (1) repeating each and every analysis in Chapters 8 and 9 excluding Afb0b, and (2) doing nothing (as DELPHI prefers). We feel neither (1) nor (2) are adequate for such a report and in a Chapter concerning SM tests. However, in order not to single out Afb0b, we also give results when dropping Alr (pulling the other way) and MW (sort of "deciding" between the two concerning MH).

L3: Page 157. Make equations 9.10 to 9.17 consistent with what is presented in chapter 1. In particular in what epsilon_1 (= delta rho) is concerned. In the paper Phys. Rev D 058 093010-1 other set of epsilon is used, so, why the set used here has been selected? Make a comment on it.

Answer: We use the expressions for the epsilons as defined by the original authors (Altarelli et al.). Note that the \ln(MH/MW) versus \ln(MH/MZ) difference to Chapter 1 is of subleading order, but the equations for the epsilons in Chapter 9 are giving only the leading order.

Chapter 10 (Conclusion)
==========

DELPHI & L3: Premature to write, wait and see the final situation on Afb0b.

Answer: Of course, the conclusions will be adapted to the final measurement results. However, a conclusion is needed in any case, and unless there are qualitative changes in the results, this is our conclusion. The same applies to the corresponding discussions in Chapters 8 and 9 and the new abstract! (We'll have some fun when the final NuTeV measurement is actually fully propagated!)

Abstract

We report on the final electroweak measurements performed with data taken at the Z resonance by the experiments operating at the electron-positron colliders SLC and LEP. The data consist of 17 million Z decays accumulated by the ALEPH, DELPHI, L3 and OPAL experiments at LEP, and 600 thousand Z decays by the SLD experiment at SLC. The measurements include cross sections, forward-backward asymmetries and polarised asymmetries. The mass and width of the Z boson, m_{Z} and Γ_{Z}, and its couplings to fermions, for example the ρ parameter and the effective electroweak mixing angle, are precisely measured:

$$\begin{aligned} m_{\mathrm{Z}} &= 91.1875 \pm 0.0021 \text{ GeV} \\ \Gamma_{\mathrm{Z}} &= 2.4952 \pm 0.0023 \text{ GeV} \\ \rho_{\ell} &= 1.0049 \pm 0.0010 \\ \sin^2\theta_{\mathrm{eff}}^{\mathrm{lept}} &= 0.23152 \pm 0.00017\,. \end{aligned}$$

The number of light neutrino species is determined to be 2.9841 ± 0.0083, in good agreement with the three observed generations of fundamental fermions.

The results are compared to the predictions of the Standard Model. At the Z-pole, electroweak radiative corrections beyond the running of coupling constants are observed with a significance of five standard deviations, and in agreement with the Standard Model. Of the many Z-pole measurements, the forward-backward asymmetry in b-quark production shows the largest difference with respect to its Standard-Model expectation, at the level of three standard deviations.

The data are also used to determine the mass of the top quark and of the W boson, through radiative corrections evaluated in the framework of the Standard Model. These indirect constraints are compared to direct measurements, providing a stringent test of the Standard Model. Using additional measurements of electroweak observables from other experiments, the data indicate that the as yet unobserved Standard-Model Higgs boson has a mass lower than about 200 GeV.

To be submitted to *Physics Reports*

Acknowledgements

We would like to thank the CERN accelerator divisions for the efficient operation of the LEP accelerator, the precise information on the absolute energy scale and their close cooperation with the four experiments. The SLD collaboration would like to thank the SLAC accelerator department for the efficient operation of the SLC accelerator. We would also like to thank members of the CDF, DØ and NuTeV Collaborations for making results available to us and for useful discussions concerning their combination. Finally, the results and their interpretation within the Standard Model would not have been possible without the close collaboration of many theorists.

Contents

List of Figures

List of Tables

Chapter 1

Introduction

$Id: physrep_intro.tex,v 1.49 2001/12/18 15:09:41 gruenew Exp $

With the observation of neutral current interactions in neutrino-nucleon scattering [1] and the discovery of the W and Z bosons in $p\overline{p}$ collisions [2, 3], the Standard Model [4] was well established experimentally. The LEP and SLC accelerators were designed to copiously produce Z bosons via e^+e^- annihilation, allowing detailed studies of the properties of the Z boson to be performed in a very clean environment.

The accumulated data are used to determine the properties of the Z boson with high precision: its mass, its partial and total widths, and its couplings to fermion pairs. These results are compared to the predictions of the Standard Model. The experimental precision is sufficient to demonstrate the existence of higher-order electroweak radiative corrections with high significance. Via the effects of these corrections, the properties of particles not produced at LEP and SLC, most notably the top quark and the Higgs boson, is inferred.

After a brief introduction to the LEP and SLC programs and the Standard Model, detailed discussions of the measurements follow. These are the Z lineshape and leptonic asymmetries in Chapter 2, the left-right polarised asymmetry (Chapter 3), tau polarisation (Chapter 4), heavy quark (b and c) measurements (Chapter 5), light quark measurements (Chapter 6) and correlations between measurements (Chapter 7). Chapter 9 discusses the derivations of the effective neutral weak coupling constants in a largely model-independent context, and Chapter 10 reviews the electro-weak measurements presented here and elsewhere and the constraints on the Standard Model that these measurements imply.

1.1 LEP and SLC data

The process under study is $e^+e^- \to f\overline{f}$, which proceeds in lowest order via photon and Z boson exchange, as shown in Figure 1.1. Between the years of 1989 and 1998, the LEP [5] and SLC [6] e^+e^- accelerators operated at energies of approximately 91 GeV, close to the mass of the Z boson. The hadronic cross-section as a function of the centre-of-mass energy is shown in Figure 1.2. There are two prominent features in the hadronic cross-section. The first is the $1/s$ fall-off, due to photon exchange (the left diagram in Figure 1.1), which leads to the peak at low energies, and the second is the peak at 91 GeV, due to Z exchange (the right diagram of Figure 1.1). Thus, at LEP and SLC, Z bosons were copiously produced.

The LEP accelerator ran from 1989 to 2000. However, only during the first years, until 1995, was the running dedicated to the Z boson region. From 1996 until 2000, the machine

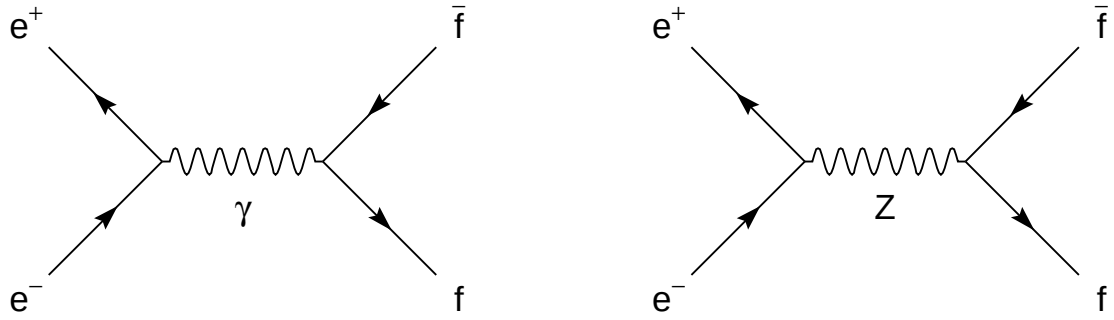

Figure 1.1: The lowest-order s-channel Feynman diagrams for $e^+e^- \to f\bar{f}$. For e^+e^- final states, the photon and the Z boson can also be exchanged via the t-channel.

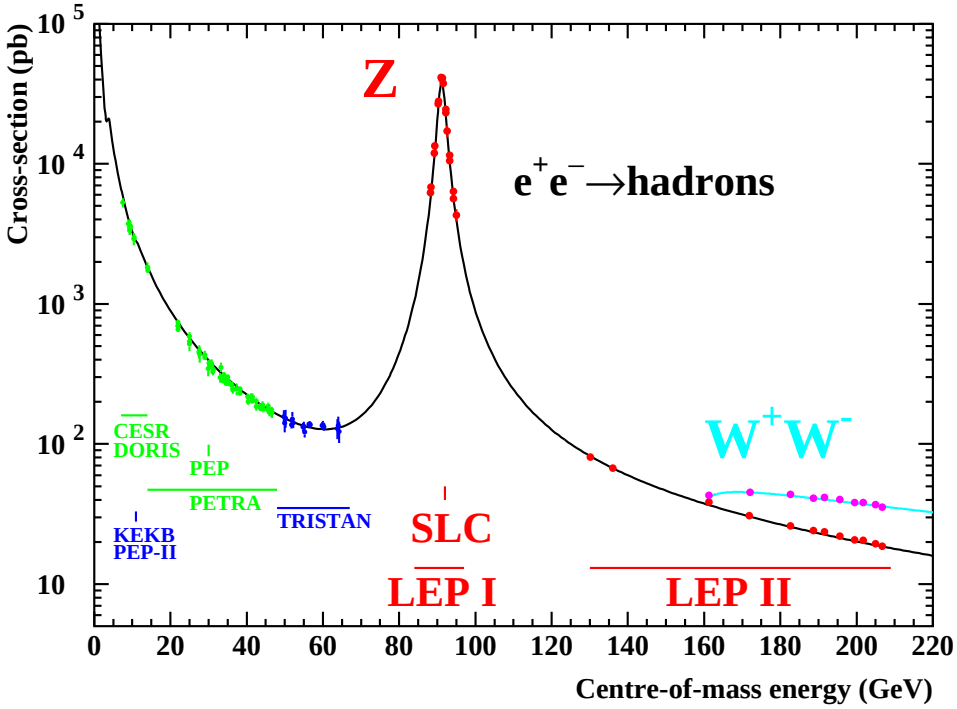

Figure 1.2: The hadronic cross-section as a function of centre-of-mass energy. The solid line is the prediction of the Standard Model, and the points are the experimental measurements. Also indicated are the energy ranges of various e^+e^- accelerators. The cross-sections have been corrected for the effects of photon radiation.

was operated at energies at and above 160 GeV, allowing the production of pairs of W bosons, $e^+e^- \rightarrow W^+W^-$, as indicated in Figure 1.2. Although some results from this later running will be used in this report, the bulk of the data stems from the Z period. When needed, the Z period will be denoted "LEP-I", and the period beginning in 1996 "LEP-II".

During the six years of running at LEP-I, the four experiments ALEPH [7], DELPHI [8], L3 [9] and OPAL [10] collected approximately 17 million Z decays in total distributed over seven points in centre-of-mass energy in the range of the Z mass plus or minus 3 GeV.

The SLC accelerator started running in 1989 and the Mark-II collaboration published the first observations of Z production in e^+e^- collisions [11]. However, it was not until 1992 that a significant longitudinal polarisation of the SLC electron beam was established. By then the SLD [12–14] detector had replaced Mark-II. From 1992 until 1998, when the accelerator was shut down, SLD accumulated approximately 600 thousand Z decays. Although the data set is much smaller than that of LEP, the presence of longitudinal polarisation allows complementary and competitive measurements of the Z couplings. Other properties of the accelerator, for example the extremely small luminous volume of the interaction point, have been used to improve the statistical power of the data.

1.1.1 LEP

LEP [5] was an electron-positron storage ring with a circumference of approximately 27 km. Four interaction regions were situated around the ring (L3, ALEPH, OPAL and DELPHI), as shown in Figure 1.3. In summer 1989 the first Z bosons were produced at LEP and observed by

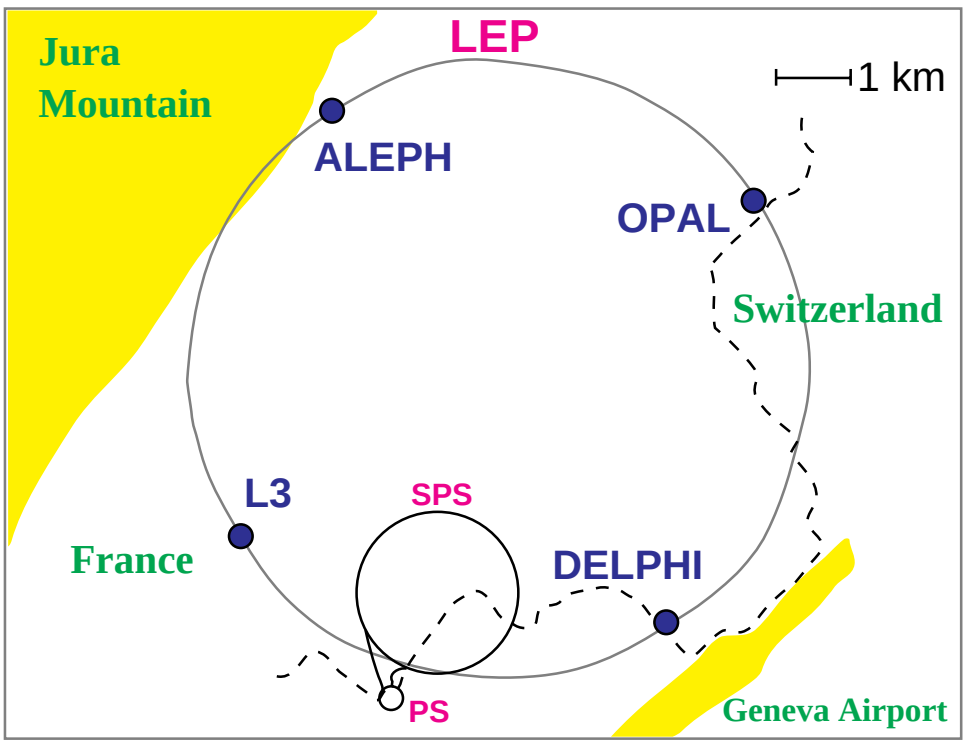

Figure 1.3: The LEP storage ring, showing the locations of the four experiments, and the existing accelerators (PS, SPS) used as pre-accelerators for the electron and positron bunches.

the four experiments. Over the following years the operation of the machine and its performance

were steadily improved. At the end of LEP data taking around the Z resonance in autumn 1995 the peak luminosity had reached nearly twice its design value. At this luminosity, approximately 1000 Z bosons were recorded every hour by each of the four experiments, making LEP a true Z factory. Table 1.1 summarises the data taking periods, the approximate centre-of-mass energies and the delivered integrated luminosities.

year	centre-of-mass energy range [GeV]	integrated luminosity [pb^{-1}]
1989	88.2 – 94.2	1.7
1990	88.2 – 94.2	8.6
1991	88.5 – 93.7	18.9
1992	91.3	28.6
1993	89.4, 91.2, 93.0	40.0
1994	91.2	64.5
1995	89.4, 91.3, 93.0	39.8

Table 1.1: Approximate centre-of-mass energies and integrated luminosities delivered per experiment. In 1990 and 1991, a total of about 7 pb^{-1} was taken at off-peak energies, and 20 pb^{-1} per year in 1993 and in 1995. The total luminosity used by the experiments in the analyses was smaller by 10–15% due to data taking inefficiencies.

The data collected in 1989 constitute only a very small subset of the total statistics and are of lower quality, and therefore these have not been used in the final analyses. In the years 1990 and 1991 "energy scans" were performed at seven different centre-of-mass energies around the peak of the Z resonance, placed about one GeV apart. In 1992 and 1994 there were high-statistics runs only at the peak energy. In 1993 and 1995 data taking took place at three centre-of-mass energies, about 1.8 GeV below and above the peak and at the peak. The accumulated event statistics amounts to about 17 million Z decays recorded by the four experiments. A detailed break-down is given in Table 1.2.

$\mathrm{Z} \to \mathrm{q\overline{q}}$					
year	A	D	L	O	all
'90/91	433	357	416	454	1660
'92	633	697	678	733	2741
'93	630	682	646	649	2607
'94	1640	1310	1359	1601	5910
'95	735	659	526	659	2579
total	4071	3705	3625	4096	15497

$\mathrm{Z} \to \ell^+\ell^-$					
year	A	D	L	O	all
'90/91	53	36	39	58	186
'92	77	70	59	88	294
'93	78	75	64	79	296
'94	202	137	127	191	657
'95	90	66	54	81	291
total	500	384	343	497	1724

Table 1.2: The $\mathrm{q\overline{q}}$ and $\ell^+\ell^-$ event statistics, in units of 10^3, used for Z analyses by the experiments ALEPH (A), DELPHI (D), L3 (L) and OPAL (O).

Much effort was dedicated to the determination of the energy of the colliding beams, which reached a precision of about 20×10^{-6} on the absolute energy scale. This level of accuracy was vital for the precision of the measurements of the mass and width of the Z. In particular the

off-peak energies in the 1993 and 1995 scans were carefully calibrated employing the technique of resonant depolarisation of the transversely polarised beams [15–18]. In order to minimise the effects of any long-term instabilities during the energy scans, the centre-of-mass energy was changed for every new fill of the machine. A fill of the machine typically provided luminosity for approximately 10 hours. Thus the data samples taken above and below the resonance are well balanced within each year. The data recorded within a year around one centre-of-mass energy were combined to give one measurement at this "energy point".

All the experiments replaced their first-generation luminosity detectors, which had systematic uncertainties around the percent level, by high-precision devices capable of pushing systematic errors on the acceptance of small-angle Bhabha scattering events below one per-mil. Silicon vertex detectors were also added to the tracking systems, which greatly improved the identification of secondary decay vertices accompanying the production of b and c quarks. As a consequence of these improvements during LEP-I running, statistical and systematic errors are much smaller for the last three years of data taking, which hence dominate the precision achieved on the Z parameters.

1.1.2 SLC

The SLC [6] was the first e^+e^- linear collider. As such, it operated in a somewhat different mode than LEP. It used the SLAC linear accelerator to accelerate alternate bunches of electrons and positrons, a set of two damping rings to reduce the size and energy spread of the electron and positron bunches, and two separate arcs to guide the bunches to a single interaction region, as shown in Figure 1.4. The repetition rate was 120 Hz (compared to either 45 kHz or 90 kHz, depending on the mode, for LEP).

The standard operating cycle began with the production of two closely spaced electron bunches, the first of which was longitudinally polarised. These bunches were accelerated part way down the linac before being stored in the specially designed electron damping rings. Before storage in the damping rings, the longitudinal polarisation was rotated to be transverse. After damping, the two bunches were extracted and accelerated in the linac. At 30 GeV, the second bunch was diverted to a target, where positrons were created. The positrons were captured, accelerated to 200 MeV and sent back to the beginning of the linac, where they were then stored in the positron damping ring. The positron bunch was then extracted just before the next two electron bunches, and accelerated. At 30 GeV, the third bunch was diverted to create positrons, while the remaining positron and electron bunches were accelerated to the final energy of ≈ 46.5 GeV to be transported in the arcs to the final focus and interaction point, losing approximately 1 GeV in the arcs due to synchrotron radiation, leading to a centre-of-mass energy of 91.25 GeV, at the maximum of the annihilation cross-section.

The era of high-precision measurements at SLC started in 1992 with the first longitudinally polarised beams. The polarisation was achieved by shining circularly polarised laser light on the gallium arsenide electron source. At that time, the polarisation was only 22%. Shortly thereafter, "strained lattice" photocathodes were introduced, and the polarisation increased significantly, as can be seen in Figure 1.5, which shows the polarisation as a function of time. Much work was invested in the SLC machine to maintain the electron polarisation at a very high value throughout the production, damping, acceleration and transfer through the arcs. In addition, to avoid as much as possible any correlations in the SLC machine or SLD detector, the electron helicity was randomly changed on a pulse-to-pulse basis by changing the circular polarisation of the laser.

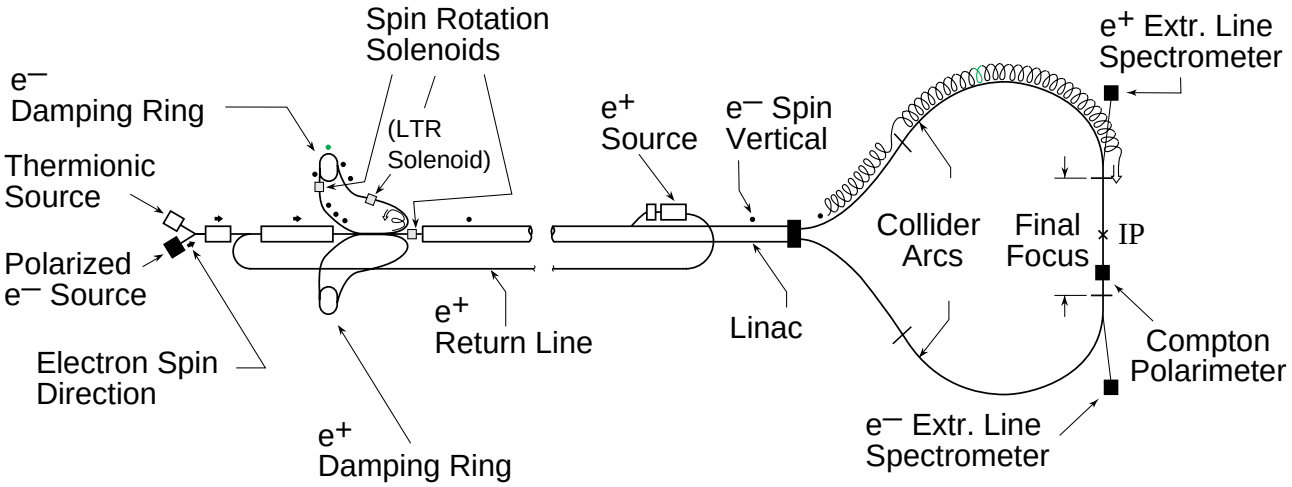

Figure 1.4: The SLC linear collider complex, showing the electron source, the damping rings, the positron source, the linac and arcs and the final focus. The helix and arrow superimposed on the upper arc schematically indicate the electron spin precession which occurs during transport.

Also evident in Figure 1.5 is that almost 60% of the data were collected in the last two years of SLC running, from 1997 to 1998, with the second to last week of running producing more than 20000 Z bosons.

1.2 LEP/SLC Detectors

The designs of the LEP and SLC detectors are quite similar, although the details vary significantly among them. As an example, the OPAL detector is shown in Figure 1.6. Starting radially from the interaction point, there is first a vertex detector, typically composed of multilayered silicon devices followed by a gas drift chamber to measure the parameters of charged particle tracks. The silicon detector significantly improves the ability to measure impact parameters and to identify secondary vertices with a resolution of approximately 300 μm. As the typical B-hadron produced in Z decays will move about 3 mm from the primary vertex before decaying, the use of these detectors allows the selection of a heavy quark sample with high purity. (The typical beam spot size was 150 μm $\times$ 5 μm for LEP and 1.5 μm $\times$ 0.7 μm for SLC.)

Surrounding the tracking system is a calorimeter system, usually divided into two sections. The first section is designed to measure the position and energy of electromagnetic showers from photons (including those from π^0 decay) and electrons. The electromagnetic calorimeter is followed by a hadronic calorimeter to measure the energy flow of hadronic particles. Finally, an outer tracking system designed to measure the parameters of penetrating particles (muons) completes the system.

The central part of the detector (at least the tracking chamber) is immersed in a solenoidal magnetic field to allow the measurement of the momentum of charged particles. In addition, particle identification systems may be installed, including ionisation loss measurements(dE/dx) in the central chamber, time-of-flight, and ring-imaging Čerenkov detectors. These measurements can be used to determine the velocity of particles; coupled with the momentum, they yield the particle masses. Special detectors are placed at small polar angles to detect Bhabha

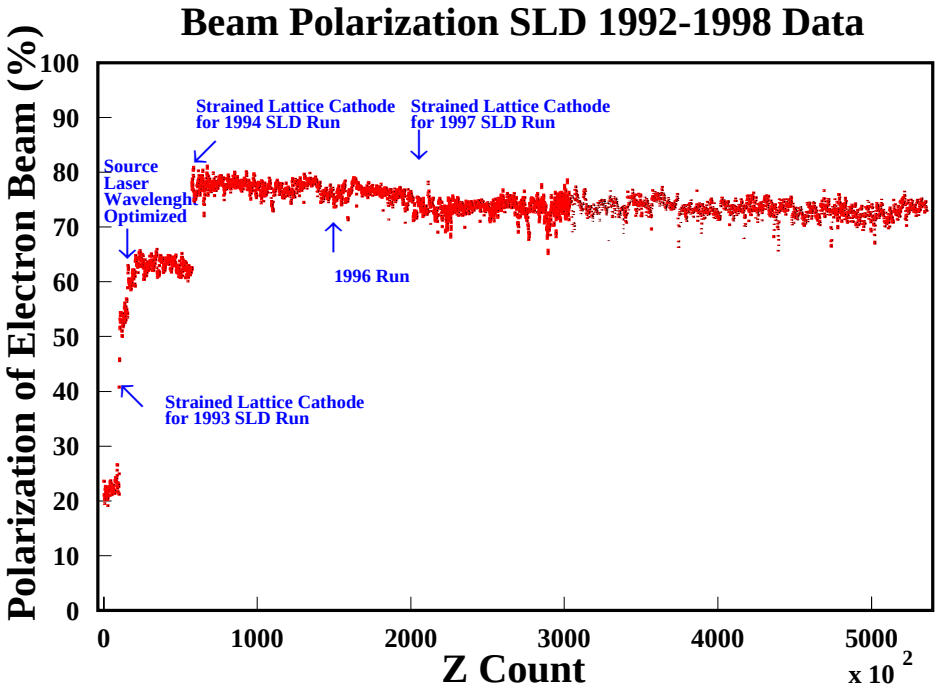

Figure 1.5: The amount of longitudinal electron polarisation as a function of time at SLC.

scattering events, used to determine the luminosity. The rate of Bhabha events was used for the luminosity determinations, as the small-angle Bhabha process is due almost entirely to QED, and the cross-section can be calculated precisely.

The somewhat different conditions at the SLC allowed some improvements in the basic design of the SLD detector. As the dimensions of the SLC beams were much smaller than the LEP beams, the vertex detectors were placed at a smaller radius. Because of the low repetition rate, slow, but very high-resolution, CCD arrays were employed instead of the micro-strip devices used at LEP. Both features allowed an improved vertex reconstruction.

All five detectors had almost complete solid angle coverage; the only holes being at very small angle due to the beam pipe. Thus, most events were fully contained in the active elements of the detectors, allowing straight-forward identification. A few typical Z decays, as seen in the detectors are shown in Figure 1.7. As can be seen, the events at LEP and SLC were extremely clean with practically no background allowing high-efficiency and high-purity selections to be made.

Shown in Figure 1.8 is a side view of an SLD event interpreted as the decay of a Z into $b\bar{b}$. The displaced vertex from the decay of a B hadron is clearly visible. This event also shows the definition of a "forward" event, as the b-quark goes into the hemisphere defined by the direction of the electron beam ($\theta < \pi/2$).

1.3 Typical measurements

Total cross-sections for a given process are determined by counting selected events, $N_{\rm sel}$, subtracting background, $N_{\rm bg}$, and normalising by the selection efficiency, $\epsilon_{\rm sel}$, and the luminosity,

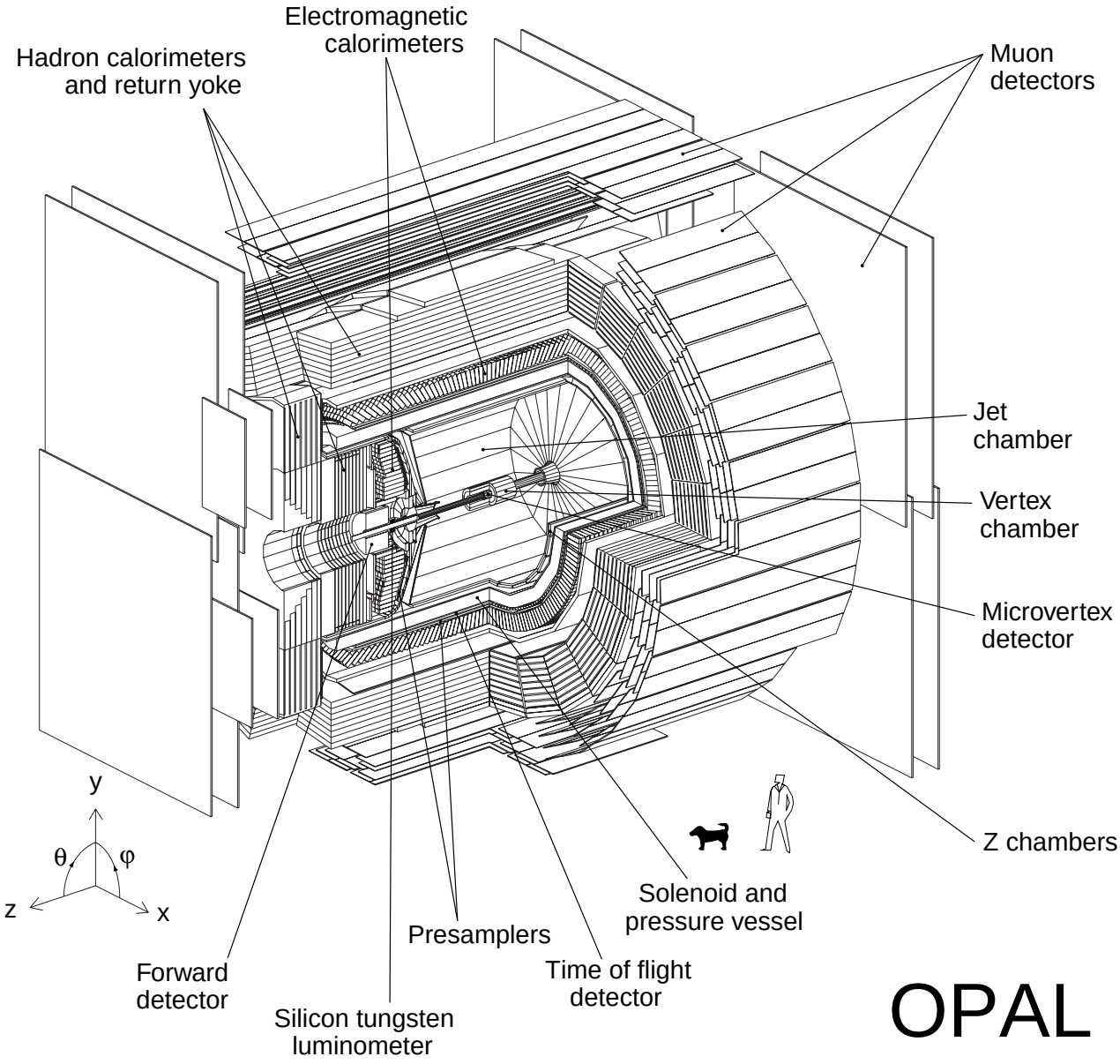

Figure 1.6: A cut-away view of the OPAL detector, as an example LEP/SLC detector.

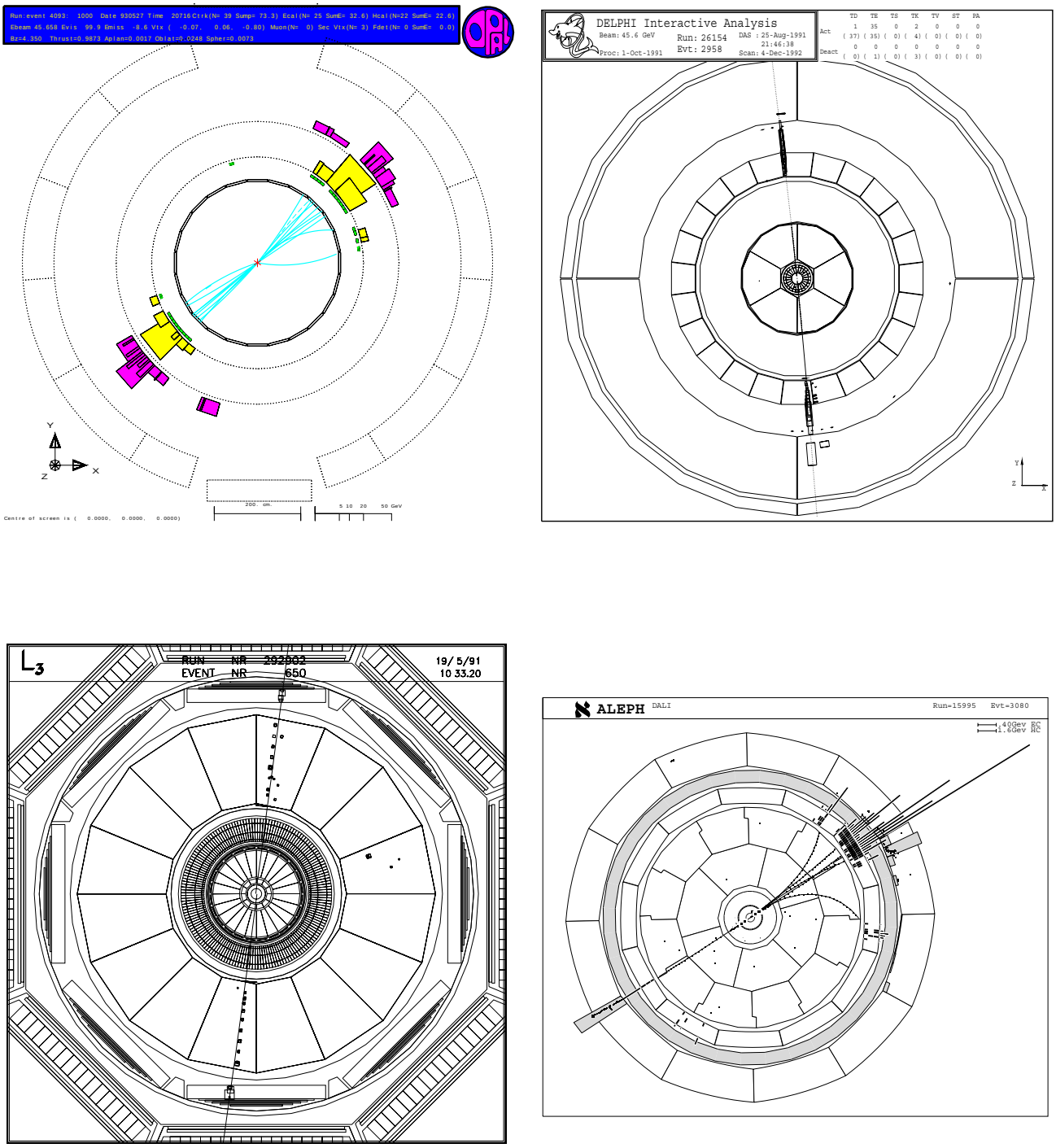

Figure 1.7: Pictures of $q\overline{q}$, e^+e^-, $\mu^+\mu^-$ and $\tau^+\tau^-$ final states, visualised with the event displays of the OPAL, DELPHI, L3 and ALEPH collaborations, respectively. In all views, the electron-positron beam axis is perpendicular to the plane of the page.

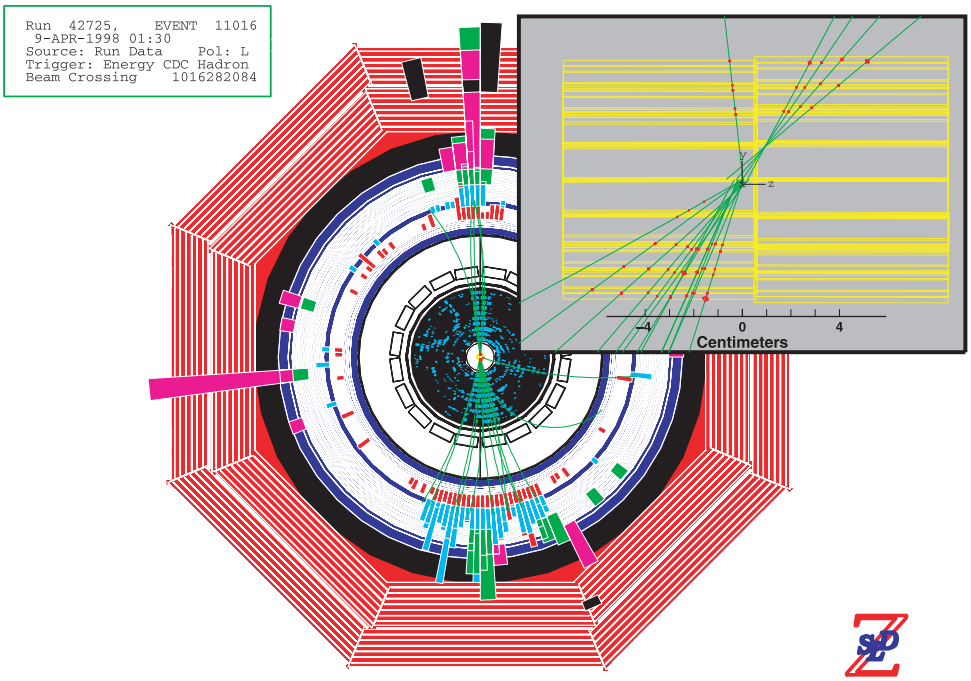

Figure 1.8: Frontview of an event classified as $Z \to b\overline{b}$. The displaced vertex is visible in the expanded side view of the vertex. From the charge of the tracks at the vertex, this event has a b-quark in the forward hemisphere, and is thus a "forward" event.

$\mathcal{L}$:

$$\sigma = \frac{N_{\rm sel} - N_{\rm bg}}{\epsilon_{\rm sel}\mathcal{L}}. \tag{1.1}$$

The expected background and the selection efficiencies are determined using Monte-Carlo event generators. The generated events are typically passed through a program that simulates the detector response and then processed by the same reconstruction program as used for the data.

Another important measurement is that of forward-backward asymmetries. The asymmetry is defined as the number of produced fermions, $N_{\rm F}$, (as opposed to anti-fermions) which travel in the same direction as the incoming electron beam (forward events) minus the number of fermions produced in the backward direction, $N_{\rm B}$, divided by the total number of produced events:

$$A_{\rm FB} \;=\; \frac{N_{\rm F} - N_{\rm B}}{N_{\rm F} + N_{\rm B}}. \tag{1.2}$$

1.4 Standard Model relations

In the Standard Model at tree level, the relationship between the weak and electromagnetic couplings is given by

$$G_{\rm F} = \frac{\pi\alpha}{\sqrt{2}m_{\rm W}^2 \sin^2\theta_{\rm W}}, \tag{1.3}$$

where $G_{\rm F}$ is the Fermi constant determined in muon decay, α is the electromagnetic fine-structure constant, $m_{\rm W}$ is the W boson mass, and $\sin^2\theta_{\rm W}$ is the electro-weak mixing angle. In addition, the relationship between the neutral and charged weak couplings fixes the ratio of the W and Z boson masses:

$$\rho = \frac{m_{\rm W}^2}{m_{\rm Z}^2 \cos^2\theta_{\rm W}}. \tag{1.4}$$

The ρ parameter [19] is determined by the Higgs structure of the theory; in the Minimal Standard Model containing only Higgs doublets, ρ is unity.

The fermions are arranged in weak-isospin doublets for left-handed particles and weak-isospin singlets for right-handed particles, as shown in Table 1.3. The interaction of the Z

Family			T	T^3	Q
$\begin{pmatrix}\nu_{\rm e}\\ {\rm e}\end{pmatrix}_L$	$\begin{pmatrix}\nu_\mu\\ \mu\end{pmatrix}_L$	$\begin{pmatrix}\nu_\tau\\ \tau\end{pmatrix}_L$	1/2	+1/2	0
				−1/2	−1
$\nu_{{\rm e}R}$	$\nu_{\mu R}$	$\nu_{\tau R}$	0	0	0
${\rm e}_R$	μ_R	τ_R	0	0	−1
$\begin{pmatrix}{\rm u}\\ {\rm d}\end{pmatrix}_L$	$\begin{pmatrix}{\rm c}\\ {\rm s}\end{pmatrix}_L$	$\begin{pmatrix}{\rm t}\\ {\rm b}\end{pmatrix}_L$	1/2	+1/2	+2/3
				−1/2	−1/3
${\rm u}_R$	${\rm c}_R$	${\rm t}_R$	0	0	+2/3
${\rm d}_R$	${\rm s}_R$	${\rm b}_R$	0	0	−1/3

Table 1.3: The weak-isospin structure of the fermions in the Standard Model. "L" and "R" stand for left-handed and right-handed fermions, T and T^3 are the total weak-isospin and its third component, and Q is the electric charge. Right-handed neutrinos can exist only if the neutrinos have non-zero masses. Note that the results presented in this report are insensitive to, and independent of, any small (< MeV) neutrino masses.

boson with fermions is given by the left- and right-handed couplings:

$$g_{\rm L} = \sqrt{\rho}(T^3 - Q\sin^2\theta_{\rm W}) \tag{1.5}$$
$$g_{\rm R} = \sqrt{\rho}Q\sin^2\theta_{\rm W}, \tag{1.6}$$

or, equivalently in terms of vector and axial-vector couplings:

$$g_{\rm V} \equiv g_{\rm L} - g_{\rm R} = \sqrt{\rho}(T^3 - 2Q\sin^2\theta_{\rm W}) \tag{1.7}$$
$$g_{\rm A} \equiv g_{\rm L} + g_{\rm R} = \sqrt{\rho}T^3. \tag{1.8}$$

These tree-level quantities are modified by radiative corrections to the propagators as shown in Figure 1.9. The bulk of the electro-weak corrections [20] can be absorbed into the definitions of the ρ parameter and the couplings, resulting in "effective" quantities:

$$\bar{\rho} = 1 + \Delta\rho \tag{1.9}$$
$$\mathcal{S}in^2\theta_{\rm eff} = (1 + \Delta\kappa)\sin^2\theta_{\rm W} \tag{1.10}$$
$$\mathcal{G}_V = \sqrt{\bar{\rho}}(T^3 - 2Q\mathcal{S}in^2\theta_{\rm eff}) \tag{1.11}$$
$$\mathcal{G}_A = \sqrt{\bar{\rho}}T^3, \tag{1.12}$$

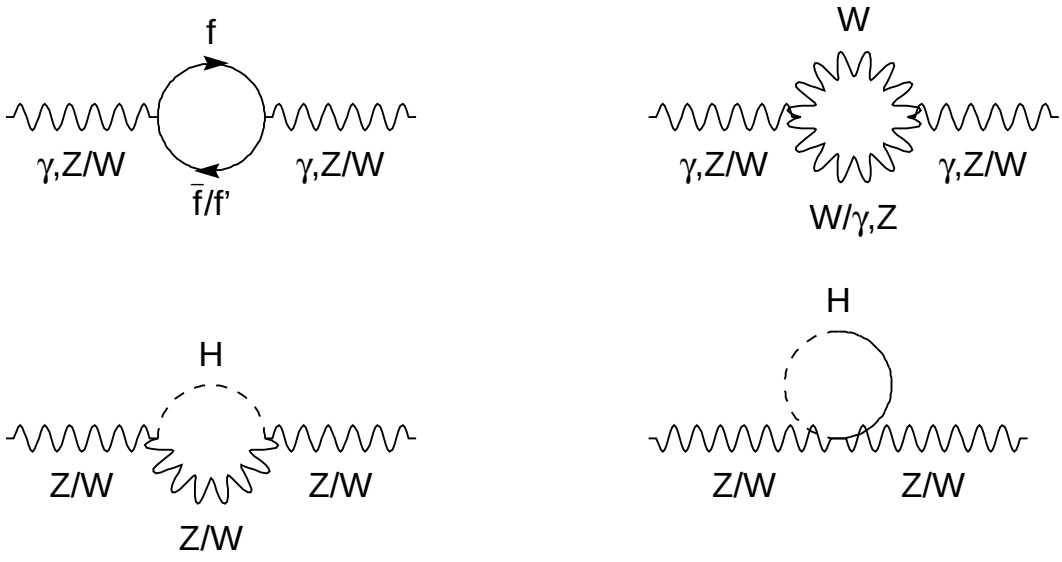

Figure 1.9: Higher order corrections to the gauge boson propagators due to boson and fermion loops.

where we use the minimal Higgs structure, resulting in $\rho = 1$. The quantities $\Delta\rho$ and $\Delta\kappa$ are small complex corrections, resulting in complex effective couplings and mixing angles. In the remainder of this report, only the real parts will be explicitly used, and thus, for simplicity, we denote

$$g_{\rm V} = g_{\rm V}^{\rm eff} \equiv \Re(\mathcal{G}_V) \tag{1.13}$$
$$g_{\rm A} = g_{\rm A}^{\rm eff} \equiv \Re(\mathcal{G}_A) \tag{1.14}$$
$$\sin^2\theta_{\rm eff} \equiv \Re(\mathcal{S}in^2\theta_{\rm eff}). \tag{1.15}$$

The distinction, however, will be kept explicit between $\sin^2\theta_{\rm W}$ given by the ratio of boson masses, and the effective parameter $\sin^2\theta_{\rm eff}$.

The leading order terms in $\Delta\rho$ and $\Delta\kappa$ are

$$\Delta\rho = \frac{3G_{\rm F}m_{\rm t}^2}{8\pi^2\sqrt{2}} - \frac{3G_{\rm F}m_{\rm W}^2}{8\pi^2\sqrt{2}}\frac{\sin^2\theta_{\rm W}}{\cos^2\theta_{\rm W}}\left(\ln\frac{m_{\rm H}^2}{m_{\rm W}^2} - \frac{5}{6}\right) + \cdots, \tag{1.16}$$
$$\Delta\kappa = \frac{3G_{\rm F}m_{\rm t}^2}{8\pi^2\sqrt{2}}\frac{\cos^2\theta_{\rm W}}{\sin^2\theta_{\rm W}} - \frac{11}{3}\frac{G_{\rm F}m_{\rm W}^2}{8\pi^2\sqrt{2}}\left(\ln\frac{m_{\rm H}^2}{m_{\rm W}^2} - \frac{5}{6}\right) + \cdots. \tag{1.17}$$

The flavour dependence is very small for all fermions, except for the b quark, where the effects of the diagrams shown in Figure 1.10 are large due to the large mass splitting between the bottom and top quarks, resulting in an additional contribution for processes involving b quarks:

$$\Delta\kappa_{\rm b} = \frac{G_{\rm F}m_t^2}{4\sqrt{2}\pi^2} + \cdots, \tag{1.18}$$
$$\Delta\rho_{\rm b} = -2\Delta\kappa_{\rm b}. \tag{1.19}$$

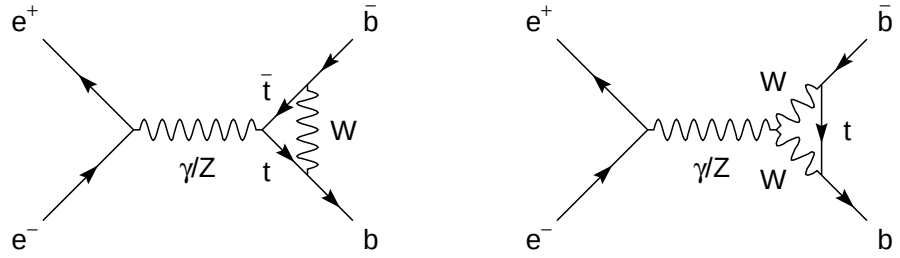

Figure 1.10: Vertex corrections to the process $Z \to b\overline{b}$.

When necessary, the parameters will be labelled, for example, ρ_b indicates the effective ρ parameter for the $b\overline{b}$ vertex, and $\sin^2\theta_{\rm eff}^{\rm lept}$ indicates the effective mixing angle for lepton vertices (assuming lepton universality).

The relationship between the couplings and the boson masses is also modified by radiative corrections:

$$G_F = \frac{\pi\alpha}{\sqrt{2}m_W^2 \sin^2\theta_W}\frac{1}{1-\Delta r}, \tag{1.20}$$

where Δr is given by

$$\Delta r = \Delta\alpha + \Delta r_w. \tag{1.21}$$

The $\Delta\alpha$ term arises from the running of the electromagnetic coupling due to fermion loops in the photon propagator, and is usually divided into 3 categories: from leptonic loops, top quark loops and light quark (u/d/s/c/b) loops:

$$\Delta\alpha(s) = \Delta\alpha_{e\mu\tau}(s) + \Delta\alpha_{top}(s) + \Delta\alpha_{had}^{(5)}(s). \tag{1.22}$$

The terms $\Delta\alpha_{e\mu\tau}(s)$ and $\Delta\alpha_{top}(s)$ can be precisely calculated, whereas the term $\Delta\alpha_{had}^{(5)}(s)$ is best determined using low-energy e^+e^- data (see Section 10.2). These effects can be absorbed into α as:

$$\alpha(s) = \frac{\alpha(0)}{1-\Delta\alpha(s)}. \tag{1.23}$$

At LEP/SLC energies, α is increased from the Thompson limit of 1/137.036 to 1/128.945. The dominant term in Δr_w is given by $\Delta\rho$, defined above:

$$\Delta r_w = -\frac{\cos^2\theta_W}{\sin^2\theta_W}\Delta\rho + \Delta r_{\rm remainder}. \tag{1.24}$$

The leading-order contributions to Δr_w depend on the top quark mass and the Higgs boson mass:

$$\Delta r^t = -\frac{3G_F m_W^2}{8\sqrt{2}\pi^2}\frac{m_t^2}{m_W^2}\frac{\cos^2\theta_W}{\sin^2\theta_W} + \cdots \tag{1.25}$$

$$\Delta r^H = \frac{11}{3}\frac{G_F m_W^2}{8\sqrt{2}\pi^2}\left(\ln\frac{m_H^2}{m_W^2} - \frac{5}{6}\right) + \cdots. \tag{1.26}$$

The radiative corrections thus have a quadratic dependence on the top quark mass and a weaker logarithmic dependence on the Higgs mass. By measuring the effects of these corrections, the

top quark mass can be determined indirectly and compared to the direct measurements. Using the measured top quark mass, information on the Higgs mass can be inferred.

It should be noted that as $G_{\rm F}$ and $m_{\rm Z}$ are better determined than $m_{\rm W}$, Equations 1.3 and 1.4 are often used to eliminate direct dependence on $m_{\rm W}$:

$$\sin^2\theta_{\rm W} = \frac{1}{2}\left(1-\sqrt{1-4\frac{\pi\alpha}{\sqrt{2}G_{\rm F}m_{\rm Z}^2}}\right) \tag{1.27}$$

$$m_{\rm W} = \frac{m_{\rm Z}^2}{2}\left(1+\sqrt{1-4\frac{\pi\alpha}{\sqrt{2}G_{\rm F}m_{\rm Z}^2}}\right). \tag{1.28}$$

In the presence of radiative corrections, these expressions are modified by replacing α with $\alpha/(1-\Delta r)$.

1.5 The process $e^+e^- \to f\bar{f}$

The differential cross-sections for fermion pair production (see Figure 1.1) around the Z resonance can be cast into a Born-type structure using the complex-valued effective coupling constants given in the previous section. Effects from photon vacuum polarisation are taken into account by the running electromagnetic coupling constant (Equation 1.23), which also acquires a small imaginary piece. Neglecting initial and final state photon radiation, final state gluon radiation and fermion masses, the electroweak kernel cross-section for unpolarised beams can thus be written as the sum of three contributions, from γ and Z exchange and from their interference [21],

$$\begin{aligned}
&\frac{2s}{\pi}\frac{1}{N_c^{\rm f}}\frac{d\sigma_{\rm ew}}{d\cos\theta}(e^+e^-\to f\bar{f}) \;=\\
&\underbrace{|\alpha(s)Q_{\rm f}|^2\,(1+\cos^2\theta)}_{\sigma^\gamma}\\
&\underbrace{-8\Re\left\{\alpha^*(s)Q_{\rm f}\chi(s)\left[\mathcal{G}_{{\rm V}e}\mathcal{G}_{{\rm V}f}(1+\cos^2\theta)+2\mathcal{G}_{{\rm A}e}\mathcal{G}_{{\rm A}f}\cos\theta\right]\right\}}_{\gamma-{\rm Z\ interference}}\\
&\underbrace{\begin{array}{c}+16|\chi(s)|^2\left[(|\mathcal{G}_{{\rm V}e}|^2+|\mathcal{G}_{{\rm A}e}|^2)(|\mathcal{G}_{{\rm V}f}|^2+|\mathcal{G}_{{\rm A}f}|^2)(1+\cos^2\theta)\right.\\ \left.+8\Re\left\{\mathcal{G}_{{\rm V}e}{\mathcal{G}_{{\rm A}e}}^*\right\}\Re\left\{\mathcal{G}_{{\rm V}f}{\mathcal{G}_{{\rm A}f}}^*\right\}\cos\theta\right]\end{array}}_{\sigma^{\rm Z}}
\end{aligned} \tag{1.29}$$

with

$$\chi(s) = \frac{G_{\rm F}m_{\rm Z}^2}{8\pi\sqrt{2}}\frac{s}{s-m_{\rm Z}^2+is\Gamma_{\rm Z}/m_{\rm Z}}. \tag{1.30}$$

where θ is the scattering angle of the out-going fermion with respect to the direction of the e^- and the colour factor $N_c^{\rm f}$ is one for leptons (f=e, μ, τ) and three for quarks (f=u, d, s, c, b), and $\chi(s)$ is the propagator term with a Breit-Wigner denominator with an s-dependent width.

The $1+\cos^2\theta$ terms in the above formula contribute to the total cross-section, whereas the terms multiplying $\cos\theta$ contribute only to the forward-backward asymmetries for an experimental acceptance symmetric in $\cos\theta$. The total cross-section is completely dominated by Z exchange. The γ–Z interference determines the energy dependence of the forward-backward

asymmetries and dominates at off-peak energies, but the leading contribution from the real parts of the couplings vanishes at $\sqrt{s} = m_{\mathrm{Z}}$.

In Bhabha final states, $\mathrm{e^+e^-} \to \mathrm{e^+e^-}$, also the t-channel diagrams contribute to the cross-sections, with a very dominant photon contribution at large $\cos\theta$, *i.e.*, in the forward direction. This contribution, and also its interference with the s-channel, add to the pure s-channel cross-section for $\mathrm{e^+e^-} \to \mathrm{e^+e^-}$. (See Section 2.3.2 for details.)

The definition of the mass and width with an s-dependent width term in the Breit-Wigner denominator is suggested [22] by phase-space and the structure of the electroweak radiative corrections within the Standard Model. It is different from another commonly used definition, the real part of the pole position in the energy-squared plane, where the propagator term takes the form $\chi(s) \propto s/(s - \overline{m}_{\mathrm{Z}}{}^2 + i\overline{m}_{\mathrm{Z}}\overline{\Gamma}_{\mathrm{Z}})$. It should be noted, however, that this fundamental choice of definition has limited consequences to the analysis. Under the transformations $\overline{m}_{\mathrm{Z}} = m_{\mathrm{Z}}/\sqrt{1 + \Gamma_{\mathrm{Z}}^2/m_{\mathrm{Z}}^2}$ and $\overline{\Gamma}_{\mathrm{Z}} = \Gamma_{\mathrm{Z}}/\sqrt{1 + \Gamma_{\mathrm{Z}}^2/m_{\mathrm{Z}}^2}$, the two formulations lead to *exactly* equivalent resonance shapes.

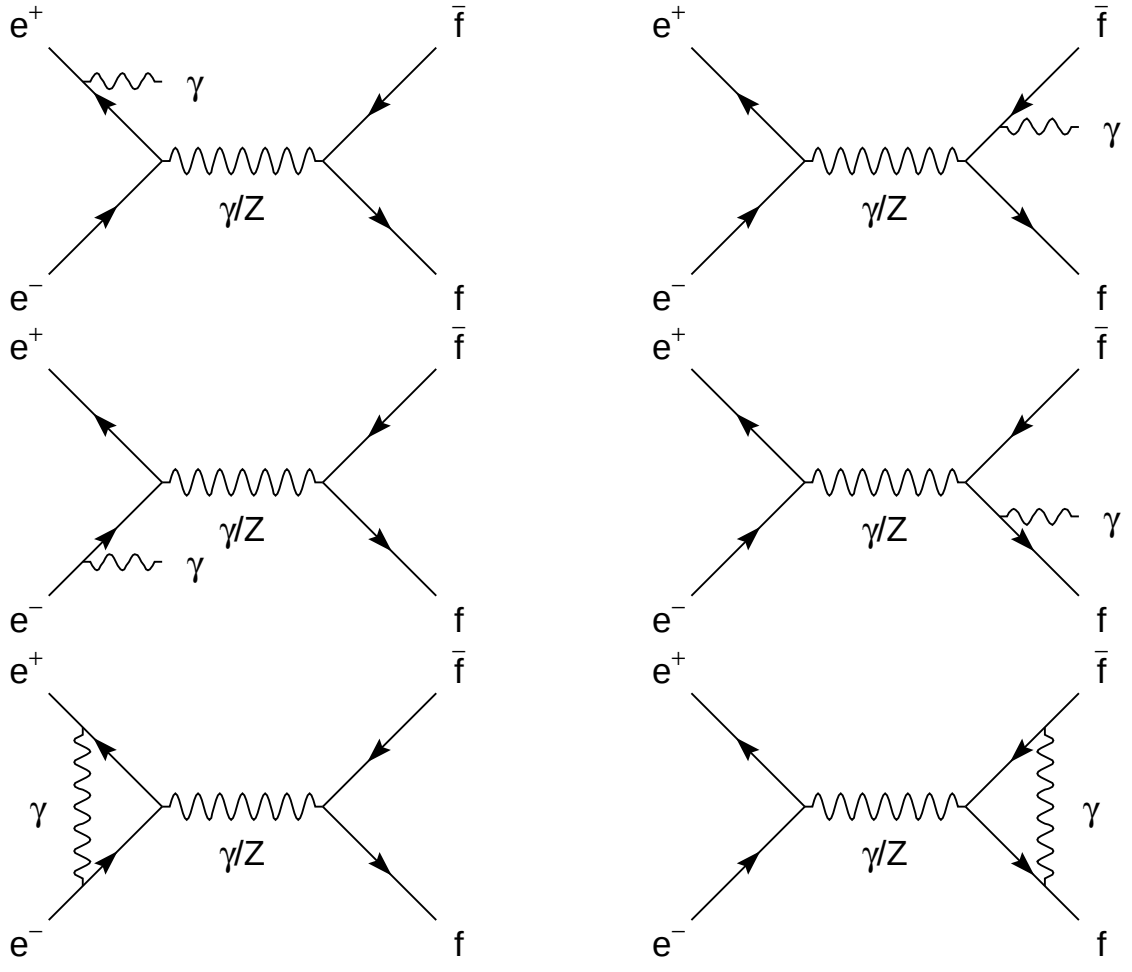

Figure 1.11: QED corrections to fermion-pair production.

Photon radiation (Figure 1.11) from the initial and final states, and their interference, is conveniently treated by convoluting the electroweak kernel cross-section, $\sigma_{ew}(s)$, with a QED

radiator, $H_{\rm QED}^{\rm tot}$,

$$\sigma(s) = \int_{4m_{\rm f}^2/s}^{1} dz H_{\rm QED}^{\rm tot}(z,s)\sigma_{ew}(zs). \tag{1.31}$$

The difference between the forward and backward cross-sections entering into the determination of the forward-backward asymmetries, $\sigma_{\rm F} - \sigma_{\rm B}$, is treated in the same way using a radiator function $H_{\rm QED}^{\rm FB}$. The effects of these QED corrections on the cross-sections and asymmetries are shown in Figure 1.12 At the peak the QED de-convoluted cross-section is 36% larger than the measured one, and the peak position is shifted downwards by about 100 MeV. The estimated precision of these important corrections is discussed in Section 2.3.4.

The partial Z decay widths are defined inclusively, *i.e.* they contain QED and QCD final state corrections and the contribution from the imaginary parts of the effective couplings,

$$\Gamma_{\rm f\bar{f}} = N_c^{\rm f}\frac{G_{\rm F}m_{\rm Z}^3}{6\sqrt{2}\pi}\left(|\mathcal{G}_{{\rm A}f}|^2 R_{\rm Af} + |\mathcal{G}_{{\rm V}f}|^2 R_{\rm Vf}\right) + \Delta_{ew/QCD}. \tag{1.32}$$

The radiator factors $R_{\rm Vf}$ and $R_{\rm Af}$ take into account final state QED and QCD corrections as well as non-zero fermion masses; $\Delta_{ew/QCD}$ accounts for small contributions from non-factorisable electroweak/QCD corrections. The inclusion of the imaginary parts of the couplings in the definition of the leptonic width, $\Gamma_{\ell\ell}$, leads to changes of 0.15 per-mil corresponding to only 15% of the LEP-combined experimental error on $\Gamma_{\ell\ell}$. The primary reason to define the partial widths including final state corrections and the contribution of the imaginary terms of the couplings is to allow the straightforward addition of the partial widths to yield the full width of the Z boson. The QCD corrections only affect final states containing quarks. To first order in $\alpha_{\rm S}$, the QCD corrections are

$$R_{\rm A,QCD} = R_{\rm V,QCD} = R_{\rm QCD} = 1 + \frac{\alpha_{\rm S}}{\pi} + \cdots \tag{1.33}$$

A measurement of the hadronic partial width can thus be used to determine $\alpha_{\rm S}$.

The total cross-section arising from the $\cos\theta$-symmetric Z production term can also be written in terms of the partial decay widths of the initial and final states, $\Gamma_{\rm ee}$ and $\Gamma_{\rm f\bar{f}}$,

$$\sigma_{\rm ff}^{\rm Z} = \sigma_{\rm ff}^{\rm peak}\frac{s\Gamma_{\rm Z}^2}{(s-m_{\rm Z}^2)^2 + s^2\Gamma_{\rm Z}^2/m_{\rm Z}^2}, \tag{1.34}$$

where

$$\sigma_{\rm ff}^{\rm peak} = \frac{1}{1+\delta_{\rm QED}}\sigma_{\rm ff}^0 \tag{1.35}$$

and

$$\sigma_{\rm ff}^0 = \frac{12\pi}{m_{\rm Z}^2}\,\frac{\Gamma_{\rm ee}\Gamma_{\rm f\bar{f}}}{\Gamma_{\rm Z}^2}. \tag{1.36}$$

The term $1/(1+\delta_{\rm QED})$ removes the final state QED correction included in the definition of $\Gamma_{\rm ee}$, and is given by $\delta_{\rm QED} = \frac{3}{4}Q_{\rm f}^2\alpha/\pi + \cdots$.

The overall hadronic cross-section is parameterised in terms of the hadronic width given by the sum over all quark final states,

$$\Gamma_{\rm had} = \sum_{\rm q,\ q\neq t} \Gamma_{\rm q\bar{q}}. \tag{1.37}$$

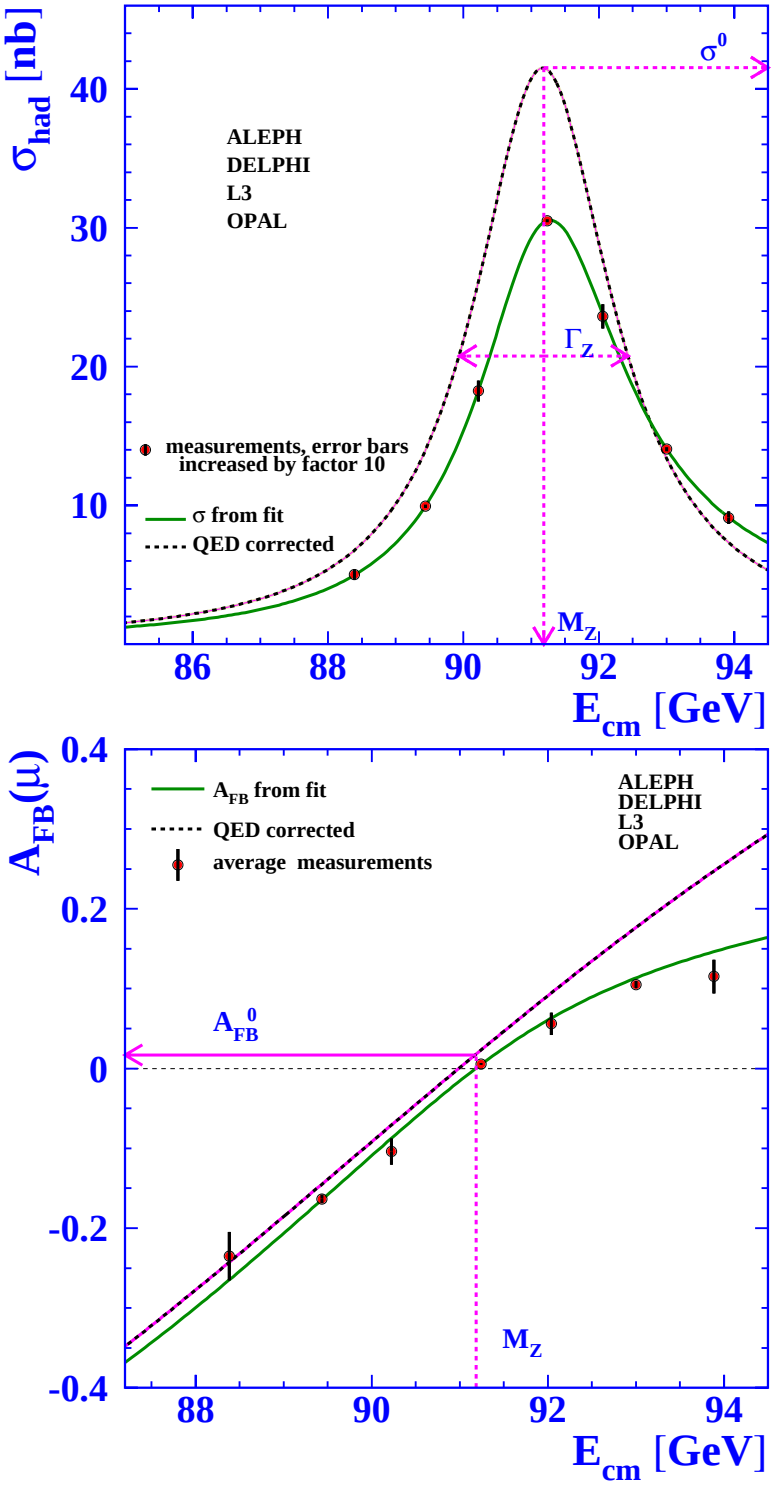

Figure 1.12: Average over measurements of the hadronic cross-sections (top) and of the muon forward-backward asymmetry (bottom) by the four experiments, as a function of centre-of-mass energy. The full line represents the results of model-independent fits to the measurements, as outlined in Section 1.5. Correcting for QED photonic effects yields the dashed curves, which define the Z parameters described in the text.

The invisible width from Z decays to neutrinos, $\Gamma_{\rm inv} = N_\nu \Gamma_{\nu\nu}$, where N_ν is the number of light neutrino species, can be determined from the measurements of the decay widths to all visible final states and the total width,

$$\Gamma_{\rm Z} = \Gamma_{\rm ee} + \Gamma_{\mu\mu} + \Gamma_{\tau\tau} + \Gamma_{\rm had} + \Gamma_{\rm inv}. \tag{1.38}$$

Because the measured cross-sections depend on products of the partial widths and also on the total width, the widths constitute a highly correlated parameter set. In order to reduce correlations among the fit parameters, an experimentally-motivated set of six parameters is used to describe the total hadronic and leptonic cross-sections around the Z peak. These are

- the mass of the Z, $m_{\rm Z}$, and its total width, $\Gamma_{\rm Z}$;
- the "hadronic pole cross-section",

$$\sigma^0_{\rm h} \equiv \frac{12\pi}{m^2_{\rm Z}} \frac{\Gamma_{\rm ee}\Gamma_{\rm had}}{\Gamma^2_{\rm Z}}; \tag{1.39}$$

- the ratios

$$R^0_{\rm e} \equiv \Gamma_{\rm had}/\Gamma_{\rm ee},\ R^0_\mu \equiv \Gamma_{\rm had}/\Gamma_{\mu\mu} \ \text{ and } \ R^0_\tau \equiv \Gamma_{\rm had}/\Gamma_{\tau\tau}. \tag{1.40}$$

- for those hadronic final states where the primary quarks can be identified, additional ratios can be defined:

$$R^0_{\rm q} \equiv \Gamma_{\rm q\bar{q}}/\Gamma_{\rm had},\ e.g.\ R^0_{\rm b} = \Gamma_{\rm b\overline{b}}/\Gamma_{\rm had}. \tag{1.41}$$

  These ratios have traditionally been treated independently of the above set, as described in Chapters 5 and 6.

It is perhaps useful to point out that if the Z had no invisible width, all partial widths could be determined without knowledge of the absolute scale of the cross-sections. Not surprisingly, therefore, the measurement of $\Gamma_{\rm inv}$ is particularly sensitive to the cross-section scale. Assuming lepton universality, and defining $R^0_{\rm inv} = \Gamma_{\rm inv}/\Gamma_{\ell\ell}$, Equations 1.38 and 1.39 can be combined to yield

$$R^0_{\rm inv} = \left(\frac{12\pi R^0_\ell}{\sigma^0_{\rm h} m^2_{\rm Z}}\right)^{\frac{1}{2}} - R^0_\ell - 3, \tag{1.42}$$

where the dependence on the absolute cross-section scale is explicit.

The leading contribution from γ–Z interference is proportional to the product of the vector couplings of the initial and final states and vanishes at $\sqrt{s} = m_{\rm Z}$, but becomes noticeable at off-peak energies and therefore affects the measurement of the Z mass. Because a determination of all quark couplings is not possible, the γ–Z interference term in the hadronic final state is fixed to its predicted Standard Model value in the analysis. The implications of this are discussed in Section 2.4.3.

Three additional parameters are needed to describe the leptonic forward-backward asymmetries. These are the "pole asymmetries", $A^{0,{\rm e}}_{\rm FB}$, $A^{0,\mu}_{\rm FB}$ and $A^{0,\tau}_{\rm FB}$ for the processes $\rm e^+e^- \to e^+e^-$, $\rm e^+e^- \to \mu^+\mu^-$ and $\rm e^+e^- \to \tau^+\tau^-$. Contrary to the case of the partial widths which are defined using the full complex couplings in order to ensure that the sum over all partial widths

equals the total width, the pole asymmetries are defined purely in terms of the real parts of the effective Z couplings,

$$A_{\rm FB}^{0,\rm f} \equiv \frac{3}{4}\mathcal{A}_{\rm e}\mathcal{A}_{\rm f} \text{ with} \tag{1.43}$$

$$\mathcal{A}_{\rm f} = \frac{2g_{\rm Vf}g_{\rm Af}}{g_{\rm Vf}^2+g_{\rm Af}^2}. \tag{1.44}$$

Due to the smallness of the leptonic forward-backward asymmetry at $\sqrt{s} = m_{\rm Z}$, QED corrections are as large as $A_{\rm FB}^{0,\ell}$ itself. Off-peak the contributions from $\gamma-{\rm Z}$ interference to the asymmetries become even larger. Since the slope of the asymmetry as a function of energy is proportional to the axial-vector couplings of the Z, which are well-determined by the measured cross-sections, only the small imaginary parts of the couplings remain to give asymmetry contributions which must be calculated rather than experimentally determined. Here it must be noted that although only the real parts of the couplings are used in the definition of the pole asymmetries, the complete complex couplings are used in the extraction of the pole asymmetries from the measured asymmetries.

The forward-backward asymmetries for hadronic states with identified quarks can also be measured, resulting in determinations of $A_{\rm FB}^{\rm q\overline{q}}$. Following the purely leptonic case, the quark pole asymmetries are corrected for QCD effects, QED radiation, γ exchange and $\gamma-{\rm Z}$ interference.

1.6 Polarised cross-sections and asymmetries

The above neglects any information concerning helicities of the incoming or outgoing particles. There are, however, four helicity configurations which are involved: left- or right-handed incoming electrons and left- or right-handed outgoing fermions. These configurations must be taken into account when dealing with any processes where polarised initial or final states are important. Taking only the Z exchange diagrams and only real couplings*, one can define the following four differential cross-sections:

$$\frac{d\sigma_{ll}}{d\cos\theta} \propto g_{\rm Le}^2 g_{\rm Lf}^2(1+\cos\theta)^2 \tag{1.45}$$

$$\frac{d\sigma_{rr}}{d\cos\theta} \propto g_{\rm Re}^2 g_{\rm Rf}^2(1+\cos\theta)^2 \tag{1.46}$$

$$\frac{d\sigma_{lr}}{d\cos\theta} \propto g_{\rm Le}^2 g_{\rm Rf}^2(1-\cos\theta)^2 \tag{1.47}$$

$$\frac{d\sigma_{rl}}{d\cos\theta} \propto g_{\rm Re}^2 g_{\rm Lf}^2(1-\cos\theta)^2. \tag{1.48}$$

From these, a set of four independent cross-sections can be defined:

$$\sigma_{\rm sum} = \sigma_{ll}+\sigma_{rr}+\sigma_{lr}+\sigma_{rl} \tag{1.49}$$

$$\sigma_{\rm LR} = \sigma_{ll}+\sigma_{lr}-\sigma_{rl}-\sigma_{rr} \tag{1.50}$$

$$\sigma_{\rm pol} = \sigma_{ll}+\sigma_{rl}-\sigma_{lr}-\sigma_{rr} \tag{1.51}$$

$$\sigma_{\rm FB} = \sigma_{ll}+\sigma_{rr}-\sigma_{lr}-\sigma_{rl} \tag{1.52}$$

The expression $\sigma_{\rm LR}$ corresponds to the difference in cross-sections between left- and right-handed incoming electrons, and can only be measured at SLC, since at LEP the incoming

*As in the previous section, the effects of radiative corrections, including the imaginary parts of couplings are taken into account in the analysis. They are neglected here to allow a clearer view of the helicity structure.

beams are not polarised. At LEP, the expression $\sigma_{\rm sum}$ is twice the total cross-section, since the incoming electron beam is 50% left-handed and 50% right-handed, and thus each term in the sum has a weight of $\frac{1}{2}$. Similarly, $\sigma_{\rm pol}$ is twice the difference in cross-sections between outgoing left-handed and right-handed fermions. $\sigma_{\rm FB}$ is $\frac{8}{3}$ times the difference between the cross-sections for outgoing fermions in the forward hemisphere and in the backward hemisphere (one factor of two for the incoming polarisations and a factor $\frac{4}{3}$ for the integral of the angular distribution over one hemisphere).

From these cross-sections, several asymmetries can be extracted, which can be related directly to $g_{\rm L}$ and $g_{\rm R}$ (or, as is used in this report, $g_{\rm V}$ and $g_{\rm A}$). Using the definition of $\mathcal{A}$ given in Equation 1.44, the asymmetries are

$$A_{\rm FB} = \frac{3}{4}\frac{\sigma_{\rm FB}}{\sigma_{\rm sum}} = \frac{3}{4}\mathcal{A}_{\rm e}\mathcal{A}_{\rm f} \tag{1.53}$$

$$A_{\rm LR} = \frac{\sigma_{\rm LR}}{\sigma_{\rm sum}} = \mathcal{A}_{\rm e} \tag{1.54}$$

$$A_{\rm pol} = \frac{\sigma_{\rm pol}}{\sigma_{\rm sum}} = \mathcal{A}_{\rm f}(= -\mathcal{P}_{\rm f}). \tag{1.55}$$

$\mathcal{P}_{\rm f}$ is the polarisation of the final state. It must be noted that experimentally the forward-backward asymmetry is measured by

$$A_{\rm FB} = \frac{N(\cos\theta_{\rm f} > 0) - N(\cos\theta_{\rm f} < 0)}{N_{\rm tot}}, \tag{1.56}$$

where $N(\cos\theta_{\rm f} > 0)$ is the number of events where the outgoing fermion is scattered in the forward direction, $N(\cos\theta_{\rm f} < 0)$ is the number of events with the fermion scattered into the backward direction, and $N_{\rm tot}$ is the total number of events. Given the functional form of Equations 1.45–1.48, this is equivalent to $\frac{3}{4}\frac{\sigma_{\rm FB}}{\sigma_{\rm sum}}$.

Similarly, $A_{\rm LR}$ is measured form the asymmetry in the Z production cross-section for left-handed and right-handed electron bunches. Thus,

$$A_{\rm LR} = \frac{N_{\rm L} - N_{\rm R}}{N_{\rm L} + N_{\rm R}}\frac{1}{\langle\mathcal{P}_e\rangle}, \tag{1.57}$$

where, irrespective of the final state $N_{\rm L}$ is the number of Z bosons produced for left-handed, $N_{\rm R}$ is the corresponding number for right-handed bunches and $\langle\mathcal{P}_e\rangle$ is the luminosity-weighted average electron polarisation. (The electron beam was not 100% polarised, but the magnitude was the same for left- and right-polarisations, see Chapter 3.)

By comparing the polarised cross-sections $\sigma_{\rm pol}$ and $\sigma_{\rm LR}$ in the forward and backward hemispheres, two additional asymmetries can be measured:

$$A_{\rm FB}^{\rm pol} = A_{\rm pol}(F) - A_{\rm pol}(B) = \frac{3}{4}\mathcal{A}_{\rm e} \tag{1.58}$$

$$A_{\rm FBLR} = A_{\rm LR}(F) - A_{\rm LR}(B) = \frac{3}{4}\mathcal{A}_{\rm f}. \tag{1.59}$$

The measurement of any of the polarised asymmetries requires the polarisation of either the initial state or the final state to be determined. The final state polarisation can only be determined for tau final states, where the charged current tau decay serves as a polarisation analyser. Therefore, $\mathcal{A}_\tau$ and $\mathcal{A}_{\rm e}$ can be determined at LEP using measurements of tau polarisation. In contrast, with the initial state polarisation available at SLC, $\mathcal{A}_{\rm e}$ can be measured using all final states and $\mathcal{A}_{\rm f}$ can be measured for each final state that can be isolated. These include

the electron, muon, tau, b-quark, c-quark and s-quark final states. Using the measurements of $\mathcal{A}_e$, the parameters $\mathcal{A}_\mu$, $\mathcal{A}_\tau$, $\mathcal{A}_b$ and $\mathcal{A}_c$ can be inferred from forward-backward asymmetry measurements at LEP. Thus, the LEP and SLC results form a complementary and practically complete set of $\mathcal{A}$ measurements.

1.7 Pseudo-observables and Standard Model remnants

The parameters introduced in Sections 1.5 and 1.6 describing the main features of all measurements around the Z resonance are not "realistic observables" as the underlying measurements themselves, but are defined quantities with significant theoretical corrections. Therefore they are commonly named "pseudo-observables". Where necessary, the pseudo-observables will be denoted by a superscript 0, *e.g.*, σ_{had} is the measured hadronic cross-section, whereas σ^0_h is the pole-cross-section derived from the measurements. Similarly, R_b is the measured b quark cross-section divided by the hadronic cross-section ($\sigma_{b\overline{b}}/\sigma_{had}$) and R^0_b is the derived ratio of Z boson partial widths, $\Gamma_{b\overline{b}}/\Gamma_{had}$.

The bulk of the differences between the realistic and pseudo-observables is due to QED effects; differences between the pseudo-observables and the QED de-convoluted observables at $\sqrt{s} = m_Z$, arising from the interference between photon and Z diagrams and from the interplay between the real and imaginary parts of the photon and Z couplings, are small in the Standard Model. The calculated value of σ^0_{ff}, given in terms of the partial decay widths, agrees to better than 0.05% for both hadrons and leptons with the QED de-convoluted cross-sections without the photon exchange contribution at $\sqrt{s} = m_Z$. This is only a fraction of the LEP combined experimental error. The difference between $A^{0,\ell}_{FB}$ and the QED de-convoluted forward-backward asymmetry at the peak amounts to 0.0013, which is slightly larger than the LEP combined error on $A^{0,\ell}_{FB}$. It is therefore important to treat the imaginary parts correctly, but there is no sensitivity of the measurements to Standard Model parameters entering through the imaginary parts.

However, these pseudo-observables cannot be considered as truly model-independent, because imaginary parts of the couplings as well as the γ–Z interference in the hadronic final state need to be fixed to their Standard Model values. This leads to small "Standard Model remnants" in any attempted "model-independent" definition of the pseudo-observables. These remnants disturb slightly the relationships given in this section; however, the effects are small with respect to the experimental errors. It should be stressed that the Standard Model is only used to fix these remnants in the later analyses (*e.g.*, Chapters 9 and 10). More details about the treatment of imaginary parts and Standard Model remnants in the theory programs TOPAZ0 [23] and ZFITTER [24] are given in Reference 25. These computer codes were developed independently, and even use different renormalization schemes ($\overline{\text{MS}}$ for TOPAZ0 and on-shell for ZFITTER). Both include the best up-to-date knowledge on QED and electroweak corrections within the minimal Standard Model and thus provide the connection between the realistic observables and the pseudo-observables. In addition, they are used to determine the important Standard Model parameters, such as the Higgs boson mass, given the pseudo- or realistic observables.

Chapter 2

The Z lineshape and the leptonic forward-backward charge asymmetries

The analyses described in this section focus on the measurements of the total production cross-sections in the four channels $e^+e^- \to q\overline{q}$, e^+e^-, $\mu^+\mu^-$ and $\tau^+\tau^-$ at different centre-of-mass energies within $\pm 3\,\mathrm{GeV}$ around $\sqrt{s} = m_Z$. Decays to neutrinos escape direct detection and are referred to as "invisible decays". Since quark flavours cannot be completely separated, an inclusive selection of all hadronic final states is performed here. The expected approximate branching fractions of the Z are 70 %, 20 % and 10 % to hadrons, neutrinos and charged leptons, respectively. The full LEP-I data set consists of about 4×200 measurements of hadronic and leptonic cross-sections and of leptonic forward-backward asymmetries at different centre-of-mass energies. Only the forward-backward asymmetries in the leptonic channels are considered here, because asymmetry measurements in $q\overline{q}$ final states require dedicated flavour tagging techniques, see Chapter 5, or inclusive methods as described in Chapter 6.

From their measurements of cross-sections and asymmetries each experiment extracted the set of pseudo-observables that describe the differential cross-section around the Z resonance, which comprise the mass, m_Z, and width, Γ_Z, of the Z, the total pole cross-section for $q\overline{q}$ production, σ^0_h, the ratio of the hadronic and leptonic decay widths, R^0_ℓ, and the leptonic forward-backward asymmetry at the peak, $A^{0,\ell}_{FB}$, as defined in Section 1.4. Although the chosen set of pseudo-observables resembles the real measurements after QED corrections, small correlations among them remain; these make it necessary to extract them simultaneously in a multi-parameter fit to all measurements of cross-sections and forward-backward asymmetries. The electroweak libraries used for that purpose are ZFITTER [24] and TOPAZ0 [23], which include QED and QCD corrections as well as those electroweak corrections according to the Standard Model which are not described by only the real parts of the Z couplings, as was discussed already in Section 1.7.

After a brief description of the key features of the analyses (Section 2.1) and the presentation of the individual experimental results(Section 2.2), the main emphasis in the following sections is given to the hitherto unpublished aspects of the combination procedure, namely the errors common to all experiments (Section 2.3) and the combination procedure, which is based on the four sets of pseudo-observables (Section 2.4). Cross-checks of the combination procedure are also discussed in this section, which is followed by the presentation of the combined result. Re-parametrisations in terms of partial widths and branching fractions will be given later (see Chapter 7).

2.1 Measurements of total cross-sections and forward-backward asymmetries

The main features of the event selection procedures for measurements of the total hadronic and the leptonic cross-sections and of the leptonic forward-backward asymmetries are briefly described below. Detailed descriptions of the individual experimental analyses are given in References [26–29]

2.1.1 Event selection

The event selection for $q\overline{q}$, e^+e^-, $\mu^+\mu^-$ and $\tau^+\tau^-$ final states in each of the experiments is aimed at high selection efficiencies within the largest possible acceptance in order to keep corrections small.

The design of the detectors and the cleanliness of the LEP beams allowed the experiments to trigger on hadronic and leptonic Z decays with high redundancy and essentially 100% efficiency. The selections accept events with initial and final state radiation as much as possible in order to benefit from cancellations between real and virtual particle emission. Good discrimination of $q\overline{q}$ from $\ell^+\ell^-$ final states is mandatory, and excellent separation of e^+e^-, $\mu^+\mu^-$ and $\tau^+\tau^-$ permits checks of the universality of the Z couplings to the different lepton species to be carried out. Machine-induced backgrounds at LEP-I were small, and background from e^+e^- processes are restricted to two-photon reactions. Event pictures of each of the final states are shown in Figure 1.7 in Chapter 1.

The separation between leptonic and hadronic events and their distinction from two-photon reactions are exemplified in Figure 2.1, in a two-dimensional distribution of the number of charged tracks and the energy sum of all tracks calculated from the measured momenta assuming the pion mass. A peak from e^+e^- and $\mu^+\mu^-$ events at high momenta and low multiplicities is clearly separated from two-photon background at relatively low multiplicities and momenta. The intermediate momentum region at low multiplicities is populated by $\tau^+\tau^-$ events. Hadronic events populate the high multiplicity region at energies below the centre-of-mass energy, since neutral particles in the jets are not measured in the central detector. The separation of electrons and muons is achieved using also the information from the electromagnetic and hadron calorimeters and from the muon chambers.

The experiments use very detailed detector simulations [30–32] to understand the selection efficiencies. Owing to the high redundancy of the detectors, cross-checks using the data themselves are possible by comparing event samples identified with different selection criteria. Various Monte Carlo generators are interfaced to the detector simulations and are used to describe the kinematics of the physics reactions of interest: $q\overline{q}$ production with gluon radiation including phenomenological modelling of the non-perturbative hadronisation process [33–35], production of $\mu^+\mu^-$ and $\tau^+\tau^-$ final states [36,37], e^+e^- final states including the t-channel contribution [38–40], and finally e^+e^- scattering in the forward direction [41], which is dominated by t-channel photon exchange and serves as the normalisation reaction for the determination of the luminosity of the colliding e^+e^- beams. The Monte Carlo generators are used to apply corrections at the edges of the experimental acceptance, and for small extrapolations of the measured cross-sections and forward-backward asymmetries from the true experimental cuts to sets of simple cuts that can be handled at the fitting stage. In the case of $q\overline{q}$ final states, the only remaining cut after all corrections is $s' > 0.01\,s$, where $\sqrt{s'}$ is the effective centre-of-mass energy after initial-state photon radiation. The treatment of the lepton channels differs in de-

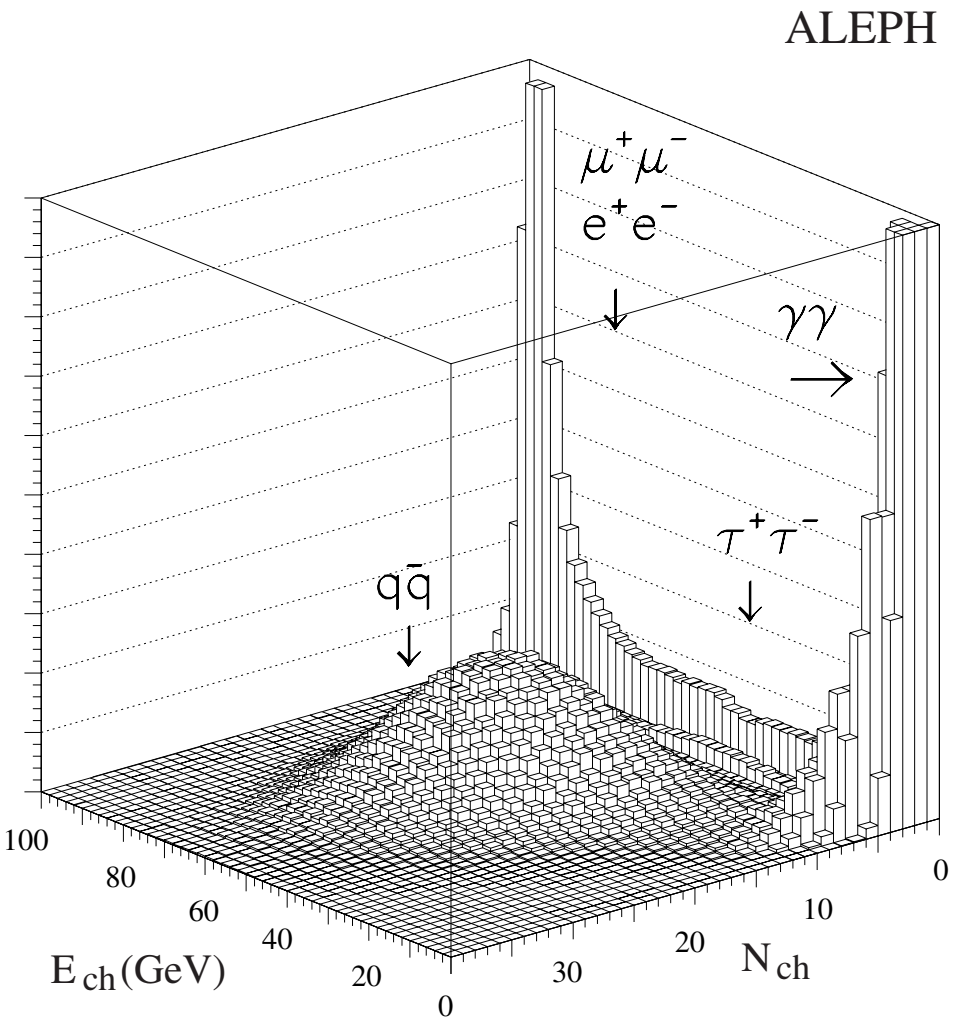

Figure 2.1: Experimental separation of the final states using only two variables, the sum of the track momenta, E_{ch}, and the track multiplicity, N_{ch},in the central detector of the ALEPH experiment.

tail among the experiments; the results are specified either with a s' cut only, within a given acceptance in the fermion production angle, $\cos\theta$, and the minimal fermion energy; additionally a cut on the maximum allowed acollinearity of the final state fermion pair may have been applied. The results quoted for the e^+e^- final state either include contributions originating from t-channel diagrams, or the t and s-t interference effects are explicitely subtracted, allowing the same treatment of e^+e^- and $\mu^+\mu^-$ or $\tau^+\tau^-$ final states in the fits for the Z parameters.

Hadronic events in the detectors are characterised by a large number of particles arising from the hadronisation process of the originally produced quark pair. This leads to high track multiplicities in the central detectors and high cluster multiplicities in the electromagnetic and hadron calorimeters. For $Z \to q\overline{q}$ events, the deposited energy is balanced along the beam line, which is generally not the case for hadronic events produced in two-photon reactions. In addition, two-photon events have an almost constant production cross-section around the Z resonance. It is thus possible to estimate the two-photon fraction directly from the data by studying the energy dependence of two event samples, one with an enriched two-photon

contribution and another with tight selection cuts for genuine $Z \to q\overline{q}$ events, which show a resonant behaviour. Background from $\tau\tau$ events is subtracted using Monte Carlo simulation.

Lepton pairs are selected by requiring low track and cluster multiplicities. Electrons are characterised by energy deposits in the electromagnetic calorimeters that match well the measured momenta in the tracking detectors. Muons have only minimum ionising energy deposits in the electromagnetic and hadron calorimeters and signals in the outer muon chambers. Tau leptons decay before reaching any detector component. Their visible decay products are either a single electron, muon or hadron, or a collimated jet consisting of three or five charged hadrons and a few neutral hadrons; in addition energy is missing due to the undetectable neutrinos. $\tau^+\tau^-$ events are therefore selected by requiring the total energy and momentum sums to be below the centre-of-mass energy to discriminate against e^+e^- and $\mu^+\mu^-$, and to be above a minimum energy to reject lepton pairs arising from two-photon reactions. The approximate direction of flight of the τ is taken to be the momentum sum of the visible decay products.

Leptonic events with photons or fermion pairs radiated from the initial- or final-state leptons are contained in the signal definition. Initial-state pairs typically remain in the beam pipe and are therefore experimentally indistinguishable from initial state photon radiation. Final-state pairs may change the selection efficiency, which is studied using four-fermion event generators [42, 43]. The classification of such four-fermion events into one of the three lepton categories is made by choosing the pair with the highest invariant mass.

2.1.2 Cross-section measurements

The total cross-section, $\sigma_{\rm tot}$, is determined from the number of selected events in a final state, N, the number of background events, $N_{\rm bg}$, the selection efficiency, ϵ, and the integrated luminosity, $\mathcal{L}$, according to $\sigma_{tot} = (N - N_{\rm bg})/(\epsilon\mathcal{L})$.

Measurement of the luminosity

The luminosity of the beams is measured [44] from the process of small-angle Bhabha scattering, with further information available in the lineshape publications [26–29]. Events with forward going electrons are recorded concurrently with all other processes, thus ensuring that they correctly reflect any data-taking inefficiencies arising from read-out dead-times and detector down-times. Furthermore, the statistical precision of this process is high, matching well even the high statistics of hadronic events at the Z resonance. The luminosity measurement requires the detection of back-to-back energy deposits by electrons and positrons close to the beam direction. Their positions and energies are precisely measured by calorimeters placed at small angles with respect to the beam line, typically covering a range in polar angle from 25 mrad to 60 mrad. Depending on the experiment, the accepted cross-section in the luminosity devices is at least twice as large as the hadronic on-peak cross-section, and therefore the statistical errors arising from the luminosity determination are small. The typical experimental signature of luminosity events is shown in Figure 2.2. The main experimental systematic error arises from the definition of the geometrical acceptance for this process. Since the angular distribution is steeply falling with increasing scattering angle ($\propto \theta^{-3}$), the precise definition of the inner radius of the acceptance region is most critical. Background arises from random coincidences between the calorimeters at the two sides and is largely beam-induced. The integrated luminosity is given by the ratio of the number of observed small-angle e^+e^- events and the calculated cross-section for this process within a given acceptance. The Bhabha cross-section at small scattering angles is dominated by the well-known QED process of t–channel scatter-

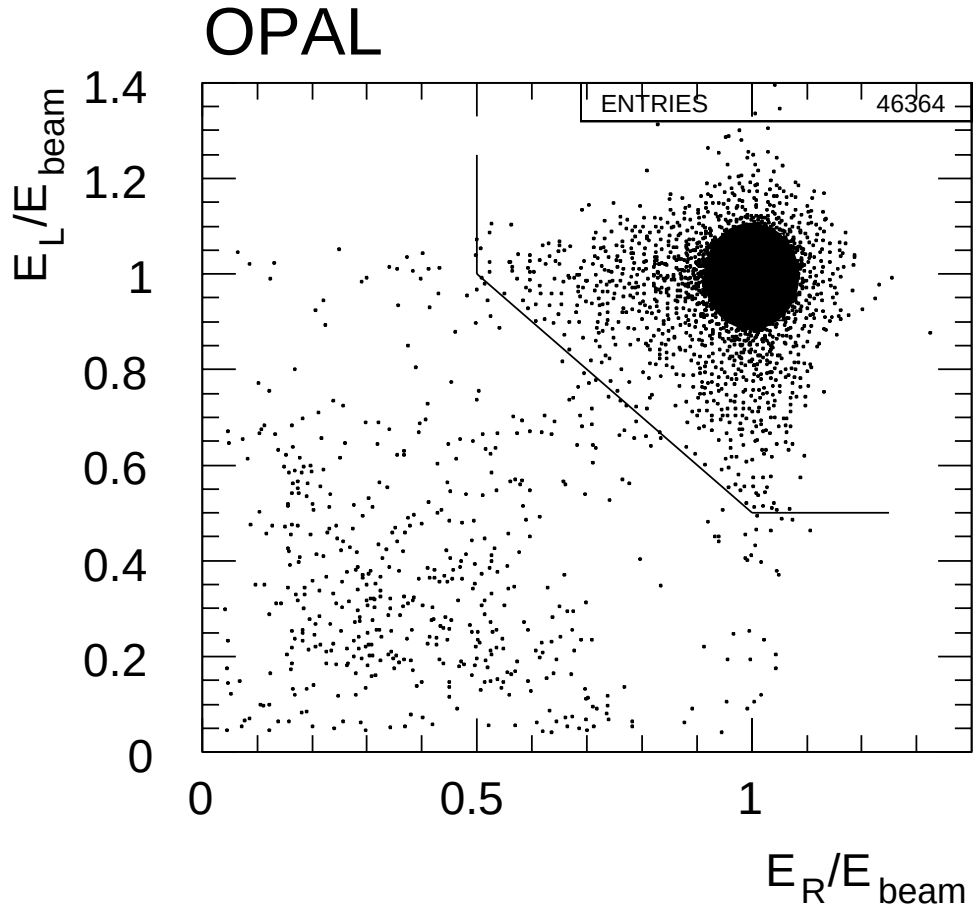

Figure 2.2: Fraction of the beam energy observed in the left and right luminosity calorimeters of the OPAL experiment, after all cuts except the one on the deposited energies. The lines indicate the acceptance region for the signal events. Initial state photon radiation leads to tails towards lower deposited energies. Background events from accidental coincidences populate the low-energy regions in both calorimeters.

ing, but nonetheless calculational uncertainties give rise to an important theoretical error of about 0.5 per-mil affecting all experiments coherently, as is discussed in Section 2.3.3. Typical experimental systematic errors on the luminosity are well below 0.1 %.

Event selection efficiency and background levels

In the hadronic channel the selection efficiencies within the acceptance are high, typically above 99 %. Backgrounds are dominated by $Z \to \tau^+\tau^-$ and non-resonant $q\overline{q}$ production from two-photon reactions. At the peak of the resonance these together contribute at a level of a few per-mil. Backgrounds in the lepton selections are typically around 1 % for e^+e^- and $\mu^+\mu^-$ and slightly larger for $\tau^+\tau^-$ final states. The dominant background in e^+e^- and $\mu^+\mu^-$ final states arises from $\tau^+\tau^-$ events, which plays no role if the total leptonic cross-section is measured. Backgrounds other than $\tau^+\tau^-$ in the e^+e^- and $\mu^+\mu^-$ channels are of $\mathcal{O}(0.1\,\%)$. Backgrounds in $\tau^+\tau^-$ events are larger, 2–3 %, and arise from low-multiplicity hadronic events, from two-photon reactions and from e^+e^- and $\mu^+\mu^-$ events with small measured lepton momenta, which may result either from undetected radiated photons or from measurement errors.

An overview of the selection efficiencies within the acceptance and of the background levels

is presented in Table 2.1. The acceptances quoted in the table are ideal ones suitable as input to the electroweak program libraries used for fitting, while the actual set of experimental cuts is more complicated. Monte Carlo event generators and detailed detector simulations in combination with dedicated corrections are used to transform the true experimental acceptances to the ideal ones. As is shown in the table, the selection efficiencies are high, above 95 % in e^+e^- and $\mu^+\mu^-$ and 70–90 % in $\tau^+\tau^-$ final states.

	ALEPH	DELPHI	L3	OPAL
$q\overline{q}$ final state				
acceptance	$s'/s > 0.01$	$s'/s > 0.01$	$s'/s > 0.01$	$s'/s > 0.01$
efficiency [%]	99.1	94.8	99.3	99.5
background [%]	0.7	0.5	0.3	0.3
e^+e^- final state				
acceptance	$-0.9 < \cos\theta < 0.7$ $s' > 4m_\tau^2$	$\lvert\cos\theta\rvert < 0.72$ $\eta < 10^\circ$	$\lvert\cos\theta\rvert < 0.72$ $\eta < 25^\circ$	$\lvert\cos\theta\rvert < 0.7$ $\eta < 10^\circ$
efficiency [%]	97.4	97.0	98.0	99.0
background [%]	1.0	1.1	1.1	0.3
$\mu^+\mu^-$ final state				
acceptance	$\lvert\cos\theta\rvert < 0.9$ $s' > 4m_\tau^2$	$\lvert\cos\theta\rvert < 0.94$ $\eta < 20^\circ$	$\lvert\cos\theta\rvert < 0.8$ $\eta < 90^\circ$	$\lvert\cos\theta\rvert < 0.95$ $m_{f\overline{f}}^2/s > 0.01$
efficiency [%]	98.2	95.0	92.8	97.9
background [%]	0.2	1.2	1.5	1.0
$\tau^+\tau^-$ final state				
acceptance	$\lvert\cos\theta\rvert < 0.9$ $s' > 4m_\tau^2$	$0.035 < \lvert\cos\theta\rvert < 0.94$ $s' > 4m_\tau^2$	$\lvert\cos\theta\rvert < 0.92$ $\eta < 10^\circ$	$\lvert\cos\theta\rvert < 0.9$ $m_{f\overline{f}}^2/s > 0.01$
efficiency [%]	92.1	72.0	70.9	86.2
background [%]	1.7	3.1	2.3	2.7

Table 2.1: Acceptances, selection efficiencies* within an idealised acceptance, and background contribution at the peak of the resonance (1994 data).

*The selection efficiencies given by the experiments were in some cases quoted for full acceptance in $\cos\theta$; here, these were corrected to the fiducial cuts in $\cos\theta$ actually used in the analyses, assuming a shape of the differential cross-section according to $(1 + \cos^2\theta)$.

The idealised acceptances are defined by the scattering angle, θ, of the negatively charged lepton in the laboratory frame, and also require a cut-off for initial-state photon radiation. The latter may either be given by a cut on the acollinearity of the two final-state leptons, η, or by an explicit cut on the invariant mass of the final-state leptons, $m_{f\overline{f}}$; alternatively, the effective centre-of-mass energy after photon radiation off the initial state, s', may be used. The experimental efficiencies for low values of $m_{f\overline{f}}$ or s' are small. Despite the differing definitions, the efficiencies given in the table are still comparable, because the acceptance difference between the wider definition $s'/s > 4m_\tau^2$ and a tight definition using an acollinearity cut at $\eta < 10^\circ$ is only 2 %.

Total cross-section

The total cross-section for the production of each final state is obtained from the efficiency and background corrected numbers of selected events normalised to the luminosity. Data taken at the same energy point and within the same year are combined into a single cross-section measurement at the average energy. As an example, the measurements of the hadronic cross-section around the three principal energies are shown in Figure 2.3. Because the hadron statistics are almost ten times larger than the lepton statistics, these measurements dominate the determination of the mass and the width of the Z.

The energy dependence of the hadronic cross-section (the "line shape") is shown in the upper plot of Figure 1.12 in Section 1.5. The energy dependence of the muon and tau cross-section is nearly identical in shape to the hadronic one. In e^+e^- final states however, diagrams involving photon exchange in the t-channel and their interference with the s-channel diagrams also contribute. The different contributions are shown as a function of centre-of-mass energy in the left-hand plot of Figure 2.4.

2.1.3 Measurements of the lepton forward-backward asymmetries

The forward-backward asymmetry, $A_{\rm FB}$, is defined by the numbers of events in which the final state lepton goes forward ($\cos(\theta_{\ell^-}) > 0$) or backward ($\cos(\theta_{\ell^-}) < 0$) with respect to the direction of the incoming electron, N_f and N_b, respectively: $A_{\rm FB} = (N_{\rm f}-N_{\rm b})/(N_{\rm f}+N_{\rm b})$. This definition of $A_{\rm FB}$ depends on the acceptance cuts applied on the production polar angle, $\cos\theta$, of the leptons. The measurements of $A_{\rm FB}(\ell^+\ell^-)$ require the determination of $\cos\theta$ and the separation of leptons and anti-leptons based on their electric charges, which are determined from the curvature of the lepton tracks in the magnetic fields of the central detectors. For $\mu^+\mu^-$ and $\tau^+\tau^-$ final states, $A_{\rm FB}$ is determined from un-binned maximum-likelihood fits to the differential cross-section distributions of the form $d\sigma/d\cos\theta \propto 1 + \cos^2\theta + 8/3\, A_{\rm FB}\cos\theta$. This procedure makes better use of the available information and hence leads to slightly smaller statistical errors. Determined this way the $A_{\rm FB}$ measurements are insensitive to any detection inefficiencies as long as these are symmetric in $\cos\theta$. Examples of the measured angular distributions for the e^+e^- and $\mu^+\mu^-$ final states are shown in Figure 2.5.

The shape of the differential cross-section in the electron final state is more complex due to contributions from the t-channel and the s-t-interference, which lead to a large number of events in which the electron is scattered in the forward direction. A maximum-likelihood fit to obtain $A_{\rm FB}(e^+e^-)$ may be performed after subtracting the t and s-t contributions, but usually the asymmetry is determined from the efficiency-corrected numbers of events with forward and backward-going electrons, according to the above definition.

The energy dependence of the forward-backward asymmetry in the $\mu^+\mu^-$ final state is shown in the lower plot of Figure 1.12 above. The forward-backward asymmetry as a function of centre-of-mass energy in the e^+e^- final state including the t, s-t contributions is illustrated in the right-hand plot of Figure 2.4

2.1.4 Systematic errors

In general, the systematic errors arising from the selection procedures are small and so the accumulated statistics can be fully exploited. Furthermore, the purely experimental errors arising from the limited understanding of detector acceptances are uncorrelated among the experiments. An overview of the experimental systematic errors is given in Table 2.2. Statistical errors per experiment are only around 0.5 per-mil in the hadronic channel and around 2.5 per-

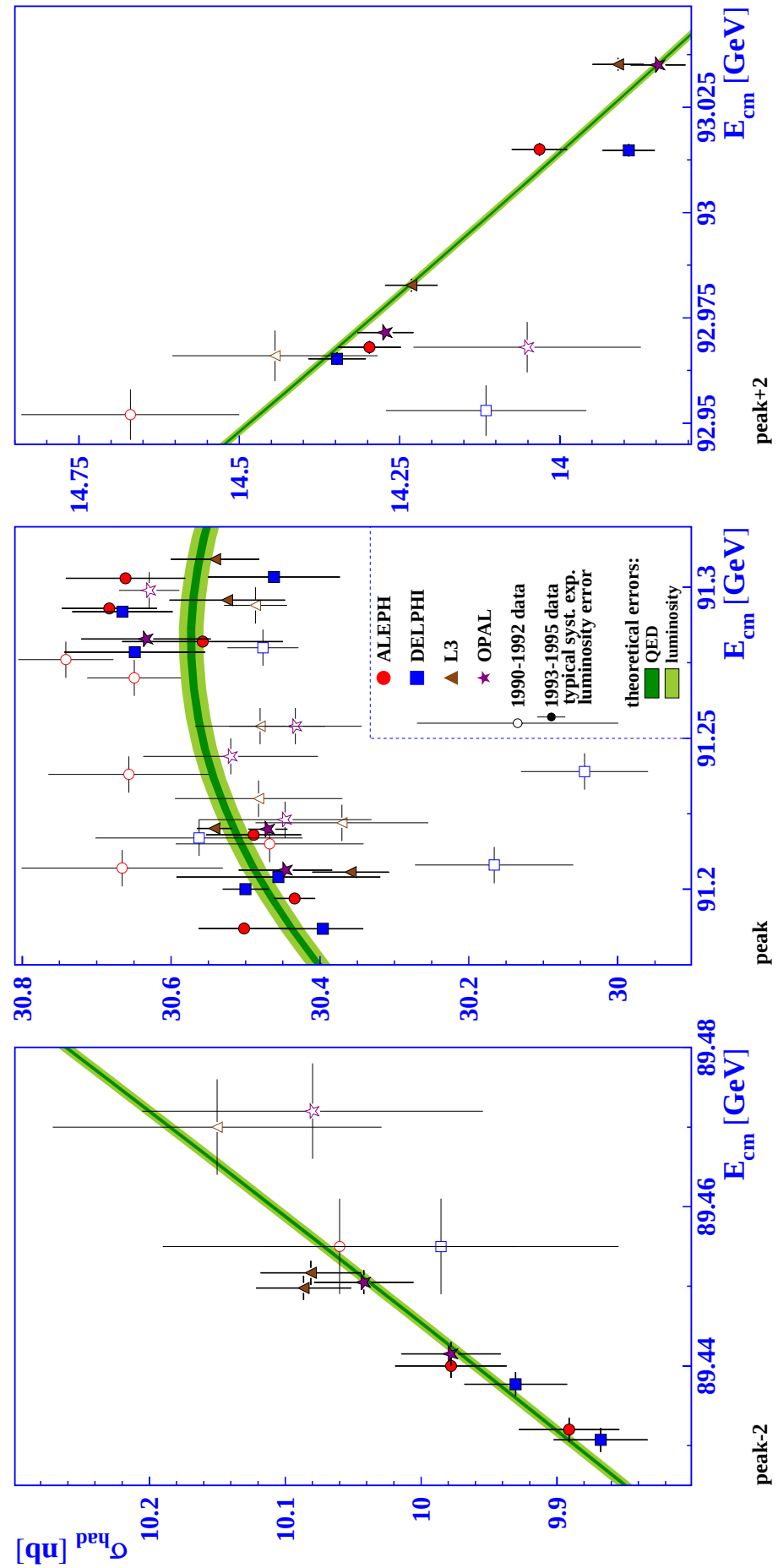

Figure 2.3: Measurements by the four experiments of the hadronic cross-sections around the three principal energies. The vertical error bars show the statistical errors only. The open symbols represent the early measurements with typically much larger systematic errors than the later ones, shown as full symbols. Typical experimental systematic errors on the determination of the luminosity are indicated in the legend; these are almost fully correlated within each experiment, but uncorrelated among the experiments. The horizontal error bars show the uncertainties in LEP centre-of-mass energy, where the errors for the period 1993–1995 are smaller than the symbol size in some cases. The bands represent the result of the model-independent fit to all data, including the two most important common theoretical errors from initial-state photon radiation and from the calculations of the small-angle Bhabha cross-section.

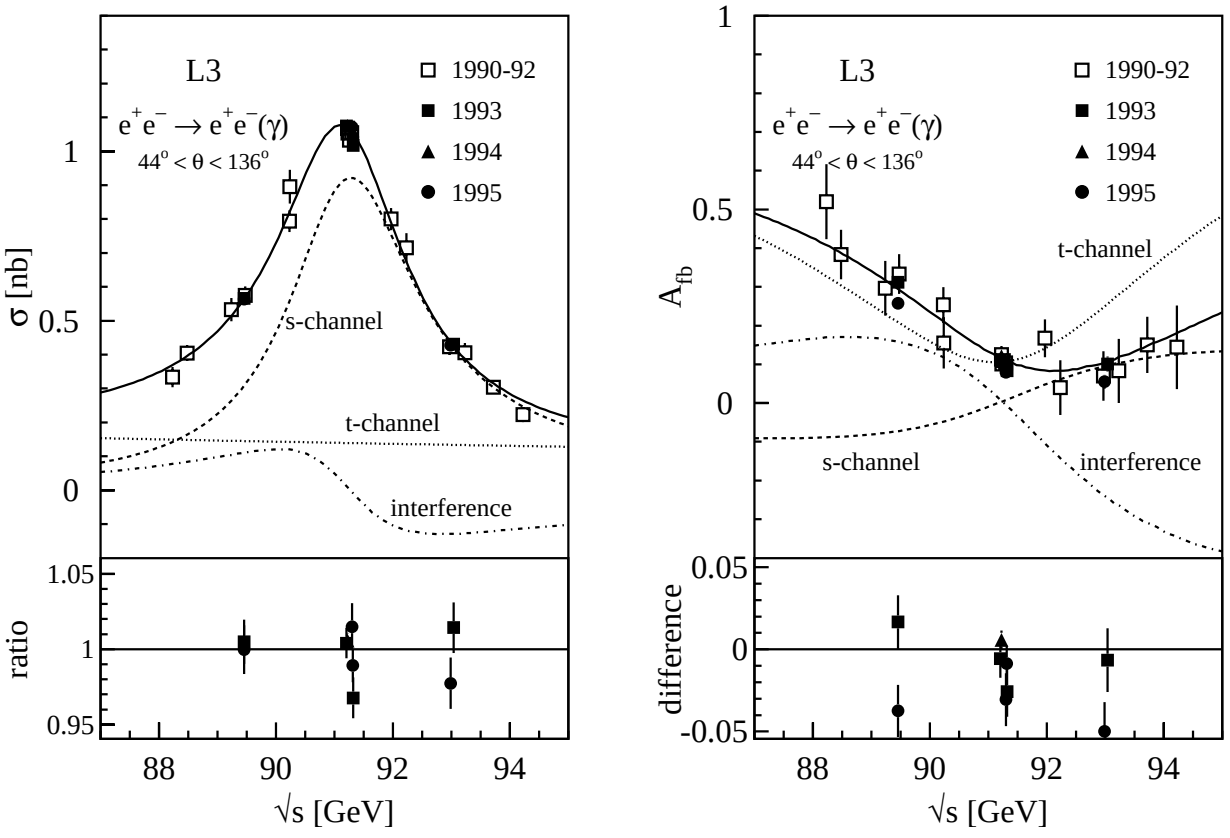

Figure 2.4: The energy dependence and the contributions from the s and t-channel diagrams and from the s-t interference for observables in the e^+e^- channel. Shown are the total cross-section (left) and the difference between the forward and backward cross-sections after normalisation to the total cross section (right). The data points measured by the L3 collaboration refer to an angular acceptance of $|\cos\theta| < 0.72$, an acollinearity $\eta < 25^\circ$ and a minimum energy of $E_{e^\pm} \geq 1$ GeV. The lines represent the model-independent fit to all L3 data.

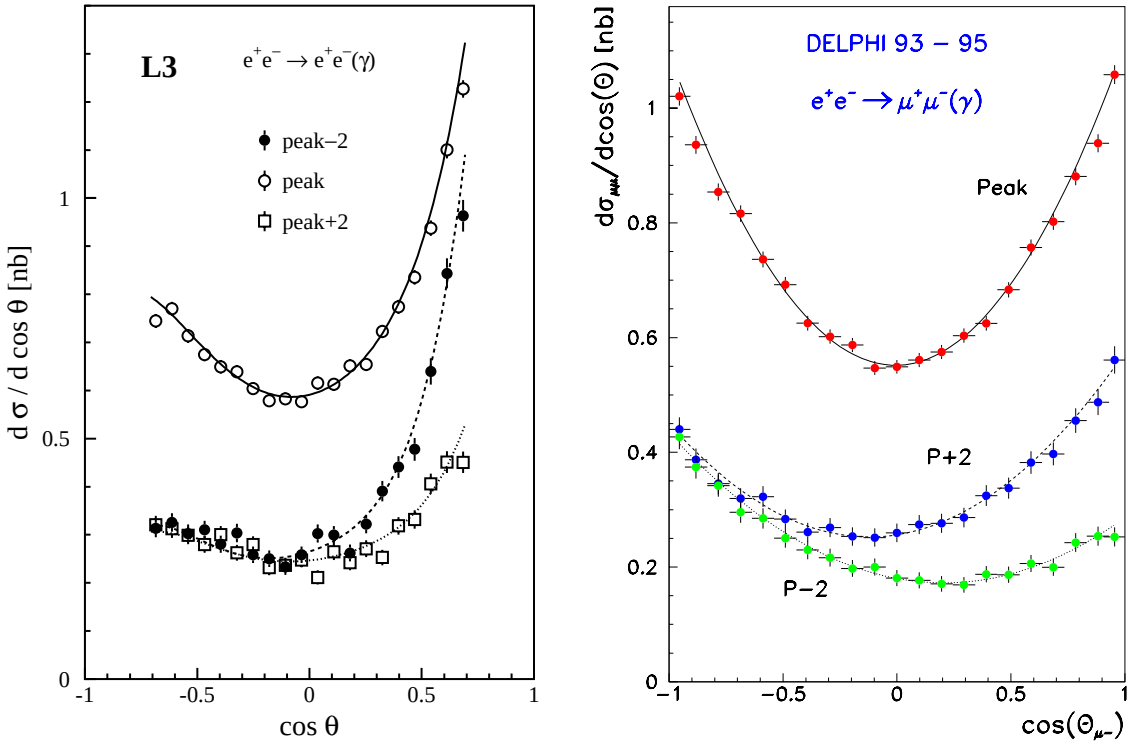

Figure 2.5: Distribution of the production polar angle, $\cos\theta$, for e^+e^- and $\mu^+\mu^-$ events at the three principal energies during the years 1993–1995, measured in the L3 (left) and DELPHI (right) detectors, respectively. The curves show the Standard Model prediction from ALIBABA for e^+e^- and a fit to the data for $\mu^+\mu^-$ assuming the lowest-order functional form of the differential cross-section given in the text.

mil in each of the three lepton channels. Statistical errors from the number of small-angle Bhabha events affect all channels in a correlated way, but even on-peak they are smaller than those in the hadronic channel by at least a factor of $\sqrt{2}$.

Errors arising from limitations in theoretical precision, such as the calculation of the small-angle Bhabha cross-section, the t-channel contribution in the e^+e^- final state or pure QED corrections to the cross-section, are common to all experiments. They are discussed in detail in Section 2.3.

2.1.5 Energy calibration

Precise knowledge of the centre-of-mass energy is essential for the determination of the mass and width of the Z resonance. The uncertainty in the absolute energy scale, *i. e.* uncertainties correlated between the energy points, directly affect the determination of the Z mass, whereas the Z width is only influenced by the error in the difference in energy between energy points. The determination of the mass and width are completely dominated by the high-statistics scans taken at the off-peak points approximately ± 2 GeVaway from the resonance in 1993 and 1995,

	ALEPH			DELPHI		
	'93	'94	'95	'93	'94	'95
$\mathcal{L}^{\text{exp.}}$	0.067%	0.073%	0.080%	0.24%	0.09%	0.09%
σ_{had}	0.069%	0.072%	0.073%	0.10%	0.11%	0.10%
σ_{e}	0.15%	0.13%	0.15%	0.46%	0.52%	0.52%
σ_{μ}	0.11%	0.09%	0.11%	0.28%	0.26%	0.28%
σ_{τ}	0.26%	0.18%	0.25%	0.60%	0.60%	0.60%
A^{e}_{FB}	0.0006	0.0006	0.0006	0.0026	0.0021	0.0020
A^{μ}_{FB}	0.0005	0.0005	0.0005	0.0009	0.0005	0.0010
A^{τ}_{FB}	0.0009	0.0007	0.0009	0.0020	0.0020	0.0020

	L3			OPAL		
	'93	'94	'95	'93	'94	'95
$\mathcal{L}^{\text{exp.}}$	0.086%	0.064%	0.068%	0.033%	0.033%	0.034%
σ_{had}	0.042%	0.041%	0.042%	0.073%	0.073%	0.085%
σ_{e}	0.24%	0.17%	0.28%	0.17%	0.14%	0.16%
σ_{μ}	0.32%	0.31%	0.40%	0.16%	0.10%	0.12%
σ_{τ}	0.68%	0.65%	0.76%	0.49%	0.42%	0.48%
A^{e}_{FB}	0.0025	0.0025	0.0025	0.001	0.001	0.001
A^{μ}_{FB}	0.0008	0.0008	0.0015	0.0007	0.0004	0.0009
A^{τ}_{FB}	0.0032	0.0032	0.0032	0.0012	0.0012	0.0012

Table 2.2: Experimental systematic errors for the Z analyses at the Z peak. The errors are relative for the cross-sections and absolute for the forward-backward asymmetries. None of the common errors discussed in Section 2.3 are included here.

and the errors due to energy calibration are therefore given by

$$\begin{array}{rcl} \Delta m_{\mathrm{Z}} & \approx & 0.5 \cdot \Delta(E_{+2} + E_{-2}) \text{ and} \\ \Delta\Gamma_{\mathrm{Z}} & \approx & \frac{\Gamma_{\mathrm{Z}}}{E_{+2}-E_{-2}} \Delta(E_{+2} - E_{-2}) \,. \end{array} \tag{2.1}$$

The average momentum of particles circulating in a storage ring is proportional to the magnetic bending field integrated over the path of the particles. The very accurate determination of the average energy of the beams in LEP was based on the technique of resonant spin depolarisation [45, 46], which became available in 1991, after transverse polarisation of the electron beam in LEP had first been observed in 1990 [47] with a Compton polarimeter [48]. Transverse polarisation of single or separated beams due to the Sokolov-Ternov mechanism [49] was observed in LEP after careful adjustment of the beam orbit in order to avoid any static depolarising resonances. The same magnetic bending field seen by the particles along their path leads to precession of the average spin vector of the polarised bunches. The beam energy is proportional to the number of spin precessions per turn, the "spin tune" ν. The spin precession frequency is measured by observing the depolarisation which occurs when an artificial spin resonance is excited with the help of a weak oscillating radial magnetic field. This method offers a very high precision as good as ± 0.2 MeV on the beam energy at the time of the measurement. The resolution of the method is illustrated in Figure 2.6, which shows the observed drop in polarisation as a function of the fractional tune of the oscillating depolarising magnetic field.

Measurements with resonant depolarisation were only possible outside normal data taking, typically at the end of fills. About 40% of the recorded off-peak luminosity in the 1993 scan and about 70% in the 1995 scan was taken during fills with at least one such precise calibration of the beam energy. Other techniques had to be employed to extrapolate these calibrations back to earlier times in a fill and to those fills where no calibrations by resonant depolarisation could be made. This required precise knowledge of the values and time evolutions of numerous parameters and careful modelling of their impacts on the beam energy [15–18].

For particles on central orbit the magnetic bending field is given by the field produced by the bending dipoles and corrector magnets and by small contributions from the Earth's magnetic field and from remnant fields in the beam pipe. In addition, magnetic fields originating from leakage DC currents produced by trains in the Geneva area must be taken into account. The magnetic field of the dipoles was initially measured with a nuclear magnetic resonance probe ("NMR") only in a reference dipole on the surface. In 1995, two NMR probes were installed in two of the tunnel dipoles, which measured the magnetic field directly above the beam pipe.

Contributions from the quadrupoles and sextupoles also must be considered for non-central orbits, which arise from geological deformations of the LEP tunnel. Among the identified origins of such deformations were tidal effects from the Sun and the Moon, the water level in the Geneva Lake and rain fall in the Jura Mountains. These could all be tracked by frequent and precise measurements of the beam orbit position inside the LEP beam pipe.

In order to obtain the energy of the particles colliding at an interaction point ("IP"), additional effects from the radio frequency system ("RF") and from a possible energy-dependence of the distribution of particle positions in a bunch, so-called "dispersion effects", had to be considered. For each experiment a value of the beam energy was provided every 15 minutes. These values were determined from a model taking taking into account the time evolutions of the effects mentioned above. Errors on the centre-of-mass energy are largely dominated by the uncertainties in this model. A summary of the typical size of the main effects and of their contributions to the error is shown in Table 2.3.

The energy errors vary slightly among the interaction points, mainly due to different configurations of the radio frequency cavities. The energy errors for different experiments and data

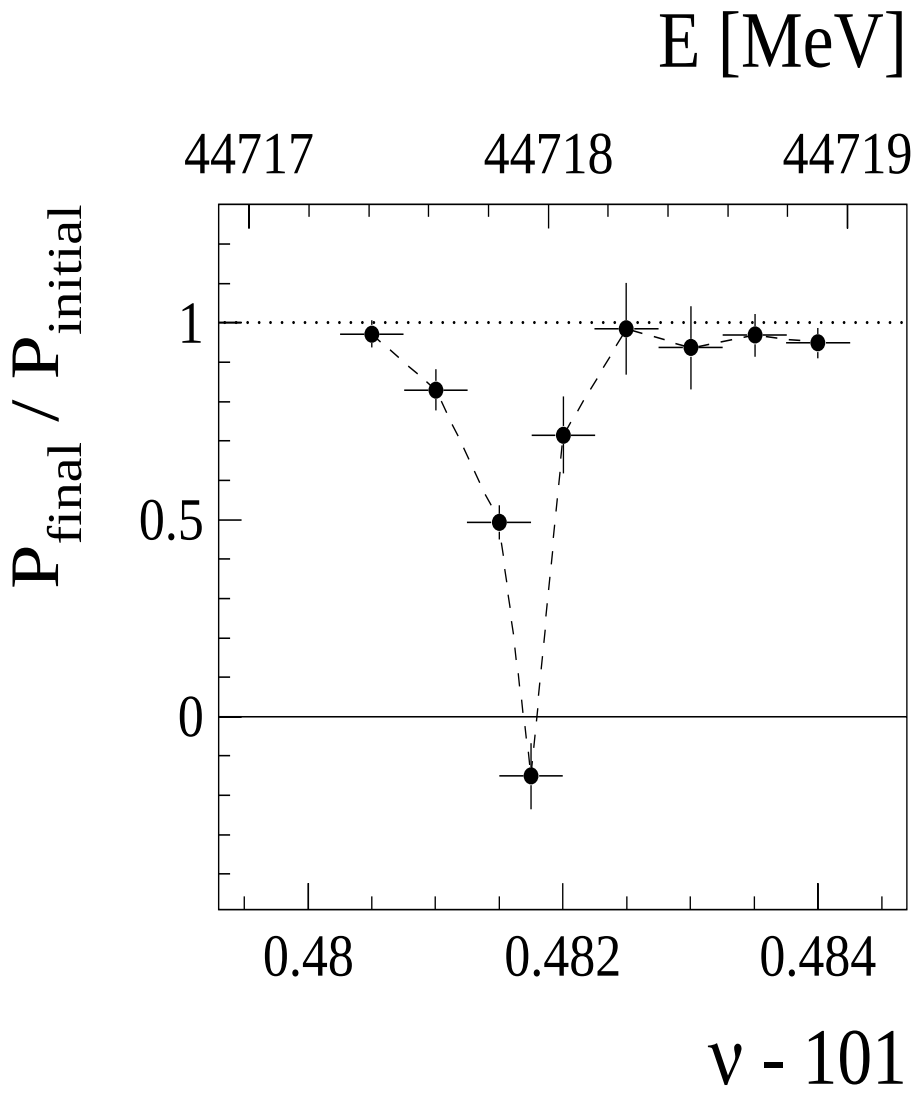

Figure 2.6: Measurement of the width of the artificially excited spin resonance which is used for the energy calibration of LEP (from Reference 46).

origin of correction	contribution to E_{CM} size [MeV]	error [MeV]	Δm_Z [MeV]	$\Delta\Gamma_Z$ [MeV]
energy measurement by resonant depolarisation		0.5	0.4	0.5
mean fill energy, from uncalibrated fills		[0.5–5.0]	0.5	0.8
dipole field changes	up to 20	[1.3–3.3]	1.7	0.6
tidal deformations	±10	[0.0–0.3]	0.0	0.1
e^+ energy difference	<0.3	0.3	0.2	0.1
bending field from horizontal correctors	[0–2]	[0.0–0.5]	0.2	0.1
IP dependent RF corrections	[0–20]	[0.5–0.7]	0.4	0.2
dispersion at IPs	0.5	[0.4–0.7]	0.2	0.1

Table 2.3: Breakdown of effects on the centre-of-mass energy, for illustrative purpose only. The last two columns give the approximate contribution of each effect to the error on m_Z and Γ_Z. The full evaluation of the energy errors used values specific to each year and energy and also took into account their correlations. (See Reference 18 for a complete discussion.)

taking periods have large common parts, and therefore the use of a full correlation matrix is necessary. Assuming that all experiments contribute with the same weight allows all the LEP energy errors to be conveniently summarised in a single error matrix, common to all interaction points, as given in Reference 18. Details on the energy calibration for the earlier years can be found in References 15–17.

The energy of individual beam particles is usually not at the mean value considered above, but oscillates around the mean energy. Therefore observables are not measured at a sharp energy, E^0_{cm}, but instead their values are averaged over a range in energies $E^0_{cm} \pm \delta E_{cm}$. With the assumption of a Gaussian shape of the energy distribution, the total cross-sections receive a correction proportional to δE^2_{cm} and the second derivative of $\sigma(E_{cm})$ w.r.t. E_{cm}. At LEP-I, typical values of the centre-of-mass energy spread are around 50 MeV. The effects of the correction lead to an increase of the cross-section at the peak of the Z resonance by 0.16% and a decrease of the width by about 5 MeV. The uncertainties on the energy spread, around ±1 MeV in 1993–1995, constitute a negligible source of error common to all experiments.

In addition to the natural energy spread, changes in the mean beam energy due to changes of machine parameters have a similar effect. Data taking periods with a very similar centre-of-mass energy were combined into a single energy point in the experimental analyses by performing a luminosity-weighted average. The additional energy spread resulting from this was only around 10 MeV, which is added in quadrature to the natural beam energy spread of the accelerator.

Uncertainties from the energy calibration as described in this sub-section and corrections for the beam energy spread were taken into account by all experiments in the fits from which the Z parameters were extracted; the related common uncertainties are discussed in Section 2.3.1.

2.2 Experimental results

The common set of parameters used for the parametrisation of the differential cross-section, as described in the introductory chapter, was extracted by each experiment from the largely model-independent fits to their measured cross-sections and forward-backward asymmetries [26–29].

The results presented here deviate slightly from those published by the experiments in

order to facilitate the combination procedure. The four dedicated sets of fit results for the combination are summarised in Table 2.4.

All fits are based on versions 6.23 of ZFITTER and 4.4 of TOPAZ0. The published ALEPH results were derived using version 6.10 of ZFITTER, which did not yet contain the improved treatment of fermion pairs radiated from the initial state [50]. For the combination presented here, the ALEPH measurements were reanalysed using version 6.23 of ZFITTER, leading to small changes at the level of a few tenths of MeV in m_{Z} and Γ_{Z}.

Each experiment used the combined energy error matrix described above. This makes a small difference at the level of 0.1 MeV on m_{Z} and Γ_{Z} and their errors only for L3, where uncertainties arising from the modelling of the radio frequency cavities are largest.

The s-t interference in the Bhabha final state has a small dependence on the value of the Z mass. Although this is practically negligible for a single experiment, a consistent treatment becomes important for the combination. Despite some different choices in the publications of the individual analyses, all experiments evaluate the t,s-t channel correction at their own value of the Z mass for the results presented here. The resulting interdependencies between the Z mass and the parameters from the Bhabha final state are explicitly included in the error correlation coefficients between m_{Z} and R^0_{e} or $A^{0,\mathrm{e}}_{\mathrm{FB}}$.

The LEP experiments agreed to use a standard set of parameters used for the calculation of the Standard Model remnants (see Section 1.7) in the theory programs. The important parameters are the Z mass, $m_{\mathrm{Z}} = 91.187\,\mathrm{GeV}$, the Fermi constant, $G_{\mathrm{F}} = 1.16637 \times 10^{-5}\ \mathrm{GeV}^{-2}$, the electromagnetic coupling constant, $\alpha(m_{\mathrm{Z}}) = 1/128.886$ *, the strong coupling constant, $\alpha_s(m_{\mathrm{Z}}) = 0.119$, the top quark mass, $m_{\mathrm{t}} = 175\,\mathrm{GeV}$, and finally the Higgs mass, $m_{\mathrm{H}} = 150\,\mathrm{GeV}$. The dependence of the fit results arising from uncertainties in these parameters is negligible except for m_{H}, as is discussed in Section 2.3.4.

All experiments also provided fits to their measured cross-sections and asymmetries with lepton universality imposed, *i.e.* R^0_{e}, R^0_{μ} and R^0_{τ} are replaced by R^0_{ℓ}, and $A^{0,\mathrm{e}}_{\mathrm{FB}}$, $A^{0,\mu}_{\mathrm{FB}}$ and $A^{0,\tau}_{\mathrm{FB}}$ are replaced by $A^{0,\ell}_{\mathrm{FB}}$ in the model-independent parametrisation of the differential cross-section. Here R^0_{ℓ} is not a simple average over the three lepton species, but refers to Z decays into pairs of one massless charged lepton species. The individual experimental results and the correlation matrices are given in Table 2.5. A graphical overview of the results is given in Figure 2.7; the averages are those discussed in Section 2.4 below.

Compared with the nine-parameter results of Table 2.4, there is a noticeable change in m_{Z} of a few tenths of MeV in all experiments. This is a consequence of the dependence of the t-channel correction on m_{Z}, as discussed in Section 2.3.2. When R^0_{e} and $A^{0,\mathrm{e}}_{\mathrm{FB}}$ are replaced by the leptonic quantities R^0_{ℓ} and $A^{0,\ell}_{\mathrm{FB}}$, their correlation with the Z mass leads to a shift, which is driven by the (statistical) difference between R^0_{e} and R^0_{ℓ} and $A^{0,\mathrm{e}}_{\mathrm{FB}}$ and $A^{0,\ell}_{\mathrm{FB}}$. Similarly, replacing R^0_{e} and $A^{0,\mathrm{e}}_{\mathrm{FB}}$ from the values of a single experiment by the LEP average introduces a shift in m_{Z} in the presence of these particular correlation coefficients. Such shifts should become smaller when averaged over the four experiments. Indeed, the average of the shifts is only $-0.2\,\mathrm{MeV}$.

2.3 Common uncertainties

Important common errors among the results from all LEP experiments arise from several sources. These include the calibration of the beam energy, the theoretical error on the calcula-

*This corresponds to a value of the correction due to hadronic vacuum polarisation of $\Delta\alpha^{(5)}_{\mathrm{had}} = 0.02804 \pm 0.00065$ [51].

		correlations								
		m_Z	Γ_Z	σ^0_h	R^0_e	R^0_μ	R^0_τ	$A^{0,e}_{FB}$	$A^{0,\mu}_{FB}$	$A^{0,\tau}_{FB}$
χ^2/N_{df} = 169/176					ALEPH					
m_Z [GeV]	91.1891 ± 0.0031	1.00								
Γ_Z [GeV]	2.4959 ± 0.0043	.038	1.00							
σ^0_h [nb]	41.558 ± 0.057	−.091	−.383	1.00						
R^0_e	20.690 ± 0.075	.102	.004	.134	1.00					
R^0_μ	20.801 ± 0.056	−.003	.012	.167	.083	1.00				
R^0_τ	20.708 ± 0.062	−.003	.004	.152	.067	.093	1.00			
$A^{0,e}_{FB}$	0.0184 ± 0.0034	−.047	.000	−.003	−.388	.000	.000	1.00		
$A^{0,\mu}_{FB}$	0.0172 ± 0.0024	.072	.002	.002	.019	.013	.000	−.008	1.00	
$A^{0,\tau}_{FB}$	0.0170 ± 0.0028	.061	.002	.002	.017	.000	.011	−.007	.016	1.00
χ^2/N_{df} = 177/168					DELPHI					
m_Z [GeV]	91.1864 ± 0.0028	1.00								
Γ_Z [GeV]	2.4876 ± 0.0041	.047	1.00							
σ^0_h [nb]	41.578 ± 0.069	−.070	−.270	1.00						
R^0_e	20.88 ± 0.12	.063	.000	.120	1.00					
R^0_μ	20.650 ± 0.076	−.003	−.007	.191	.054	1.00				
R^0_τ	20.84 ± 0.13	.001	−.001	.113	.033	.051	1.00			
$A^{0,e}_{FB}$	0.0171 ± 0.0049	.057	.001	−.006	−.106	.000	−.001	1.00		
$A^{0,\mu}_{FB}$	0.0165 ± 0.0025	.064	.006	−.002	.025	.008	.000	−.016	1.00	
$A^{0,\tau}_{FB}$	0.0241 ± 0.0037	.043	.003	−.002	.015	.000	.012	−.015	.014	1.00
χ^2/N_{df} = 158/166					L3					
m_Z [GeV]	91.1897 ± 0.0030	1.00								
Γ_Z [GeV]	2.5025 ± 0.0041	.065	1.00							
σ^0_h [nb]	41.535 ± 0.054	.009	−.343	1.00						
R^0_e	20.815 ± 0.089	.108	−.007	.075	1.00					
R^0_μ	20.861 ± 0.097	−.001	.002	.077	.030	1.00				
R^0_τ	20.79 ± 0.13	.002	.005	.053	.024	.020	1.00			
$A^{0,e}_{FB}$	0.0107 ± 0.0058	−.045	.055	−.006	−.146	−.001	−.003	1.00		
$A^{0,\mu}_{FB}$	0.0188 ± 0.0033	.052	.004	.005	.017	.005	.000	.011	1.00	
$A^{0,\tau}_{FB}$	0.0260 ± 0.0047	.034	.004	.003	.012	.000	.007	−.008	.006	1.00
χ^2/N_{df} = 155/194					OPAL					
m_Z [GeV]	91.1858 ± 0.0030	1.00								
Γ_Z [GeV]	2.4948 ± 0.0041	.049	1.00							
σ^0_h [nb]	41.501 ± 0.055	.031	−.352	1.00						
R^0_e	20.901 ± 0.084	.108	.011	.155	1.00					
R^0_μ	20.811 ± 0.058	.001	.020	.222	.093	1.00				
R^0_τ	20.832 ± 0.091	.001	.013	.137	.039	.051	1.00			
$A^{0,e}_{FB}$	0.0089 ± 0.0045	−.053	−.005	.011	−.222	−.001	.005	1.00		
$A^{0,\mu}_{FB}$	0.0159 ± 0.0023	.077	−.002	.011	.031	.018	.004	−.012	1.00	
$A^{0,\tau}_{FB}$	0.0145 ± 0.0030	.059	−.003	.003	.015	−.010	.007	−.010	.013	1.00

Table 2.4: Individual results on Z parameters and their correlation coefficients for the four experiments.

		correlations				
		m_{Z}	Γ_{Z}	σ^0_{h}	R^0_ℓ	$A^{0,\ell}_{\mathrm{FB}}$
$\chi^2/N_{\mathrm{df}} = 172/180$		ALEPH				
m_{Z} [GeV]	91.1893 ± 0.0031	1.00				
Γ_{Z} [GeV]	2.4959 ± 0.0043	.038	1.00			
σ^0_{h} [nb]	41.559 ± 0.057	−.092	−.383	1.00		
R^0_ℓ	20.729 ± 0.039	.033	.011	.246	1.00	
$A^{0,\ell}_{\mathrm{FB}}$	0.0173 ± 0.0016	.071	.002	.001	−.076	1.00
$\chi^2/N_{\mathrm{df}} = 183/172$		DELPHI				
m_{Z} [GeV]	91.1863 ± 0.0028	1.00				
Γ_{Z} [GeV]	2.4876 ± 0.0041	.046	1.00			
σ^0_{h} [nb]	41.578 ± 0.069	−.070	−.270	1.00		
R^0_ℓ	20.730 ± 0.060	.028	−.006	.242	1.00	
$A^{0,\ell}_{\mathrm{FB}}$	0.0187 ± 0.0019	.095	.006	−.005	.000	1.00
$\chi^2/N_{\mathrm{df}} = 163/170$		L3				
m_{Z} [GeV]	91.1894 ± 0.0030	1.00				
Γ_{Z} [GeV]	2.5025 ± 0.0041	.068	1.00			
σ^0_{h} [nb]	41.536 ± 0.055	.014	−.348	1.00		
R^0_ℓ	20.809 ± 0.060	.067	.020	.111	1.00	
$A^{0,\ell}_{\mathrm{FB}}$	0.0192 ± 0.0024	.041	.020	.005	−.024	1.00
$\chi^2/N_{\mathrm{df}} = 158/198$		OPAL				
m_{Z} [GeV]	91.1853 ± 0.0029	1.00				
Γ_{Z} [GeV]	2.4947 ± 0.0041	.051	1.00			
σ^0_{h} [nb]	41.502 ± 0.055	.030	−.352	1.00		
R^0_ℓ	20.822 ± 0.044	.043	.024	.290	1.00	
$A^{0,\ell}_{\mathrm{FB}}$	0.0145 ± 0.0017	.075	−.005	.013	−.017	1.00

Table 2.5: Results on Z parameters and error correlation matrices by the four experiments with lepton universality imposed.

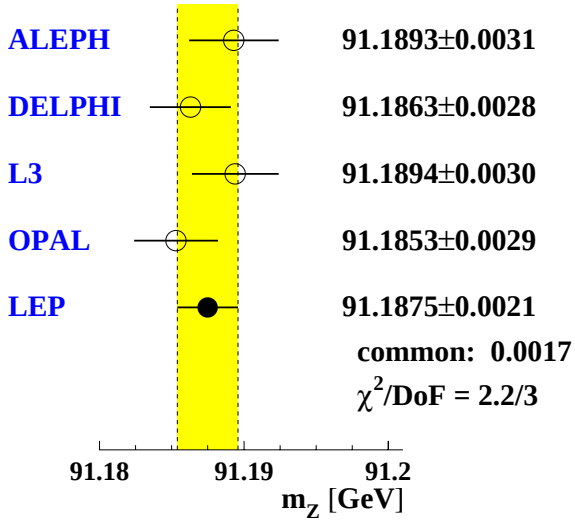

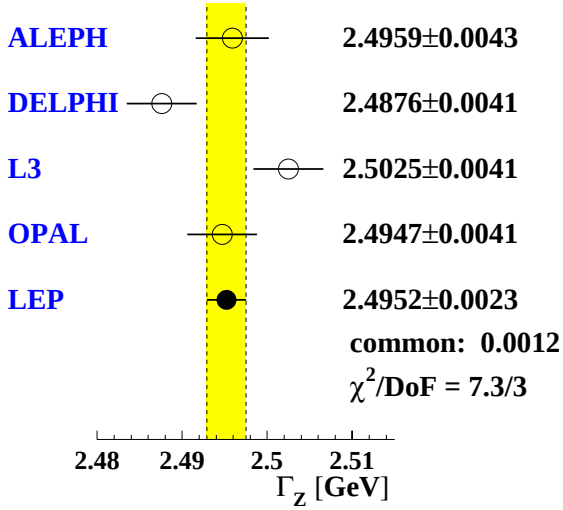

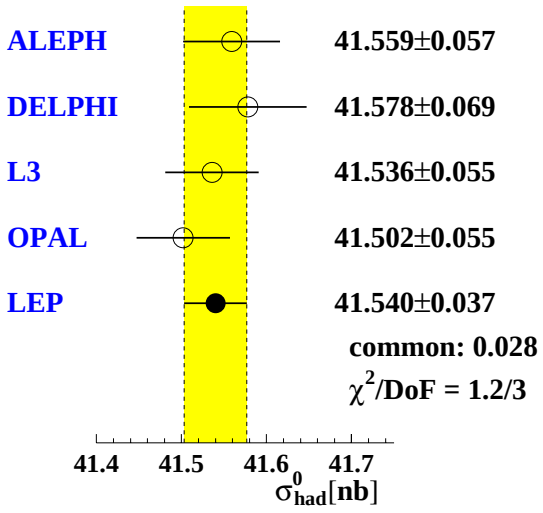

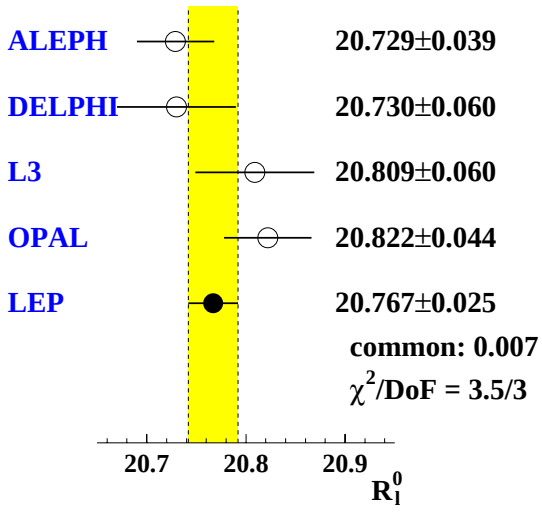

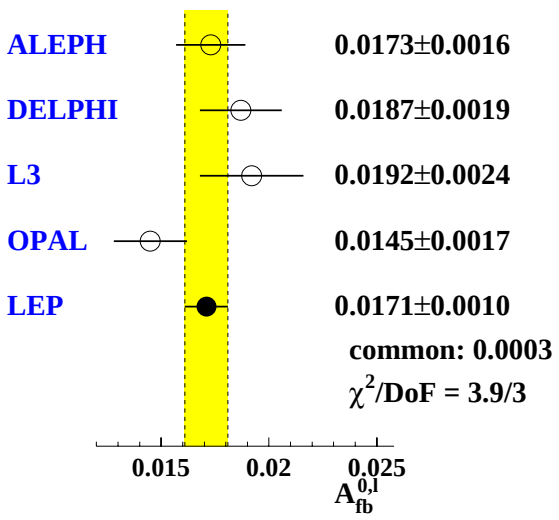

Figure 2.7: Measurements of m_{Z}, Γ_{Z}, σ^0_{h}, R^0_ℓ and $A^{0,\ell}_{\mathrm{FB}}$. The averages indicated were obtained using the common errors and combination method discussed in the next two sections. The value of χ^2 per degree of freedom is the diagonal χ^2 calculated from the independent errors among the measurements of the same parameter, but neglecting correlations among different parameters.

	m_{Z}	Γ_{Z}	σ^0_{h}	R^0_{e}
m_{Z} [GeV]	0.0017			
Γ_{Z} [GeV]	−0.0006	0.0012		
σ^0_{h} [nb]	−0.0018	−0.0027	0.011	
R^0_{e}	0.0017	−0.0014	0.0073	0.013

	$A^{0,\mathrm{e}}_{\mathrm{FB}}$	$A^{0,\mu}_{\mathrm{FB}}$	$A^{0,\tau}_{\mathrm{FB}}$
$A^{0,\mathrm{e}}_{\mathrm{FB}}$	0.0004		
$A^{0,\mu}_{\mathrm{FB}}$	−0.0003	0.0003	
$A^{0,\tau}_{\mathrm{FB}}$	−0.0003	0.0003	0.0003

Table 2.6: Common energy errors for nine-parameter fits. Values are given as the signed square root of the covariance matrix elements; elements above the diagonal have been omitted for simplicity. The anti-correlation between electron and muon or tau asymmetries arises from the different energy dependence of the electron asymmetry due to the t-channel contribution.

tion of the small-angle Bhabha cross-section used as the normalisation reaction, the theoretical uncertainties in the t-channel and s-t interference contribution to the differential large-angle Bhabha cross-section, the theoretical uncertainties in the calculations of QED radiative effects and, finally, from small uncertainties in the parametrisation of the electroweak cross-section near the Z resonance in terms of the standard set of pseudo-observables. These common errors are quantified below and are used in the combination.

Other sources of common errors may arise from the use of common Monte Carlo generators and detector simulation programs. However, each experiment uses its own tuning procedures and event selections which best suit their detector, and therefore the related errors are treated as uncorrelated among the experiments.

For the purpose of combining the experimental results at the parameter level, the common sources of error on each individual cross-section or asymmetry measurement need to be transformed into errors on the extracted pseudo-observables. This is in general achieved by comparing the error matrices obtained in special fits with artificially reduced errors with the original error matrix.

2.3.1 Common energy uncertainties

The first step in the determination of common energy related uncertainties on the pseudo-observables is to scale the energy errors by factors of $1 \pm \epsilon$, while maintaining the experimental errors fixed. Typical values of ϵ used are between 5 % and 20 %. Performing the standard fits with these scaled errors generates two pseudo-observable covariance matrices, $V_{\pm}$, from which the covariance matrix due to energy errors, V_E, can be separated from the other errors, V_{exp}, using the relation $(V_{\pm}) = (1 \pm \epsilon)^2 (V_E) + (V_{\mathrm{exp}})$. The validity of this procedure was verified using a data set restricted to the hadronic cross-section measurements of the years 1993–1995, which were combined both at the cross-section level and at the parameter level.

The estimated energy errors differ slightly depending on which experimental data set is used to derive them. Combinations may be attempted based on each of them, or on the average. The central values and errors of each of the averaged parameters agree to well within 5 % of the error on that average. It is therefore most appropriate to take the average of the error estimates over the experiments as the common energy errors, which are shown in Table 2.6.

2.3.2 Common t-channel uncertainties

The t channel and s-t interference contributions are calculated in the Standard Model using the programs ALIBABA [52] and TOPAZ0 [23]. The theoretical uncertainty on the t-channel

	R_{e}^{0}	$A_{\mathrm{FB}}^{0,\mathrm{e}}$
R_{e}^{0}	0.024	
$A_{\mathrm{FB}}^{0,\mathrm{e}}$	−0.0054	0.0014

Table 2.7: Common uncertainties arising from the t channel and s-t interference contribution to the $\mathrm{e^+e^-}$ final states, given as the signed square root of the covariance matrix elements.

correction is discussed in detail in Reference 53. The size of the uncertainty is typically 1.1 pb for the forward cross-section and 0.3 pb for the backward cross-section and depends slightly on the acceptance cuts [54]. All collaborations incorporate the theory uncertainty as an additional error on the electron pair cross-section and asymmetry. In order to evaluate the common error due to the t, s-t theory error, each collaboration performed two fits, with and without the theory error, and the quadratic differences of the covariance matrix elements for R_{e}^{0} and $A_{\mathrm{FB}}^{0,\mathrm{e}}$ are taken as an estimate of the common error. The unknown error correlation between energy points below and above the peak are included in the error estimates by adding in quadrature the observed shifts in mean values of R_{e}^{0} and $A_{\mathrm{FB}}^{0,\mathrm{e}}$ when varying these correlations between -1 and $+1$. The t, s-t related errors estimated by individual experiments are all very similar, and therefore the average is taken as the common error matrix, as shown in Table 2.7.

The s-t interference contribution to the t-channel correction in Bhabha final states depends on the value of the Z mass. For the purpose of this combination, all experiments parametrise the t and s-t contributions as a function of m_{Z}. This allows the t, s-t correction to follow the determination of m_{Z} in the fits, which results in a correlation between m_{Z} and R_{e}^{0} or $A_{\mathrm{FB}}^{0,\mathrm{e}}$. The change in correlation coefficients introduced by explicitly taking the m_{Z} dependence of the t-channel into account in the fits is about $+10\,\%$ for the correlation m_{Z}–R_{e}^{0} and $-10\,\%$ for m_{Z}–$A_{\mathrm{FB}}^{0,\mathrm{e}}$. These correlation coefficients properly take into account the changes in R_{e}^{0} and $A_{\mathrm{FB}}^{0,\mathrm{e}}$ when m_{Z} takes its average value in the combination of the four experiments.

2.3.3 Common luminosity uncertainties

The four collaborations use similar techniques to measure the luminosity of their data samples by counting the number of small-angle Bhabha-scattered electrons. The experimental details of the four measurements differ sufficiently that no correlation is believed to exist in the experimental component of the luminosity errors. All four collaborations, however, use BHLUMI 4.04 [41], the best available Monte Carlo generator of small-angle Bhabha scattering, to calculate the acceptance of their luminosity counters. Therefore significant correlations exist in the errors assigned to the scale of the measured cross-sections due to the uncertainty in this common theoretical calculation.

This uncertainty is estimated to be 0.061 % [55] without applying a correction for the production of light fermion pairs, which are not calculated in BHLUMI, and enter as a contribution to the estimated error. A recent calculation of the contribution of light pairs [56] has allowed OPAL to explicitly correct for light pairs and reduce its theoretical luminosity uncertainty to 0.054 %. This 0.054 % error is taken to be correlated with the errors of the other three experiments, which among themselves share a mutual correlated error of 0.061 %.

These errors almost exclusively affect the hadronic pole cross-section, and contribute about half its total error after combination. The common luminosity error also introduces a small contribution to the covariance matrix element between Γ_{Z} and σ_{h}^{0}. This was neglected in the

common error tables given above, as it had no noticeable effect on the combined result.

2.3.4 Common theory uncertainties

An additional class of common theoretical errors arises from the approximations and special choices made in the fitting codes. These comprise contributions from QED radiative corrections, including initial-state pair radiation, and the parametrisation of the differential cross-section around the Z resonance in terms of pseudo-observables defined precisely at the peak and for pure Z exchange only. In order to estimate the uncertainties from the parametrisation of the electroweak cross-sections near the Z resonance the two most advanced calculational tools, ZFITTER [24] and TOPAZ0 [23] were compared. In addition, there are "parametric uncertainties" arising from parameters of the Standard Model that are needed to fix the Standard Model remnants.

QED uncertainties

The effects of initial state radiation (ISR) and the radiation of fermion pairs (ISPP) lead to large corrections in the vicinity of the Z resonance and therefore play a central role in the extraction of the pseudo-observables from the measured cross-sections and asymmetries. Such radiative effects are more than two orders of magnitude larger than the experimental precision, which is below the per-mil level in the case of the hadronic cross-section.

The most up-to-date evaluations of photonic corrections to the measurements are complete in $\mathcal{O}(\alpha^2)$ and for the total cross-sections also include the leading contributions up to $\mathcal{O}(\alpha^3)$. Two different schemes are available to estimate the remaining uncertainties:

1. KF: $\mathcal{O}(... \ \alpha^2L^2,\alpha^2L,\alpha^2L^0)$ calculations [57] including the exponentiation scheme of Kuraev-Fadin [58] with $\mathcal{O}(\alpha^3L^3)$ [59]. †

2. YFS: the 2nd order inclusive exponentiation scheme of References 60, 61, based on the YFS approach [62]. Third order terms are also known and have only a small effect [63].

Differences between these schemes, which are both implemented in ZFITTER, TOPAZ0 and MIZA [64], and uncertainties due to missing higher order corrections [63], amount to at most $\pm 0.1\,\mathrm{MeV}$ on m_Z and Γ_Z, and $\pm 0.01\,\%$ on σ^0_h.

The influence of the interference between initial and final state radiation on the extracted parameters has also been studied recently [65], and uncertainties on m_Z of at most $\pm 0.1\,\mathrm{MeV}$ from this source are expected for experimental measurements given with only a small cut on s', the effective squared centre-of-mass energy after photon radiation from the initial state. The methods for the extrapolation of the leptonic s-channel cross-sections to full angular acceptance and from large to small s' differ among the experiments and therefore the resulting uncertainties are believed to be largely uncorrelated.

QED related uncertainties are dominated by the radiation of fermion pairs from the initial state. Starting from the full second order pair radiator [57, 66], a simultaneous exponentiation scheme for radiated photons and pairs was proposed in Reference [67]. A third-order pair radiator was calculated recently [50] and compared with the other existing schemes, which are all available in the latest version of ZFITTER. Independent implementations of some schemes exist in TOPAZ0 and in MIZA. The largest uncertainty arises from the contribution of hadronic pairs. The maximum differences are $0.3\,\mathrm{MeV}$ on m_Z, $0.2\,\mathrm{MeV}$ on Γ_Z and $0.015\,\%$ on σ^0_h.

† Third-order terms for the KF scheme had also been calculated earlier [60].

Δm_{Z} [GeV]	$\Delta\Gamma_{\mathrm{Z}}$ [GeV]	$\Delta\sigma^0_{\mathrm{h}}$ [nb]	ΔR^0_ℓ	$\Delta A^{0,\ell}_{\mathrm{FB}}$
0.0001	0.0001	0.001	0.004	0.0001

Table 2.8: Differences in fit results obtained with TOPAZ0 and ZFITTER, taken as common systematic errors.

In summary, comparing the different options for photonic and fermion-pair radiation leads to error estimates of ± 0.3 MeV on m_{Z} and ± 0.2 MeV on Γ_{Z}. The observed differences in σ^0_{h} are slightly smaller than the error estimate of $\pm 0.02\,\%$ in Reference 63, which is therefore taken as the error for the QED-related uncertainties.

Choice of parametrisation of line shape and asymmetries

In a recent very detailed comparison of TOPAZ0 and ZFITTER [25], cross-sections from Standard Model calculations and from differing choices in the model-independent parametrisation were considered. Uncertainties on the fitted pseudo-observables may be expected to arise from these choices in parametrisation of the electroweak cross-sections near the Z resonance. To evaluate such differences, cross-sections and forward-backward asymmetries were calculated with TOPAZ0 and the standard fit performed with ZFITTER. Errors were assigned to the calculated cross-sections and forward-backward asymmetries which reflect the integrated luminosity taken at each energy, thus ensuring that each energy point entered with the appropriate weight.

The dominant part of the small differences between the two codes results from details of the implementation of the cross-section parametrisation in terms of the pseudo-observables. This is particularly visible for the off-peak points, where the assignment of higher-order corrections to the Z resonance or to the Standard Model remnants is not in all cases unambiguous. The size of the differences also depends on the particular values of the pseudo-observables, since these do not necessarily respect the exact Standard Model relations. Slightly different choices are made in the two codes if the Standard Model relations between the pseudo-observables are not fulfilled. Finally, variations of factorisation schemes and other options in the electroweak calculations may affect the fit results through the Standard Model remnants, but were found to have a negligible effect.

In Table 2.8 differences between TOPAZ0 and ZFITTER are shown, which are taken as systematic uncertainties. They were evaluated around the set of pseudo-observables representing the average of the four experiments; cross-sections and asymmetries were calculated for full acceptance with only a cut on $s' > 0.01\,s$. The only important systematic error of this kind is the one on R^0_ℓ, which amounts to 15 % of the combined error.

Putting all sources together, the overall theoretical errors as listed in Table 2.9 are obtained, and these are used in the combination.

Parametric uncertainties

Through the Standard Model remnants the fit results depend slightly on the values of some Standard Model parameters. Varying these within their present experimental errors, or between 100 GeV and 1000 GeV in case of the Higgs boson mass, leads to observable effects only on the Z mass, which is affected through the γ-Z interference term. The dominant dependence is on m_{H}, followed by $\alpha^{(5)}(m_{\mathrm{Z}})$.

	m_{Z}	Γ_{Z}	σ^0_{h}	R^0_{e}	R^0_{μ}	R^0_{τ}	$A^{0,\mathrm{e}}_{\mathrm{FB}}$	$A^{0,\mu}_{\mathrm{FB}}$	$A^{0,\tau}_{\mathrm{FB}}$
m_{Z}[GeV]	0.0003								
Γ_{Z}[GeV]		0.0002							
σ^0_{h}[nb]			0.008						
R^0_{e}				0.004					
R^0_{μ}				0.004	0.004				
R^0_{τ}				0.004	0.004	0.004			
$A^{0,\mathrm{e}}_{\mathrm{FB}}$							0.0001		
$A^{0,\mu}_{\mathrm{FB}}$							0.0001	0.0001	
$A^{0,\tau}_{\mathrm{FB}}$							0.0001	0.0001	0.0001

Table 2.9: Theoretical errors from programs due to photon and fermion-pair radiation and the choice of model-independent parametrisation, given as the signed square root of the covariance matrix elements.

The effect on m_{Z} from a variation of $1/\alpha^{(5)}(m_{\mathrm{Z}})$ by its error of ± 0.090 is ∓ 0.05 MeV, which is negligibly small compared to the systematic error on m_{Z} arising from other QED-related uncertainties (see Table 2.9). The change in m_{Z} due to m_{H} amounts to $+0.23$ MeV per unit change in $\log_{10}(m_{\mathrm{H}}/\mathrm{GeV})$. Note that this is small compared to the total error on m_{Z} of ± 2.1 MeV and is not considered as an error, but rather as a correction to be applied once the Higgs boson mass is known. The consequences of a completely model-independent treatment of the γ-Z interference in the hadronic channel are discussed in Section 2.4.3.

2.4 Combination of results

The combination of results on the Z parameters is based on the nine parameters m_{Z}, Γ_{Z}, σ^0_{h}, R^0_{e}, R^0_{μ}, R^0_{τ}, $A^{0,\mathrm{e}}_{\mathrm{FB}}$, $A^{0,\mu}_{\mathrm{FB}}$ and $A^{0,\tau}_{\mathrm{FB}}$ and the common errors given in the previous chapter.

For this purpose it is necessary to construct the full $(4 \times 9) \times (4 \times 9)$ covariance matrix of the errors. The four diagonal 9×9 matrices consist of the four error matrices specified by each experiment (Table 2.4). The 9×9 common error matrices build the off-diagonal elements.

A symbolic representation of the full error matrix is shown in Table 2.10 . Each table element represents a 9×9 matrix; $(\mathcal{C}_{exp})$ for exp = A, D, L and O are the covariance matrices of the experiments (see Table 2.4), and $(\mathcal{C}_c) = (\mathcal{C}_E) + (\mathcal{C}_{\mathcal{L}}) + (\mathcal{C}_t) + (\mathcal{C}_{\mathrm{QED,th}})$ is the matrix of common errors. $(\mathcal{C}_E)$ (Table 2.6) is the error matrix due to LEP energy uncertainties, $(\mathcal{C}_{\mathcal{L}})$ (Section 2.3.3) arises from the theoretical error on the small-angle Bhabha cross-section calculations, $\mathcal{C}_t$ (Table 2.7) contains the errors from the t-channel treatment in the $\mathrm{e^+e^-}$ final state, and $(\mathcal{C}_{\mathrm{QED,th}})$ contains the errors from initial state photon and fermion pair radiation and from the model-independent parametrisation (Table 2.9). Since the latter errors were not included in the experimental error matrices, they were also added to the block matrices in the diagonal of Table 2.10 .

The combined parameter set and its covariance matrix are obtained from a χ^2 minimisation, with

$$\chi^2 = (\mathbf{X} - \mathbf{X_m})^T (\mathcal{C})^{-1} (\mathbf{X} - \mathbf{X_m}); \tag{2.2}$$

$(\mathbf{X} - \mathbf{X_m})$ is the vector of residuals of the combined parameter set to the individual results.

$(\mathcal{C})$	ALEPH	DELPHI	L3	OPAL
A	$(\mathcal{C}_A) + (\mathcal{C}_{\mathrm{QED,th}})$			
D	(C_c)	$(\mathcal{C}_D) + (\mathcal{C}_{\mathrm{QED,th}})$		
L	(C_c)	(C_c)	$(\mathcal{C}_L) + (\mathcal{C}_{\mathrm{QED,th}})$	
O	(C_c)	(C_c)	(C_c)	$(\mathcal{C}_O) + (\mathcal{C}_{\mathrm{QED,th}})$

Table 2.10: Symbolic representation of the covariance matrix, $(\mathcal{C})$, used to combine the line shape and asymmetry results of the four experiments. Elements above the diagonal are the same as those below, but are left blank for simplicity. The components of the matrix are explained in the text.

Some checks of the combination procedure outlined above are described in the following subsections, and the combined results are given in the tables of Section 2.5.

2.4.1 Multiple-m_{Z} fits

In 1993 and 1995, the two years when LEP performed precision energy scans to measure the Z line shape, the experimental errors are very comparable, but the LEP energy was appreciably better understood in 1995 than in 1993. In determining the optimum value of m_{Z}, therefore, the four experiments combined should give more weight to the 1995 data than they each do in their independent determinations. To quantify this issue the measurements of each experiment were fit to determine independent values of m_{Z} for the three periods 1990–1992, 1993–94 and 1995. In this "eleven-parameter fit", each of the three mass values m_{Z}^{90-92}, m_{Z}^{93-94} and m_{Z}^{95} has its specific energy error reflecting the different systematic errors on the absolute energy scale of LEP. In the combination, the relative importance of energy-related and independent experimental errors on the mass values is properly treated.

When the three values of m_{Z} are condensed into a single one, the effects of the time dependence of the precision in the energy calibration is taken into account. The difference of -0.2 MeV w.r.t. the m_{Z} value from the nine-parameter fits corresponds to 10 % of the combined error. All other parameters are identical to their values from the nine-parameter fit to within less than 5 % of the combined error. This result justifies using the standard combination based on the nine parameters.

The averages over the four experiments of the three values m_{Z}^{90-92}, m_{Z}^{93-94} and m_{Z}^{95} also provide a cross-check on the consistency of the energy calibration, which dominates the errors on m_{Z} in each of the periods considered. The mass values for the three different periods and the correlated and uncorrelated parts of their errors are shown in Figure 2.8. The differences amount to $|m_{\mathrm{Z}}^{90-92} - m_{\mathrm{Z}}^{93-94}| = 31\,\%$, $|m_{\mathrm{Z}}^{90-92} - m_{\mathrm{Z}}^{95}| = 56\,\%$ and $|m_{\mathrm{Z}}^{93-94} - m_{\mathrm{Z}}^{95}| = 43\,\%$ of the uncorrelated error, *i. e.* the three Z mass values are consistent.

2.4.2 Shifts for halved experimental errors

When the average over the experiments is performed at the level of the pseudo-observables, information on the individual contribution of particular data points to the average is lost. Performing the average over the data points instead may therefore lead to changes of the relative importance of independent experimental errors w.r.t. the common errors. The examples of m_{Z} and the importance of the t-channel errors for R_ℓ^0, as discussed in the previous subsections,

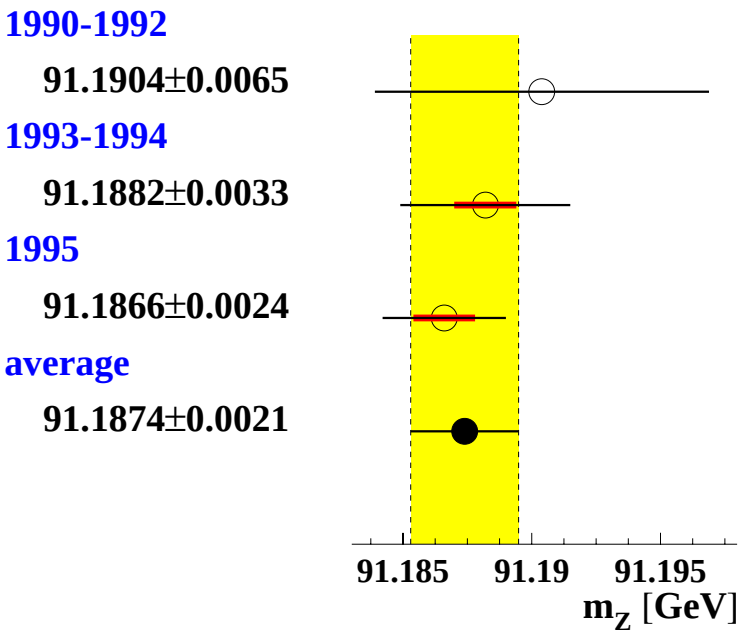

Figure 2.8: m_{Z} in GeV for three different periods of data taking, before 1993, 1993–1994 and 1995. The second, smaller error bar represents the correlated error component of 1.2 MeV between m_{Z}^{93-94} and m_{Z}^{95}. m_{Z}^{90-92} is essentially uncorrelated with the other two.

provide good illustrations of such effects. It was demonstrated that averaging the shifts in m_{Z} which each experiment observed when halving its experimental errors to simulate the generic "combined" experiment also reproduced the results of the full fit to the combined hadronic cross-section measurements.

While m_{Z} is properly treated by the eleven-parameter fits, other pseudo-observables may suffer from similar changes due to weight changes. Shifts in central values when halving the independent experimental errors in each experiment can be used as a monitoring tool for such effects. The average of these changes over the four LEP experiments serves to control the differences between an average at the parameter level compared to a full cross-section average. Of course, this assumes that all measurements from individual experiments enter into the average with the same weight. The observed shifts are summarised in Table 2.11. The shift downwards in m_{Z} of 0.3 MeV corresponds to the slightly smaller shift of 0.2 MeV already seen in the multiple-m_{Z} fits.

Thus, the average changes in m_{Z}, σ_{h}^{0}, R_{e}^{0}, $A_{\mathrm{FB}}^{0,\mu}$ and $A_{\mathrm{FB}}^{0,\tau}$ amount to about 10 % of the combined errors, in all other cases they are even smaller. This is an estimate of the magnitude of the changes in the final results that would arise from a combination of the four experiments at the cross-section level w.r.t the averaging at the parameter level. Given the smallness of the observed effects it is obvious that the parameter-level average is adequate.

	A	D	L	O	average	% of error
m_{Z} [GeV]	−0.0006	0.0000	−0.0004	−0.0001	−0.00028	13
Γ_{Z} [GeV]	−0.0002	+0.0001	−0.0004	0.0000	−0.00013	5
σ^0_{h} [nb]	+0.006	0.000	+0.008	+0.0036	+0.0037	10
R^0_{e}	+0.004	+0.017	0.000	+0.004	+0.0063	13
R^0_{μ}	0.000	0.000	0.000	+0.001	0.0000	0
R^0_{τ}	0.000	0.000	−0.001	+0.002	+0.0003	1
$A^{0,\mathrm{e}}_{\mathrm{FB}}$	−0.0001	−0.0003	0.0000	−0.0000	−0.00011	5
$A^{0,\mu}_{\mathrm{FB}}$	+0.0002	+0.0003	0.0000	+0.0001	+0.00014	11
$A^{0,\tau}_{\mathrm{FB}}$	+0.0002	+0.0003	0.0000	+0.0001	+0.00015	9

Table 2.11: Shifts in central values of the fitted pseudo-observables seen when halving the independent experimental errors, for individual experiments and the average.

2.4.3 Influence of the γ-Z interference term

In the nine-parameter analyses discussed here, the γ-Z interference terms in the differential cross-sections for leptons are expressed using the effective coupling constants and the electric charges of the electron, Q^{e}, and the final state fermion, Q^{f} (see equation for the differential cross-section in Section 1.5). For the hadronic final state, however, the γ-Z interference terms must be fixed to the Standard Model values, as individual quark flavours are not separated. Fits with a free interference term are possible in the S-matrix scheme [68]. The OPAL collaboration also studied a similar approach based on an extension of the standard parameter set [29]. In the S-Matrix approach the interference terms are considered as free and independent parameters. The hadronic interference term is described by the parameter $j^{\mathrm{had}}_{\mathrm{tot}}$, given in the Standard Model by

$$j^{\mathrm{had}}_{\mathrm{tot}} = \frac{G_{\mathrm{F}} m_{\mathrm{Z}}^2}{\sqrt{2}\pi\alpha(m_{\mathrm{Z}})}\, Q^{\mathrm{e}}\, g_{\mathrm{Ve}} \times 3 \sum_{\mathrm{q}} Q^{\mathrm{q}}\, g_{\mathrm{V}q}\,. \tag{2.3}$$

Note that the running of α as well as final state QED and QCD corrections are also included in the definition of the S-matrix parameters. The Standard Model value of $j^{\mathrm{had}}_{\mathrm{tot}}$ is 0.21 ± 0.01.

The dependence of the nine parameters on the hadronic γ-Z interference term is studied by considering a set of ten parameters consisting of the standard nine parameters extended by the parameter $j^{\mathrm{had}}_{\mathrm{tot}}$ from the S-Matrix approach. The γ-Z interference terms in the lepton channels are fixed by the leptonic Z couplings. In the existing S-Matrix analyses of LEP-I data [69], a large anti-correlation between m_{Z} and $j^{\mathrm{had}}_{\mathrm{tot}}$ appears, leading to errors on m_{Z} enlarged by a factor of almost three. The dependence of m_{Z} on $j^{\mathrm{had}}_{\mathrm{tot}}$ is given by

$$\frac{\mathrm{d}m_{\mathrm{Z}}}{\mathrm{d}j^{\mathrm{had}}_{\mathrm{tot}}} = -1.6\,\mathrm{MeV}/0.1\,.$$

The changes in all other parameters are below 20 % of their combined error for a change in $j^{\mathrm{had}}_{\mathrm{tot}}$ of 0.1 .

Better experimental constraints on the hadronic interference term are obtained by including measurements of the hadronic total cross-section at centre-of-mass energies further away from the Z pole than just the off-peak energies at LEP-I. Including the measurements of the TRISTAN collaborations at KEK, TOPAZ [70] and VENUS [71], at $\sqrt{(}s)$=58 GeV, the error on

$j^{\mathrm{had}}_{\mathrm{tot}}$ is reduced to ± 0.1, while its central value is in good agreement with the Standard Model expectation. Measurements at centre-of-mass energies above the Z resonance at LEP-II [72–75] also provide constraints on $j^{\mathrm{had}}_{\mathrm{tot}}$, but in addition test modifications to the interference terms arising from the possible existence of a heavy Z′ boson.

The available experimental constraints on $j^{\mathrm{had}}_{\mathrm{tot}}$ thus lead to uncertainties on m_{Z}, independent of Standard Model assumptions in the hadronic channel, which are already smaller than its error. No additional error is assigned to the standard nine-parameter results from effects which might arise from a non-Standard Model behaviour of the γ-Z interference.

2.4.4 Direct Standard Model fits to the measured cross-sections and forward-backward asymmetries

Since an important use of the combined results presented here is to determine parameters of the Standard Model and to test its validity, it is crucial to verify that the parameter set chosen for the combination represents with no significant loss in precision the four sets of experimental measurements from which they were extracted. When the set of pseudo-observables is used in the framework of the Standard Model, the role of m_{Z} changes from an independent parameter to that of a Lagrangian parameter of the theory. This imposes additional constraints which can be expected to shift the value of m_{Z}.

To check whether the nine parameters adequately describe the reaction to these constraints, each collaboration provided results from direct Standard Model fits to their cross-section and asymmetry data. The comparison of these results with those obtained by using the set of pseudo-observables as fit input instead is shown in Table 2.12. m_{H} and α_s were free parameters in these fits, while the additional inputs m_{t}=174.3±5.1 GeV [76] and $\Delta\alpha^{(5)}_{\mathrm{had}} = 0.02804 \pm 0.00065$ [51] (corresponding to $1/\alpha(m_{\mathrm{Z}}) = 128.886 \pm 0.090$) provided external constraints.

Significant shifts in m_{Z} of up to 20 % of its error are observed in some experiments, which however cancel out to almost zero in the average over the four experiments. One anticipated source of these shift has already been mentioned: the Z couplings defining the γ-Z interference term depend on m_{H}, which is allowed to move freely in the first fit, but is fixed to 150 GeV for the extraction of the pseudo-observables. The approximate values of m_{H} preferred by the Standard Model fit to the cross-sections and asymmetries are indicated in the second part of the table. Using the dependence of m_{Z} on the value of m_{H} given in Section 2.3.4, the differences in m_{Z} can be corrected to a common value of the Higgs mass of $m_{\mathrm{Z}} = 150\,\mathrm{GeV}$, as is shown in the last line of Table 2.12. The results indicate that the expected m_{Z} dependence on m_{H} is not the dominant mechanism responsible for the differences. Since the two procedures compared here represent different estimators for m_{Z}, such differences may be expected due to fluctuations of the measurements around the exact Standard Model expectations.

It was verified that the two procedures agree on pseudo-data calculated according to the Standard Model. If the origin of the shifts is due to fluctuations of the measurements within errors, a reduction of the shifts with increased statistical precision is expected to occur, which is indeed what is observed when averaging over the four experiments. The net average difference in m_{Z} directly from the realistic observables or through the intermediary of the pseudo-observables is less than 0.1 MeV. Shifts in the other Standard Model parameters, in the individual data sets as well as in the average, are all well under 5 % of the errors, and therefore also negligible.

The conclusion of this study is that Standard Model parameters extracted from the pseudo-observables are almost identical to the ones that would be obtained from the combined cross-sections and asymmetries. Within the Standard Model the combined set of pseudo-observables

	A	D	L	O	average	% of error
$\chi^2/N_{\rm df}$	174/180	184/172	168/170	161/198		
$\Delta m_{\rm Z}$ [MeV]	−0.7	+0.5	0.0	+0.1	−0.03	1
$\Delta m_{\rm t}$ [GeV]	0.0	0.0	0.0	0.0	0.0	<2
$\Delta \log_{10}(m_{\rm H}/{\rm GeV})$	−0.01	+0.04	+0.02	+0.04	+0.02	4
$\Delta\alpha_s$	0.0000	−0.0002	+0.0002	+0.0002	+0.0001	4
$\Delta(\Delta\alpha^{(5)}_{\rm had})$	+0.00002	−0.00004	0.00000	−0.00004	−0.00002	2
fit value of $m_{\rm H}$ [GeV]	40.	10.	35.	390.		
$\Delta m_{\rm Z}$ [MeV] corr. to 150 GeV $m_{\rm H}$	−0.6	+0.7	+0.1	0.0	+0.05	2

Table 2.12: Shifts in Standard Model parameters, when fit directly to the cross-sections and forward-backward asymmetries compared to when fit to the the nine-parameter results. The numbers in the last line of the table give the shifts in $m_{\rm Z}$ if the results from the first line are corrected to a common value of the Higgs mass of 150 GeV.

provides a description of the measurements of the Z parameters that is equivalent to the full set of cross-sections and asymmetries. This is also true for any theory beyond the Standard Model which leads to corrections that are absorbed in the pseudo-observables. An exception to this are those theories with an additional Z′-bosons which lead to significant modifications of the γ-Z interference term. (See the discussion in Section 2.4.3.)

2.5 Combined results

The result of the combination of the four sets of nine pseudo-observables including the experimental and common error matrices is given in Table 2.13. The parametric uncertainties due to the residual dependence on the choice of Standard Model parameters used to calculate the remnants are not included. The only significant such uncertainty concerns the value of the Higgs boson mass, which is taken to be 150 GeV and is relevant only for the value of $m_{\rm Z}$. $m_{\rm Z}$ changes by +0.23 MeV per unit change in $\log_{10}(m_{\rm H}/{\rm GeV})$, as was discussed in Section 2.3.4.

In principle, the lepton-universality average over the four experiments could also be performed at the level of the five-parameter results. When this is attempted, good agreement is seen with the results in the lower part of Table 2.13 except for R^0_ℓ, where the difference amounts to 0.005 or 20 % of the total error. The origin of this shift are changes of weight for the $\rm e^+e^-$ final state due to the common t-channel error. If the average over the leptonic measurements is performed by each experiment individually, the weight given to the electron channel is larger than for the case where the averages over individual lepton species are averaged at the end. Extracting the results with lepton universality from the nine parameters is therefore the appropriate method.

The value of χ^2 per degree of freedom of the combination is 32.6/27 and corresponds to a probability of 21 % to find a value of χ^2 which is smaller than the one actually observed. The correlation matrix of the combined result shows significant correlations of $\sigma^0_{\rm h}$ with $\Gamma_{\rm Z}$ and $R^0_{\rm e}$, R^0_μ and R^0_τ and between $R^0_{\rm e}$ and $A^{0,{\rm e}}_{\rm FB}$.

without lepton universality		correlations								
$\chi^2/N_{\rm df}$ = 32.6/27		$m_{\rm Z}$	$\Gamma_{\rm Z}$	$\sigma^0_{\rm h}$	$R^0_{\rm e}$	R^0_μ	R^0_τ	$A^{0,{\rm e}}_{\rm FB}$	$A^{0,\mu}_{\rm FB}$	$A^{0,\tau}_{\rm FB}$
$m_{\rm Z}$ [GeV]	91.1876± 0.0021	1.00								
$\Gamma_{\rm Z}$ [GeV]	2.4952 ± 0.0023	−.024	1.00							
$\sigma^0_{\rm h}$ [nb]	41.541 ± 0.037	−.044	−.297	1.00						
$R^0_{\rm e}$	20.804 ± 0.050	.078	−.011	.105	1.00					
R^0_μ	20.785 ± 0.033	.000	.008	.131	.069	1.00				
R^0_τ	20.764 ± 0.045	.002	.006	.092	.046	.069	1.00			
$A^{0,{\rm e}}_{\rm FB}$	0.0145 ± 0.0025	−.014	.007	.001	−.371	.001	.003	1.00		
$A^{0,\mu}_{\rm FB}$	0.0169 ± 0.0013	.046	.002	.003	.020	.012	.001	−.024	1.00	
$A^{0,\tau}_{\rm FB}$	0.0188 ± 0.0017	.035	.001	.002	.013	−.003	.009	−.020	.046	1.00

with lepton universality						
$\chi^2/N_{\rm df}$ = 36.5/31		$m_{\rm Z}$	$\Gamma_{\rm Z}$	$\sigma^0_{\rm h}$	R^0_ℓ	$A^{0,\ell}_{\rm FB}$
$m_{\rm Z}$ [GeV]	91.1875± 0.0021	1.00				
$\Gamma_{\rm Z}$ [GeV]	2.4952 ± 0.0023	−.023	1.00			
$\sigma^0_{\rm h}$ [nb]	41.540 ± 0.037	−.045	−.297	1.00		
R^0_ℓ	20.767 ± 0.025	.033	.004	.183	1.00	
$A^{0,\ell}_{\rm FB}$	0.0171 ± 0.0010	.055	.003	.006	−.056	1.00

Table 2.13: Combined results for the Z parameters of the four sets of nine pseudo-observables from Table 2.4.
The errors include all common errors except the parametric uncertaintiy on $m_{\rm Z}$ due to the choice of $m_{\rm H}$.

A comparison of the leptonic quantites $R^0_{\rm e}$, R^0_μ and R^0_τ and of $A^{0,{\rm e}}_{\rm FB}$, $A^{0,\mu}_{\rm FB}$ and $A^{0,\tau}_{\rm FB}$ shows that they agree within errors. Note that R^0_τ is expected to be larger by 0.23 % because of τ mass effects. Figure 2.9 shows the corresponding 68 % level contours in the R^0_ℓ–$A^{0,\ell}_{\rm FB}$ plane.

Imposing the additional requirement of lepton universality in the combination leads to the results shown in the second part of Table 2.13. Note that R^0_ℓ is defined for massless leptons. The value of $\chi^2/N_{\rm df}$ of 36.5/31 for the combination of the four sets of nine pseudo-observables into the five parameters of Table 2.13 corresponds to a χ^2-probability of 23 %. The central ellipse in Figure 2.9 shows the 68 %-CL contour for the combined values of R^0_ℓ and $A^{0,\ell}_{\rm FB}$ determined from all three lepton species.

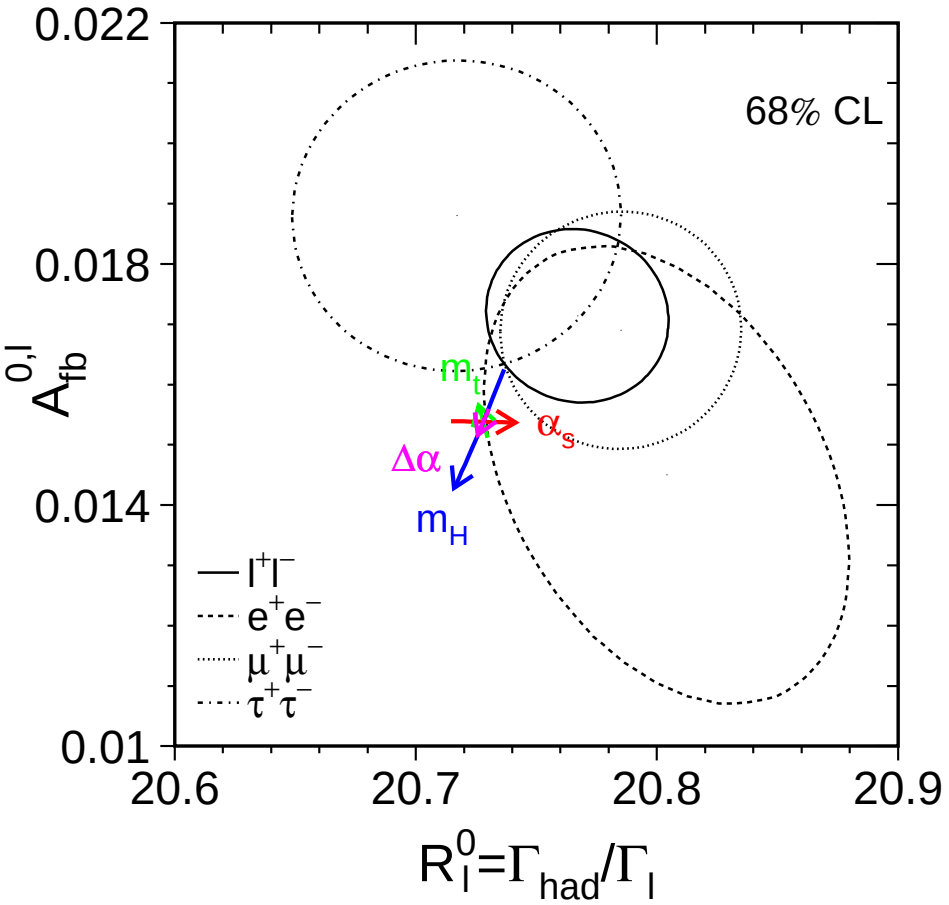

Figure 2.9: Contour lines (68 % CL) in the R^0_ℓ–$A^{0,\ell}_{\rm FB}$ plane for e^+e^-, $\mu^+\mu^-$ and $\tau^+\tau^-$ final states and for all leptons combined. For better comparison the results for the τ lepton are corrected to correspond to the massless case. The Standard Model prediction for $m_{\rm Z} = 91.1875$ GeV, $m_{\rm t} = 174.3$ GeV, $m_{\rm H} = 300$ GeV, and $\alpha_{\rm S}(m^2_{\rm Z}) = 0.119$ is also shown. The lines with arrows correspond to the variation of the Standard Model prediction when $m_{\rm t}$, $m_{\rm H}$ and $\alpha_{\rm S}(m^2_{\rm Z})$ are varied in the intervals $m_{\rm t} = 174.3 \pm 5.1$ GeV, $m_{\rm H} = 300^{+700}_{-200}$ GeV, and $\alpha_{\rm S}(m^2_{\rm Z}) = 0.119 \pm 0.002$, respectively. The arrows point in the direction of increasing values of $m_{\rm t}$, $m_{\rm H}$ and $\alpha_{\rm S}$.

Chapter 3

Measurement of $A_{\rm LR}$ and the Lepton Asymmetries at the SLC

3.1 The $A_{\rm LR}$ Measurement

The measurement of the left-right cross section asymmetry ($A_{\rm LR}$) by SLD [77, 78] at the SLC provides a determination of the coupling $\mathcal{A}_{\rm e}$, and is presently the most precise single measurement, with the smallest systematic error, of this quantity. In addition $A_{\rm LR}$, along with the tau polarisation measurements, are the most sensitive among the asymmetries to the effective weak mixing angle, with $\delta A_{\rm LR} \approx 7.85\delta(\sin^2\theta^{\rm lept}_{\rm eff})$.

In principle the analysis is straightforward: one counts the numbers of Z bosons produced by left and right longitudinally polarised electrons, forms an asymmetry, and then divides by the luminosity-weighted e^- beam polarisation magnitude (the e^+ beam is not polarised):

$$A_{\rm LR} = \frac{N_{\rm L} - N_{\rm R}}{N_{\rm L} + N_{\rm R}} \frac{1}{\langle \mathcal{P}_e \rangle}. \tag{3.1}$$

The method requires no detailed final state event identification (e^+e^- final state events are removed due to non-resonant t-channel contributions, as are all other backgrounds not due to Z decay) and is insensitive to all acceptance and efficiency effects. In order to convert $A_{\rm LR}$ at a particular value of E_{cm} into a determination of the effective weak mixing angle, the result is converted into a "Z-pole" value by the application of $\sim 2.0\%$ correction for initial state radiation and $\gamma - Z$ interference [24], which is relatively small compared to other asymmetry measurements.

$$A_{\rm LR}(E_{CM}) \rightarrow A_{\rm LR} + \Delta A_{\rm LR} = A^0_{\rm LR} \equiv \mathcal{A}_{\rm e}. \tag{3.2}$$

This calculation requires accurate and precise knowledge of the luminosity-weighted average centre-of-mass collision energy E_{cm}.

For the most recent data (1997-1998), the small total systematic error of 0.65% relative is dominated by the 0.50% relative systematic error in the determination of the luminosity-weighted average e^- polarisation, with the second largest error (0.39%) arising from uncertainties in the determination of the luminosity-weighted average centre-of-mass energy. A number of very much smaller contributions to the systematic error will be discussed below. The relative statistical error on $A_{\rm LR}$ from all data is about 1.3%.

In what follows, some of the details of the $A_{\rm LR}$ measurement will be described and some historical context for the $A_{\rm LR}$ program at SLC/SLD (1992-1998) will be provided.

3.1.1 Electron Polarisation at the SLC

In section 1.1.2, the operation of the SLC was briefly outlined, and Figure 1.4 provided a schematic of the machine. The SLC produced longitudinally polarised electrons by illuminating a Gals photo cathode with a circularly polarised Hi-Sapphire laser. Following the advent of high polarisation "strained lattice" Gals photocathodes (1994) [79], where mechanical strain induced in a thin (0.1 micron) Gals layer lifts an angular momentum degeneracy in the valence band of the material, the average electron polarisation at the e^+e^- interaction point (IP) (slightly lower than the value produced at the source) was in the range 73% to 77% (see Figure 1.5). Corresponding values were about 22% in 1992 using a unstrained "bulk" GaAs cathode, and 63% in 1993 using a thicker (0.3 micron) strained layer cathode design. The electron helicity is chosen randomly pulse-to-pulse at the machine repetition rate of 120 Hz by controlling the circular polarisation of the source laser.

The electron spin orientation is longitudinal at the source and remains longitudinal until it is transported to the damping ring (DR). In the linac-to-ring (LTR) transport line, the electron spins precess due to the dipole magnets, where the spin precession angle is given in terms of the anomalous magnetic moment g : $\theta_{precession} = (\frac{g-2}{2})\frac{E}{m}\theta_{bend}$. By design, the bend angle θ_{bend} results in transverse spin orientation at the entrance to the LTR spin rotator magnet. This superconducting solenoid magnet is used to rotate the polarisation about the beam direction into the vertical orientation for storage in the DR. This is necessary as any horizontal spin components precess rapidly and completely dissipate during the 8.3 msec (1/120 seconds) storage time due to energy spread in the bunch. The polarised electron bunches can be stored in one of two possible configurations by the reversal of the LTR spin rotator solenoid magnet. These reversals, typically done after three month intervals, were useful for identifying and minimising the small ($\mathcal{O}(10^{-4})$) polarisation asymmetries produced at the source.

Manipulation of the electron spin in the SLC north arc, necessary for maximal longitudinal polarisation at the IP, was possible as the betatron phase advance closely matched the spin precession (1080 and 1085 degrees respectively) in each of the 23 bending-magnet assemblies ("acromats") used in the arc - and hence the north arc operated close to a spin-tune resonance [80]. As a result, excepting 1992 running, two additional SLC spin rotator solenoids were not necessary for spin orientation, and were used only in a series of specialised polarisation experiments.

3.1.2 Polarimetry at the SLC

In Compton scattering of longitudinally polarised electrons from circularly polarised photons, the differential cross section in terms of the normalised scattered photon energy fraction x is given by

$$\frac{d\sigma}{dx} = \frac{d\sigma_0}{dx}[1 - \mathcal{P}_\gamma \mathcal{P}_e A(x)], \tag{3.3}$$

where $\frac{d\sigma_0}{dx}$ is the unpolarised differential cross section, $\mathcal{P}_{\gamma,e}$ are the photon and electron polarisations, and $A(x)$ is the Compton asymmetry function. The asymmetry arises due to the difference between spin parallel and spin anti-parallel cross sections ($\sigma_{j=3/2} > \sigma_{j=1/2}$). In a polarimeter, the Compton scattered photons or electrons are detected, and the requisite instrumental effects are incorporated into an energy dependent detector response function. The convolution of $A(x)$ with $\frac{d\sigma_0}{dx}$ and the response function $R(x)$ (all functions of the fractional

energy x), normalised by the convolution of $R(x)$ and $\frac{d\sigma_0}{dx}$, is known as the "analysing power" a :

$$a = \frac{\int A(x)R(x)\frac{d\sigma_0}{dx}dx}{\int R(x)\frac{d\sigma_0}{dx}dx}, \tag{3.4}$$

where the integration is over the relevant acceptance in x (for a multichannel detector, a_i and $R_i(x)$ can be defined for the ith channel). When $\mathcal{P}_\gamma$ and the analysing power are known, the experimental determination of the $j = 3/2$ to $j = 1/2$ scattering asymmetry determines $\mathcal{P}_e$, and hence the utility of this elementary QED process to electron polarimetry. The SLD precision Compton polarimeter detected beam electrons that had been scattered by photons from a circularly polarised laser. The choice of a Compton-scattering polarimeter was dictated by the requirements that the device be operated continually while beams were in collision and that uncertainties in the physics of the scattering process not be a limiting factor in the systematic error; both troublesome issues for Møller scattering instruments due to their magnetic alloy targets. In addition, the pulse-to-pulse controllability of the laser polarisation sign, as well as its high polarisation value (99.9%), are additional advantages over other options.

Figure 3.1 illustrates the essential features of the polarimeter : Frequency doubled (532 nm) Nd:YAG laser pulses of 8 ns duration and peak power of typically 25 MW were produced at 17 Hz, circularly polarised by a linear polariser and a Pockels cell pair. The laser beam was transported to the SLC beamline by four sets of phase-compensating mirror pairs and into the vacuum chamber through a reduced-strain quartz window. About 30 meters downstream from the IP, the laser beam was brought into head-on collisions with the outgoing electron beam (10 mrad crossing angle) at the Compton Interaction Point (CIP), and then left the beampipe through a second window to an analysis station. The pair of Pockels cells on the optical bench allowed for full control of elliptical polarisation and was used to automatically scan the laser beam polarisation at regular intervals in order to monitor, and maximise, laser polarisation at the CIP. This procedure significantly improved the magnitude of the laser circular polarisation, and the precision of its determination [81]. In colliding a $\sim 45GeV$ electron beam with a visible light, the scattered photons are very strongly boosted along the electron beam direction and are essentially collinear with the Compton scattered electrons * Downstream from the CIP, a pair of bend magnets swept out the off-energy Compton-scattered electrons (typically of order 1000 per laser pulse) which passed through a thin window and out of the beamline vacuum into a 9 channel (1 cm per channel) transversely segmented gas Cherenkov detector. By detecting scattered electrons with a threshold Cherenkov device (the threshold for the 1 atm. propane gas used was about 11 MeV), large beamstrahlung backgrounds in the SLC environment were dramatically reduced.

The minimum energy 17.4 GeV electrons, corresponding to full backscattering, generally fell into the 7th channel. At this point in the electron spectrum, known as the "Compton edge", the polarisation asymmetry function reached its maximum value of 0.748. Small deviations from the theoretical Compton energy dependent asymmetry function (of order 1% near the Compton edge) were determined by modelling the detector response functions for each of the nine channels. An EGS simulation was used for this calculation, which included a detailed Monte Carlo of the detector geometry and relevant beamline elements, the Cherenkov light generation and transport, and the magnetic spectrometer [82, 83]. The detector was mounted on a movable platform and the Compton Edge was scanned across several channels at regular

*Compton scattered photons with energies in the range from the kinematically allowed maximum of 28 GeV down to 1 GeV are contained within an angle of about 100 μrad w.r.t. the electron beam direction.

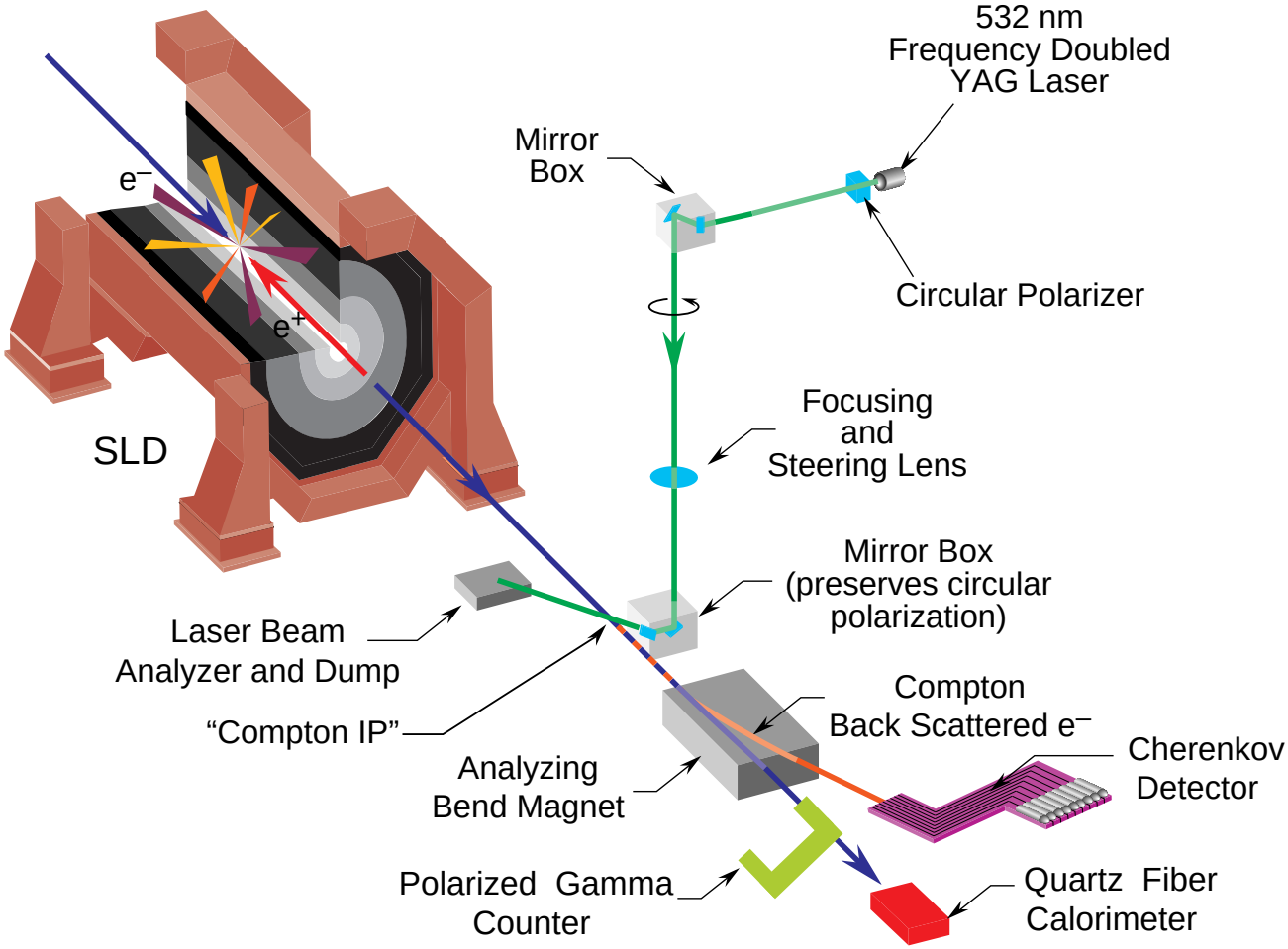

Figure 3.1: A conceptual diagram of the SLD Compton Polarimeter. The laser beam is circularly polarised and transported into head-on collision with the electron beam approximately 30 meters from the IP. Following the laser/electron-beam collision, the electrons and Compton-scattered photons (which are strongly boosted along the electron beam direction), continue downstream until analysing bend magnets deflect the Compton-scattered electrons into a transversely- segmented Cerenkov detector. The photons continue undeflected and are detected by a gamma counter and a calorimeter which are used to cross-check the polarimeter calibration.

intervals in order to monitor the location of the Compton edge and to experimentally constrain the detector/spectrometer simulation. For each "edge scan", a multiparameter fit to the channel scan data was performed to the spectrometer setup, channel gains, luminosity at each platform position, and the "polarisation product" $\mathcal{P}_\gamma \mathcal{P}_e$. From these fits, the reliability of the simulation was tested, in particular, the tails of the channel response functions were shown to be well modelled. This procedure was essential for the precise determination of the analysing power of the important outer channels. Additional cross checks tracked the stability of the analysing powers during time periods between edge scans (for example, the ratio of selected channel asymmetries were monitored). Representative data showing the corrected Compton asymmetry as well as the magnitude of the correction, as a function of position and scattered electron energy, is shown in Figure 3.2. There is good agreement between the corrected asymmetry and the data in each channel.

Detector effects such as non-linearity (in the electronics and/or the photomultiplier tubes), and electronic noise (mainly due to pickup from the laser Q-switch used to produce the short high peak power laser pulse) are measured from the data. The highly variable e^+e^- collision-related backgrounds in the polarimeter were put to good use as they effectively scanned the total per-channel response over a very wide dynamic range (the "zero-backgrounds" condition was determined from polarisation measurements taken without the positron beam), as shown in Figure 3.3. Electronic pickup effects were conveniently studied using the occasional machine cycles without beam. A number of offline electronics tests and specialised data configurations during running (for example, photomultiplier tube voltage scans) were also useful in establishing the size of systematic uncertainties

Starting in 1996, two additional polarimeter detectors [84, 85] that were sensitive to the Compton-scattered photons and which were operated in the absence of positron beam, were used to verify the precision polarimeter calibration. These two devices were of different design (one was a threshold-gas Cherenkov detector and the other was a quartz-fiber calorimeter) with different systematic errors, and had in common with the primary electron polarimeter only the instrumental errors due to the polarised laser. The cross check provided by these photon detectors was used to establish a calibration uncertainty of 0.4%, as shown in Figure 3.4. The systematic errors due to polarimetry are summarised in Table 3.1. During the period 1992-1998, this total fractional systematic error decreased from 2.7% to its present value of 0.50%, with the most significant reductions coming from greatly improved understanding of the laser polarisation and Cherenkov detector nonlinearities. The dominant error is now due to the analysing power calibration discussed above.

The polarimeter result was corrected for higher order QED and accelerator-related effects (a total of $-0.22 \pm 0.15\%$ for 1997-1998 data). The higher order QED offset was very small and well-determined (-0.1%) [86]. The primary accelerator-related effect arose from energy-to-polarisation correlations and energy-to-luminosity correlations, that together with the finite energy spread in the beam, caused the average beam polarisation measured by the Compton Polarimeter to differ slightly from the luminosity-weighted average beam polarisation at the IP. In 1994-1998 a number of changes in the operation of the SLC and in monitoring procedures (smaller and better determined beam energy spread and polarisation energy dependence) reduced the size of this *chromaticity* correction and its associated error to below 0.2% from its value of $1.1 \pm 1.7\%$ when it was first observed in 1993. An effect of comparable magnitude arose due to the small precession of the electron spin in the final focusing elements between the IP and the polarimeter. The contribution of collisional depolarisation was determined to be negligible as expected, by comparing polarimeter data taken with and without beams in

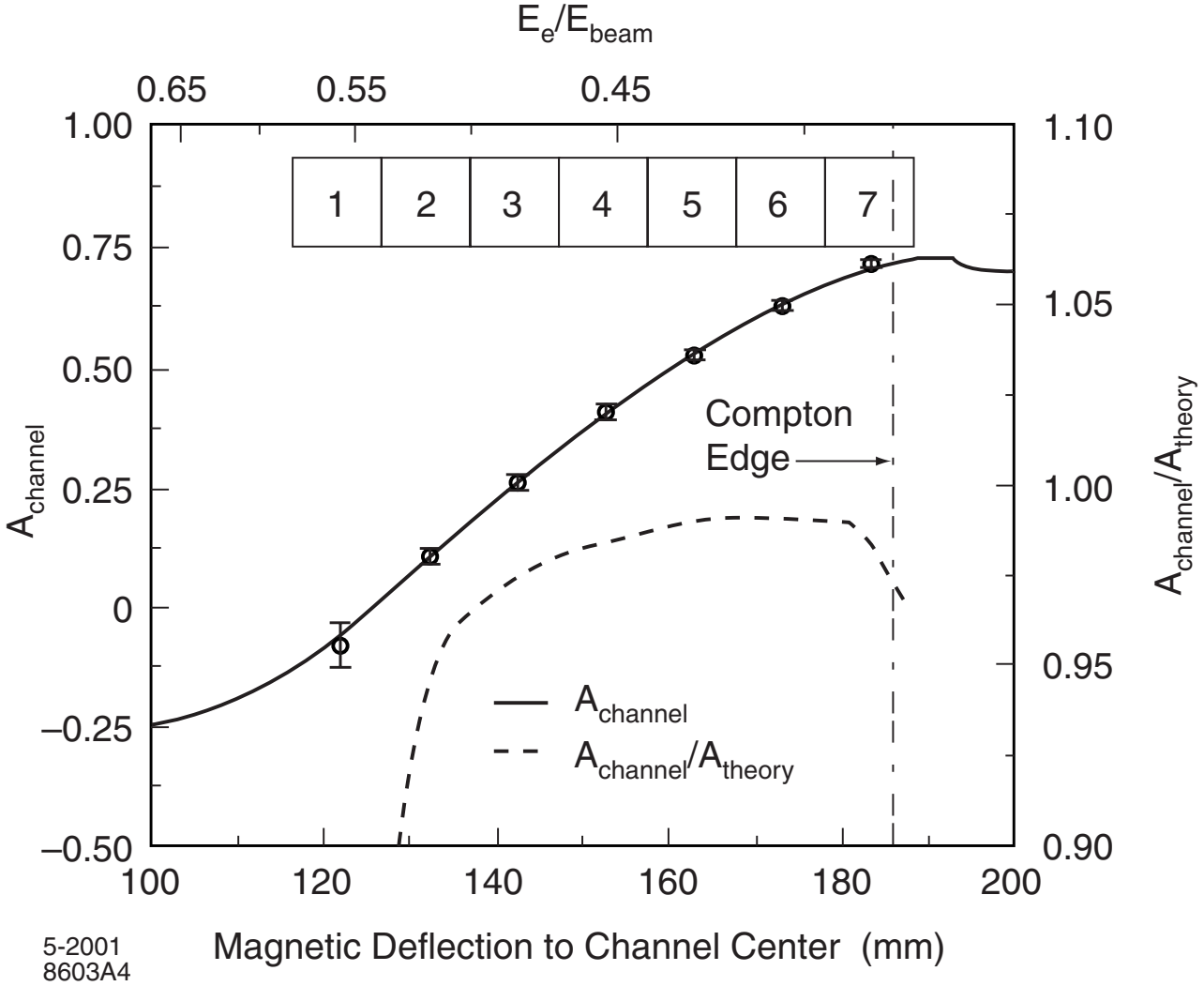

Figure 3.2: Compton scattering asymmetry as a function of channel position. The deflection of the electron beam in the spectrometer is shown on the horizontal axis as the distance in mm from the centre of the detector channels (1 cm wide each) to the path of a hypothetical infinite momentum electron beam. The inset shows the seven inner detector channels, sized to match the horizontal scale. The per channel data is plotted as open circles, and the corrected asymmetry function is the solid curve. The relative size of the correction to the theoretical QED calculation is indicated by the dashed curve, and the right-side vertical scale.

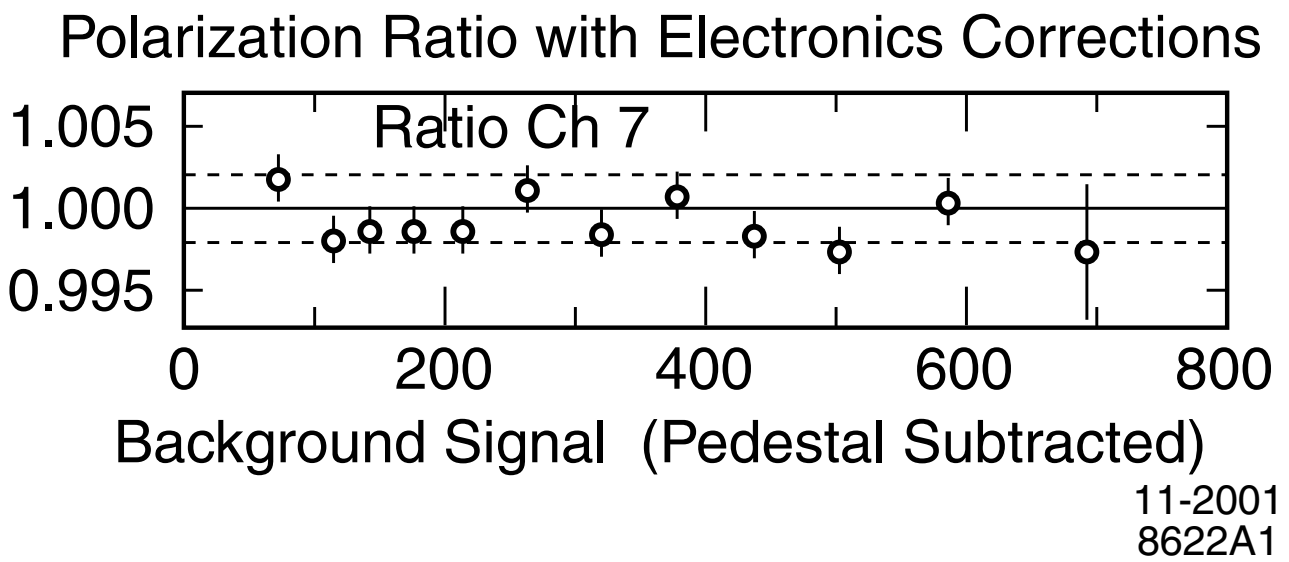

Figure 3.3: The linearity of channel 7 is shown for a wide range of detector background levels (expressed here in pedestal subtracted ADC counts). Plotted on the vertical axis is the fully corrected polarisation result, normalised to the "zero background" case (no beam collisions). The result here is seen to be constant to within 0.2% over the full range.

collision. All effects combined yielded a correction with the uncertainty given in Table 3.1.

The luminosity-weighted average polarisation $\langle \mathcal{P}_e \rangle$ for each run was estimated from measurements of $\mathcal{P}_e$ made when Z events were recorded,

$$\langle \mathcal{P}_e \rangle = (1 + \xi) \cdot \frac{1}{N_Z} \sum_{i=1}^{N_Z} \mathcal{P}_i \tag{3.5}$$

where N_Z is the total number of Z events, $\mathcal{P}_i$ is the polarisation measurement associated in time with the i^{th} event, and ξ is the small total correction described in the previous paragraph. The polarimeter was operated continually, where typically about three minutes were required to achieve a relative statistical precision of order 1% for each polarisation measurement.

The fully corrected luminosity weighted average polarisations corresponding to each of the SLD runs are given in Table 3.1.6. The evolution of GaAs photocathode performance is evident in 1993 and again in 1994-1995. Changes in the achieved polarisation in later years mainly reflect variations in photocathode manufacture.

3.1.3 Energy Spectrometry

The SLC employed a pair of energy spectrometers located in the electron and positron extraction lines (Figure 1.4). The beam defection by a precision dipole magnet was detected and measured using the separation between synchrotron radiation swathes emitted by the beam in deflector magnets, oriented perpendicular to the bending plane and located before and after the bend (see Figure 3.5). These devices were first operated in their final configuration in 1989 by the Mark II experiment, and the calibration of the two precision spectrometer magnets was performed in 1988 [87]. Their expected precision was about ±20 MeV on the measured centre-of-mass collision energy E_{cm}. The importance of these devices to the $A_{\rm LR}$ measurement

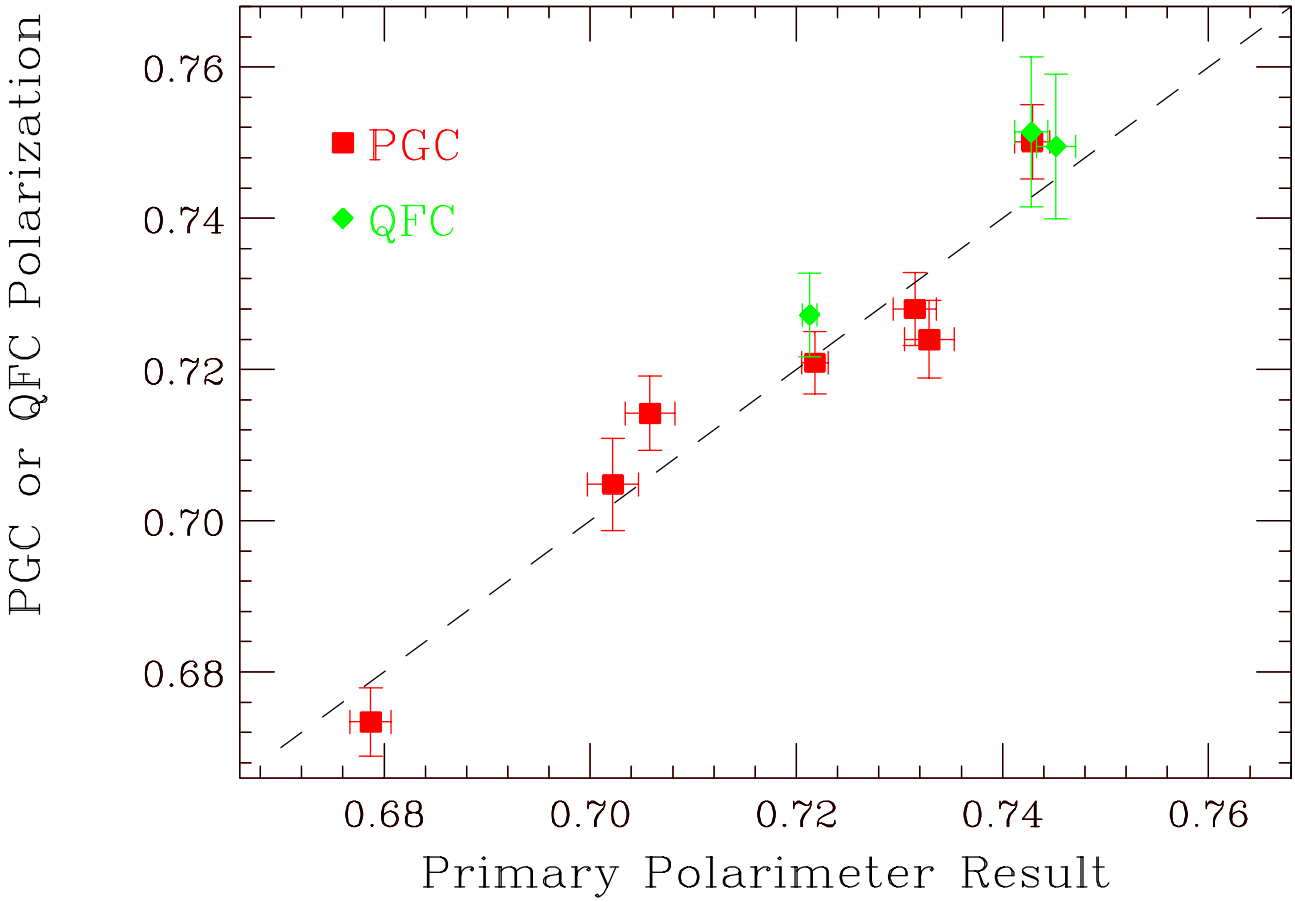

Figure 3.4: The PGC and QFC photon detector polarisation results (vertical axis) compared to the primary electron detector polarimeter measurements (horizontal axis).

is quantified by the approximate rule of thumb that an 80 MeV uncertainty in E_{cm} corresponds to a 1% error on the Z-pole asymmetry $A^0_{\rm LR}$. For this reason, in 1998 a Z peak scan was performed in order to calibrate the spectrometers to the LEP measurement of the Z mass. The scan used two optimised offpeak points at +0.88 and −0.93 GeV and approximately 9,000 Z equivalents of luminosity to reach a statistical precision on the peak position of 20 MeV. The results of a complete analysis of systematic effects determined an offset of -46 MeV and a total E_{cm} uncertainty of 29 MeV (a 0.39% uncertainty on $A^0_{\rm LR}$, as shown in Table 3.1) [88].

Uncertainty	$\delta\mathcal{P}_e/\mathcal{P}_e$ (%)	$\delta A_{\rm LR}/A_{\rm LR}$ (%)	$\delta A^0_{\rm LR}/A^0_{\rm LR}$ (%)
Laser polarisation	0.10		
Detector linearity	0.20		
Analysing power calibration	0.40		
Electronic noise	0.20		
Total polarimeter uncertainty	0.50	0.50	
Chromaticity and IP corrections		0.15	
Corrections in Eq. 3.6		0.07	
$A_{\rm LR}$ Systematic uncertainty		0.52	0.52
Electroweak interference correction			0.39
$A^0_{\rm LR}$ Systematic uncertainty			0.64

Table 3.1: Systematic uncertainties that affect the $A_{\rm LR}$ measurement for 1997/98. The uncertainty on the electroweak interference correction is caused by the uncertainty on the SLC energy scale.

3.1.4 Event Selection

A simple calorimetric event selection in the Liquid Argon Calorimeter (LAC), supplemented by track multiplicity and topology requirements in the Central Drift Chamber (CDC), were used to select hadronic Z decays. For each event candidate, energy clusters were reconstructed in the LAC. Selected events were required to contain at least 22 GeV of energy observed in the clusters and to manifest a normalised energy imbalance of less than 0.6 [†]. The left-right asymmetry associated with final state e^+e^- events is expected to be diluted by the t-channel photon exchange subprocess. Therefore, we excluded e^+e^- final states by requiring that each event candidate contain at least 4 selected CDC tracks, with at least 2 tracks in each hemisphere (defined with respect to the beam axis), or at least 4 tracks in either hemisphere. This track topology requirement excludes Bhabha events which contain a reconstructed gamma conversion. Small backgrounds in the $A_{\rm LR}$ data sample were due to residual e^+e^- final state events, and to two-photon events, beam-related noise, and cosmic rays. For the most recent data (1996-98) the total background contamination was estimated to be $< 0.05\%$ for a selection efficiency of $91 \pm 1\%$.

[†]The energy imbalance is defined as a normalised vector sum of the energy clusters as follows, $E_{\rm imb} = |\sum \vec{E}_{\rm cluster}|/\sum |E_{\rm cluster}|$.

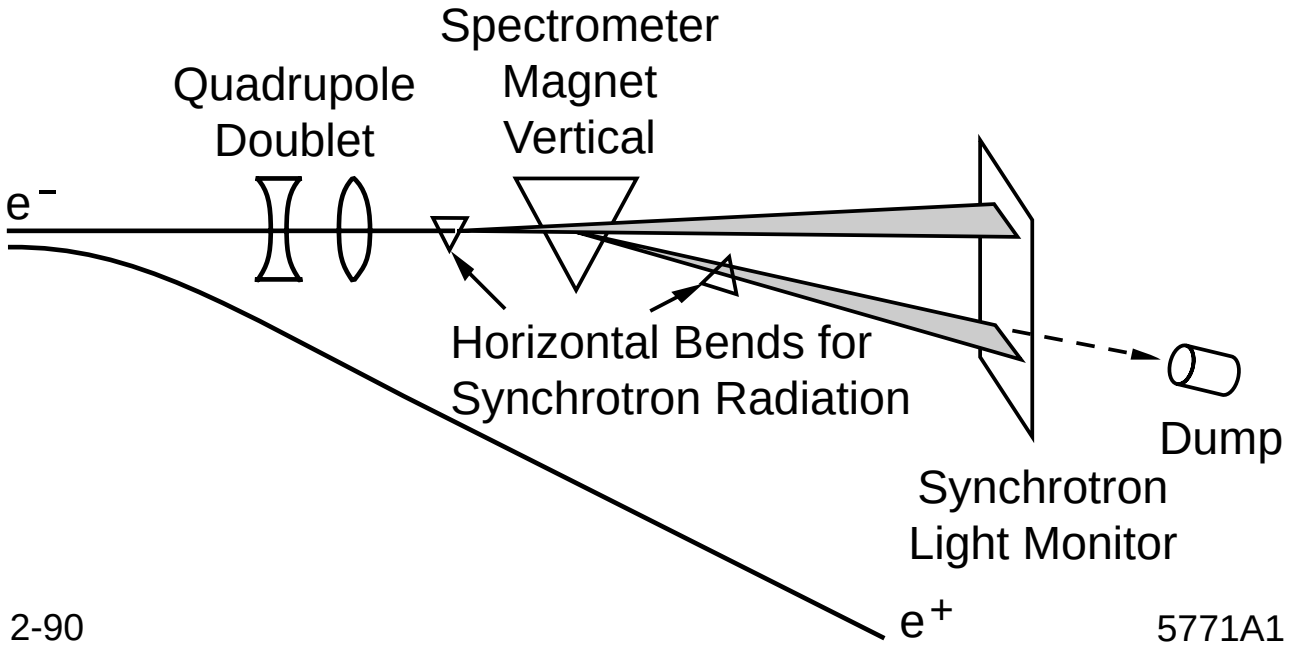

Figure 3.5: The energy spectrometer for electrons (a similar device is used on the positron side) uses a precision bend magnet and synchrotron-radiation-producing deflector magnets before and after the bend, in order to determine the beam bend angle.

3.1.5 Control of Systematic Effects

The $A_{\rm LR}$ measurement is remarkably resistant to detector dependent systematic effects and Monte Carlo modelling uncertainties that are significant issues for all other electroweak precision measurements. By far the dominant systematic effects arise from polarimetry and from the determination of the collision energy, rather than from any details of the analysis or the operation of the SLD. The simple expression given in equation 3.1 applies to the ideal case in the absence of systematic effects, and as such it is a good approximation to better than a relative 0.2%.

Nevertheless, systematic left-right asymmetries in luminosity, polarisation, beam energy, and acceptance, as well as background and positron polarisation effects, can be incorporated into an extended expression for the cross section asymmetry. (Note that while the random helicity of the delivered electron bunches is exactly 50% right-handed, it is in principle possible that the magnitude of the luminosity is not equal for the two helicities. In addition, the individual polarisation measurements of equation 3.5 average over many beam crossings and over any systematic left-right polarisation difference, and hence additional information is needed to make the required correction.) One finds the measured asymmetry A_m is related to $A_{\rm LR}$ by the following expression which incorporates a number of small correction terms in lowest-order approximation,

$$\begin{aligned} A_{\rm LR} &= \frac{A_m}{\langle\mathcal{P}_e\rangle} + \frac{1}{\langle\mathcal{P}_e\rangle}\Big[f_{bkg}(A_m - A_{bkg}) - A_{\mathcal{L}} + A_m^2 A_{\mathcal{P}} \\ &\qquad - E_{cm}\frac{\sigma'(E_{cm})}{\sigma(E_{cm})}A_E - A_\varepsilon + \langle\mathcal{P}_e\rangle\mathcal{P}_p\Big], \end{aligned} \tag{3.6}$$

where $\langle\mathcal{P}_e\rangle$ is the mean luminosity-weighted polarisation; f_{bkg} is the background fraction; $\sigma(E)$

is the unpolarised Z boson cross section at energy E; $\sigma'(E)$ is the derivative of the cross section with respect to E; A_{bkg}, $A_{\mathcal{L}}$, $A_{\mathcal{P}}$, A_E, and A_ε are the left-right asymmetries [‡] of the residual background, the integrated luminosity, the beam polarisation, the centre-of-mass energy, and the product of detector acceptance and efficiency, respectively; and $\mathcal{P}_p$ is any longitudinal positron polarisation of constant helicity. Since the colliding electron and positron bunches were produced on different machine cycles and since the electron helicity of each cycle was chosen randomly, any positron helicity arising from the polarisation of the production electrons was uncorrelated with electron helicity at the IP. The net effect of positron polarisation from this process vanishes rigorously. However, positron polarisation of constant helicity would affect the measurement.

The close ties between this measurement and the SLC accelerator complex is evident from numerous dedicated accelerator-based experiments dedicated to the SLD physics program, for which the energy-calibrating Z-peak scan is one example. Other examples include :

- *Communication of the e^- bunch helicity from the polarised source was verified (1992-1993).* Although the electron bunch polarisation state was transmitted via reliable and redundant paths to the SLD detector/polarimeter complex, the SLD electroweak group proposed a series of independent tests of the synchronisation of this data and the SLD event data. In one such test, the laser optics at the SLC polarised source were temporarily modified by the addition of a polariser and quarter-wave plate so that photocathode illumination was nulled for one of the two circular polarisation states. The positron beam was turned off, and the electron beam was delivered to the IP. Beam-related background in the SLD liquid-argon calorimeter (LAC) was detected, but only for the non-extinct pulses. By this means, the expected correlation between helicity and the presence of beam, and hence the LAC data stream, was verified [89].

- *Moderate precision Møller and Mott polarimeters confirmed the high precision Compton polarimeter result to $\sim 3\%$ (1993-1995).* Møller polarimeters located at the end of the SLAC Linac and in the SLC electron extraction line were used to cross-check the Compton polarimeter. The perils of employing a less reliable method to test a precision device were apparent when large corrections for atomic electron momentum effects in the Møller target were discovered [90], after which, good agreement was obtained. In addition, a less direct comparison was provided by Mott polarimeter bench tests of the GaAs photocathodes [91].

- *SLC arc spin transport was extensively studied (1993-1998), and was frequently monitored and adjusted.* A series of experiments were done that studied the beam polarisation reported by the Compton polarimeter as a function of beam energy, beam energy spread and beam trajectory in the SLC arcs. Two spin rotators (in the Linac, and in the ring-to-linac return line) were scanned in order to determine the IP polarisation maximum. An important result of these experiments was the discovery that the SLC arcs operate near a spin tune resonance, leading to the advent of spin manipulation via "spin bumps" in the SLC arcs mentioned earlier. This procedure eliminated the need for the two spin rotators and allowed the spin chromaticity ($d\mathrm{P}/dE$) to be minimised, reducing the resulting polarisation correction from $> 1\%$ in 1993 to $< 0.2\%$ by 1995. In subsequent years the spin transport properties of the SLC arcs were monitored at regular intervals.

[‡]The left-right asymmetry for a quantity Q is defined as $A_Q \equiv (Q_L - Q_R)/(Q_L + Q_R)$ where the subscripts L and R refer to the left- and right-handed beams, respectively.

- *Positron polarisation was experimentally constrained.* In 1998, a dedicated experiment was performed in order to directly test the expectation that accidental polarisation of the positron beam was negligible ; the positron beam was delivered to a Møller polarimeter in the SLAC End Station A (ESA). Experimental control was assured by first delivering the polarised electron beam, and then an unpolarised electron beam (sourced from SLAC's thermionic electron gun), to the ESA, confirming polarimeter operation. In addition, the spin rotator magnet located in the Linac was reversed halfway through the positron beam running, reversing the sense of polarisation at the Møller target and reducing systematic error. The final result verified that e^+ polarisation was consistent with zero ($-0.02 \pm 0.07\%$) [92].

The asymmetries in luminosity, polarisation, and beam energy (approximately 10^{-4}, 10^{-3} and 10^{-7} respectively) were all continually monitored using a small-angle radiative Bhabha counter located $\approx$ 40m from the IP, beamstrahlung monitors, beam current monitors, the Compton polarimeter, and energy spectrometer data. The long-term average values of all asymmetries of this type were reduced by the roughly tri-monthly reversal of the transverse polarisation sense in the electron damping ring referred to in section 3.1. The dominant cause of the observed asymmetries was the small current asymmetry produced at the SLC polarised source. This effect arose because of the source photocathode sensitivity to linear polarised light, together with residual linear polarisation in the source laser light that was correlated with the light helicity. This effect was minimised by a polarisation control and intensity feedback system starting in 1993, and was generally maintained at below 10^{-4}.

The value of $A_{\rm LR}$ is unaffected by decay-mode-dependent variations in detector acceptance and efficiency provided, for the simple case of Z decay to a fermion pair, that the efficiency for detecting a fermion at some polar angle (with respect to the electron direction) is equal to the efficiency for detecting an antifermion at the same polar angle. In hadronic Z decays, the fermions in question are the initial quark-antiquark pair, which materialise as multi-particle jets. These facts, and the high degree of polar symmetry in the SLD detector, render A_ε completely negligible. Finally, $\mathcal{P}_p$ was experimentally demonstrated to be consistent with zero to a precision of 7×10^{-4} as described above (Calculations based on polarisation buildup in the positron damping ring suggested a much smaller number, $\mathcal{P}_p < \mathcal{O}(10^{-5})$; hence, no correction for $\mathcal{P}_p$ was applied to the data).

The systematic effects discussed in this section are summarised in Table 3.1.5. The corrections for backgrounds and accelerator asymmetries and the associated uncertainties, were much smaller than the leading systematic errors due to polarimetry and energy uncertainties, as can be seen by comparing the last three rows of Table 3.1.5.

3.1.6 Results

The run-by-run $A_{\rm LR}$ results are shown in Table 3.1.6. The E_{cm} dependent radiative correction, and its uncertainty, is evident in the difference between $A_{\rm LR}$ and $A^0_{\rm LR}$.

These five results show a χ^2 of 7.44 for 4 degrees of freedom, corresponding to a probability of 11.4% (Figure 3.6). The $\sin^2\theta^{\rm lept}_{\rm eff}$ results derive from the equivalence $A^0_{\rm LR} \equiv \mathcal{A}_{\rm e}$, which provides that

$$A^0_{LR} = \frac{2(1 - 4\sin^2\theta^{\rm lept}_{\rm eff})}{1 + (1 - 4(\sin^2\theta^{\rm lept}_{\rm eff})^2}. \tag{3.7}$$

The average for the complete SLD data sample is:

	1992	**1993**	**1994-95**	**1996**	**1997-98**
N_L	5,226	27,225	52,179	29,016	183,335
N_R	4,998	22,167	41,465	22,857	148,259
A_m	0.0223 ±0.0099	0.1024 ±0.0045	0.1144 ±0.0032	0.1187 ±0.0044	0.1058 ±0.0017
$f_{\rm bkg}$ (%)	1.4 ±1.4	0.25 ±0.10	0.11 ±0.08	0.029 ±0.021	0.042 ±0.032
$A_{\rm bkg}$		0.031 ±0.010	0.055 ±0.021	0.033 ±0.026	0.023 ±0.022
$A_{\mathcal{L}}$ (10^{-4})	1.8 ± 4.2	0.38 ± 0.50	−1.9 ± 0.3	+0.03 ± 0.50	−1.3 ± 0.7
$A_{\mathcal{P}}(10^{-4})$	−29	−33 ± 1	+24 ± 10	+29 ± 43	+28 ± 69
A_E (10^{-4})		0.0044 ±0.0001	0.0092 ±0.0002	−0.0001 ±0.0035	+0.0028 ±0.0014
$E_{\rm cm}\frac{\sigma'(E_{\rm cm})}{\sigma(E_{\rm cm})}$		−1.9	0.0 ± 2.5	2.0 ± 3.0	4.3 ± 2.9
A_ε	0	0	0	0	0
$\mathcal{P}_p$ (10^{-4})	< 0.16	< 0.16	< 0.16	< 0.16	−2 ± 7
Total correction, $\Delta A_{\rm LR}/A_{\rm LR}$, (%)	*+ 2.2 ± 2.3*	+ 0.10 ± 0.08	+ 0.2 ± 0.06	+0.02 ± 0.05	+0.16 ± 0.07
$\delta\mathcal{P}_e/\mathcal{P}_e$ (%)	2.7	1.7	0.67	0.52	0.52
Electroweak interference correction [relative (%)]	*− 2.4 ± 1.4*	+ 1.7 ± 0.3	+ 1.8 ± 0.3	+ 2.2 ± 0.4	+ 2.5 ± 0.39
Total systematic error [relative (%)]	3.9	1.7	0.75	0.63	0.64

Table 3.2: Z event counts and corrections (see equation 3.6) for all SLD run periods. Also shown are the total polarimetry errors (including chromaticity and IP effects), the relative errors due to the electroweak interference correction needed for the conversion of $A_{\rm LR}$ to $A^0_{\rm LR}$, and the total systematic errors. Note that due to low statistics a number of effects were ignored for the 1992 data and no corrections were applied (given here in italics). Also, the systematic error reported in 1992 (3.6%) ignored the uncertainty due to the electroweak correction.

	$\langle \mathcal{P}_e \rangle$	A_{LR}	A^0_{LR}	$\sin^2\theta^{\rm lept}_{\rm eff}$
1992	0.244 ± 0.006	0.100 $\pm 0.044 \pm 0.004$	0.100 $\pm 0.044 \pm 0.004$	0.2378 $\pm 0.0056 \pm 0.0005$
1993	0.630 ± 0.011	0.1628 $\pm 0.0071 \pm 0.0028$	0.1656 $\pm 0.0071 \pm 0.0028$	0.2292 $\pm 0.0009 \pm 0.0004$
1994/95	0.7723 ± 0.0052	0.1485 $\pm 0.0042 \pm 0.0010$	0.1512 $\pm 0.0042 \pm 0.0011$	0.23100 $\pm 0.00054 \pm 0.00014$
1996	0.7616 ± 0.0040	0.1559 $\pm 0.00572 \pm 0.00084$	0.15929 $\pm 0.00573 \pm 0.00101$	0.22996 $\pm 0.00073 \pm 0.00013$
1997/98	0.7292 ± 0.0038	0.1454 $\pm 0.00237 \pm 0.00077$	0.14906 $\pm 0.00237 \pm 0.00096$	0.23126 $\pm 0.00030 \pm 0.00012$
All combined			0.15138 ± 0.00216	0.23097 ± 0.00027

Table 3.3: Summary of the SLD A_{LR} measurements for all runs. Listed are the Luminosity-weighted mean electron polarisation ($\langle \mathcal{P}_e \rangle$), the measured A_{LR}, its value corrected to the Z-pole ($A^0_{\rm LR}$) and $\sin^2\theta^{\rm lept}_{\rm eff}$. For $\langle \mathcal{P}_e \rangle$ the total error shown is dominantly systematic. For the other quantities, the errors are the statistical and systematic components respectively.

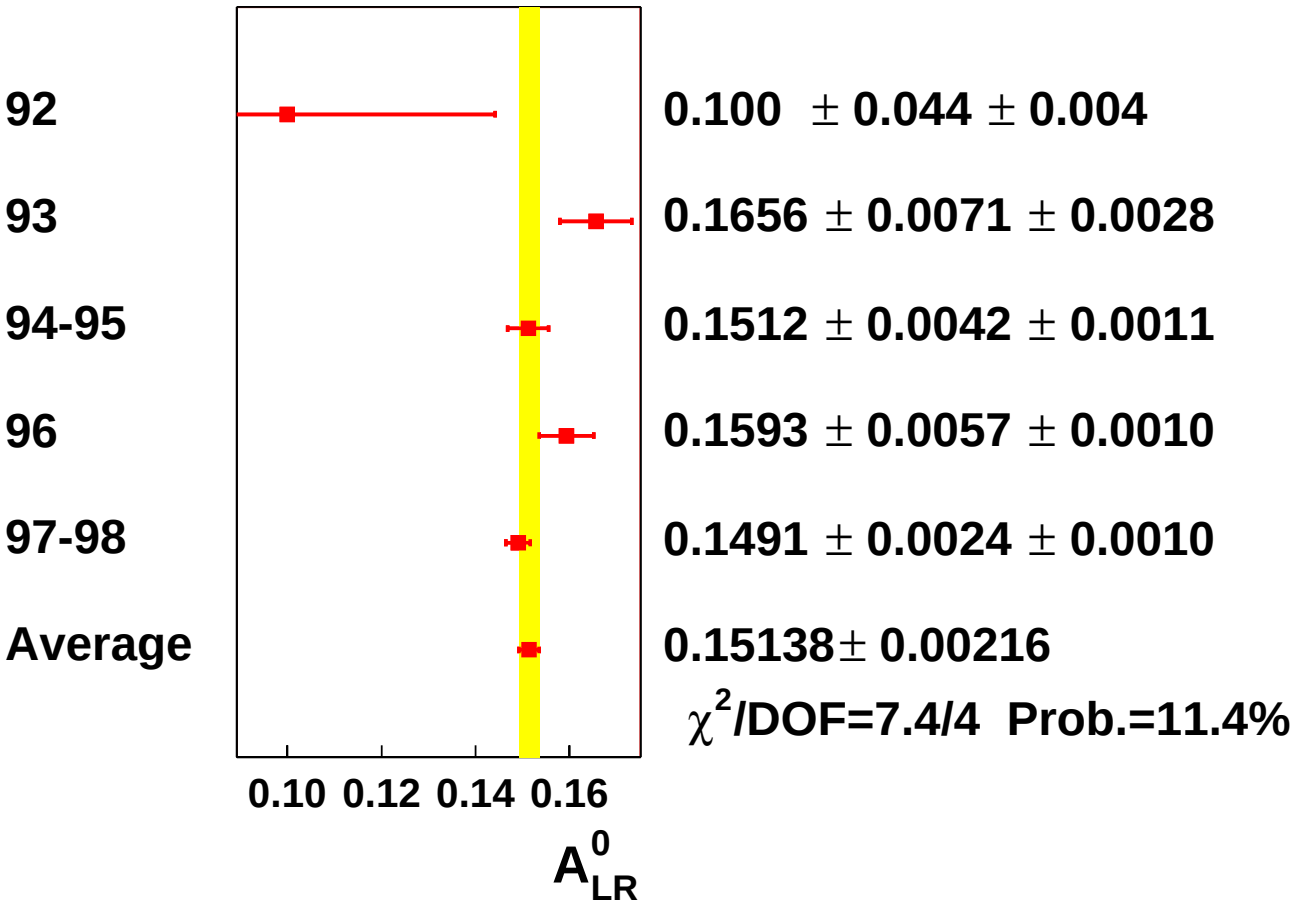

Figure 3.6: A compilation of the published SLD $A^0_{\rm LR}$ results, ordered by year. The final average is formed including correlations in systematic errors.

$$A^0_{LR} = 0.15138 \pm\ 0.00216(0.0011)$$
$$\sin^2\theta^{\rm lept}_{\rm eff}\ = 0.23097 \pm\ 0.00027(0.00013).$$

Small correlated systematic effects are accounted for in forming this average. The estimated systematic uncertainty for these results is shown in parentheses.

3.2 Measurement of the Lepton Asymmetries A_e, A_μ and A_τ at the SLC

The SLD collaboration determined the individual lepton asymmetry parameters using lepton final-state events [93, 94]. Electron polarisation allows one to *directly* measure the final state asymmetry parameter A_l for lepton l using the left-right forward-backward asymmetry ($A^{LR}_{FB} = \frac{3}{4}|\mathcal{P}_e|A_l$), while the LEP experiments measure the product of initial and final state asymmetry parameters ($A_{FB} = \frac{3}{4}A_e \cdot A_l$). The LEP measurements of the tau polarisation yield A_e and A_τ separately, but the SLD provided the only direct measurement of A_μ (although errors are of order 10%). An additional advantage of polarisation is that with $\mathcal{P}_e = 75\%$, the left-right forward-backward asymmetries yield a statistical precision equivalent to measurements of the unpolarised forward-backward asymmetry using a 25 times larger event sample.

Event Sample	Background as % of Selected Events	Efficiency in $\lvert\cos\theta\rvert < 0.9$	# of Selected Events
$e^+e^- \to e^+e^-$	0.7% $\tau^+\tau^-$	75%	15675
$Z \to \mu^+\mu^-$	0.2% $\tau^+\tau^-$	77%	11431
$Z \to \tau^+\tau^-$	e^+e^-:$\mu^+\mu^-$:2-γ:had. 0.9%:2.9%:0.9%:0.6%	70%	10841

Table 3.4: Summary of event selections, efficiency, and purity for $e^+e^- \to \ell^+\ell^-$ for the 1997-1998 SLD data

If lepton universality is assumed, the results for all three lepton flavours can be combined to yield a determination of $\sin^2\theta_{\rm eff}^{\rm lept}$, which in turn can be combined with the more precise result from $A_{\rm LR}$. The event sample used for $A_{\rm LR}$ was purely hadronic (there is a very small $0.3 \pm 0.1\%$ admixture of tau pair events) - and hence the left-right asymmetry of the lepton events was an independent measurement. While the lepton final state analysis described in what follows is more sophisticated than an $A_{\rm LR}$-style counting measurement, essentially all the information on $\sin^2\theta_{\rm eff}^{\rm lept}$ is obtained from the left-right asymmetry of these events. The inclusion of the distributions in polar angle that are essential for the extraction of the final state asymmetries improves the resulting precision on $\sin^2\theta_{\rm eff}^{\rm lept}$, but only to ± 0.00076 compared to about ± 0.00078 obtained from a simple left-right event count.

The differential cross section for the pure Z amplitude $e^+e^- \to {\rm Z} \to {\rm f\bar{f}}$ is factorized as follows :

$$\begin{aligned} \frac{d}{dx}\sigma_Z(x, s, \mathcal{P}_e; A_e, A_l) &\equiv f_Z(s)\Omega_Z(x, \mathcal{P}_e; A_e, A_l) \\ &= f_Z(s)\left[(1 - \mathcal{P}_e A_e)(1 + x^2) + (A_e - \mathcal{P}_e)A_l 2x\right] , \end{aligned} \tag{3.8}$$

where f_Z isolates dependence on s, the squared centre-of-mass energy, and Ω_Z contains the dependence on $x = \cos\theta$, which gives the direction of the outgoing lepton (l^-) with respect to the electron-beam direction. For a complete description of lepton pair production, photon exchange terms and, if the final state leptons are electrons, t-channel contributions have to be taken into account, as we describe below.

3.2.1 The Analysis Method

Leptonic final state events are identified, and Table 3.2.1 summarises the selection efficiencies, backgrounds and numbers of selected candidates for e^+e^-, $\mu^+\mu^-$, and $\tau^+\tau^-$ final states.

Figure 3.7 shows the $\cos\theta$ distributions for e^+e^-, $\mu^+\mu^-$, and $\tau^+\tau^-$ candidates for the 1997-1998 data. The pre-1997 results are similar but have smaller acceptance ($\lvert\cos\theta\rvert \leq 0.8$), reflecting the improved acceptance of an upgraded vertex detector used for the newer data, which allowed for efficient track finding up to $\lvert\cos\theta\rvert = 0.9$. The SLD event totals, including all data, are 22,254, 16,844 and 16,084 for the electron-, muon- and tau-pair final states respectively.

An event-by-event maximum likelihood fit was used to incorporate the contributions of all the terms in the cross section and to include the effect of initial state radiation. There are three likelihood functions for individual lepton final states. All three lepton asymmetry parameters, A_e and A_μ (A_τ), were obtained from $\mu^+\mu^-$ ($\tau^+\tau^-$) final states. The A_e results were combined with A_e obtained from the e^+e^- final state.

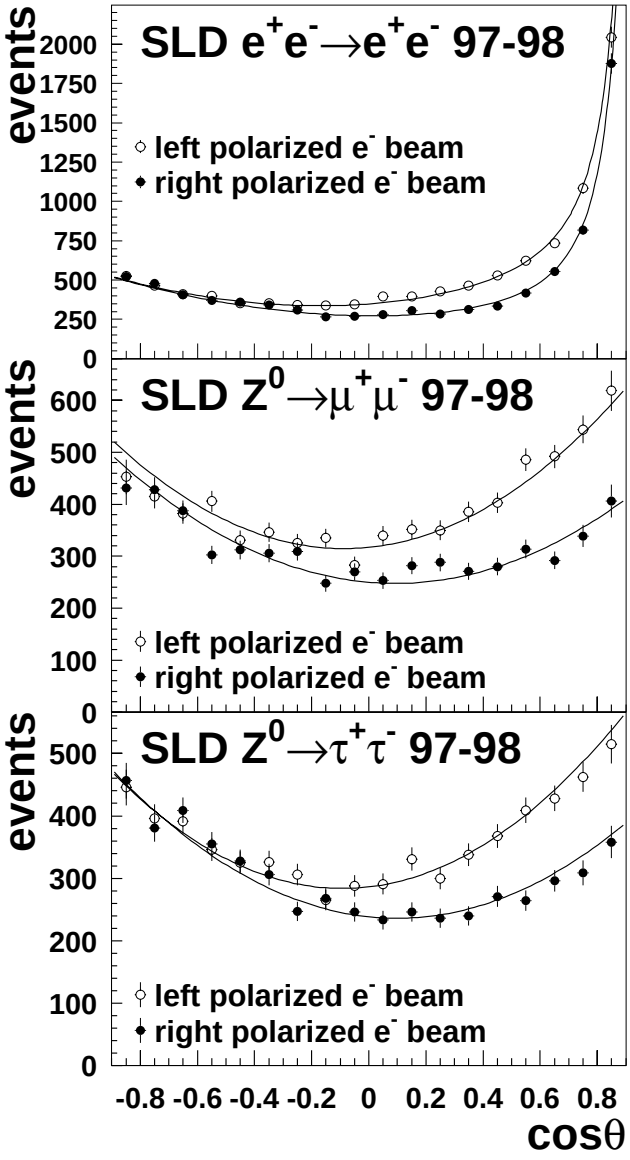

Figure 3.7: Polar-angle distributions for Z decays to e, μ and τ pairs for the 1997-1998 SLD run. The solid line represents the fit, while the points with error bars show the data in bins of 0.1 in $\cos\theta_{thrust}$. For $|\cos\theta_{thrust}| > 0.7$, the data are corrected for a decrease in the detection efficiency with increasing $|\cos\theta_{thrust}|$.

The likelihood function for muon- and tau-pair final states was defined as follows:

$$\mathcal{L}(x,s,\mathcal{P}_e;A_e,A_l) = \int ds' H(s,s') \left\{ \frac{d}{dx}\sigma_Z(x,s',\mathcal{P}_e;A_e,A_l) + \frac{d}{dx}\sigma_{Z\gamma}(x,s',\mathcal{P}_e;A_e,A_l) + \frac{d}{dx}\sigma_\gamma(x,s') \right\}, \quad (3.9)$$

where A_e and A_l ($=A_\mu$ or A_τ) are free parameters and $H(s,s')$ is a radiator function. The integration over s' is done with the program MIZA [64] to take into account the initial state radiation. The spread in the beam energy had a negligible effect. $(d\sigma_Z/dx)(...)$, $(d\sigma_\gamma/dx)(...)$, and $(d\sigma_{Z\gamma}/dx)(...)$ are the tree-level differential cross sections for Z exchange, photon exchange, and their interference. The integration was performed before the fit to obtain the coefficients $\bar{f}_Z$, $\bar{f}_{Z\gamma}$, and $\bar{f}_\gamma$, and the likelihood function becomes

$$\mathcal{L}(x,s,\mathcal{P}_e;A_e,A_l) = \bar{f}_Z(s)\Omega_Z(x,\mathcal{P}_e;A_e,A_l) + \bar{f}_{Z\gamma}(s)\Omega_{Z\gamma}(x,\mathcal{P}_e;A_e,A_l) + \bar{f}_\gamma(s)\Omega_\gamma(x), \quad (3.10)$$

where the differential cross sections have been factorized in analogy with equation 3.8. These coefficients gave the relative sizes of the three terms at the SLC centre-of-mass energy (e.g. $\sqrt{s} = 91.237 \pm 0.029$ GeV for the 1997-1998 run).

The e^+e^- final state includes both s-channel and t-channel Z and photon exchanges which yields four amplitudes and ten cross-section terms. All ten terms are energy-dependent. A maximum likelihood function for e^+e^- final states was defined by modifying Equations 3.9 and 3.10 to include all ten terms. The integration over s' was performed with DMIBA [95] to obtain the coefficients for the relative size of the ten terms.

3.2.2 Systematic Errors

Systematic uncertainties are summarised in Table 3.5, where it is made clear that this measurement is entirely statistics dominated. The errors for the 1997-98 dataset, which dominates the sample, are shown.

Source	A_e^e	A_e^μ	A_e^τ	A_μ^μ	A_τ^τ
Statistics	110	130	130	180	180
Polarisation	8	8	8	8	8
Backgrounds	5	–	13	–	14
Radiative Correction	23	2	2	3	2
V-A	–	–	–	–	18
Charge Confusion	–	–	–	7	11
Detector asymmetry	–	–	–	–	4
Nonuniform efficiency	2	–	–	–	–

Table 3.5: Summary of statistical and systematic uncertainties in units of 10^{-4} for the 1997-1998 SLD $e^+e^- \to \ell^+\ell^-$ data. The superscript on each asymmetry refers to the lepton sample from which it was derived (electrons, muons or taus).

The uncertainty on the beam polarisation is correlated among all the measurements and corresponds to an uncertainty on A_l of ± 0.0008. The uncertainty in the amount of background and its effect on the fitted parameters are taken into account. The background contaminations

have been derived from detailed Monte Carlo simulations as well as from studying the effect of cuts in background-rich samples of real data.

The radiative correction and their systematic errors are estimated using the MIZA [64] and DMIBA [95] programs whose inherent 1 per mil precision leads to negligible effects compared to our $\sqrt{s}$ uncertainty. The uncertainty in the asymmetry parameters due to a $\pm 1\sigma$ variation of $\sqrt{s}$ (which affects radiative corrections) is of the order 10^{-4}, except for the A_e determination from e^+e^- final states for which it is of order 10^{-3}.

The dominant systematic error in the tau analysis results from the V-A structure of tau decay, which introduces a selection bias in the analysis. For example, if both taus decay to $\pi\nu$, helicity conservation requires that both pions generally have lower momentum for a left-handed τ^- and right-handed τ^+ and higher momentum otherwise. This effect, which biases the reconstructed event mass, is large at the SLD because the high beam polarisation induces a very high and asymmetric tau polarisation as a function of polar angle. The value of A_e extracted from $\tau^+\tau^-$ final states is not affected since the overall relative efficiencies for left-handed beam and right-handed beam events are not changed significantly (only the polar angle dependence of the efficiencies are changed).

3.2.3 Results

Results for all SLD runs are combined while accounting for small effects due to correlations in systematic uncertainties (polarisation and average SLD centre-of-mass energy). From purely leptonic final states, one obtains $A_e = 0.1544 \pm 0.0060$. This A_e result is combined with the left-right asymmetry measurement in the final tabulation of SLD leptonic asymmetry results given below :

$$\begin{array}{rcrcll} A_e & = & 0.1516 & \pm & 0.0021 \text{ (with } A^0_{LR}) & ; \\ A_\mu & = & 0.142 & \pm & 0.015 & ; \text{and} \\ A_\tau & = & 0.136 & \pm & 0.015. & \end{array} \tag{3.11}$$

These results are consistent with lepton universality and hence can be combined into A_l, which in the context of the standard model is simply related to the electroweak mixing angle. The result is discussed in the following section.

	$\mathcal{A}_\mathrm{e}$	$\mathcal{A}_\mu$	$\mathcal{A}_\tau$
$\mathcal{A}_\mathrm{e}$	1.000		
$\mathcal{A}_\mu$	0.038	1.000	
$\mathcal{A}_\tau$	0.033	0.007	1.000

Table 3.6: Correlation coefficients for the SLD measurements of $\mathcal{A}_\mathrm{e}$, $\mathcal{A}_\mu$ and $\mathcal{A}_\tau$

3.3 Combined Results for $\sin^2\theta^{\mathrm{lept}}_{\mathrm{eff}}$

The final A_{LR} result is an average, formed while accounting for correlated systematic effects, of all SLD A_{LR} measurements (1992, 1993, 1994-1995, 1996, and 1997-1998). The combined result for A^0_{LR} is 0.15138 ± 0.00216.

Assuming lepton universality, the $A_{\rm LR}$ result and the results on the leptonic left-right forward-backward asymmetries can be combined, where small correlated systematics are accounted for, yielding

$$\mathcal{A}_\ell = 0.15130 \pm 0.00207(0.0011), \tag{3.12}$$

where the estimated systematic error is shown in parentheses. The correlation matrix is given in Table 3.6. This measurement is equivalent to a determination

$$\sin^2\theta_{\rm eff}^{\rm lept} = 0.23098 \pm 0.00026, \tag{3.13}$$

where the total error includes the estimated systematic error of ± 0.00011.

Chapter 4

The τ Polarisation Measurements

4.1 Introduction

Parity violation in the weak neutral current results in a non-zero longitudinal polarisation of fermion pairs produced in the reaction $e^+e^- \rightarrow f\overline{f}$, with the τ lepton being the only fundamental final-state fermion whose polarisation is experimentally accessible at LEP [96]. The τ polarisation, $\mathcal{P}_\tau$, is given by

$$\mathcal{P}_\tau \equiv (\sigma_+ - \sigma_-)/(\sigma_+ + \sigma_-)$$

where σ_+ represents the cross section for producing positive helicity τ^- leptons and σ_- those of negative helicity. The g_L and g_R neutral current couplings, introduced in Equations 1.5 and 1.6, quantify the strength of the interaction between the Z and the chiral states of the fermions. A subtle, but important, point is that the polarisation measurements involve the fermion helicity states, as opposed to their chiral states. The $(1 \pm \gamma_5)/2$ operators project out states of a definite chirality: $(1 + \gamma_5)/2$ projects out the left-handed chiral fermion (and right-handed anti-fermion) states and (1 - γ_5)/2 the right-handed chiral fermion (and left-handed anti-fermion) states. In contrast, helicity is the projection of the spin onto the direction of the fermion momentum: if the spin and momentum are oppositely aligned, the helicity is negative whereas if the spin and momentum are aligned, the helicity is positive. In the extreme relativistic limit, $(1 + \gamma_5)/2$ projects out negative helicity states and (1 - γ_5)/2 positive helicity states. The left-handed chiral fermion (and right-handed anti-fermion) states become indistinguishable from the measured negative helicity states and the right-handed chiral fermion (and left-handed anti-fermion) states from the positive helicity states. Consequently, at LEP, where the τ leptons are produced with highly relativistic energies, $\mathcal{P}_\tau$ provides a direct measurement of the chiral asymmetries of the neutral current. By convention, $\mathcal{P}_\tau = \mathcal{P}_{\tau^-}$ and since, to a very good approximation, the τ^- and τ^+ have opposite helicities at LEP, $\mathcal{P}_{\tau^-} = -\mathcal{P}_{\tau^+}$.

For pure Z exchange in the interaction of the unpolarised e^+e^- beams at LEP, the dependence of $\mathcal{P}_\tau$ on θ_{τ^-}, the angle between the τ^- momentum and e^- beam, can be described by a simple relation expressed in terms of the two neutral current asymmetry parameters, $\mathcal{A}_\tau$ and $\mathcal{A}_e$, and the forward-backward asymmetry of the tau, A^τ_{FB}:

$$\mathcal{P}_\tau(\cos\theta_{\tau^-}) = -\frac{\mathcal{A}_\tau(1 + \cos^2\theta_{\tau^-}) + 2\mathcal{A}_e\cos\theta_{\tau^-}}{(1 + \cos^2\theta_{\tau^-}) + \frac{8}{3}A^\tau_{FB}\cos\theta_{\tau^-}}. \tag{4.1}$$

The τ polarisation measurements allow for the determination of $\mathcal{A}_\tau$ and $\mathcal{A}_e$ and are largely insensitive to A^τ_{FB}.

The four LEP experiments use kinematic distributions of the observable τ decay products, and the V-A nature of the decays, to measure the polarisation as a function of $\cos\theta_{\tau^-}$ in data collected during the 1990-95 Z running period. Because the actual reaction does not only contain the pure Z propagator but also includes contributions from the photon propagator, γ-Z interference, and other photonic radiative corrections, the parameters obtained using Equation 4.1 are approximations to $\mathcal{A}_\tau$ and $\mathcal{A}_\mathrm{e}$. In order to distinguish between these pure Z parameters and those which include the small non-Z effects, the measured parameters are denoted as $\langle\mathcal{P}_\tau\rangle$ and $A_\mathrm{FB}^\mathrm{pol}$ in the literature. $\langle\mathcal{P}_\tau\rangle$ is the average τ polarisation over all production angles and $A_\mathrm{FB}^\mathrm{pol}$ is the forward-backward polarisation asymmetry. If one had only pure Z exchange, these would be trivially related to the neutral current asymmetry parameters: $\langle\mathcal{P}_\tau\rangle = -\mathcal{A}_\tau$ and $A_\mathrm{FB}^\mathrm{pol} = -\frac{3}{4}\mathcal{A}_\mathrm{e}$. ZFITTER [24] is used to convert from $\langle\mathcal{P}_\tau\rangle$ and $A_\mathrm{FB}^\mathrm{pol}$ to $\mathcal{A}_\tau$ and $\mathcal{A}_\mathrm{e}$, respectively, by correcting for the contributions of the photon propagator, γ-Z interference and electromagnetic radiative corrections for initial state and final state radiation. These corrections have a $\sqrt{s}$ dependence which arise from the non-Z contributions to $\langle\mathcal{P}_\tau\rangle$ and $A_\mathrm{FB}^\mathrm{pol}$. This latter feature is important since the off-peak data are included in the event samples for all experiments. Ultimately, all LEP collaborations express their τ polarisation measurements in terms of $\mathcal{A}_\tau$ and $\mathcal{A}_\mathrm{e}$.

It is important to remark that this method of measuring $\mathcal{P}_\tau(\cos\theta_{\tau^-})$ yields nearly independent determinations of $\mathcal{A}_\tau$ and $\mathcal{A}_\mathrm{e}$. Consequently, the τ polarisation measurements provide not only a determination of $\sin^2\theta_\mathrm{eff}^\mathrm{lept}$ but also test the hypothesis of the universality of the couplings of the Z to the electron and τ lepton.

A general overview describing the experimental methods for measuring the tau polarisation at LEP is contained in section 4.2. This is followed in section 4.3 by a discussion of the dominant systematic errors relevant to these measurements. The results for $\mathcal{A}_\tau$ and $\mathcal{A}_\mathrm{e}$ from each of the four LEP experiments are presented in section 4.4 as well as the combined results with and without assuming lepton universality. The treatment of correlations between the measurements in the combined results is also discussed in that section.

4.2 Experimental Methods

The polarisation measurements rely on the dependence of kinematic distributions of the observed τ decay products on the helicity of the parent τ lepton. Because the helicity of the parent cannot be determined on an event-by-event basis, the polarisation measurement is performed by fitting the observed kinematic spectrum of a particular decay mode to a linear combination of the positive and negative helicity spectra associated with that mode.

For the simplest case, that of the two-body decay of a τ lepton to a spin-zero π meson and ν_τ, $\tau \to \pi\nu_\tau$, the maximum sensitivity is provided by the energy spectrum of the π in the laboratory frame. The pure V-A charged current decay of the τ together with angular momentum conservation produces a π with momentum preferentially aligned with the helicity of the τ as depicted in Figure 4.1. In the laboratory frame this means that a π^- produced from the decay of a positive-helicity τ^- will, on average, be more energetic than a π^- produced from the decay of a negative-helicity τ^-. In the τ rest frame the partial decay width, depicted in Figure 4.2a for both τ helicity states, is

$$\frac{1}{\Gamma}\frac{d\Gamma}{d\cos\theta^*} = 1 + \mathcal{P}_\tau\cos\theta^* \tag{4.2}$$

where θ^* is the angle between the direction of the τ spin and π momentum in the τ rest frame.

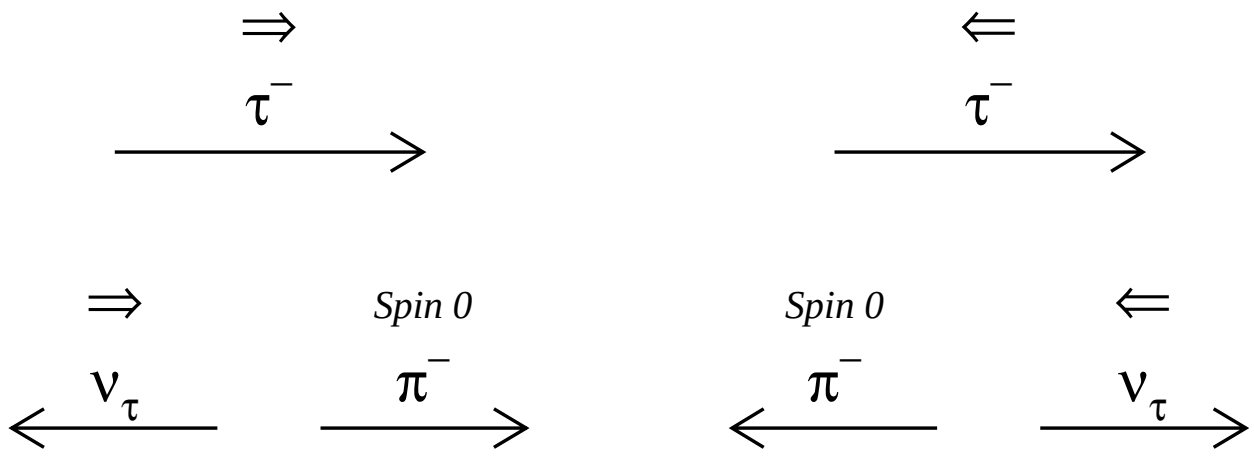

Figure 4.1: Decay configurations for two τ helicity states for the decay $\tau \to \pi\nu_\tau$. The positive helicity configuration is on the left and the negative configuration is on the right. For each particle, the long arrow depicts the momentum direction while the short arrow that of the spin.

When boosted into the laboratory frame this transforms to

$$\frac{1}{\Gamma}\frac{d\Gamma}{dx_\pi} = 1 + \mathcal{P}_\tau(2x_\pi - 1) \tag{4.3}$$

neglecting terms of order $(m_\pi/m_\tau)^2$, where $x_\pi = E_\pi/E_\tau$ is the pion energy scaled by the maximum energy available.

More complex is the $\tau \to \rho\nu$ decay. The charged ρ is a vector meson with a 770 MeV mass which decays promptly via $\rho \to \pi\pi^0$. Having spin-1, the ρ itself is polarised with either helicity=0 or helicity=$\pm$1 for each τ helicity configuration. The cases in which the ρ is polarised with helicity=0 are equivalent to the $\tau \to \pi\nu$ configurations, but the helicity=$\pm$1 polarised cases produce the opposite angular distribution.

The partial width for $\tau \to \rho\nu$ is given in the tau rest frame by [97]

$$\frac{1}{\Gamma}\frac{d\Gamma^{hel=0}}{d\cos\theta^*} = \frac{m_\tau^2/2}{m_\tau^2 + 2m_\rho^2}(1 + \mathcal{P}_\tau \cos\theta^*) \tag{4.4}$$

for the helicity=0 polarised ρ and

$$\frac{1}{\Gamma}\frac{d\Gamma^{hel=\pm1}}{d\cos\theta^*} = \frac{m_\rho^2}{m_\tau^2 + 2m_\rho^2}(1 - \mathcal{P}_\tau \cos\theta^*) \tag{4.5}$$

for the helicity=$\pm$1 polarised ρ, where θ^* is the angle between the ρ and the τ flight direction in the rest frame of the τ. The transverse case effectively diminishes the sensitivity to $\mathcal{P}_\tau$ when only the θ^* angle is used, or, equivalently, in the laboratory frame when only the ρ energy is used.

Much of this sensitivity, however, may be recovered by using information from the ρ decay products by, in effect, spin-analysing the ρ. The kinematic variable that provides this information is the angle between the charged pion relative to the flight direction of the ρ in the ρ rest frame, ψ. The two variables can be combined to form a single variable without loss of polarisation sensitivity [98]. This 'optimal variable', ω_ρ, is given by

$$\omega_\rho = \frac{\mathrm{W}_+(\theta^*, \psi) - \mathrm{W}_-(\theta^*, \psi)}{\mathrm{W}_+(\theta^*, \psi) + \mathrm{W}_-(\theta^*, \psi)}, \tag{4.6}$$

where $W_{+(-)}$ is proportional to the partial decay width for positive (negative) helicity τ leptons, as a function of θ^* and ψ. The distributions of ω_ρ, for both positive and negative helicity τ decays, are shown in Figure 4.2b.

As with the $\tau \to \rho\nu$ decay, the $\tau \to a_1\nu$ channel exhibits significantly reduced polarisation sensitivity when only the a_1 energy is measured in the laboratory frame. The a_1 is an axial-vector meson with mass and width of approximately 1230 MeV and 500 MeV, respectively, and decays to $\pi^-\pi^-\pi^+$ or $\pi^-\pi^0\pi^0$ with nearly equal probability. There are again two possible spin configurations where much of the sensitivity can be regained through a spin analysis of the a_1 decay. In this case six variables are used which include: the angle θ^* between the a_1 and τ momenta in the τ rest frame; the angle (ψ) between the perpendicular to the a_1 decay plane and the a_1 flight direction in the rest frame of the a_1; the angle (γ) in the a_1 rest frame between the unlike-sign pion momentum in the a_1 rest frame and the a_1 flight direction projected into the a_1 decay plane; the 3π-invariant mass; and the two unlike-sign pion mass combinations present in the decays. In complete analogy with the $\tau \to \rho\nu$, the polarisation information from these six variables is fully contained in a single optimal variable, ω_{a_1} [98]. The ω_{a_1} distributions for both positive and negative helicity τ decays are plotted in Figure 4.2c.

For the leptonic channels, $\tau \to e\nu\overline{\nu}$ and $\tau \to \mu\nu\overline{\nu}$, the situation is less favourable: all three final state particles carry off angular momentum, but only one of the particles is measured. This causes a substantial unrecoverable reduction in sensitivity relative to the $\tau \to \pi\nu$ channel. For these decays the optimal variable is the scaled energy of the charged decay product: $x_e = E_e/E_\tau$ and $x_\mu = E_\mu/E_\tau$. The decay distributions of the two leptonic channels are almost identical. Ignoring the masses of the daughter leptons, the partial decay width is:

$$\frac{1}{\Gamma}\frac{d\Gamma}{dx_\ell} = \frac{1}{3}\left[(5 - 9x_\ell^2 + 4x_\ell^3) + \mathcal{P}_\tau(1 - 9x_\ell^2 + 8x_\ell^3)\right]. \tag{4.7}$$

Shown in Figure 4.2d are the distributions for both positive and negative helicity $\tau \to \mu\nu\overline{\nu}$ decays where the decrease in sensitivity is apparent. It should also be noted that, in contrast to the $\tau \to \pi\nu$ channel, the positive helicity case now produces a charged particle with lower energy on average than the negative helicity case.

Each LEP experiment measures $\mathcal{P}_\tau$ using the five τ decay modes $e\nu\overline{\nu}$, $\mu\nu\overline{\nu}$, $\pi\nu$, $\rho\nu$ and $a_1\nu$ [99–102] comprising approximately 80% of τ decays *. As just demonstrated, the five decay modes do not all have the same sensitivity to the τ polarisation. The maximum sensitivity for each decay mode, defined as $\frac{1}{\sqrt{N}\sigma}$ where σ is the statistical error on the polarisation measurement using N events for $\mathcal{P}_\tau$=0, is given in Table 4.1. It assumes that all the available information in the decay is used with full efficiency both for the case when the three-dimensional τ direction information is not used and for the case when it is used. The additional information provided by the tau direction is an azimuthal angle of the decay of the hadronic system in the τ rest frame [98]. When included in the decay distributions of spin-1 hadronic channels with even modest precision an improvement in the sensitivity is achieved. A measure of the weight with which a given decay mode ideally contributes to the overall measurement of the polarisation is given by that decay mode's sensitivity squared multiplied by its branching ratio. Normalised ideal weights, which are calculated assuming maximum sensitivity and perfect identification efficiency and purity, for each decay mode, are also given in Table 4.1. As can be seen, the $\tau \to \rho\nu$ and $\tau \to \pi\nu$ channels are expected to dominate the combined polarisation measurement,

*As no experiment discriminates between charged pions and kaons, the $\tau \to \pi\nu$ channel also includes $\tau \to K\nu$ decays and the $\tau \to \rho\nu$ channel also includes $\tau \to K\pi^0\nu$ decays. Negligible sensitivity is lost by combining these modes.

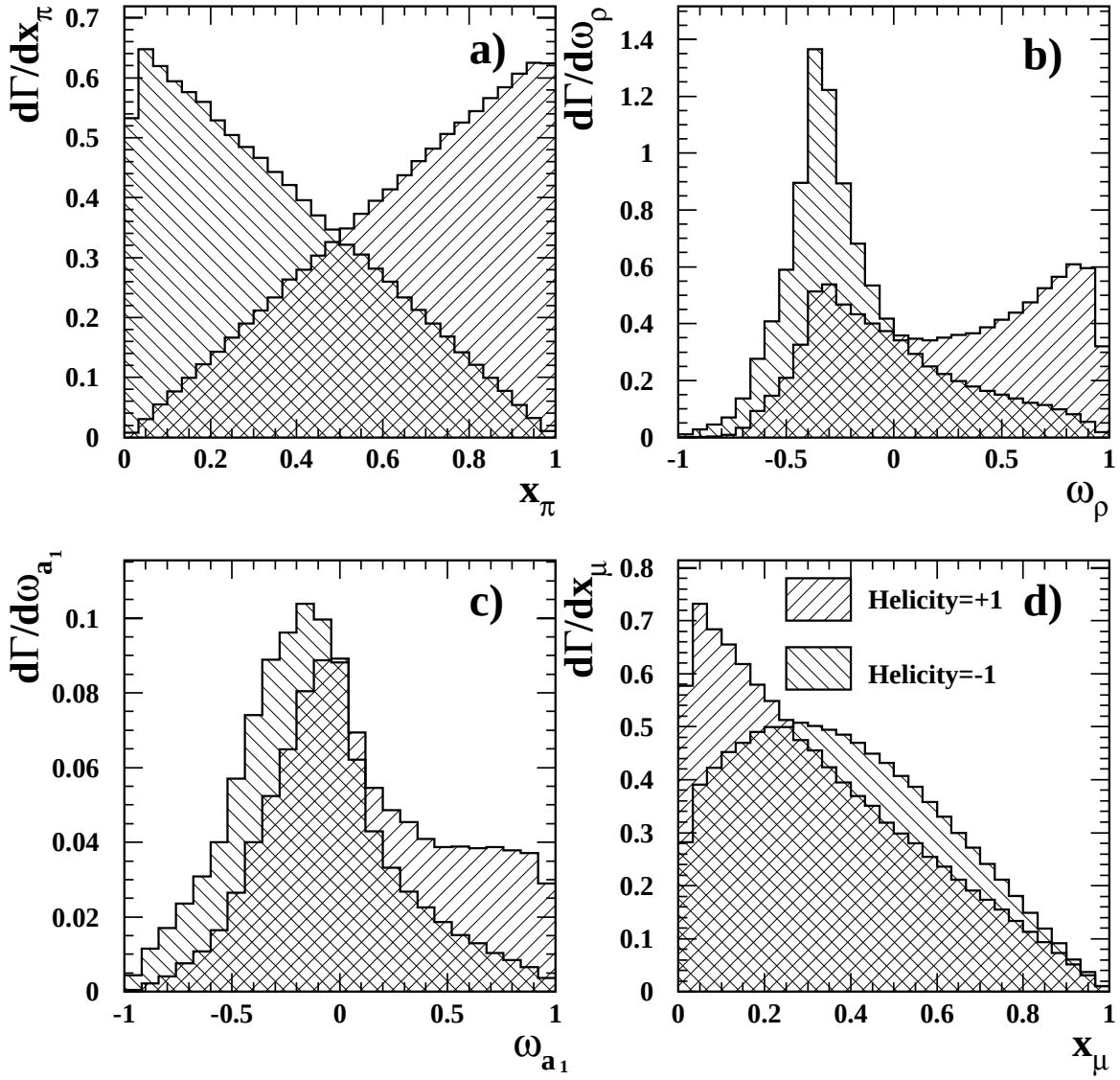

Figure 4.2: Monte Carlo simulated distributions of polarisation sensitive kinematic variables for (a) $\tau \to \pi\nu$, (b) $\tau \to \rho\nu$, (c)$\tau \to a_1\nu$ and (d) $\tau \to \mu\nu\overline{\nu}$ decays for positive and negative helicity τ leptons excluding the effects of selection and detector response.

especially if information from the tau direction is not used. The actual sensitivity achieved by each experiment for its selected event sample is degraded because of inefficiencies in the process of selecting a sample of decays, by the presence of background in the sample and, to a lesser extent, by resolution effects. Much of the background from cross-contamination from other τ decay channels, however, retains some polarisation information which is exploited by the fitting procedure.

	$\tau \to \rho\nu$	$\tau \to \pi\nu$	$\tau \to \mathrm{e}\nu\overline{\nu}$	$\tau \to \mu\nu\overline{\nu}$	$\tau \to \mathrm{a}_1\nu$ $\mathrm{a}_1 \to \pi^{\pm}\pi^{+}\pi^{-}$
Branching ratio	0.25	0.12	0.18	0.17	0.09
Maximum Sensitivity					
(no 3D τ direction)	0.49	0.58	0.22	0.22	0.45
(with 3D τ direction)	0.58	0.58	0.27	0.27	0.58
Normalised ideal weight					
(no 3D τ direction)	0.44	0.30	0.06	0.06	0.13
(with 3D τ direction)	0.47	0.22	0.07	0.07	0.17

Table 4.1: The branching ratios, maximum sensitivity [98] and normalised ideal weight for the five decay modes listed. The ideal weight is calculated as the product of the branching ratio and the square of the maximum sensitivity. Presented in the last two lines of the table is the ideal weight for each channel divided by the sum of the ideal weights of the five channels.

In all analyses, a value of $\mathcal{P}_\tau$ is extracted from the data by fitting linear combinations of positive and negative helicity distributions in kinematic variables appropriate to each τ decay channel to the data, where the two distributions are obtained from Monte Carlo simulation. As discussed above, in the $\tau \to \mu\nu\overline{\nu}$, $\tau \to \mathrm{e}\nu\overline{\nu}$ and $\tau \to \pi\nu$ channels, the energy of the charged particle decay divided by the beam energy is the appropriate kinematic variable while for the $\tau \to \rho\nu$ and $\tau \to \mathrm{a}_1\nu$ channels, the appropriate optimal variable, ω, is employed. Using Monte Carlo distributions in the fitting procedure allows for simple inclusion of detector effects and their correlations, efficiencies and backgrounds. Any polarisation dependence in the backgrounds from other τ decays are automatically incorporated into these analyses. The systematic errors associated with the detector then amount to uncertainties in how well the detector response is modelled by the Monte Carlo simulation of the detector, whereas the errors associated with uncertainties in the underlying physics content in the distributions arise from uncertainties in the Monte Carlo generators of the signal and backgrounds. The spin correlations between the two τ-leptons produced in a Z decay are treated differently in the different experiments and are discussed below.

All four LEP experiments analyse the five exclusive channels listed in Table 4.1 [99–102]. In addition to those, ALEPH and L3 include the $\tau \to \pi 2\pi^0\nu$ mode in their exclusive channel analyses. ALEPH also uses information from the τ direction for the hadronic decays, as discussed in [98]. The addition of the tau direction information ideally increases the sensitivity of the $\tau \to \mathrm{a}_1\nu$ and $\tau \to \rho\nu$ channels by the amounts indicated in Table 4.1.

To their exclusive channel analyses, DELPHI [100] and L3 [101] add an inclusive hadronic decay analysis in which the single charged track (one-prong) hadronic decay modes are collectively analysed. This approach yields a high overall efficiency for these modes by sacrificing the optimal sensitivity characterising the analysis of high purity channels. For DELPHI and L3 the correlations between the polarisation measurements from their inclusive hadronic analysis

and measurements using separately identified single-track hadronic channels are small enough that significant improvements are achieved when both results are combined.

The OPAL [102] $\mathcal{A}_\tau$ and $\mathcal{A}_e$ results are based entirely on an analysis in which all five exclusive channels listed in Table 4.1 are combined in a global binned maximum likelihood analysis. A single fit to all distributions in the kinematic observables of all decay modes and $\cos\theta_{\tau^-}$ yield $\langle\mathcal{P}_\tau\rangle$ and $A_{\rm FB}^{\rm pol}$. When both τ^+ and τ^- decays of a given event are identified, the event is analysed as a whole. This global analysis approach fully accounts for the intrinsic correlation between the helicities of the τ^+ and τ^- produced in the same Z decay, an effect which is accounted for by the other experiments by applying a correction to the statistical errors of the fit results. In such a global analysis, the evaluation of the systematic errors automatically incorporate all correlations between the systematic uncertainties in the different channels. For the channel-by-channel analyses of ALEPH, L3 and DELPHI, the correlation in the systematic errors between channels are taken into account in the combination.

DELPHI [100] augments their exclusive five channel and inclusive one-prong analysis with a separate neural network analysis of its 1993-1995 one-prong data set. The neural network is used to classify all one-prong decays as either $\tau \to \rho\nu$, $\tau \to \pi\nu$, $\tau \to e\nu\overline{\nu}$, $\tau \to \mu\nu\overline{\nu}$ or $\tau \to \pi 2\pi^0\nu$. A simultaneous fit for $\mathcal{P}_\tau$ as a function of $\cos\theta_{\tau^-}$ is performed with $\mathcal{A}_\tau$ and $\mathcal{A}_e$ determined from a separate fit to the $\mathcal{P}_\tau(\cos\theta_{\tau^-})$ functional form as described below. As with OPAL's global analysis, the channel-to-channel correlated systematic errors are automatically evaluated in this analysis.

ALEPH [99] and L3 [101] complement their analyses of the kinematic distributions of the different decay modes, by including information from event acollinearity to measure the tau polarisation. Although of modest polarisation sensitivity, this information has the advantage of being sensitive to detector related systematics errors that are different from those associated with the measurements of spectra.

Examples of the different kinematic distributions from the different experiments are shown in Figures 4.4 to 4.6.

In order to extract $\mathcal{A}_\tau$ and $\mathcal{A}_e$ from their data, ALEPH, DELPHI and L3 measure the polarisation as a function of $\cos\theta_{\tau^-}$ and then perform a separate fit for the two parameters using the theoretical expectation of the dependence. The results quoted by OPAL [102], which depend on a single maximum likelihood fit, do not explicitly use measurements of the polarisation as a function of $\cos\theta_{\tau^-}$, although such fits are performed as cross checks and for graphical presentation. ALEPH, L3 and OPAL use Equation 4.1 in their fits but treat $A_{\rm FB}^\tau$ differently as discussed in section 4.3. Small corrections for the effects of initial state radiation, the photon propagator and γ-Z interference, and the fact that not all data are collected at the peak of the Z resonance are incorporated into the quoted values of $\mathcal{A}_\tau$ and $\mathcal{A}_e$. These corrections, on the order of $\mathcal{O}(0.005)$, are calculated using ZFITTER [24]. DELPHI incorporates these corrections directly into the fit they perform by using the $\mathcal{A}_\tau$ and $\mathcal{A}_e$ dependent ZFITTER prediction as an estimation of $\mathcal{P}_\tau(\cos\theta_{\tau^-})$ averaged over the luminosity-weighted centre-of-mass energies. This automatically includes the QED and weak effects as a function of $\cos\theta_{\tau^-}$, rather than as a separate correction as in the approach taken by the other three LEP experiments.

Although the size of the event samples used by the four experiments are roughly equal, smaller errors on the asymmetries is quoted by ALEPH. This is largely associated with the higher angular granularity of the ALEPH electromagnetic calorimeter. The tau 'jets' produced in hadronic tau decays are tightly collimated at LEP energies which results in a substantial overlap of the energy deposited in the calorimeter by different particles. A calorimeter with a higher granularity is better able to identify the individual photons from π^0 decay and therefore

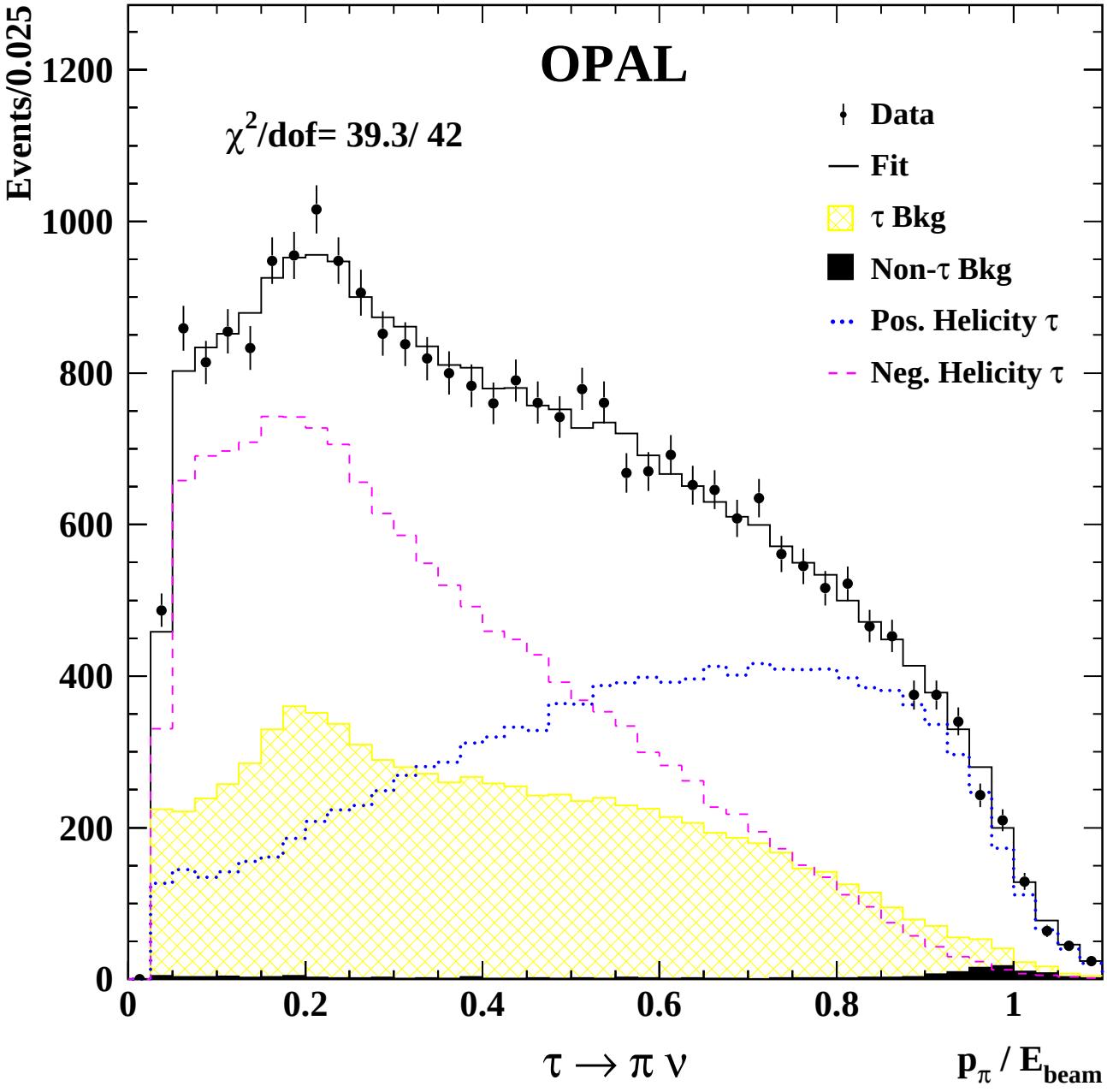

Figure 4.3: The measured distributions in the polarisation-sensitive variable for the $\tau \to \pi\nu$ decays in the OPAL experiment. The variable is the ratio of the measured charged hadron momentum to the beam energy. The data, shown by points with error bars, are integrated over the whole $\cos\theta_{\tau^-}$ range. Overlaying this distribution are Monte Carlo distributions for the positive (dotted line) and negative (dashed line) helicity τ leptons and for their sum including background, assuming a value for $\langle\mathcal{P}_\tau\rangle$ equal to the fitted polarisation. The hatched histogram represents the Monte Carlo expectations of contributions from cross-contamination from other τ decays and the dark shaded histogram the background from non-τ sources. The level of agreement between the data and Monte Carlo distributions is quantified by quoting the χ^2 and the number of degrees of freedom.

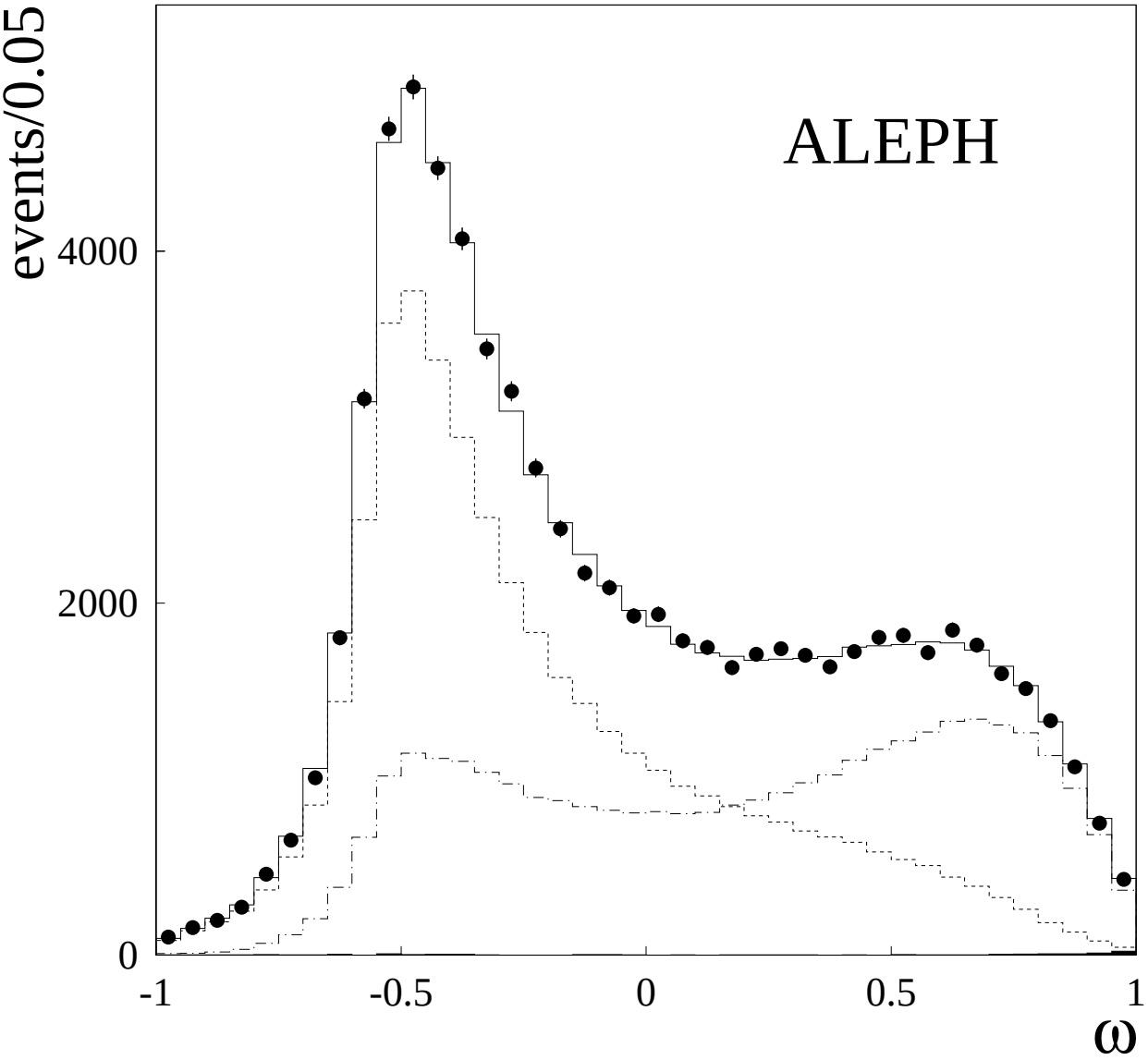

Figure 4.4: The measured spectrum of the polarisation-sensitive variable for the $\tau \to \rho\nu$ decays in the ALEPH experiment. The variable is the optimal variable ω. The dotted and dashed lines correspond to the contributions of negative and positive helicity τ's respectively. The small shaded area near ω=1 is the non-τ background contribution.

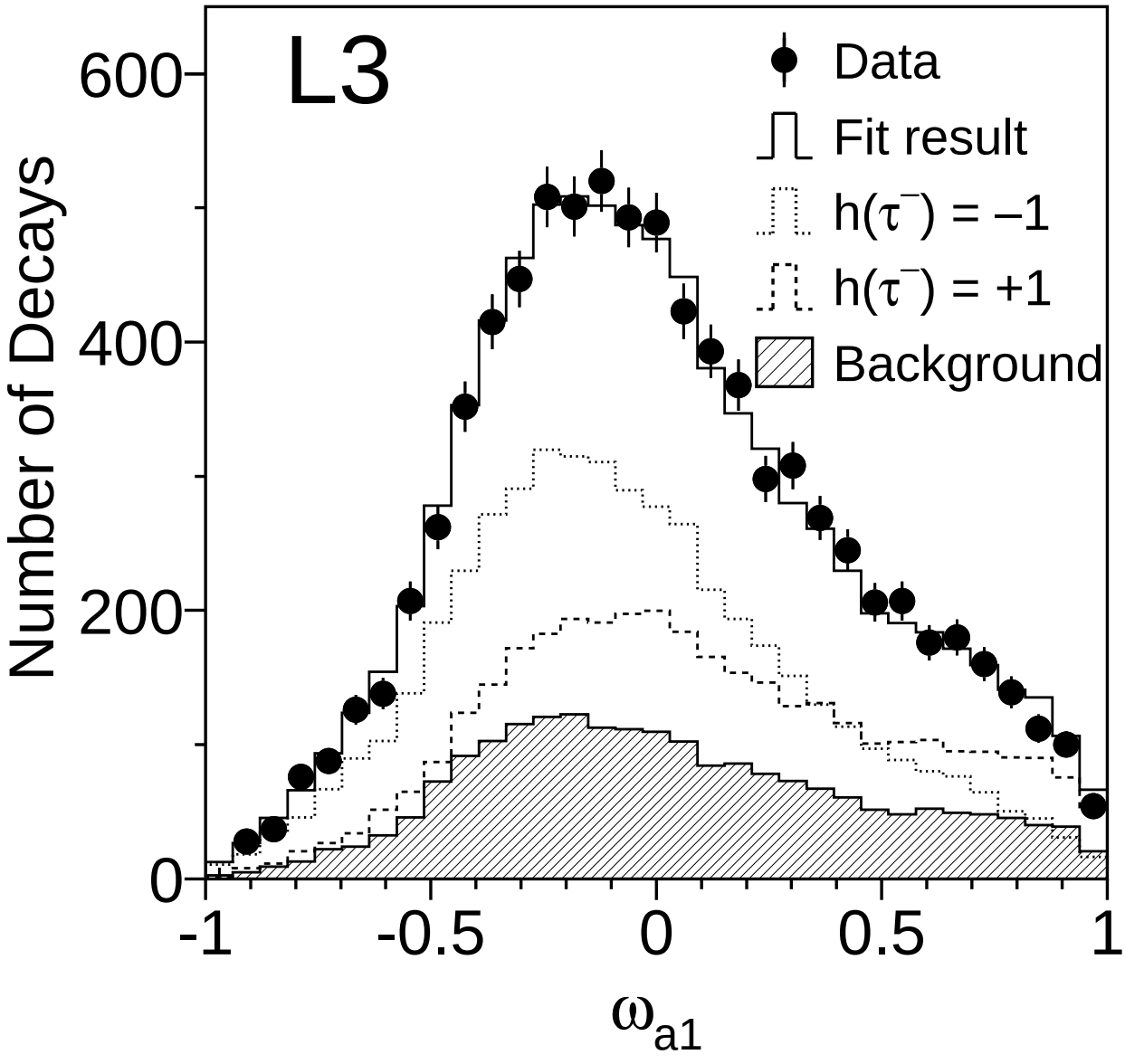

Figure 4.5: The measured spectrum of the polarisation-sensitive variable for the $\tau \to \mathrm{a}_1\nu$ decays in the L3 experiment. The distribution is of the optimal variable, ω_{a_1}, described in the text, combined for both $a_1^- \to \pi^-\pi^+\pi^-$ and $a_1^- \to \pi^-\pi^0\pi^0$ decays. The two helicity components and the background are shown separately.

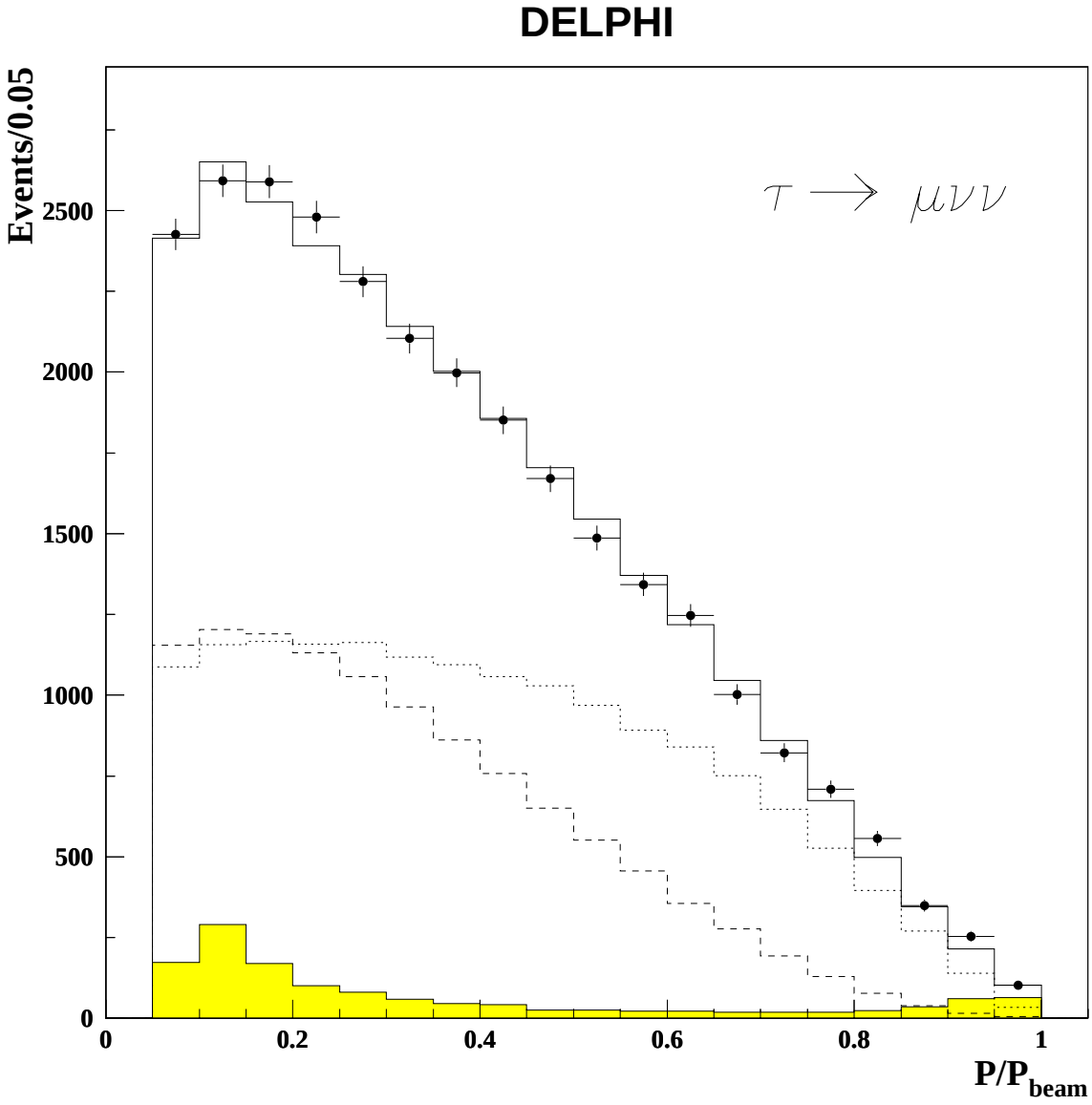

Figure 4.6: The measured spectrum of the polarisation-sensitive variable for the $\tau \to \mu\nu\bar{\nu}$ decays in the DELPHI experiment. The variable is the ratio of the measured muon momentum to the beam energy. The data are compared to the results of the polarisation fit. The circles are data and the solid line is simulated data for the fitted values of $\mathcal{A}_\tau$ and $\mathcal{A}_\mathrm{e}$. The shaded area is background and the dashed and dotted lines correspond to the positive and negative helicity contributions respectively.

provides greater discrimination between hadronic decay channels of the tau. This results in improved signal-to-noise thereby providing greater polarisation sensitivity and lower systematic errors.

The LEP combination is made using the overall results of $\mathcal{A}_\tau$ and $\mathcal{A}_\mathrm{e}$ from each experiment, rather than by first combining the results for each decay mode. Correlations between decay channels are dominated by detector-specific systematic errors which are most reliably taken into account by the individual experiments as discussed in Section 4.3. The combinations of the eight measurements, four each of $\mathcal{A}_\tau$ and $\mathcal{A}_\mathrm{e}$, take into account all other correlations and are presented in the following sections.

4.3 Systematic Errors

The combined statistical errors on $\mathcal{A}_\tau$ and $\mathcal{A}_\mathrm{e}$ are 0.0035 and 0.0048, respectively. Systematic errors on these parameters which are less than 0.0003 will not alter the combined errors when two significant figures are quoted. Therefore, such systematic errors are considered to be negligible.

The systematic errors on $\mathcal{A}_\mathrm{e}$ are considerably smaller that the systematic errors on $\mathcal{A}_\tau$ because, for the most part, the systematic effects are symmetric in $q \times \cos\theta$ and consequently cancel in $\mathcal{A}_\mathrm{e}$ but not in $\mathcal{A}_\tau$. This includes large cancellations of the Monte Carlo statistical errors which arise by using the same Monte Carlo samples in reflected $\cos\theta$ bins. Different approaches to evaluating the degree of cancellation of the $\mathcal{A}_\mathrm{e}$ systematic errors are adopted by the four experiments and are detailed in References [99–102].

There are two broad categories of systematic error in these measurements: those associated with the uncertainty of the underlying physics assumptions and their treatment, and those associated with the modelling of the detector. The latter category of systematic error depend on the details of each of the individual detectors. Although three of the four experiments depend on the same detector simulation software, GEANT [30], the designs of the four detectors are sufficiently different that these detector related errors are uncorrelated between experiments. However, these uncertainties can be strongly correlated between measurements from different decay channels performed with the same detector. For example, the uncertainty in the momentum scale for one of the detectors is independent of that in the other three detectors, but the momentum scale error is correlated between the $\mathcal{P}_\tau$ measurements from different decay modes made with the same detector. Because each of the experiments takes these correlations into account when quoting a systematic error on the measurements of $\mathcal{A}_\tau$ and $\mathcal{A}_\mathrm{e}$ using all channels, only the global results from each of the four experiments can be reliably combined to give a LEP average.

Turning now to the uncertainty of the treatment of the physics of τ production and decay, there are a number of systematic uncertainties in this category that are common to all four experiments. One set of these uncertainties affect all decay modes in the same way while others are different for each τ decay mode. The origins of some of the common uncertainties are the common software tools that are used to describe the production and decay of the τ [36] and the major backgrounds [33, 36, 103–106]; and the tools used to interpret the data in terms of the Standard Model [24]. Another source of the common errors arise from reliance on the same physics input used in the analyses of the four experiments, such as the branching ratios of the τ.

In the category of systematic uncertainty that affects all decay modes, the following have been identified as potential sources of error common to all experiments:

- Electromagnetic radiative corrections for initial state radiation from the e^+ and e^- and final state radiation from the τ^+ and τ^-. This radiation influences the measurement in two ways. The first relates to the fact that the experiments measure $\langle \mathcal{P}_\tau \rangle$ and $A_{\rm FB}^{\rm pol}$ which are integrated over s'; s' being the centre-of-mass energy of the τ-pair system excluding initial state radiation. This effect is included in the ZFITTER correction discussed below. The second influence relates to changes to the kinematic distributions caused by initial and final state radiation and potential s' biases introduced in the selection procedure. In this case, the four experiments rely on the KORALZ Monte Carlo event generator to take these effects into account. This radiation is calculated to $\mathcal{O}(\alpha^2)$ and includes exclusive exponentiation in both initial and final state radiation. Although interference between the initial and final state radiation is not included in the generator when producing the simulated events, such effects have negligible impact on the $\mathcal{P}_\tau$ measurements. Because of its precision, the treatment of initial and final state radiation, although common to all experiments, introduces no significant contribution to the systematic error.

- ZFITTER treatment of $\sqrt{s}$ dependence of $\mathcal{P}_\tau$, including the effects of initial state radiation, and of photon propagator and γ-Z interference. This amounts to the application of the Standard Model interpretation of $\langle \mathcal{P}_\tau \rangle$ and $A_{\rm FB}^{\rm pol}$ in terms of $\mathcal{A}_\tau$ and $\mathcal{A}_{\rm e}$. Although the experiments introduce this interpretation at different stages of their analyses, it effectively amounts to corrections of $\mathcal{O}(0.005)$ to both $\langle \mathcal{P}_\tau \rangle$ and $A_{\rm FB}^{\rm pol}$ and it is estimated that the uncertainty on this correction is negligible. For example, variations of the unknown parameters in the model, such as the Higgs mass, alter this correction by ± 0.0002. Since all experiments rely on ZFITTER for this treatment, the error is common across experiments as well as to $\mathcal{A}_\tau$ and $\mathcal{A}_{\rm e}$.

- Born level mass terms leading to helicity flip configurations. At the $\mathcal{O}(10^{-3})$ level, the τ^- and τ^+ will have the same instead of opposite helicities. Although this effect cannot be seen in the quoted measurements at this level of precision, it is included in the KORALZ treatment nonetheless.

- The value of $A_{\rm FB}^\tau$ used in the fit. The different experiments treat this differently. ALEPH and DELPHI use the Standard Model values of $A_{\rm FB}^\tau$ with appropriate $\sqrt{s}$ dependence. OPAL uses its measured values of $A_{\rm FB}$ for τ-pairs at the different values of $\sqrt{s}$. L3 assumes the relation $A_{\rm FB}^\tau = \frac{3}{4}\mathcal{A}_{\rm e}\mathcal{A}_\tau$ in the denominator of Equation 4.1. Since $A_{\rm FB}^\tau$ enters into the analysis as a small number in the normalisation, its uncertainty introduces a correspondingly small systematic error for each experiment. Although the Standard Model assumptions regarding $A_{\rm FB}^\tau$ by ALEPH, DELPHI and L3 imply that some correlation exists from this source between the measurements of these three experiments, it is negligible and consequently ignored in the combined LEP results. The OPAL treatment introduces a small correlation between between the τ-polarisation measurement and the OPAL $A_{\rm FB}^\tau$ measurement. Varying the value of $A_{\rm FB}^\tau$ by 0.001 introduces negligible changes to the $\mathcal{A}_\tau$ and $\mathcal{A}_{\rm e}$ measurements.

In conclusion, all of these effects are theoretically well defined and have been calculated to adequate precision for the measurements at hand thereby contributing nearly negligible uncertainty to the common systematic error. Of these, the ZFITTER error of ± 0.0002 is included as a common error in the LEP combination.

Concerning the category of uncertainty that affects each decay mode separately, the following sources of potentially common systematic error have been identified:

- Branching ratios of the various τ decay modes. These arise since the purity for selecting any particular decay mode for polarisation analysis is not unity. All experiments use the world average values of the branching ratios as determined by the Particle Data Group [76, 107], along with the quoted errors. Consequently, the components of the systematic error which are associated with the uncertainty in the branching ratios is an error correlated between experiments. These errors are taken into account in the combined error, and are shown in Table 4.2 for the combined error on $\mathcal{A}_\tau$ and $\mathcal{A}_\mathrm{e}$ for each of the experiments.

- Radiative corrections for τ leptonic final states. The radiation in the decays $\tau \to \mathrm{e}\nu\overline{\nu}$ and $\tau \to \mu\nu\overline{\nu}$ are treated exactly to $\mathcal{O}(\alpha)$ in KORALZ and negligible contributions to the systematic error are introduced by this treatment.

- Bhabha background. ALEPH and OPAL use the BHWIDE Monte Carlo generator [103] to describe this background while DELPHI uses the BABAMC [38] and UNIBAB [39] in addition to BHWIDE. L3 uses the BHAGENE generator [40]. The use of BHWIDE by three of the experiments potentially introduces a common systematic error. The contributions from the use of this generator to the errors on the measurements from each experiment are shown in Table 4.2. In the case of experiments where there is very little Bhabha background, the errors are negligible. It should be noted that much of the uncertainty is detector-specific, and therefore does not constitute a large common systematic error.

- The background from two-photon events can be problematic since the two-photon Monte Carlo generators used by the experiments do not include initial state radiation. There is a potential danger that the measured event transverse momentum (p_T), a quantity which discriminates between τ-pair events, which have large p_T, and two-photon events which have small p_T, is sensitive to initial state radiation: low energy events, which can have a high $\mathcal{P}_\tau$ analysing power, are not perfectly modelled in the simulation. This is common to all experiments, but the sensitivity of a given experiment to the effect depends on the effectiveness with which two-photon events are identified and removed from the sample. These errors are taken into account in the combined error with the contributions from each experiment shown in Table 4.2 but do not represent a significant correlation because some experiments make corrections to this background based on control samples in their own data.

- Hadronic decay modelling. Model dependent uncertainties in a_1 decay have been evaluated by all experiments. These uncertainties arise both in the analysis of the $\tau \to \mathrm{a}_1\nu$ channel itself and in the analysis of channels where backgrounds from the a_1 can be significant, such as the $\tau \to \rho\nu$. These errors can be common to all experiments, but will vary in sensitivity depending on the purity of the the samples and details of the analysis. The KORALZ [108] Monte Carlo simulation of the $\tau \to \nu_\tau\pi > 2\pi^0$ and $\tau \to \nu_\tau 3\pi^\pm > \pi^0$ decays, which are backgrounds to some of the $\mathcal{P}_\tau$ analysing channels, also have model dependencies with a corresponding uncertainty. Consequently, the experiments estimate how much these deficiencies affect the $\mathcal{P}_\tau$ measurements.

  Another aspect of hadronic decay modelling is the treatment of radiative corrections for τ hadronic final states. Unlike radiation from leptons, there is no precise formalism for handling these corrections. The KORALZ generator uses an $\mathcal{O}(\alpha)$ correction in the

leading logarithmic approximation as implemented in the PHOTOS software package [109]. In the $\tau \to \pi\nu$ channel, this radiation affects the polarisation at the 0.01 level absolute while for the $\tau \to \rho\nu$ the effects are less than half that. Theoretical work [110, 111] indicates that the treatment of radiation in the decay $\tau \to \pi\nu\gamma$ is valid to the 5% level of the decay rate. Consequently, the uncertainties in the decay radiation treatment contribute at the 0.0005 level to the systematic error of the $\tau \to \pi\nu$ measurement of $\mathcal{A}_\tau$, and much less than that to the error on the combined measurements. Unfortunately, no analogous theoretical studies have been performed for the $\tau \to \rho\nu\gamma$ decay. Following reference [109], the error on the treatment of the radiation is approximately $1/\ln(m_\tau/m_\rho)$ of the magnitude of the effect of the radiation on the measurement of $\mathcal{P}_\tau$. This results in an error of no more than 0.001 on $\mathcal{A}_\tau$ and a negligible error on $\mathcal{A}_\mathrm{e}$. The equivalent radiation effects for the other hadronic decay modes introduce a negligible contribution to the combined systematic error. These hadronic modelling errors are summarised in Table 4.2 and are found to contribute a small effect to the measurements over all channels.

- The modelling uncertainty of the multihadronic background introduces negligible errors in all channels but the $\tau \to \mathrm{a}_1\nu$. However, because the background itself is small and the weight of the $\tau \to \mathrm{a}_1\nu$ measurement is not high, this is a negligible contribution to the error on $\mathcal{P}_\tau$ from all channels.

- The modelling of μ-pair background has a negligible error. Any uncertainty arising from μ-pair events is evaluated as a detector-related systematic error.

	ALEPH		DELPHI		L3		OPAL	
	$\delta\mathcal{A}_\tau$	$\delta\mathcal{A}_\mathrm{e}$	$\delta\mathcal{A}_\tau$	$\delta\mathcal{A}_\mathrm{e}$	$\delta\mathcal{A}_\tau$	$\delta\mathcal{A}_\mathrm{e}$	$\delta\mathcal{A}_\tau$	$\delta\mathcal{A}_\mathrm{e}$
(1) ZFITTER	0.0002	0.0002	0.0002	0.0002	0.0002	0.0002	0.0002	0.0002
(2) τ branching ratios	0.0003	0.0000	0.0016	0.0000	0.0007	0.0012	0.0011	0.0003
(3)Bhabha background	0.0000	0.0000	0.0012	0.0000	0.0000	0.0000	0.0000	0.0000
(4)two-photon background	0.0000	0.0000	0.0005	0.0000	0.0007	0.0000	0.0000	0.0000
(5)hadronic decay modelling	0.0012	0.0008	0.0010	0.0000	0.0010	0.0001	0.0025	0.0005

Table 4.2: The magnitude of the major common systematic errors on $\mathcal{A}_\tau$ and $\mathcal{A}_\mathrm{e}$ by category for each of the LEP experiments.

4.4 Results

The results for $\mathcal{A}_\tau$ and $\mathcal{A}_\mathrm{e}$ obtained by the four LEP collaborations [99–102] are shown in Table 4.3. The measurements from all experiments are consistent with each other and are combined to give values of $\mathcal{A}_\tau$ and $\mathcal{A}_\mathrm{e}$ from a fit which includes the effects of correlated errors. The combined results are included in Table 4.3 and are also summarised in Figure 4.8. Figure 4.7 shows the measured values of $\mathcal{P}_\tau$ as a function of $\cos\theta_{\tau^-}$ for all four LEP experiments. The curves overlaying the figure depict Equation 4.1 for the combined results with and without assuming lepton universality. It is interesting to remark that if lepton universality is assumed, $\mathcal{P}_\tau$ is forced to be zero at $\cos\theta_{\tau^-} = -1$, regardless of the actual values of the Standard Model couplings. From Figure 4.7 it is evident that the data are indeed consistent with $\mathcal{P}_\tau$=0 at $\cos\theta_{\tau^-} = -1$.

There are small ($\leq 5\%$) statistical and, in some cases, systematic correlations between $\mathcal{A}_\tau$ and $\mathcal{A}_\mathrm{e}$ performed by a single experiment. There are also systematic correlations between the different experimental values as discussed in the previous section. Therefore a single fit to all of the data using the complete 8×8 error correlation matrix, given in Table 4.4, is used to obtain the LEP combined values of these two parameters.

We take the ±0.0002 ZFITTER errors to be fully correlated between $\mathcal{A}_\tau$ and $\mathcal{A}_\mathrm{e}$. Other systematic errors listed in Table 4.2 are taken to be fully correlated between either $\mathcal{A}_\tau$ or $\mathcal{A}_\mathrm{e}$ measurements. These are used to calculate the inter-experiment off-diagonal elements of the error correlation matrix. The correlated errors between $\mathcal{A}_\tau$ and $\mathcal{A}_\mathrm{e}$ for a given experiment as quoted by the experiment are also included in the error correlation matrix.

The fitted values for $\mathcal{A}_\tau$ and $\mathcal{A}_\mathrm{e}$ with no assumption of lepton universality are:

$$\mathcal{A}_\tau = 0.1439 \pm 0.0043 \tag{4.8}$$

$$\mathcal{A}_\mathrm{e} = 0.1498 \pm 0.0049\,, \tag{4.9}$$

where the χ^2 is 3.9 for six degrees of freedom and the correlation is 0.012. These asymmetries are consistent with each other, in agreement with lepton universality. Assuming $\mathrm{e}-\tau$ universality, the values for $\mathcal{A}_\tau$ and $\mathcal{A}_\mathrm{e}$ can be combined in a fit with a single lepton asymmetry parameter which yields a result of:

$$\mathcal{A}_\ell = 0.1465 \pm 0.0033 \tag{4.10}$$

where the χ^2 is 0.8 for one degree of freedom, considering this to be a combination of $\mathcal{A}_\tau$ and $\mathcal{A}_\mathrm{e}$. If one considers there to be eight measurements of $\mathcal{A}_\ell$, the χ^2 is 4.7 for seven degrees of freedom. This value of $\mathcal{A}_\ell$ corresponds to a value of:

$$\sin^2\theta^{\mathrm{lept}}_{\mathrm{eff}} = 0.23159 \pm 0.00041\,. \tag{4.11}$$

Experiment	$\mathcal{A}_\tau$	$\mathcal{A}_\mathrm{e}$
ALEPH	$0.1451 \pm 0.0052 \pm 0.0029$	$0.1504 \pm 0.0068 \pm 0.0008$
DELPHI	$0.1359 \pm 0.0079 \pm 0.0055$	$0.1382 \pm 0.0116 \pm 0.0005$
L3	$0.1476 \pm 0.0088 \pm 0.0062$	$0.1678 \pm 0.0127 \pm 0.0030$
OPAL	$0.1456 \pm 0.0076 \pm 0.0057$	$0.1454 \pm 0.0108 \pm 0.0036$
LEP	$0.1439 \pm 0.0035 \pm 0.0026(0.0043)$	$0.1498 \pm 0.0048 \pm 0.0010(0.0049)$

Table 4.3: LEP results for $\mathcal{A}_\tau$ and $\mathcal{A}_\mathrm{e}$. The first error is statistical and the second systematic. To form the LEP combinations, statistical and systematic errors are combined in quadrature. The total error on the combined results are shown in parentheses on the last line. This total error is also decomposed into statistical and systematic components to illustrate the relative weight of systematic errors on the final combined results.

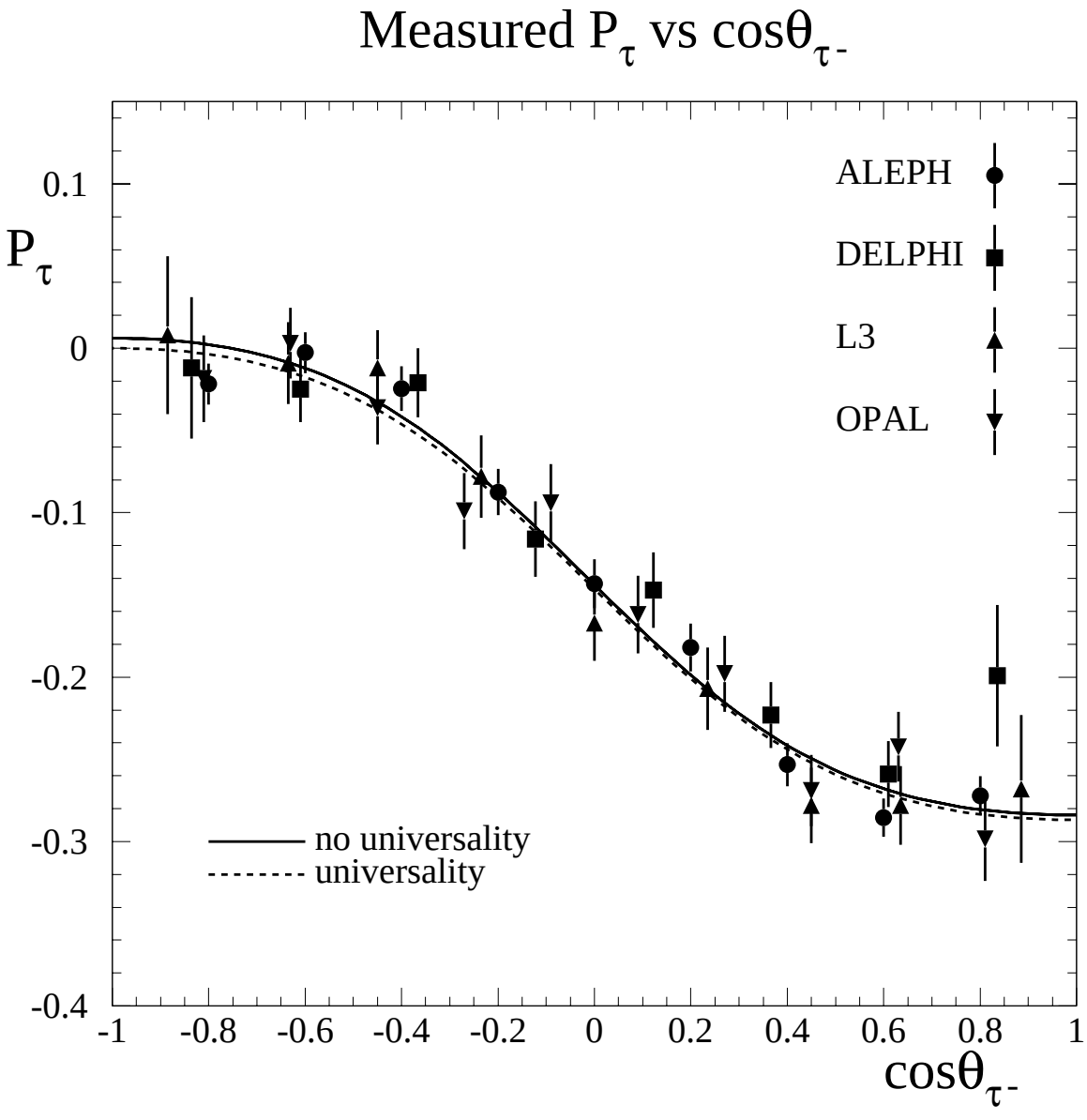

Figure 4.7: The values of $\mathcal{P}_\tau$ as a function of $\cos\theta_{\tau^-}$ as measured by each of the LEP experiments. Only the statistical errors are shown. The values are not corrected for radiation, interference or pure photon exchange. The solid curve overlays Equation 4.1 for the LEP values of $\mathcal{A}_\tau$ and $\mathcal{A}_e$. The dashed curve overlays Equation 4.1 under the assumption of lepton universality for the LEP value of $\mathcal{A}_\ell$.

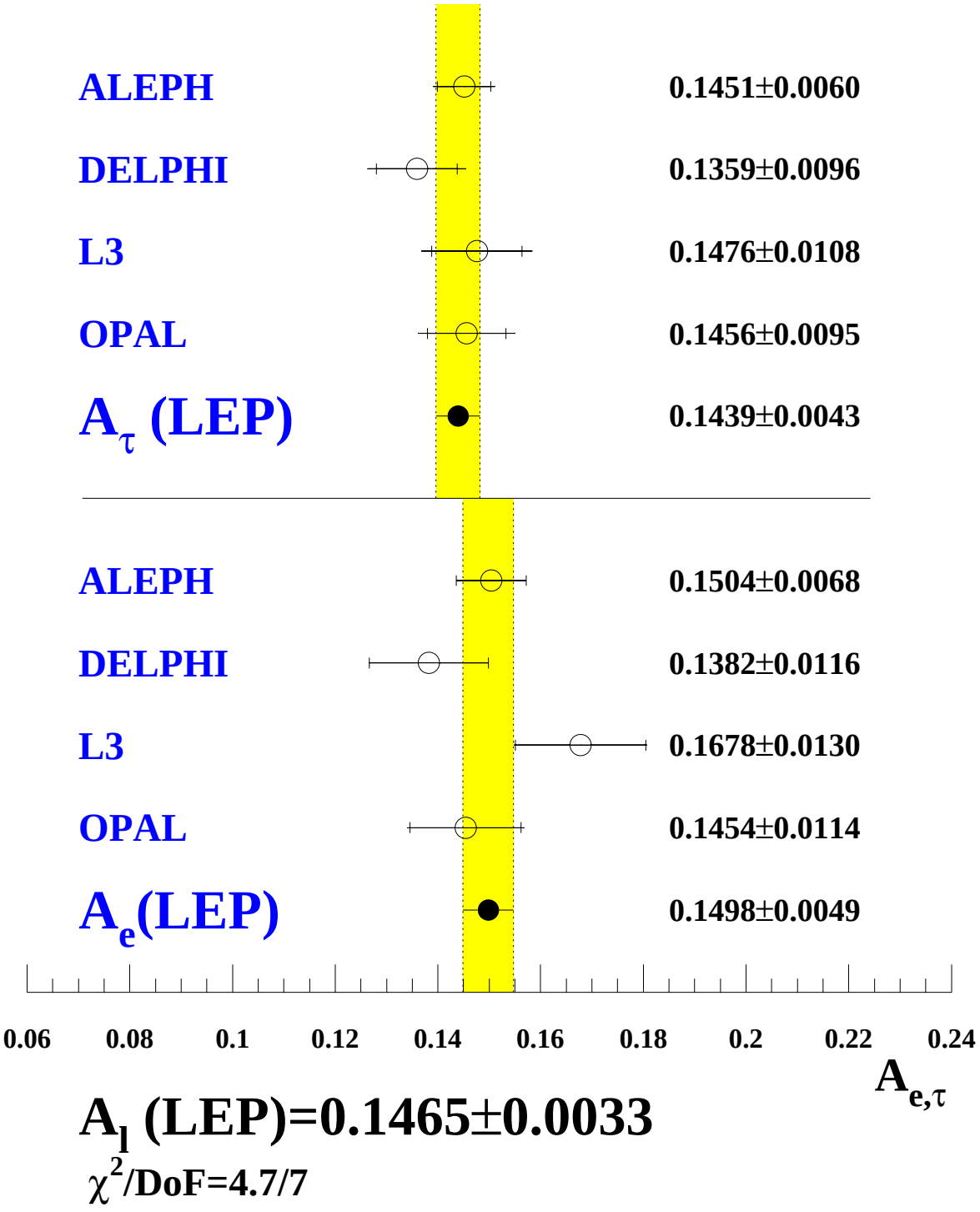

Figure 4.8: Measurements of $\mathcal{A}_e$ and $\mathcal{A}_\tau$ from the four LEP experiments. The error bars indicate the quadrature sum of the statistical and systematic errors. The magnitude of the statistical errors alone are indicated by the small tic marks on the error bar. The value of $\mathcal{A}_\ell$ and the χ^2 of the fit assuming lepton universality is also quoted.

	$\mathcal{A}_\tau$(A)	$\mathcal{A}_\tau$(D)	$\mathcal{A}_\tau$(L)	$\mathcal{A}_\tau$(O)	$\mathcal{A}_e$(A)	$\mathcal{A}_e$(D)	$\mathcal{A}_e$(L)	$\mathcal{A}_e$(O)
$\mathcal{A}_\tau$(A)	1.000							
$\mathcal{A}_\tau$(D)	0.029	1.000						
$\mathcal{A}_\tau$(L)	0.022	0.024	1.000					
$\mathcal{A}_\tau$(O)	0.059	0.047	0.032	1.000				
$\mathcal{A}_e$(A)	-0.002	0.000	0.000	0.000	1.000			
$\mathcal{A}_e$(D)	0.000	0.025	0.000	0.000	0.000	1.000		
$\mathcal{A}_e$(L)	0.000	0.000	0.032	0.000	0.001	0.000	1.000	
$\mathcal{A}_e$(O)	0.000	0.000	0.000	0.025	0.005	0.000	0.002	1.000

Table 4.4: Error correlation matrix used for the combination of the LEP results for $\mathcal{A}_\tau$ and $\mathcal{A}_e$. The order is: $\mathcal{A}_\tau$ for ALEPH, DELPHI, L3 and OPAL; followed by $\mathcal{A}_e$ for ALEPH, DELPHI, L3 and OPAL.

Chapter 5

Results from b and c quarks

5.1 Introduction

The high efficiency and purity with which b- and c- quarks can be tagged allow precise electroweak measurements to be made with heavy flavour samples. As already explained in chapter 1 their partial widths, normalised to the total hadronic width of the Z, R_{b}^0, R_{c}^0, the forward-backward asymmetries with unpolarised beams, $A_{\mathrm{FB}}^{\mathrm{b\overline{b}}}$, $A_{\mathrm{FB}}^{\mathrm{c\overline{c}}}$, and, with polarised beams, the left-right-forward-backward asymmetries, $A_{\mathrm{FBLR}}^{\mathrm{b\overline{b}}}$, $A_{\mathrm{FBLR}}^{\mathrm{c\overline{c}}}$, can be measured. These measurements probe the fundamental charge and weak iso-spin structure of the Standard Model couplings for quarks. R_{b}^0 is of special interest since it probes vertex corrections to the $\mathrm{Zb\overline{b}}$ vertex which is sensitive to new physics for example from a supersymmetric Higgs sector. On the contrary $A_{\mathrm{FB}}^{\mathrm{q\overline{q}}}$ are, due to numerical cancellations, clean probes of the initial state $\mathrm{Ze^+e^-}$-couplings. $A_{\mathrm{FBLR}}^{\mathrm{q\overline{q}}}$ is basically constant in any model where new physics appears only in loops and is thus a good test for new Born-level physics like Z-Z' mixing. Due to the much worse tagging possiblitites for light quarks, as discussed in chapter 6, electroweak tests of similar interest are not possible for uds-quarks.

The LEP experiments and SLD measure these quantities with a variety of methods. Since all the measurements make some assumptions about the fragmentation and decays of b- and c-quarks, there are many sources of systematic correlations between them. In addition, different observables are sometimes measured simultaneously, giving rise to statistical correlations between the results. For these two reasons a simple average of the different results is not sufficient. A more sophisticated procedure is needed and is described below.

To derive consistent averages the experiments have agreed on a common set of input parameters and their errors. These parameters are described in section 5.6. Some of the input parameters measured at LEP and SLD are either measured within the same analyses as some of the electroweak quantities or they share systematic uncertainties with them. To treat correctly the dependencies of these parameters with the electroweak ones they are included as auxiliary parameters in the electroweak heavy flavour fit. They are:

- the $\mathrm{B^0\overline{B^0}}$ effective mixing parameter $\overline{\chi}$, which is the probability that a semi-leptonically decaying b-quark has been produced as an anti-b-quark,
- the prompt and cascade semileptonic branching fraction of the b-hadrons $\mathrm{BR(b \to \ell^-)}$* and $\mathrm{BR(b \to c \to \ell^+)}$ and the prompt semileptonic branching fraction of the c-hadrons $\mathrm{BR(c \to \ell^+)}$.

*Unless otherwise stated, charge conjugate modes are always included

- the fraction of charm hemispheres fragmenting into a specified weakly decaying charmed hadron, $f(\mathrm{D}^+)$, $f(\mathrm{D_s})$, $f(\mathrm{c_{baryon}})^\dagger$,
- the probability that a c-quark fragments into a D^{*+} that decays into $\mathrm{D}^0\pi^+$, $\mathrm{P}(\mathrm{c} \to \mathrm{D}^{*+}) \times \mathrm{BR}(\mathrm{D}^{*+} \to \pi^+\mathrm{D}^0)$.

The methods to tag heavy flavours at LEP and SLD are described in section 5.2. The different measurements of the electroweak and auxiliary parameters used in the heavy flavour combinations are outlined in sections 5.3-5.5. Section 5.6 descibes the agreed common input parameters. In section 5.7 the corrections to the electroweak parameters due to physics effects like QED and QCD corrections are described and the combination precedure is expalined in section 5.8. Finally the results are summarised in section 5.9.

5.2 Heavy flavour tagging methods

In principle, the rate measurements $R_\mathrm{q} = \sigma_\mathrm{q}/\sigma_\mathrm{had}$ only require a selection of the flavour q from hadronic events with a tag that has efficiencies and purities known to a high precision. The asymmetry measurements require in addition that a distinction between quark and antiquark is made, with a known charge tagging efficiency. Cancellation in the asymmetry definition makes these measurements largely independent of the flavour tagging efficiency, apart from background corrections.

At LEP and SLD basically three different methods are used for flavour tagging. In the lifetime tags the long lifetime of heavy quarks is used. Due to the somewhat longer lifetime and the larger mass these methods are especially efficient for b-quarks. They tag only the flavour of the quarks. To obtain also the quark charge additional methods have to be used. The second and historically oldest method is the tag of prompt leptons. b- and c-quarks decay semileptonically where, because of the higher b-mass, the two quark species can be separated by the transverse momentum of the lepton. For direct decays the sign of the quark charge is equal to the one of the lepton, so that leptons tag simultaneously the quark flavour and charge. The third method is the reconstruction of charmed hadrons. Most charmed hadrons have few-prong decay modes with relatively high branching ratios so that they can be used for flavour tagging. Since most charmed hadron decays are not charge symmetric they can also be used for quark charge tagging. Charmed hadrons tag charm quarks and, via the decay $\mathrm{b} \to \mathrm{c}$, b-quarks and properties of the fragmentation or lifetime tags have to be used to separate the two.

5.2.1 Lifetime Tagging

The two most efficient and pure ways of selecting b-hadrons from Z decays are based on the reconstruction of secondary vertices and on the measurement of the large impact parameter of the b-hadron decay products. Since the average b lifetime is about 1.5 ps and the b-hadrons are produced with a most probable energy of 30 GeV at the Z peak, they travel for about 3 mm before decaying. Their mean charged multiplicity is $\sim$5 (see section 5.6.3). The silicon vertex detectors of the LEP experiments and SLD have a resolution for the secondary vertex position about one order of magnitude smaller than the mean decay length.

$^\dagger f(\mathrm{D}^0)$ is calculated from the constraint $f(\mathrm{D}^0) + f(\mathrm{D}^+) + f(\mathrm{D_s}) + f(\mathrm{c_{baryon}}) = 1$.

	ALEPH	DELPHI	L3	OPAL	SLD
Num. of layers	2	3	2	2	3
Radius of layers (cm)	6.5/11.3	6.3/9/11	6.2/7.7	6.1/7.5	2.9-4.1
$R\phi$ imp. par. res. (μm)	25*	20	30	16	13
z imp. par. res. (μm)		30	100	35	24
Primary Vertex res. $x \times y \times z$ (μm)	$58 \times 10 \times 60$	$22 \times 10 \times 22$	$77 \times 10 \times 100$	$80 \times 12 \times 85$	$6.4 \times 6.4 \times 15$

Table 5.1: Vertex detector characteristics and experimental resolutions.
The impact parameter resolution is given for 45 GeV muons and the vertex resolution is given for $b\overline{b}$-events when including the beam spot information.
* for ALEPH the 3D impact parameter resolution is given.

Since the b-hadron decay vertex is separated from the interaction point, each of the tracks originating in the decay will in general appear to miss the primary vertex. The impact parameter is defined as the distance of closest approach of the reconstructed track to the interaction point. It is given by

$$\delta = \gamma\beta c\tau \sin\psi\,, \tag{5.1}$$

where τ is the particle proper decay time and ψ is the angle between the secondary particle and the b-hadron flight direction.

For a high momentum track, $\sin\psi$ is proportional to $1/\beta\gamma$, and the average impact parameter is then proportional to the average lifetime τ: $\delta \propto c\tau$, independent of the b-hadron energy. Since at LEP the b-hadron momentum is high, the uncertainty on the b-hadron momentum distribution, i.e. the b fragmentation function, has only a small effect on the impact parameter distribution. The impact parameter of the b-hadrons is about 300μm, to be compared with the experimental resolution of 20 to 70 μm, depending on the track momentum. ALEPH, L3, and SLD compute the impact parameter in 3D space, while DELPHI and OPAL compute the impact parameter separately in the two projections $R\phi$ and Rz. The two projections are then treated as two separate variables.

The precise determination of the Z decay point, the so called primary vertex, is required in lifetime b-tagging techniques. It is determined separately for each hadronic event using the current envelope of such vertices (the beam spot) as a constraint. The beam spot is defined as the interaction region of the electron and the positron beams. At LEP the width along the horizontal x-axis varies with time but is typically 100 to 150 μm. The width along the vertical y-axis is around 5 μm, which is below the detector resolution, and the longitudinal length along the z-axis is about 1 cm. Since the beam spot width in z is much larger than the detector resolution, the details do not influence the tagging efficiencies. At SLC the beam spot is only a few microns wide in the transverse (xy) plane giving an almost point-like primary vertex resolution.

The event primary vertex is determined by a fit to all tracks after having excluded tracks classified to originate from decays of long lived particles or hadronic interaction products. The accuracy of the reconstructed primary vertex position depends on the algorithm used, on the geometry of the silicon vertex detectors and on the size of the beam spot. The parameters of the various vertex detectors and the resolution on the relevant quantity for a lifetime b-tag are summarised for the LEP and SLC experiments in Table 5.1.

A lifetime sign is assigned to each track impact parameter. This is positive if the extrapolated track is consistent with a secondary vertex which lies on the same side of the primary vertex as the track itself, otherwise it is negative. Due to the finite resolution of the detector, the relevant quantity for the identification of the b-quark is the impact parameter significance S, defined as the lifetime signed impact parameter divided by its error. In Figure 5.1 the projection in the $R\phi$ plane of the lifetime-signed impact parameter significance distribution is shown for tracks coming from the different quark flavours. Tracks coming from the decays of K^0_s and Λ are removed, so that the distribution of the light quark reflects the resolution of the apparatus (DELPHI in this case).

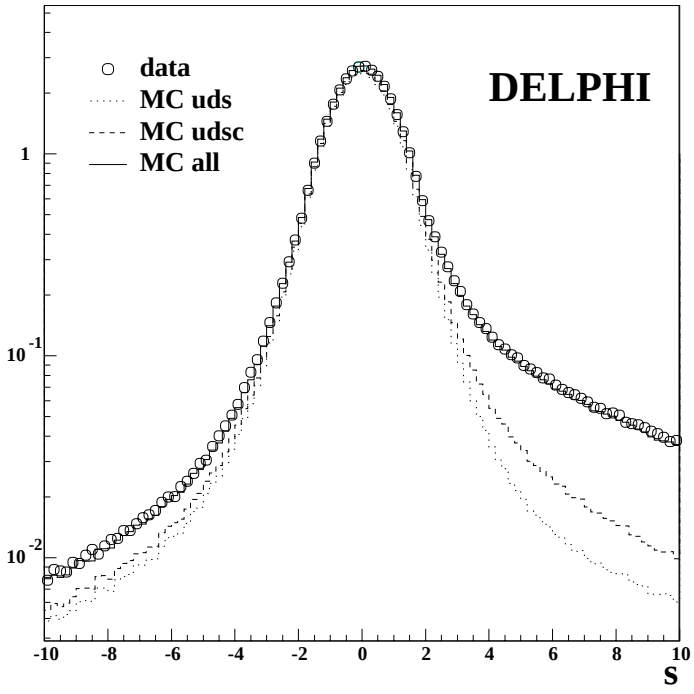

Figure 5.1: Impact parameter significance from DELPHI for data and simulation. The contributions of the different quark flavours are shown separately.

A good description of S in the simulation is crucial for a reliable estimate of the tagging efficiencies. Negative significance values arise from light quark contributions, which have essentially no lifetime information and from the effects of finite resolution. This allows tag calibration from the negative side of the significance distribution. A good understanding of the impact parameter uncertainty is required to correctly describe the b-tagging efficiency in the simulation. Even for primary tracks the distribution of S is expected to be non Gaussian. This is caused by pattern recognition mistakes, non-Gaussian tails of multiple scattering and elastic hadronic interactions. It has been verified by simulation that these tails are symmetric for primary tracks.

A simple b-tag can use the number of tracks with a large positive significance. A better estimator is constructed by combining all the positive track significances: first the negative part of the significance distribution is fitted to a functional form that defines the resolution of the detector, then for each track the integral of this function from negative infinity to the S of the track is computed giving the probability that the track comes from the primary vertex, which by construction is flat from zero to one. The probability that all tracks in a jet, hemisphere

or event, come from the primary vertex is calculated by combining the probabilities for all tracks in that jet, hemisphere or event. By construction it is flat if all tracks originate from the primary vertex. The probability for a group of tracks coming from an uds event is then flat between zero and one. The probability for a group of tracks coming from a b quark event, however, is peaked at zero.

Figure 5.2 shows the distribution of the L3 b-tagging variable D which is the negative logarithm of the hemisphere impact parameter probability. It can be seen that at large values of D high tag purities can be achieved with impact parameters only.

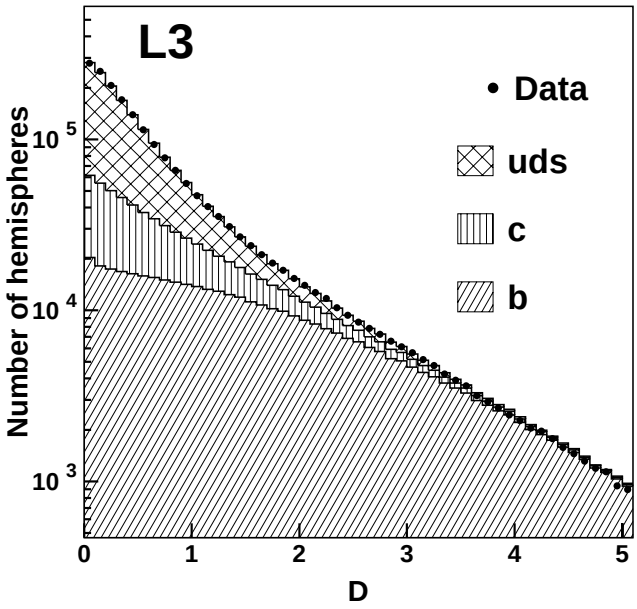

Figure 5.2: Impact parameter b-tag from L3.

An alternative lifetime-based tag uses the reconstruction of secondary vertices. OPAL fits all well-reconstructed high momentum tracks in a jet to a single secondary vertex, then progressively removes those which do not fit well. The decay length significance L/σ_L (the reconstructed distance between the primary and secondary vertices divided by its error) is used as the b-tagging variable, signed depending on whether the secondary vertex is reconstructed in front of or behind the primary vertex (see Figure 5.3). This allows the background from light quark events with $L/\sigma_L > 0$ to be estimated using the number of events with $L/\sigma_L < 0$.

The extremely precise SLD vertex detector and small stable SLC beam spot allow a novel approach to secondary vertex finding, based on representing tracks as Gaussian 'probability tubes' [112]. Spatial overlaps between the probability tubes give regions of high probability density corresponding to candidate vertices, to which tracks are finally attached.

This algorithm found at least one secondary vertex in 73% (29%) of the hemispheres in $b\overline{b}$ ($c\overline{c}$) events. Among the b hemispheres that had at least one secondary vertex, two or more secondary vertices were found in 30% of them.

To obtain the best description of a b hadron, it is crucial to identify all its decay products. Since the basic decay vertex topology was established with well-measured tracks only, an attempt was made to incorporate lower-quality tracks or even unlinked VXD segments. To do so, a vertex axis was formed by joining the IP to a "seed" vertex combining both secondary and tertiary tracks, and the distance D between the IP and this vertex was computed. For

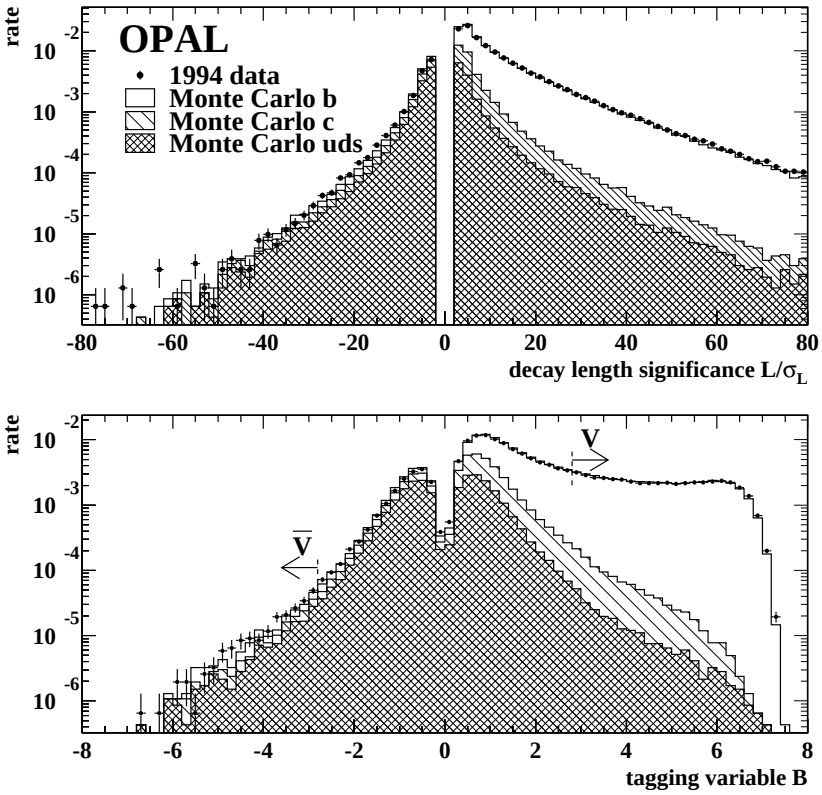

Figure 5.3: Decay length significance L/σ_L (top) and neural network tagging variable (bottom) for the OPAL secondary vertex based b-tag. The gaps around zero significance are due to neural network preselection cuts removing jets with no significant secondary vertex.

each track, the three-dimensional distance of closest approach T to the vertex axis and the longitudinal distance L between the IP and the point of closest approach on the vertex axis were calculated. Typical requirements for attaching a track to the seed vertex were $T < 1$mm, $L > 250\mu$m, and $L/D > 0.25$. This track attachment procedure was further improved by means of a neural network combining the information on $T, L, L/D$, and track angle with respect to the vertex axis. There were on average 3.9 quality secondary tracks in the seed vertex, and 0.9 additional tracks were attached per b hemisphere. The VXD segments were used only for vertex charge determination, and on average 0.2 VXD-alone segment was attached per b hadron decay. The sum of the identified secondary tracks and VXD segments corresponds to an average of 82% of all prompt b hadron decay tracks, with a track assignment purity of 96.8%.

5.2.2 Combined lifetime tag

The pure lifetime tags have an intrinsic limitation because D-mesons have a lifetime comparable to B-mesons. However this can be overcome if additional information is used. Since B-mesons are much heavier than D-mesons, the most obvious variable is the invariant mass of the particles fitted to the secondary vertex. In SLD this mass is used as a b-tag with an additional correction for the neutral decay products of the B. From the flight direction of the B, calculated from the primary and the B-decay vertex, and the momentum vector of the charged decay products of the B, fitted to the secondary vertex, the transverse momentum, p_t, of the sum of the neutral decay products can be calculated. Adding a massless pseudo particle with momentum p_t to the

secondary vertex gives an improved lower limit for the mass of the decaying particle.

In Figure 5.4 the p_t-corrected mass of the secondary vertex is shown for b events and for the uds and c background. The high efficiency for assigning the correct tracks to the decay vertex results in a very high b-tagging purity of 98% for almost 50% efficiency, simply by requiring the p_t-corrected mass to be above the D-meson mass. A further improvement of the performance has been recently obtained with the introduction of a neural network to optimise the track to vertex association and a second neural network to improve the c-b separation by using the vertex decay length, multiplicity and momentum in addition to the p_t-corrected vertex mass. With this improved tag the b-tagging efficiency increases to 62% with the same purity.

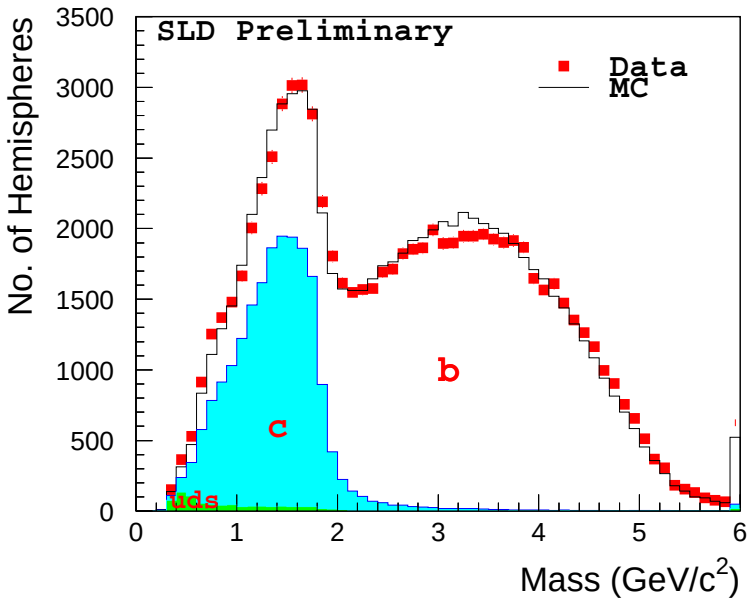

Figure 5.4: Reconstructed vertex mass from SLD for data and simulation.

The LEP beam spot is much larger in the x and y directions than that of SLC, and the innermost silicon layers of the LEP vertex detectors has to be at approximately twice the innermost radius of the SLD vertex detector, as indicated in table 5.1. This limits the b-tagging performance of the LEP detectors and motivates development of tags that combine additional information together with the impact parameter or decay length information.

DELPHI utilises a likelihood technique combining 4 variables: the probability that the tracks in the jet come from the primary vertex (see section 5.2.1), the mass of the reconstructed secondary vertex, the energy of the charged tracks belonging to the secondary vertex and their rapidity. Combining track properties with the information from the reconstructed secondary vertices makes the tag more robust against detector resolution effects. A considerable improvement can be obtained if the direction defined by the primary and secondary vertex is used as the b-hadron direction, instead of the jet axis.

ALEPH uses a linear combination of two lifetime-related variables. The first is the probability that the tracks from each hemisphere come from the primary vertex (as defined in section 5.2.1). The second variable is correlated with the mass of the hadron produced. In each jet the tracks are combined in order of decreasing inconsistency with the primary vertex until their mass exceeds 1.8 GeV/c^2. The mass-sensitive variable is defined as the impact parameter probability of the last track added.

	ALEPH	DELPHI	L3	OPAL	SLD
b Purity %	97.8	98.6	84.3	96.7	98.3
b Efficiency %	22.7	29.6	23.7	25.5	61.8

Table 5.2: b-Tagging performance of the different experiments at the cut where the R_{b} analyses are performed. The OPAL tag is an OR of a secondary vertex and a lepton tag.

L3 identify b-hemispheres using the impact parameter tag only.

OPAL uses a vertex tag based on a neural network combining five variables. The first four are derived from the reconstructed secondary vertex: the decay length significance L/σ_L, the decay length L, the number of tracks in the secondary vertex and a variable that measures the stability of the vertex against mismeasured tracks. The fifth variable exploits the high mass of b-hadrons. For each track in the jet, the relative probabilities that it came from the primary and secondary vertex are calculated, using impact parameter and kinematic information. As in the ALEPH tag, these tracks are then combined in decreasing order of secondary vertex probability until the charm-hadron mass is exceeded, and the secondary vertex probability of the last track added is used as input to the main neural network. The neural network output is signed according to the sign of L, preserving the 'folding' symmetry of the simple L/σ_L tag and allowing the light quark background to be subtracted (see Figure 5.3).

The b-tag performance of SLD and the LEP experiments at their R_{b} working points are shown in table 5.2.

5.2.3 Lepton tagging

The semi-leptonic decays of heavy quarks provide a particularly clean signature that was the basis of the first methods used to identify the flavour composition of jets. Due to the hard fragmentation and the large mass, leptons from b-decays are characterised by large total and transverse momenta. Leptons from c-decays also have high momentum, but a significantly smaller transverse momentum. The charge of the lepton from a b- or c-decay is correlated to the charge of the decaying quark. Therefore in the asymmetry measurements the lepton tag can be used simultaneously to tag the quark flavour and to distinguish between the quark and the antiquark. b- and c-quarks decay semileptonically into either electrons or muons with approximately equal branching fractions of about 10%. The dominant semi-leptonic decay modes are $\mathrm{b} \to \ell^-$and $\mathrm{c} \to \ell^+$. While the lepton always carries the sign of the parent quark charge, for the c-quark the decay of a fermion gives rise to an anti-fermion, rather than a fermion. Due to the fermion / anti-fermion flip in the case of c- but not b-quarks, and because the sign of the two quark asymmetries is the same this leads to a large sensitivity of the asymmetry measurements with leptons to the sample composition. Apart from these three main sources there are also some other sources with different charge correlations, mainly $\mathrm{b} \to \overline{\mathrm{c}} \to \ell^-$, $\mathrm{b} \to \tau^- \to \ell^-$ and $\mathrm{b} \to (J/\psi, \psi') \to \ell\ell$. In addition there are misidentified hadrons and electrons from photon conversion.

The transverse momentum, p_t, of the decay lepton with respect to the decaying hadron direction is limited to half the hadron mass. The direction of the jet containing the lepton, which experimentally serves as the reference for measuring p_t provides a good approximation of the hadron direction. Since b-quarks fragment harder than c-quarks, additional separation power is given by the lepton momentum. Figure 5.5 shows the muon p and p_t spectrum from

L3 compared to the simulation of the different sources. $b \to \ell$ can be separated cleanly with a simple cut on p_t. However the other sources overlap strongly and can only be separated on a statistical basis.

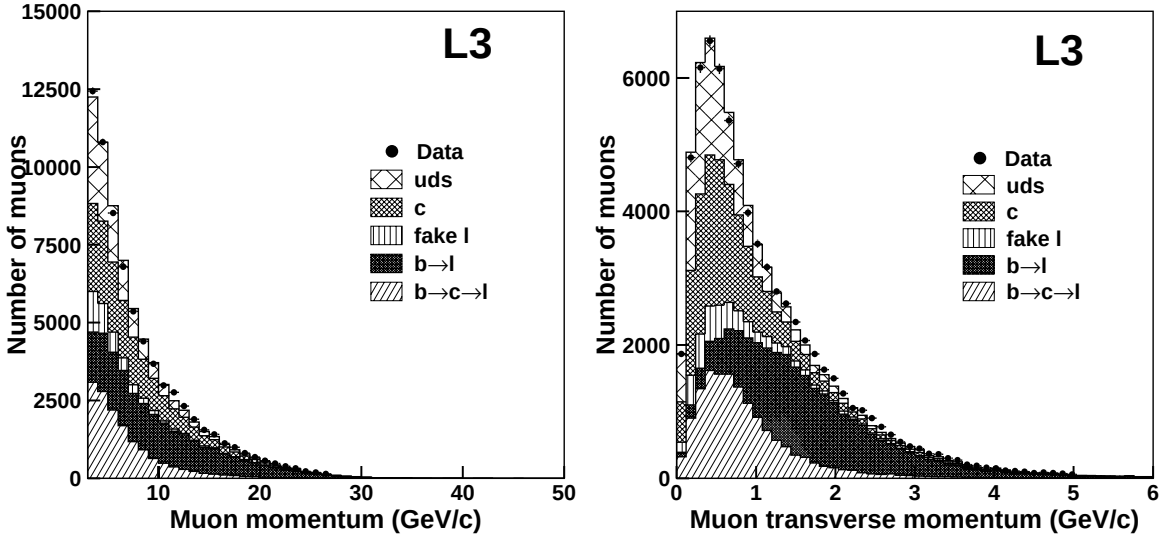

Figure 5.5: Muon momentum and transverse momentum spectra obtained by L3, together with simulation expectations of the contributions from the various sources.

5.2.4 D-meson tags

Since charmed hadrons are only rarely produced during light quark fragmentation, their presence tags c-quarks coming either from the primary Z-decay or from decay products of a b-quark. Charmed hadrons from a primary c-quark have on average a higher momentum than those from a b-decay (see Figure 5.6). In addition, decay length information can be used to separate the two sources.

At LEP and SLD the weakly decaying charmed hadrons D^0, D^+, D_s and Λ_c can be reconstructed in particular exclusive final states (see Figure 5.7). The charm tagging efficiency is limited by the low branching fractions for these decay modes, which are typically only a few percent. The decay $D^{*+} \to \pi^+ D^0$ can be reconstructed particularly cleanly, due to the small mass difference $\Delta m = m_{D^{*+}} - m_{D^0}$, which leads to a characteristic narrow peak with little background, as shown in Figure 5.8. Because of the good resolution, even D^0 decays which are not fully reconstructed, such as $D^0 \to \ell\nu X$ or $D^0 \to K^-\pi^+\pi^0$, where the π^0 is not seen, can be used.

The decay $D^{*+} \to \pi^+ D^0$ can also be tagged inclusively without specifically recognising any of the decay products of the D^0. The small mass difference between the D^{*+} and D^0 and the low mass of the pion result in a very low pion momentum in the D^{*+} rest-frame. Therefore in the laboratory frame the pion closely follows the D^{*+} direction and has a very low transverse momentum, p_t, with respect to the jet direction. As shown in Figure 5.9, the number of D^{*+} in a sample can thus be measured from the excess in the p_t^2 spectrum at very low values. Because of the large background, this tag is typically used only in conjunction with other tags.

The flavour of D-mesons also measures the flavour of the original quark. In $c\bar{c}$-events the primary quark is directly contained in the D-meson, while in $b\bar{b}$-events the c-quark is coming

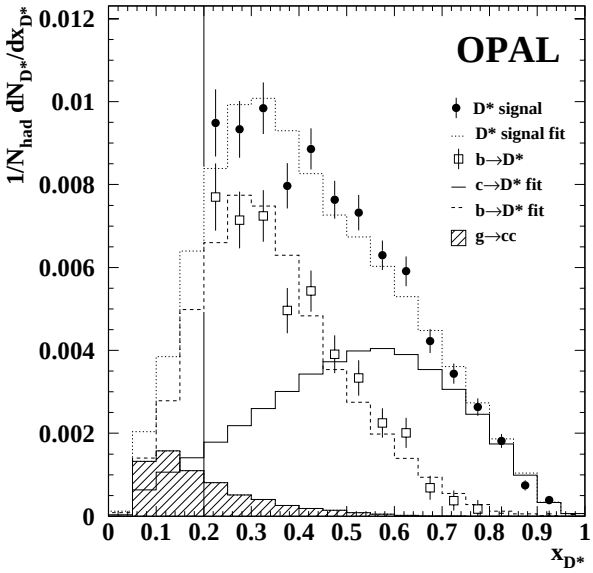

Figure 5.6: $D^{*\pm}$ momentum spectrum for all events and for $b\overline{b}$ and $c\overline{c}$ events from OPAL normalised to the beam energy after subtraction of combinatorial background.

from the decay chain $b \to c$. The decay $b \to \bar{c}$ (via $b \to cW^-, W^- \to \bar{c}s$) is strongly suppressed, so that the quark flavour tag using D-mesons in basically unique, contrary to the lepton tag, where the $b \to \ell^-$ and $b \to c \to \ell^+$ decays have to be separated. Also with D-mesons one separates directly the quark from the antiquark and not positively from negatively charged quarks as in the lepton case, so that the sensitivity of the asymmetry measurements to the sample composition is largely reduced. Since the absolute efficiency cancels in the asymmetries many different states can be used. Because of the low background the most sensitive decay, however, is $D^{*+} \to \pi^+ D^0$ with $D^0 \to K^-\pi^+$.

5.3 Partial width measurements

In principle, the rate measurements only require a selection of the flavour q from hadronic events with a tag that has efficiencies and purities known to a high precision and then simply count the fraction of tagged events. This "single-tag" approach has been adopted in some of the R_c measurements.

With an effective tag, where the efficiency for the tagging flavour is much larger than for the background flavours, the sensitivity to the background efficiencies is small, generally enabling a sufficient understanding of them to be achieved. However the high sensitivity to the tagging efficiency makes it difficult to obtain a sufficiently precise understanding, motivating the so called double tag methods. These methods use tags based on information from single hemispheres of events enabling comparisons between single and double tag rates to be made which provide the additional information needed to make a simultaneous determination of the tagging efficiency and the quark rate.

A summary of all individual measurements of R_b and R_c, used in the combination is given in Appendix A.

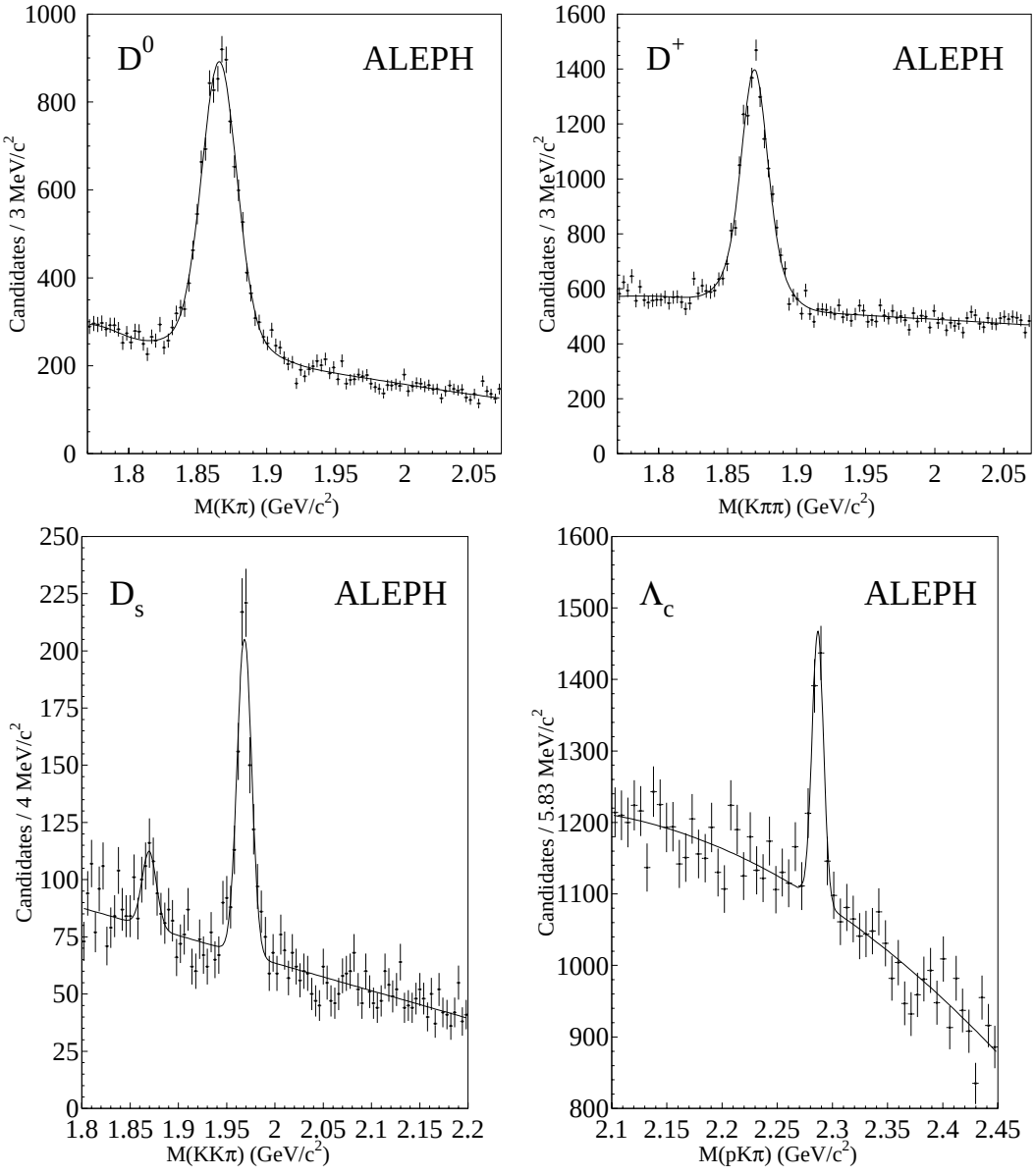

Figure 5.7: Mass spectra for $D^0 \to K^-\pi^+$, $D^+ \to K^-\pi^+\pi^+$, $D_s \to K^+K^-\pi^+$ and $\Lambda_c \to pK^-\pi^+$ obtained by ALEPH.

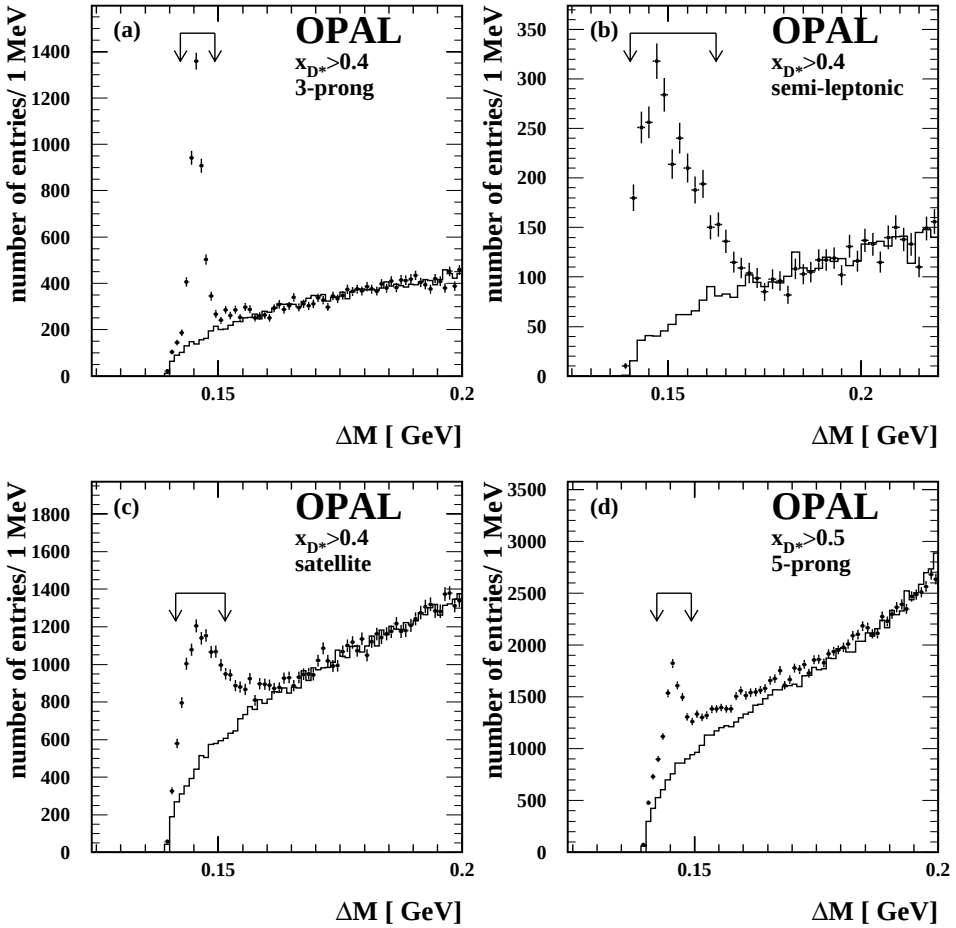

Figure 5.8: $\mathrm{m}(K^-\pi^+) - \mathrm{m}(K^-\pi^+\pi^+)$ mass difference spectrum from OPAL in different channels. In the plot labelled "satellite" the decay mode $\mathrm{D}^0 \to K^-\pi^+\pi^0$ is used, where the π^0 is not reconstructed. This $\mathrm{K}^-\pi^+$ mass peak is enhanced due to the large polarisation of the intermediate ρ^+ produced in the $\mathrm{D}^0 \to \mathrm{K}^-\rho^+ \to \mathrm{K}^-\pi^+\pi^0$ decay.

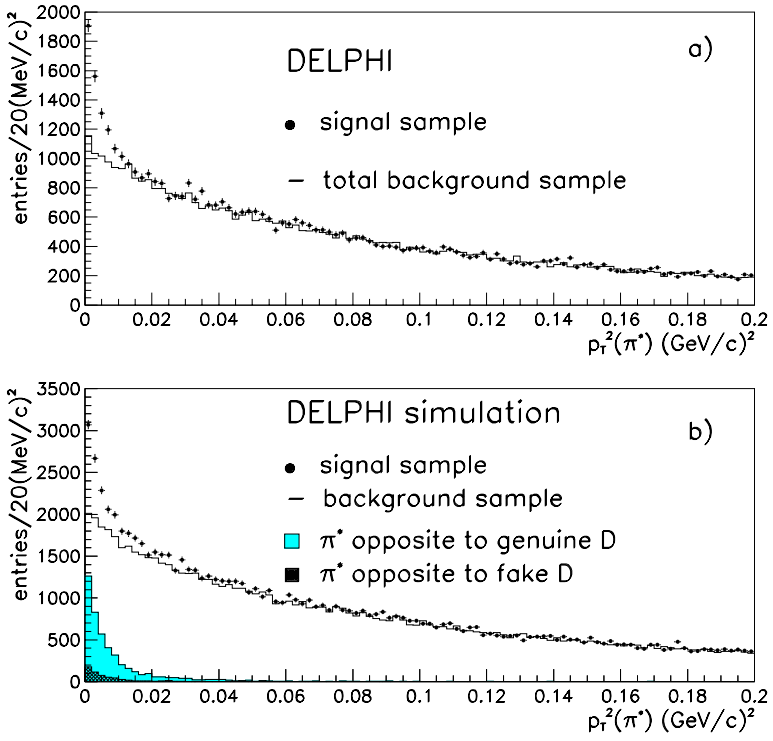

Figure 5.9: p_t spectrum opposite a high energy $D^{*\pm}$ for pions with the opposite (points) and same (histogram) sign as the $D^{*\pm}$. The data is shown in a) and the simulation in b), with the signal component indicated separately.

5.3.1 R_b measurements

The double tag method

All precise measurements of R_b are primarily based on counting events with either one or both hemispheres tagged. The fraction of hemispheres which are b-tagged f_s and the fraction of events where both hemispheres are tagged f_d are given by:

$$\begin{aligned} f_s &= \varepsilon_b R_b + \varepsilon_c R_c + \varepsilon_{uds}(1 - R_b - R_c) \\ f_d &= \varepsilon_b^{(d)} R_b + \varepsilon_c^{(d)} R_c + \varepsilon_{uds}^{(d)}(1 - R_b - R_c)\,, \end{aligned} \tag{5.2}$$

where ε_f is the hemisphere tagging efficiency for flavour f. The double tagging efficiency $\varepsilon_f^{(d)}$ can be written as

$$\varepsilon_f^{(d)} = (1 + \mathcal{C}_f)\varepsilon_f^2 \tag{5.3}$$

where the correction factor $\mathcal{C}_f \neq 0$ accounts for the fact that the two hemispheres in an event are slightly correlated. For the pure b-tags $\mathcal{C}_c$ and $\mathcal{C}_{uds}$ can be safely neglected. Neglecting all hemisphere correlations and background one has $R_b = f_s^2/f_d$, independent of the b-tagging efficiency ε_b which then does not need to be determined from simulation. In reality, corrections dependent on the background efficiencies ε_c, ε_{uds} and hemisphere correlations $\mathcal{C}_b$ must be applied and these have to be determined from Monte Carlo. The uncertainties on these parameters are included in the systematic errors. The effect of an uncertainty $\Delta\varepsilon_x$ from a background source x is approximately given by $\Delta R_b = 2\frac{\Delta\varepsilon_x}{\varepsilon_b} R_x$ and for an uncertainty on the correlation

by $\Delta R_{\rm b} = \Delta\mathcal{C}_b R_{\rm b}$. Therefore it is essential to develop a high efficiency and high purity b-tag to enable the double tag scheme to achieve the necessary statistical and systematic precision. Details about the hemisphere correlations are explained in section 5.6.7.

OPAL [113] and SLD [114] measure $R_{\rm b}$ with the double-tag technique using a single tagging method, OPAL with a logical OR of secondary vertex and lepton tags and SLD with only their neural network improved vertex mass tag.

The multi tag method

In the double tag method, hemispheres are tagged simply as b or non-b. This leads to two equations and five unknowns, $R_{\rm b}$, $R_{\rm c}$, $\varepsilon_{\rm c}$, $\varepsilon_{\rm uds}$ and $\mathcal{C}_b$. Three of them ($\varepsilon_{\rm c}$, $\varepsilon_{\rm uds}$ and $\mathcal{C}_b$) are taken from simulation and $R_{\rm c}$ is fixed. The $R_{\rm c}$-dependence is then accounted for in the systematic error of the experimental publications and in the combination procedure described in section 5.8. The method can be extended by adding more tags, *e.g.* additional b-tags with lower purity, or charm and light flavour tags [115]. The tags are made exclusive, such that each hemisphere is counted as tagged by only one tag method, and the untagged hemispheres are counted as an extra 'null' tag.

With T separate hemisphere tags, there are then $T(T+1)/2$ double tag fractions f_d^{ij} $(i,j = 1,T)$, given (analogously with Equations 5.2) by:

$$f_d^{ij} = \varepsilon_{\rm b}^i\varepsilon_{\rm b}^j(1+\mathcal{C}_{\rm b}^{ij})R_{\rm b} + \varepsilon_{\rm c}^i\varepsilon_{\rm c}^j(1+\mathcal{C}_{\rm c}^{ij})R_{\rm c} + \varepsilon_{\rm uds}^i\varepsilon_{\rm uds}^j(1+\mathcal{C}_{\rm uds}^{ij})(1-R_{\rm b}-R_{\rm c})\,, \tag{5.4}$$

where ε_f^i is the hemisphere tagging efficiency for flavour f with tag i, and $\mathcal{C}_{\rm f}^{ij}$ is the hemisphere correlation coefficient for tagging an event of flavour f with tag i in one hemisphere and j in the other. The single tag rates don't give additional information in this case, since they can be written as sums over the appropriate double tag fractions.

With T tags and F event types, there are $F(T-1)$ unknown efficiencies $\varepsilon_{\rm q}^j$ (since the T efficiencies for each flavour must add up to one) and $F-1$ unknown partial widths ratios R_f. If all the correlation coefficients $\mathcal{C}_{\rm f}^{ij}$ are taken from simulation, that leaves $F(T-1)+(F-1) = TF-1$ unknowns to be determined from $T(T+1)/2-1$ independent double tag rates f_d^{ij}. With $F=3$ event types (b, c, uds), the minimum number of tags for an over-constrained system is six.

ALEPH [116,117] and DELPHI [118] both use this multitag method for measuring $R_{\rm b}$. The six tags used are: three b-tags with different purities, a charm tag, a light quark tag and the "untagged" hemispheres. However, even with these six tags, the solution for all efficiencies and partial widths is still not well determined. This problem is solved by exploiting the very high purity of the primary b-tag, taking the small background efficiencies for charm and light quark events from Monte Carlo, as in the simple double tag analysis. $R_{\rm c}$ is also fixed to its Standard Model value.

If the primary b-tag has the same efficiency and purity as in the double tag method, the statistical error is reduced, since the auxiliary b-tags also contribute to the measurement of $R_{\rm b}$, their backgrounds being measured by the charm and light quark tags. The systematic error due to the backgrounds in the primary b-tag stays the same as in the double tag method. It can be reduced by changing the working point of the primary b-tag towards higher purity, thus sacrificing some of the gain in statistical error. Many additional hemisphere correlations have to be estimated from Monte Carlo, but the impact of the most important, between two hemispheres tagged with the primary b-tag, is reduced. The total systematic uncertainty from hemisphere correlations is therefore almost unchanged.

L3 [119] also use a multitag analysis for R_b, but with only two tags, based on lifetime and leptons, and determine the background efficiencies for both tags from simulation. The b-tagging efficiency for the lepton tag is used to provide a measurement of the semileptonic branching fraction BR($b \to \ell^-$).

5.3.2 R_c measurements

For R_c the situation is more complicated than for R_b. Especially at LEP the c-tags are less efficient and less pure than the b-tags. To obtain the optimal R_c precision under these circumstances a variety of methods has been derived.

Double tag measurements

In the normal double tag analyses the statistical error is determined by the size of the double tagged sample, which is proportional to the square of the tagging efficiency. Thus only SLD is able to present a high precision R_c measurement with the normal double tagging technique [120]. The charm tag is based on the same neural network used for the b tag. An output value of the network greater than 0.75 is considered a b tag and a value below 0.3 a charm tag. In addition two intermediate tags are introduced covering values from 0.3 to 0.5 and 0.5 to 0.75. The charm tag has an efficiency of 18% at a purity of 85%. The tag has a very low uds-background, which can be estimated reliably from simulation. The b-background is relatively high, but can be measured accurately in hemispheres opposite a high purity b-tag. R_c is extracted from a simultaneous fit to the count rates of the 4 different tags. The b and charm efficiencies are fitted from data.

ALEPH also presents a double tag measurement of R_c using fully reconstructed D-mesons. However due to the small branching fractions the efficiency is low and the statistical error relatively large [121].

Inclusive/exclusive double tags

At LEP more precise results can be obtained with the inclusive/exclusive double tag method. In the first step $R_c P(c \to D^{*+}) \times BR(D^{*+} \to \pi^+ D^0)$ is measured from a sample of exclusively reconstructed D^{*+} (the 'exclusive tag'). In the second step $P(c \to D^{*+}) \times BR(D^{*+} \to \pi^+ D^0)$ is obtained using an inclusive D^{*+} tag where only the charged pion from the D^{*+} decay is identified (see section 5.2.4). A fit is made to the π^- p_t spectrum in hemispheres tagged as containing a charm quark using a high energy D^{*+} reconstructed in the other hemisphere of the event. The uds background in this tagged charm sample is estimated from the sidebands in the mass spectra of the high energy D^{*+}, and the b-background is measured using lifetime tags and the D^{*+} momentum distribution. The fragmentation background under the low p_t pion D^{*+} signal can be estimated by exploiting the charge correlation between the pion and the D^* in the opposite hemisphere. Genuine signal pions have the opposite charge to that of the D^*, while background pions can have either charge (see Figure 5.9).

In this method the reconstruction efficiency for the D^0 and the relevant decay branching fraction (normally $D^0 \to K^-\pi^+$) still need to be known from simulation or external measurements. However the probability that a c-quark fragments into a D^{*+}, which is hard to calculate, is measured from the data. ALEPH [121], DELPHI [122, 123] and OPAL [124] present such inclusive/exclusive double tag measurements. DELPHI and OPAL give both R_c

and $P(c \to D^{*+}) \times BR(D^{*+} \to \pi^+ D^0)$ as results while ALEPH does the unfolding internally and presents only R_c.

Charm counting

Another method for measuring R_c is known as charm counting. All charm quarks finally end up in a weakly decaying charmed hadron. The production rate of a single charmed hadron D_i is proportional to $R_c f(D_i)$, where $f(D_i)$ is the fraction of charm quarks that eventually produce a D_i. However if all weakly decaying charmed hadrons can be reconstructed, the constraint $\sum_i f(D_i) = 1$ can be exploited and R_c can be measured without the unknown fragmentation probabilities $f(D_i)$. In practice D^0, D^+, D_s and Λ_c are reconstructed and small corrections for unmeasured strange charmed baryons have to be applied:

$$f(D^0) + f(D^+) + f(D_s) + (1.15 \pm 0.05) f(\Lambda_c) = 1\,. \tag{5.5}$$

The background from b-decays is determined using lifetime tags and the momentum of the reconstructed charmed hadrons. The efficiency to reconstruct a given decay channel has to be taken from simulation. As a by-product these measurements obtain the production rates of the weakly decaying charmed hadrons $f(D_i)$, which are needed to calculate the charm tagging efficiency of the lifetime b-tags. ALEPH [125], DELPHI [123] and OPAL [126] present a charm counting R_c analysis. The method is however limited by the knowledge of the decay modes used, especially for the D_s and the Λ_c.

Lepton tag

ALEPH also measures R_c with leptons [121]. They measure the lepton total and transverse momentum spectrum and subtract the contribution from b decays. This is determined from the lepton spectra measured in b events tagged in the opposite hemisphere by a lifetime-based b-tag. The result is proportional to $R_c BR(c \to \ell^+)$, where $BR(c \to \ell^+)$ is measured by DELPHI [122] and OPAL [127] in charm events tagged in the opposite hemisphere by a high energy D^{*+}.

5.4 Asymmetry measurements

The forward backward asymmetry for a quark flavour q is defined as

$$A_{FB}^{q\overline{q}} = \frac{\sigma_F^q - \sigma_B^q}{\sigma_F^q + \sigma_B^q}\,, \tag{5.6}$$

where the cross sections are integrated over the full forward (F) and backward (B) hemisphere. The differential cross section with respect to the scattering angle is given by

$$\frac{\partial \sigma^q}{\partial \cos\theta} = \sigma_{tot}^q \left[\frac{3}{8}\left(1 + \cos^2\theta\right) + A_{FB}^{q\overline{q}} \cos\theta\right]\,. \tag{5.7}$$

This dependence can be used to correct for a non-uniform efficiency or can be fitted directly to the data. The asymmetry at a quark production angle θ can be written as

$$A_{FB}^{q\overline{q}}(\cos\theta) = \frac{8}{3} A_{FB}^{q\overline{q}} \frac{\cos\theta}{1 + \cos^2\theta}\,. \tag{5.8}$$

Most experimental analyses measure $A_{\rm FB}^{\rm q\overline{q}}(\cos\theta)$ and then use Equation (5.8) to fit $A_{\rm FB}^{\rm q\overline{q}}$. This is statistically slightly more powerful than simple event counting and all angular dependent efficiencies cancel.

To define the direction θ the thrust axis of the event is used, signed by the charge tagging methods described in the following. The thrust axis is infrared and collinear stable, so that it can be calculated in perturbative QCD and it is relatively insensitive to fragmentation effects.

In order to measure a quark asymmetry two ingredients are needed. The quark flavour needs to be tagged and the quark has to be separated from the antiquark. For the flavour tagging the methods described in section 5.2.1-5.2.4 can be used. For the charge tagging essentially five methods are in use: leptons, D-mesons, jet-charge, vertex-charge and kaons. Some analyses also combine the information from the different methods.

In any analysis the measured asymmetry is given by

$$A_{\rm FB}^{\rm meas} = \sum_{\rm q}(2\omega_{\rm q}-1)\eta_{\rm q}A_{\rm FB}^{\rm q\overline{q}}\,, \tag{5.9}$$

where $\eta_{\rm q}$ is the fraction of $\rm q\overline{q}$ events in the sample, $\omega_{\rm q}$ is the probability to tag the quark charge correctly and the sum is taken over all quark flavours.

As an example, Figure 5.10 shows the reconstructed $\cos\theta$ distribution from the ALEPH $A_{\rm FB}^{\rm b\overline{b}}$ and $A_{\rm FB}^{\rm c\overline{c}}$ measurement with leptons. The asymmetry of about 10% for $A_{\rm FB}^{\rm b\overline{b}}$ and 6% for $A_{\rm FB}^{\rm c\overline{c}}$ can clearly be seen.

The SLD experiment measures the forward-backward-left-right asymmetry, defined as

$$A_{\rm FBLR}^{\rm q\overline{q}} = \frac{1}{\mathcal{P}}\frac{\sigma_{\rm L,F}^{\rm q}-\sigma_{\rm L,B}^{\rm q}-\sigma_{\rm R,F}^{\rm q}+\sigma_{\rm R,B}^{\rm q}}{\sigma_{\rm L,F}^{\rm q}+\sigma_{\rm L,B}^{\rm q}+\sigma_{\rm R,F}^{\rm q}+\sigma_{\rm R,B}^{\rm q}}\,, \tag{5.10}$$

where L,R denote the cross sections with left- and right-handed beams and $\mathcal{P}$ is the beam polarisation. Equation (5.7) is separately valid for left- and right polarised beams, so that equation (5.8) is also valid for $A_{\rm FBLR}^{\rm q\overline{q}}$. As for $A_{\rm FB}^{\rm q\overline{q}}$ the total tagging efficiencies and the luminosity drops out of the calculation of $A_{\rm FBLR}^{\rm q\overline{q}}$. However, the luminosity ratio for the two polarisation states needs to be known.

$A_{\rm FBLR}^{\rm q\overline{q}}$ is a direct measurement of the quark asymmetry-parameter $\mathcal{A}_{\rm q}$, unlike $A_{\rm FB}$, which is proportional to the product of electron and the quark asymmetry-parameter. Figure 5.11 shows the angular distribution from the SLD vertex charge analysis with polarised beams. Here the asymmetries are much larger due to the beam polarisation of 0.75 compared to $\mathcal{A}_{\rm e}$ of 0.15.

5.4.1 Lepton and D-meson measurements

As described in sections 5.2.3 and 5.2.4 leptons and D-mesons simultaneously provide flavour and charge tagging. A simple cut on the lepton transverse momentum provides good enhancement of $\rm b\to\ell$, as seen in Figure 5.5. Table 5.3 provides an example of sample compositions for the ALEPH lepton sample with a transverse momentum cut of $p_t > 1.25$GeV together with the correlation between the lepton charge and decaying quark charge. The quark charge at production is however the relevant quantity for the asymmetry determination, requiring correction for the effects of $\rm B^0\overline{B^0}$ mixing via the integrated mixing parameter $\overline{\chi}$.

To enhance the sensitivity of lepton-based analyses to $A_{\rm FB}^{\rm c\overline{c}}$, the experiments use additional information like lifetime tagging, jet charge in the opposite hemisphere or hadronic information from the lepton jet. Also tagging D-mesons provides a relatively pure charm sample after a momentum cut and additional b-tagging requirements are used to enhance the sensitivity to $A_{\rm FB}^{\rm b\overline{b}}$.

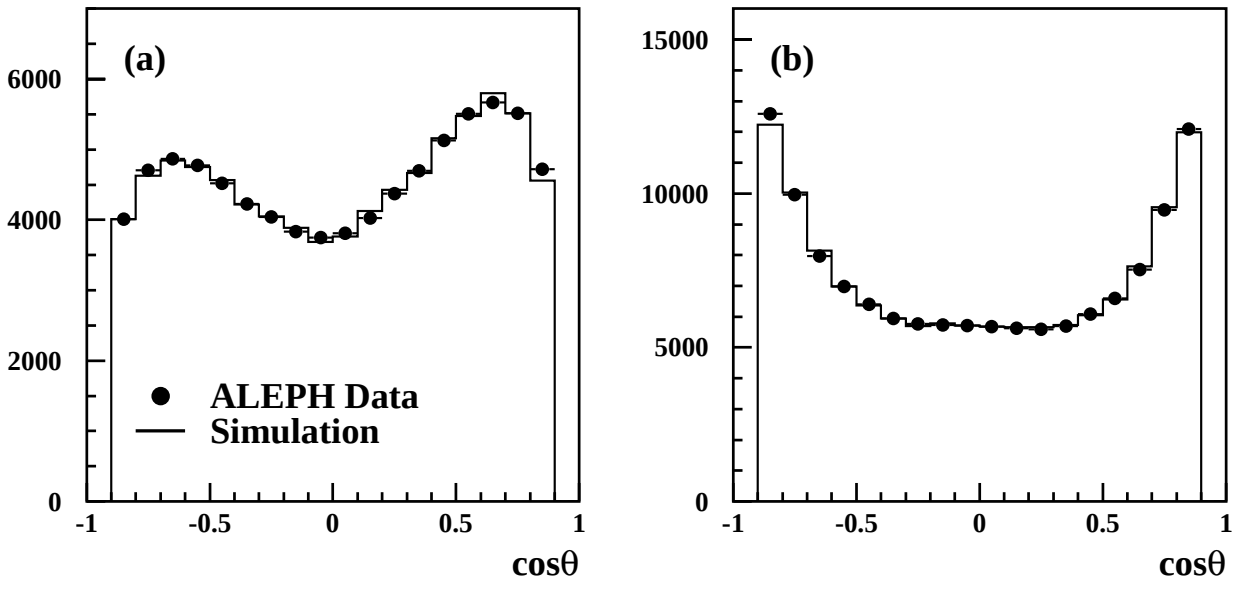

Figure 5.10: Reconstructed $\cos\theta$ distribution from the ALEPH b-asymmetry measurement with leptons for a) the b-enriched and b) the c-enriched sample.

Lepton source	charge correlation	fraction for $p_t > 1.25$GeV
$b \to \ell^-$, $b \to \overline{c} \to \ell^-$	1	0.795
$b \to c \to \ell^+$	-1	0.046
$c \to \ell^+$	1	0.048
background	weak	0.111

Table 5.3: Correlation between the lepton charge and the quark charge at decay time. The sample composition for $p_t > 1.25$GeV in the ALEPH lepton sample is also shown.

In both cases the sample composition is usually taken from simulation. For the lepton tag analyses the uncertainties on the sample composition due to the modelling of the semileptonic decays are generally rather large. Therefore, in addition to the asymmetries, the experiments measure the $B^0\overline{B^0}$ effective mixing parameter $\overline{\chi}$, the prompt and cascade semileptonic branching fraction of the b-hadrons BR($b \to \ell^-$) and BR($b \to c \to \ell^+$) and the prompt semileptonic branching fraction of the c-hadrons BR($c \to \ell^+$). If the same analysis cuts are used in both cases, these auxiliary measurements serve as an effective parametrisation of the lepton spectrum, greatly reducing the modelling errors.

In the case of the D-meson analyses the fragmentation function for D-mesons from b- and c-quarks is measured from data. However, there is only one important source of D-mesons per quark flavour, and the correlation between the quark flavour and the D-meson flavour is the same for b- and c-quarks, so that the sign of the D-meson asymmetry for the two quark species is the same. For these reasons the sensitivity to the sample composition is much smaller than in the lepton case.

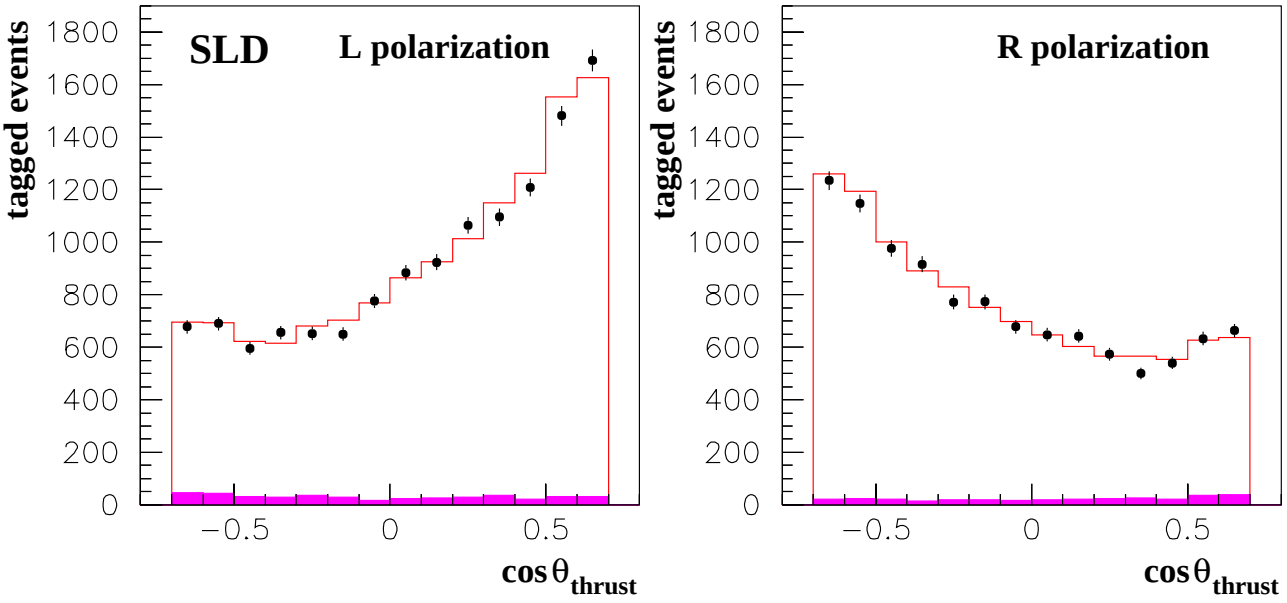

Figure 5.11: Reconstructed $\cos\theta$ distribution from the SLD vertex charge analysis with left- and right-handed beam polarisation.

5.4.2 Jet and vertex charge

The average charge of all particles in a jet, or jet charge, retains some information on the original quark charge. Usually the jet charge is defined as:

$$Q_h = \frac{\sum_i q_i p_{\parallel i}^{\kappa}}{\sum_i p_{\parallel i}^{\kappa}}, \tag{5.11}$$

where the sum runs over all charged particles in a hemisphere with charge q_i and longitudinal momentum with respect to the thrust axis $p_{\parallel i}$, and κ is a tunable parameter with typical values between 0.3 and 1.

For B- and D-mesons the meson charge is correlated to the flavour of the b- or c-quark. If all charged particles of a jet can be uniquely assigned to the primary or the decay vertex, the charge sum of the decay vertex, if non zero, uniquely tags the quark charge. At SLD the b-asymmetry measurement with vertex charge is the most precise measurement of this quantity. At LEP the vertex charge has also been used in conjunction with other tags, however the impact parameter resolutions at LEP limit the efficiencies in comparison with SLD.

For both charge tagging methods, it is difficult estimate the charge tagging efficiency from simulation due to uncertainties from fragmentation and B-decays. However, the efficiency can be obtained reliably from data using double tags. If in a cut based analysis ω_q is the efficiency to tag the quark charge correctly in a pure sample of q-quarks, the fraction of same sign double tags in the sample of all double tags is given by

$$f_{SS} = 2\omega_q(1-\omega_q), \tag{5.12}$$

apart from small corrections due to hemisphere correlations. Equation 5.12 can then be used to obtain ω_q. Corrections from background and hemisphere correlations are obtained from simulation.

Since the charge tagging efficiency for the jet charge is rather modest, a statistical method to extract the asymmetry is usually used. With $Q_{\mathrm{F/B}}$ being the jet charge of the forward/backward hemisphere and $Q_{\mathrm{q/\overline{q}}}$ the jet charge of the quark/antiquark hemisphere, one has

$$\begin{aligned} \langle Q_{\mathrm{FB}} \rangle &= \langle Q_{\mathrm{F}} - Q_{\mathrm{B}} \rangle \\ &= \delta_{\mathrm{q}} A_{\mathrm{FB}}^{\mathrm{q\overline{q}}} \\ \delta_{\mathrm{q}} &= \langle Q_{\mathrm{q}} - Q_{\bar{\mathrm{q}}} \rangle \,, \end{aligned} \tag{5.13}$$

for a pure sample of $\mathrm{q\overline{q}}$-events. The resolution parameter δ_{q} can be measured from data using[‡]

$$\left(\frac{\delta_{\mathrm{q}}}{2}\right)^2 = \frac{\langle Q_{\mathrm{F}} \cdot Q_{\mathrm{B}} \rangle + \rho_{\mathrm{q\overline{q}}} \sigma(Q)^2 + \mu(Q)^2}{1 + \rho_{\mathrm{q\overline{q}}}}, \tag{5.14}$$

where $\mu(Q)$ is the mean value of Q for all hemispheres and $\sigma(Q)$ its variance. $\mu(Q)$ is slightly positive due to an excess of positive particles in secondary hadronic interactions. The hemisphere correlations, $\rho_{\mathrm{q\overline{q}}}$, arise from charge conservation, hard gluon radiation and some other small effects and have to be taken from simulation.

The analyses select a relatively pure sample of $\mathrm{b\overline{b}}$ events using lifetime tagging techniques. Light quark background is always subtracted using Monte Carlo simulation. The charge separation for charm is either taken from Monte Carlo or determined by performing the analysis in bins of different b-purities and fitting δ_{b} and δ_{c} from the data. It should be noted that dilution due to $\mathrm{B^0\overline{B^0}}$-mixing is completely absorbed into the measured δ_{b}. Effects from gluon radiation are also included to a large extent, so that the residual QCD correction is very small.

The above formalism can be generalised to any variable sensitive to the quark charge, including the combination of several different charge tagging techniques. As an example Figure 5.12 shows the charge tagging from ALEPH, which combines jet charge, vertex charge and charged kaon information using a neural net to reach almost perfect tagging at high Q_{FB} values.

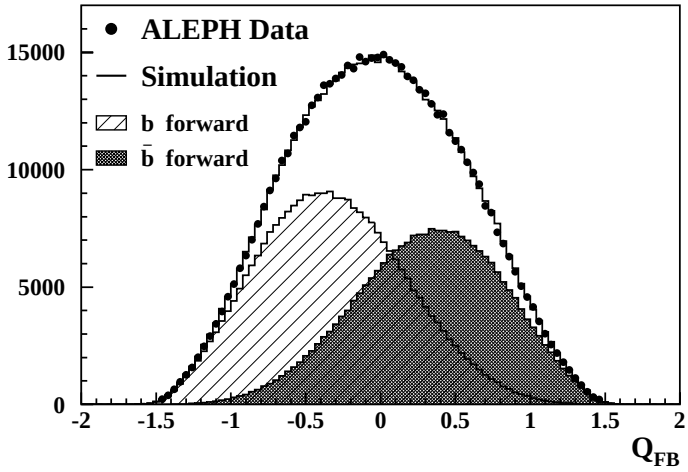

Figure 5.12: Charge separation of the ALEPH neural net tag using jet charge, vertex charge and charged kaons. The asymmetry reflects $A_{\mathrm{FB}}^{\mathrm{b\overline{b}}}$ diluted by the non-perfect charge tagging.

[‡]The exact formulae used by the experiments vary slightly, however the general formalism is identical.

5.4.3 Kaons

Charged kaons from b- and c-decays are also sensitive to the quark flavour, via the decay chain (b $\rightarrow$)c $\rightarrow$ s. Only kaons with large impact parameters are used, to suppress those produced in the fragmentation process, As with other methods, the charge tagging efficiency is measured using the double tag technique.

In the SLD measurements of asymmetries using kaons, only identified kaons coming from a secondary vertex are used. For the A_b measurement with kaon insufficient statics are available to do a self calibration and the charge tag efficiency is the dominant systematic error. In the measurement of A_c the kaon charge tag efficiency is cross-calibrated against the vertex charge tag efficiency.

5.4.4 Asymmetry measurements used in the combination

The forward-backward asymmetry measurements included in the average are:

- Lepton measurements from ALEPH [128], DELPHI [129], L3 [130] and OPAL [131]: L3 measures $A_{\rm FB}^{\rm b\overline{b}}$ only from a sample of high p_t leptons. ALEPH, DELPHI and OPAL measure $A_{\rm FB}^{\rm b\overline{b}}$ and $A_{\rm FB}^{\rm c\overline{c}}$ using leptons combined with lifetime tagging and some additional information. ALEPH adds properties of hadrons in the events and information from the missing energy due to escaping neutrinos. OPAL also uses hadronic properties while DELPHI includes the jet charge of the hemisphere opposite the lepton.

- Measurements of $A_{\rm FB}^{\rm b\overline{b}}$ based on lifetime tagged events with a jet charge measurement using the weight method (see Equation 5.13) from DELPHI [132], L3 [133] and OPAL [134] and a similar analysis from ALEPH [135] with a charge tag combining jet charge vertex charge and kaons in a neural net.

- Analyses with D-mesons from ALEPH [136], DELPHI [137] and OPAL [138]: ALEPH measures $A_{\rm FB}^{\rm c\overline{c}}$ only from a sample of high momentum D-mesons. DELPHI and OPAL measure $A_{\rm FB}^{\rm b\overline{b}}$ and $A_{\rm FB}^{\rm c\overline{c}}$ by fitting the momentum spectrum of the D-mesons and including lifetime information.

- A DELPHI analysis of $A_{\rm FB}^{\rm b\overline{b}}$ combining jet charge, vertex charge, kaons and some other variables sensitive to the b-quark charge in a neural net [139] using a cut on the charge estimator.

The left-right-forward-backward asymmetry measurements from SLD are directly quoted in terms of $\mathcal{A}_{\rm b}$ and $\mathcal{A}_{\rm c}$. The following results are included:

- Measurements of $\mathcal{A}_{\rm b}$ and $\mathcal{A}_{\rm c}$ using leptons [140, 141];

- A measurement of $\mathcal{A}_{\rm c}$ using D-mesons [142];

- A measurement of $\mathcal{A}_{\rm b}$ using jet charge [143];

- A measurement of $\mathcal{A}_{\rm b}$ using vertex charge [144];

- A measurement of $\mathcal{A}_{\rm b}$ using kaons [145];

- A measurement of $\mathcal{A}_{\rm c}$ using vertex charge and kaons [146].

All these measurements are listed in detail in Appendix A.

5.5 Auxiliary measurements

The measurements of the charmed hadron fractions $P(c \to D^{*+}) \times BR(D^{*+} \to \pi^+ D^0)$, $f(D^+)$, $f(D_s)$ and $f(c_{baryon})$ are included in the R_c analyses and are described there.

ALEPH [128,147], DELPHI [148], L3 [119,130,149] and OPAL [131,150] measure $BR(b \to \ell^-)$, $BR(b \to c \to \ell^+)$ and $\overline{\chi}$ or a subset from a sample of leptons opposite a b-tagged hemisphere and from a double lepton sample. DELPHI [122] and OPAL [127] measure $BR(c \to \ell^+)$ from a sample opposite a high energy $D^{*\pm}$. All the auxiliary measurements used in the combination are listed in Appendix A.

5.6 External inputs to the heavy flavour combination

All the measurements contributing to the electroweak fit require some input from simulated events. Quantities derived from the simulation are affected by uncertainties related to the modelling of the detector response, as well as by the limited knowledge of the physics processes that are simulated. These latter sources are common to all experiments, and they have to be treated as correlated when averaging individual results. Furthermore, in order to produce consistent averages, the input physics parameters or models used in the simulation must be the same for all analyses in all experiments.

The choice of the input physics parameters and models relevant for electroweak heavy flavour analyses is discussed below. Whenever possible measurements at LEP/SLD or at lower energies are used to constrain the models used in the simulations. The uncertainties due to the knowledge of the input parameters to the fitted partial widths and asymmetries can be seen from Table 5.9. If a parameters does not appear in Table 5.9 the error is negligible either because the parameter is relatively unimportant or because it is known very precisely.

In many cases the world averages of the Particle Data Group are used. They are consistently taken from the 1998 edition of the RPP [107]. It has been checked that updates published in the 2000 edition [76] do not change any of the results.

5.6.1 The heavy quark fragmentation

The process of hadron production is modelled as the convolution of a perturbative part (hard gluon radiation), and a non perturbative part, called fragmentation, described with phenomenological models.

In the JETSET [33] simulation the fragmentation model by Peterson *et al.* [151] is used, which describes the process in terms of the variable $z = (E + p_\parallel)_{\rm hadron}/(E + p_\parallel)_{\rm quark}$, where $p_\parallel$ is the momentum component in the direction of the fragmenting quark. The model contains one free parameter, ε_Q, which is tuned to reproduce a given value of the mean energy of the heavy hadrons produced. Such tuning depends on the cut-off used for the transition between the perturbative and the non-perturbative part, therefore ε_Q can not be given an absolute meaning. The energy spectrum is more conveniently described in terms of the variable x_Q, defined as the energy of the weakly-decaying hadron containing the heavy quark Q normalised to the beam energy.

The analyses quoted in Reference [152–156], which provide a value for the mean energy of b hadrons, are averaged obtaining:

$$\langle x_b \rangle = 0.702 \pm 0.008 \qquad (5.15)$$

where the error includes the uncertainty due to the modelling of the fragmentation function. This uncertainty is estimated by using the functional forms proposed by Collins and Spiller [157], and by Kartvelishvili *et al.* [158] as alternatives to Peterson *et al.* [151] when extracting $\langle x_b \rangle$.

The energy of charmed hadrons is measured in analyses which make use of lepton tags or inclusive reconstruction of D^0/D^+-mesons [126,153], and in analyses with full reconstruction of D^{*+}-mesons [159–161]. The former have a larger dependence on the modelling of the spectrum, while the latter need an additional correction to obtain the energy of the weakly-decaying hadron. In all cases the contribution from charmed hadrons produced by hard gluons splitting to heavy quarks is removed. The average energy of weakly-decaying c-hadrons is found to be

$$\langle x_c \rangle = 0.484 \pm 0.008 \tag{5.16}$$

which again includes the estimated uncertainty from the modelling of the spectrum.

5.6.2 Heavy quarks from gluon splitting

Hard gluons can occasionally split to heavy quark pairs. In several analyses these contributions need to be subtracted. In particular the uncertainty on the rate of gluons splitting to $b\overline{b}$ pairs is the single largest contribution to the systematic error on the R_b world average.

The rates $g_{c\bar{c}}$ and $g_{b\bar{b}}$ are defined as the number of hadronic Z decays containing a hard gluon splitting to a $c\overline{c}$ or $b\overline{b}$ pair, normalised to the total number of hadronic Z decays.

Measurements of $g_{b\bar{b}}$ rely on an inclusive lifetime-based tag applied to the jets reconstructed in the event [162], while measurements of $g_{c\bar{c}}$ make use of exclusive D^* reconstruction, final states containing leptons, or are based on the combination of event shape variables [125, 163, 164].

Averaging published results yields:

$$\begin{aligned} g_{c\bar{c}} &= 0.0296 \pm 0.0038\,, \\ g_{b\bar{b}} &= 0.00254 \pm 0.00051\,, \end{aligned} \tag{5.17}$$

with only a very small correlation between the two values.

5.6.3 Multiplicities in heavy flavour decays

Many analyses make use of inclusive b tagging methods which exploit the long lifetimes of b hadrons. The discrimination is based on the presence, in a jet, or a hemisphere, or the whole event, of charged tracks with significant impact parameter from the primary vertex of the events. Therefore the tagging efficiency is directly affected by the number of charged tracks produced in the long-lived hadron decay.

In R_b measurements the tag is applied to hemispheres, and the b efficiency is measured directly in the data from the fraction of events with both hemispheres tagged. The b charged multiplicity only enters through the hemisphere correlation, which is computed with the simulation. Measurements of the average b charged multiplicity performed at LEP are used. Results from lower energy experiments cannot be used because of the different b-hadron mixture.

However, the charm selection efficiency is taken from the simulation, at least for the samples with highest purity. It is therefore crucial to propagate correctly the uncertainty due to the decay charged multiplicities of the various charmed hadrons. This is done separately for each hadron species due to the significant differences in lifetimes.

The charm selection efficiency also depends on the number of neutral particles accompanying the charged particles in a given topological decay channel. The size of this effect depends on

how invariant mass cuts are implemented and might vary substantially in different analyses. The uncertainty is evaluated varying the K^0 and π^0 production rates in charmed hadron decays.

Average charged multiplicity in b hadron decays

Inclusive measurements of the mean b-hadron charged multiplicity at LEP [165] are combined to obtain:

$$\langle n_b^{ch} \rangle = 4.955 \pm 0.062 \ . \tag{5.18}$$

Particles coming from the decay of $B^{\star\star}$ or other possible excited b states are excluded; the result is also corrected to exclude charged particles originating from the decay of K^0 and Λ.

Charged multiplicities of c hadron decays

Inclusive topological branching fractions have been measured for D^0, D^+ and D_s [166]. For each species, each channel is varied within its uncertainty, except for the channel with the highest rate, which is used to compensate the variation. The resulting errors are combined using the corresponding correlation coefficients.

The values f_i of the branching fractions for the decays into i charged particles, the corresponding errors σ_i and correlation coefficients C_{ij} are given in Table 5.4.

D^0	$f_0 = 0.054$	$f_2 = 0.634$	$f_4 = 0.293$	$f_6 = 0.019$
	$\sigma_0 = 0.011$		$\sigma_4 = 0.023$	$\sigma_6 = 0.009$
	$C_{04} = 0.07$	$C_{46} = -0.46$	$C_{06} = 0$	
D^+	$f_1 = 0.384$	$f_3 = 0.541$	$f_5 = 0.075$	
	$\sigma_1 = 0.023$		$\sigma_5 = 0.015$	
	$C_{15} = -0.33$			
D_s	$f_1 = 0.37$	$f_3 = 0.42$	$f_5 = 0.21$	
	$\sigma_1 = 0.10$		$\sigma_5 = 0.11$	
	$C_{15} = -0.02$			

Table 5.4: Topological rates for the different charm-meson species, with estimated errors and correlation coefficients. The subscripts indicate the number of charged particles produced.

Neutral particle production in c hadron decays

The procedure to estimate the residual dependence of the lifetime tag efficiency on the average rate of neutral particles produced in charm decays is tailored, case by case, on the specific properties of the tag and based on the measurements available [107]. Although the procedures differ somewhat between experiments, the resulting estimated uncertainties are taken as fully correlated.

5.6.4 Heavy flavour lifetimes

The lifetimes of heavy hadrons are relevant to many analyses, in particular all those which make use of lifetime-based b tagging methods. As for the charged multiplicity, in the case of the R_b analyses charm lifetimes enter directly in the estimate of the charm contamination

in high purity samples, whereas b hadron lifetimes only affect the estimate of the hemisphere correlations.

Average b hadron lifetime

The average lifetime of b hadrons is taken to be [107]

$$\tau_b = 1.576 \pm 0.016 \text{ ps} , \tag{5.19}$$

which is obtained from analyses of fully inclusive b final states. The lifetime difference between b species has in general little impact in all analyses. It is considered as a source of uncertainty in the R_b analyses either by using the individual lifetimes [107] or by enlarging the error to 0.05 ps.

Lifetimes of c hadrons

The lifetimes of the different c hadron species are considered as individual sources of uncertainties. The values and errors are [107]

$$\begin{aligned} \tau(D^0) &= 0.415 \pm 0.004 \text{ ps} , \\ \tau(D^+) &= 1.057 \pm 0.015 \text{ ps} , \\ \tau(D_s) &= 0.467 \pm 0.017 \text{ ps} , \\ \tau(\Lambda_c) &= 0.206 \pm 0.012 \text{ ps} . \end{aligned} \tag{5.20}$$

5.6.5 Charmed hadron decays to exclusive final states

Charm counting measurements determine the production rates of individual c-hadron species by tagging exclusive final states, using the branching fraction for the appropriate decay mode as input. The values and errors used are [107, 167]:

$$\begin{aligned} \mathrm{BR}(D^0 \to K^-\pi^+) &= 0.0385 \pm 0.0009 , \\ \mathrm{BR}(D^+ \to K^-\pi^+\pi^+) &= 0.090 \pm 0.006 , \\ \mathrm{BR}(D_s^+ \to \phi\pi^+) &= 0.036 \pm 0.009 , \\ \frac{\mathrm{BR}(D_s^+ \to \bar{K}^{*0}K^+)}{\mathrm{BR}(D_s^+ \to \phi\pi^+)} &= 0.92 \pm 0.09 , \\ \mathrm{BR}(\Lambda_c \to pK^-\pi^+) &= 0.050 \pm 0.013 . \end{aligned} \tag{5.21}$$

5.6.6 Heavy flavour leptonic decays

Many analyses rely on semileptonic final states in order to tag the presence of heavy hadrons and possibly their charge. Assessing the performance of such tags involves estimating the rates of the different sources of lepton candidates in hadronic events, and modelling the kinematics of the leptons produced in the decay of heavy hadrons.

The rates for the major sources (direct decays, $\mathrm{b} \to \ell^-$ and $\mathrm{c} \to \ell^+$, cascade b decays, $\mathrm{b} \to \mathrm{c} \to \ell^+$) are measured at LEP, and included as fitted parameters. The modelling of the decay kinematics is a common source of systematic uncertainty. The rates for the other sources are taken from external measurements.

Modelling of direct semileptonic b decays

For the semileptonic decays of B^0- and B^+-mesons the CLEO collaboration has compared decay models to their data and measured the free parameters of the models. Based on the CLEO fits [168], the LEP experiments quote results for three different models.

- The model proposed by Altarelli *et al.* [169], is an extension of the free quark model which attempts to account for non-perturbative effects kinematically. The two free parameters of the model, the Fermi momentum of the constituent quarks inside the heavy meson and the mass of the final quark, are determined from CLEO data to be $p_{\mathrm{F}} = 298$ MeV/c, $m_c = 1673$ MeV/c^2.
- The form-factor model proposed by Isgur *et al.* [170], with the model prediction that 11% of semileptonic B-meson decays result in an L=1 charm-meson, $D^{\star\star}$.
- The same model with the rate of $D^{\star\star}$-mesons increased to 32%, as preferred by the CLEO data [168, 170].

The model of Altarelli *et al.* is used to derive the central values of the analyses, while the two others, which give respectively harder and softer lepton spectra, are used to give an estimate of the associated uncertainty.

Reweighting functions are constructed to adjust the lepton spectrum of semileptonic B^0 and B^+ decays in the LEP Monte Carlo samples to the three models based on CLEO data. For use in Z decays, the same reweighting functions have been assumed to be valid for the B_s-meson and b-baryons. This would be correct in the simplest spectator model, and is thought more generally to be adequate for the B_s. The baryons contribution is only about 10%, and no additional systematic error is assigned.

Modelling of direct semileptonic c decays

The measurements of DELCO [171] and MARK III [172] for D^0 and D^+ semileptonic decays have been combined and parameterised using the model of Altarelli *et al.* as a convenient functional form. The D boost and the experimental resolution are taken into account in the fit to the data. Based on this fit [173], the model parameters are fixed to $p_{\mathrm{F}} = 0.467$ GeV/c, $m_s = 0.001$ GeV/c^2 and they are varied to $p_{\mathrm{F}} = 0.353$ GeV/c, $m_s = 0.001$ GeV/c^2 and $p_{\mathrm{F}} = 0.467$ GeV/c, $m_s = 0.153$ GeV/c^2 to derive an estimate of the associated uncertainty. The reweighting functions derived from D^0 and D^+ decays are assumed to be valid for all charm hadrons.

Modelling of cascade semileptonic b decays

For the cascade decays, $b \to c \to \ell^+$, the three models used for $c \to \ell^+$ decays are combined with the measured $b \to D$ spectrum from CLEO [174] to generate three models for the lepton momentum spectrum in the rest frame of the b hadron. The CLEO $b \to D$ spectrum can be conveniently modelled by a Peterson function [151] with free parameter $\varepsilon = 0.42 \pm 0.07$. The effect of this $b \to D$ model uncertainty on the $b \to c \to \ell^+$ spectrum is negligible compared to the uncertainty from the $c \to \ell^+$ models.

The rate of $b \to \bar{c} \to \ell^-$ transitions

Several quantities related to the rate of leptons from c hadrons produced from the "upper vertex" in b-hadron decays have been measured. An estimate of this rate is therefore possible, based upon experimental results.

The inclusive and flavour-specific $B \to D$ and $B \to \Lambda_c^+$ rates measured at CLEO [175] are combined with the $B \to DD(X)$ rates measured in ALEPH [176] to extract the probabilities of producing the different c-hadrons from the upper vertex in b decays. These are combined with the c-hadron semileptonic branching fractions to obtain a value for the $BR(b \to \bar{c} \to \ell^-)$.

The estimate obtained is

$$BR(b \to \bar{c} \to \ell^-) = 0.0162\,^{+0.0044}_{-0.0036}\,. \tag{5.22}$$

Other semileptonic decays

The rate for $b \to \tau^- \to \ell^-$ decays is derived from existing measurements of $BR(b \to \tau)$ [177] combined with the τ leptonic branching fraction [107]. The procedure yields:

$$BR(b \to \tau^- \to \ell^-) = 0.00419 \pm 0.00055\ . \tag{5.23}$$

The rate for $b \to (J/\psi, \psi') \to \ell\ell$ decays is calculated from the production rate of J/ψ and ψ' in $Z \to b\bar{b}$ decays, and the J/ψ and ψ' leptonic branching fractions [107], yielding

$$BR(b \to (J/\psi, \psi') \to \ell\ell) = 0.00072 \pm 0.00006\ . \tag{5.24}$$

5.6.7 Hemisphere correlations in double-tag methods

In analyses where a b-tagging algorithm is applied in one hemisphere, the tagging efficiency can be measured from the data by comparing the fraction of hemispheres that are tagged and the fraction of events with both hemispheres tagged. However, the correlation between the tagging efficiencies in the two hemispheres, defined in Equation 5.3, must then be estimated from simulation. This is particularly crucial for the precise R_b double tag measurements.

There are basically three physics sources for such a correlation:

- detector inhomogeneities,
- the use of a common primary vertex,
- kinematic correlations, mainly due to gluon radiation.

Detector effects are easily controllable from the data by measuring the tagging rate as a function of jet direction and then folding the two hemispheres in an event. This error source is clearly uncorrelated between the experiments.

The second of these sources is relatively small for algorithms based on the reconstruction of the b decay length, since this is dominated by the uncertainty on the position of the secondary vertex. However, it is a major issue for tags based on track impact parameters, and it is particularly difficult to control since it heavily influences the other sources. Therefore in the R_b analyses the primary vertex is generally reconstructed independently in the two hemispheres, rendering this source of correlation negligible.

The kinematic correlations are correlated between the experiments. They mainly arise from the fact that the tagging efficiency depends on the b-hadron momentum and that a gluon emitted at a large angle reduces the energy of both quarks.

If the efficiency is proportional to the b-hadron momentum the efficiency correlation is directly given by the momentum correlation. Analytic $\mathcal{O}(\alpha_s)$ QCD calculations predicts effects of about 1.4% [178] for the correlation between the two b-quark momenta. At the parton level, fragmentation models agree to the 0.2% level with this number. At the hadron level HERWIG [34] gives an up to 0.8% larger correlation than the other models.

Since the proportionality between the B-momentum and the tagging efficiency is only approximate, in practice the experiments have derived test quantities that are sensitive to the kinematical correlations and the systematic uncertainties are derived from data/Monte Carlo comparisons. As an example the momentum of the fastest jet assuming a three jet topology can be calculated and the tagging rate for the hemisphere containing this jet and the opposite one is measured. Although these errors have a large statistical component, they are conservatively taken as fully correlated between the experiments.

Events where the radiated gluon is so hard that the two b-hadrons are in the same hemisphere are particularly relevant for the estimate of the correlation. The rate of such events (about 1% of all $Z \to b\bar{b}$ events) is varied by 30%, motivated by a comparison of matrix element and parton shower models.

Furthermore, the hemisphere correlation also depends on b hadron production and decay properties. Such a dependence is a small second order effect for analyses which reconstruct the primary vertex independently in the two hemispheres, but can be substantial if a common primary vertex is used, due to the inclusion of tracks which actually come from b-hadrons in the primary vertex determination. The sources of uncertainty considered are:

- average charged track multiplicity in b-hadron decay,
- b fragmentation,
- b hadron lifetimes,

and the errors are evaluated according to the prescription in this section.

5.6.8 Light quark background in lifetime tagged samples

The amount of light quark background in lifetime-tagged samples is mainly determined by the rate of long-lived light hadrons, namely K^0_s and Λ, produced in the fragmentation. This is only a significant source of uncertainty for the precise R_b measurements. In the case of forward-backward asymmetry measurements, details of light quark fragmentation are relevant in the extraction of the asymmetry from the measured charge flow.

The rate of long-lived light hadrons

All experiments have measured the rates of long-lived light hadrons and tuned their fragmentation model accordingly. Variations of 10% around the central value are used to estimate the uncertainty.

The fragmentation of light quarks

The JETSET model contains many free parameters, several of which influence the charge flow predictions. These parameters have been tuned individually by the experiments and it is not possible to define a common procedure to evaluate the errors due to light quark fragmentation.

Fortunately these errors turn out to be relatively small, and they are assumed to be fully correlated even if the procedures to evaluate them vary between the experiments.

5.7 Corrections to the measured electroweak parameters

5.7.1 Corrections to R_b, R_c

Small corrections have to be applied to the raw experimental measurements. The R_b and R_c analyses measure the ratio of production cross sections $R_q = \sigma_{q\bar{q}}/\sigma_{had}$. To obtain the ratios of partial widths $R_q^0 = \Gamma_{q\bar{q}}/\Gamma_{had}$, small corrections for photon exchange and $\gamma - Z$-interference have to be applied. These corrections are typically $+0.0002$ for R_b and -0.0002 for R_c, and are applied by the experiments before the combination as their size depends slightly on the invariant mass cutoff of the $q\bar{q}$-system imposed in the analysis.

5.7.2 QCD corrections to the heavy flavour forward-backward asymmetries

The measured forward backward asymmetries do not correspond to the underlying quark asymmetries due to QCD effects. The dominant corrections are due to radiation of gluons from the final state quarks. The QCD corrections do not depend on the beam polarisation and are thus identical for the unpolarised forward-backward asymmetry and the left-right-forward-backward asymmetries. Any $A_{FB}^{q\overline{q}}$ in this section has thus to be read as $A_{FB}^{q\overline{q}}$ or $A_{FBLR}^{q\overline{q}}$

Theoretical calculations use either the quark direction or the thrust direction to compute the asymmetry. Since the reconstructed thrust axis is generally used as the heavy quark direction estimator in experimental measurements, calculations based on the thrust axis are considered.

The effect on the asymmetry at the scale $\mu^2 = m_Z^2$ is parametrised as [179]:

$$\begin{aligned} \left(A_{FB}^{q\overline{q}}\right)_{meas} &= (1 - C_{QCD}) \left(A_{FB}^{q\overline{q}}\right)_{no\,QCD} \\ &= \left(1 - \frac{\alpha_s(m_Z^2)}{\pi} c_1 - \left(\frac{\alpha_s(m_Z^2)}{\pi}\right)^2 c_2\right) \left(A_{FB}^{q\overline{q}}\right)_{no\,QCD} . \end{aligned} \tag{5.25}$$

The first-order corrections are known including mass effects [180]. Taking the thrust axis as the direction and using the pole mass, they are $c_1 = 0.77$ for $A_{FB}^{b\overline{b}}$ and $c_1 = 0.86$ for $A_{FB}^{c\overline{c}}$.

The second order corrections have recently been recalculated [181, 182] and found to be in disagreement with previous results [180]. The calculation of [182] is strictly massless and also neglects the corrections from triangle diagrams involving top quarks, given in [180]: corrections arising from diagrams which lead to two-parton final states are the largest, and they can be added to the results of [182], as they apply in the same way to calculations based either on the thrust or the quark direction.

The second order coefficients used are $c_2 = 5.93$ for $A_{FB}^{b\overline{b}}$ and $c_2 = 8.5$ for $A_{FB}^{c\overline{c}}$. The final QCD correction coefficients, including fragmentation effects and using the thrust axis as reference direction ($C_{QCD}^{had,T}$), are $C_{QCD}^{had,T} = 0.0354 \pm 0.0063$ for $A_{FB}^{b\overline{b}}$ and $C_{QCD}^{had,T} = 0.0413 \pm 0.0063$ for $A_{FB}^{c\overline{c}}$. The breakdown of the errors is given in Table 5.5.

The procedure to implement QCD corrections in the experimental analyses is non-trivial. It is described in detail in [179] and briefly summarised in the following.

Error on $C_{\mathrm{QCD}}^{\mathrm{had,T}}$		$\mathrm{b\overline{b}}$	$\mathrm{c\overline{c}}$
Higher orders	[182]	0.0025	0.0046
Mass effects	[179]	0.0015	0.0008
Higher order mass	[182]	0.005	0.002
$\alpha_s = 0.119 \pm 0.003$		0.0012	0.0015
Hadronisation	[179]	0.0023	0.0035
Total		0.0063	0.0063

Table 5.5: Error sources for the QCD corrections to the forward-backward asymmetries.

The corrections provided by theoretical calculations are not directly applicable to experimental measurements for two main reasons. First, the thrust axis used in theoretical calculations is defined using partons; a further smearing is caused by the hadronisation of partons into physical particles. This effect, typically ten times smaller than the correction itself, is taken from the simulation using the JETSET model, and its full size is taken as an additional uncertainty. Second, and much more important, the experimental selection and analysis method can introduce a bias in the topology of the events used, or intrinsically correct for the effects. This analysis bias is calculated using the full detector simulation with JETSET for event-generation, where it has been verified, that JETSET reproduces the analytical calculations very well for full acceptance. It turns out that analyses based on semileptonic decays typically need between 50% and 70% of the full correction. In the jetcharge analyses the QCD corrections are largely hidden in the hemisphere correlations which are corrected for internally. The remaining corrections are very small.

Because of the analysis dependence of the QCD corrections all asymmetries quoted in this chapter are corrected for QCD effects.

The uncertainty on the theoretical calculation of the corrections, as well as on the additional effect due to hadronisation, are taken as fully correlated between the different measurements. The "scaling factor" applied for each individual analysis to account for the experimental bias is instead evaluated case by case together with its associated uncertainty, and these errors are taken as uncorrelated.

5.7.3 Other corrections to the asymmetries

The forward backward asymmetries at LEP vary strongly as a function of the centre of mass energy because of $\gamma - \mathrm{Z}$-interference. Since the mean energies at the different points vary slightly with time, the mean energies of the results of the different analyses are also not completely identical. The experiments quote the mean centre of mass energy for each asymmetry measurement. In a first fit the asymmetries are corrected to the closest of the three energies $\sqrt{s} = 89.55\mathrm{GeV}(-2),\ 91.26\mathrm{GeV}(\mathrm{pk}),\ 92.94\mathrm{GeV}(+2)$ assuming Standard Model energy dependence.

The slope of the asymmetries depends only on the well known fermion charges and axial couplings while the asymmetry value on the Z-pole is sensitive to the effective weak mixing angle. In the first fit it is verified that the energy dependence is indeed consistent with the one expected in the Standard Model. In a second fit all asymmetries are then corrected to the peak energy (91.26 GeV) before fitting.

To obtain the pole asymmetry, $A_{\mathrm{FB}}^{0,\mathrm{q}}$, which is defined as the asymmetry at the Z-mass for

pure Z-exchange, the fitted asymmetries at the peak energy, denoted as $A_{\rm FB}^{\rm q\overline{q}}({\rm pk})$ need to be corrected further as summarised in Table 5.6. These corrections are due to the energy shift from 91.26 GeV to $m_{\rm Z}$, initial state radiation, γ exchange and γ-Z interference. A very small correction due to the nonzero value of the b quark mass is also included in the correction called γ-Z interference. All corrections are calculated using ZFITTER [24].

Source	$\delta A_{\rm FB}^{\rm b\overline{b}}$	$\delta A_{\rm FB}^{\rm c\overline{c}}$
$\sqrt{s} = m_{\rm Z}$	-0.0014	-0.0036
QED corrections	$+0.0039$	$+0.0108$
γ, γ-Z, quark-mass	-0.0001	-0.0009
Total	$+0.0024$	$+0.0063$

Table 5.6: Corrections to be applied to the quark asymmetries as $A_{\rm FB}^{0,\,{\rm q}} = A_{\rm FB}^{\rm q\overline{q}}({\rm pk}) + \delta A_{\rm FB}$.

Similar corrections have been applied to the left-right-forward-backward asymmetries. However the corrections are only about one tenth of the experimental error and the asymmetries are directly presented in terms of $\mathcal{A}_{\rm b}$ and $\mathcal{A}_{\rm c}$ by SLD.

5.8 Combination procedure

The heavy flavour results are combined using a χ^2 minimisation technique [173]. In the case of the lineshape, each experiment measures the same 5 or 9 parameters. Here, the set of measurements is different for each experiment. Nonetheless, a χ^2 minimisation can be used to find the best estimates of each of the electroweak parameters. The formulation must be sufficiently flexible to allow any number of measurements of each electroweak parameter by each experiment. The measured values of closely related parameters, detailed in section 5.5 are included in the averaging procedure. Their treatment will be explained more fully below.

In order to write down an expression for this χ^2, the average value, i.e. the best estimate of the set of electroweak parameters is denoted x^μ, where the index μ refers to the parameter.

$$
\begin{aligned}
x^\mu \;=\; & R_{\rm b}, \\
& R_{\rm c}, \\
& A_{\rm FB}^{\rm b\overline{b}}(-2), \\
& A_{\rm FB}^{\rm c\overline{c}}(-2), \\
& A_{\rm FB}^{\rm b\overline{b}}({\rm pk}), \\
& A_{\rm FB}^{\rm c\overline{c}}({\rm pk}), \\
& A_{\rm FB}^{\rm b\overline{b}}(+2), \\
& A_{\rm FB}^{\rm c\overline{c}}(+2), \\
& \mathcal{A}_{\rm b}, \\
& \mathcal{A}_{\rm c}, \\
& {\rm BR}({\rm b} \to \ell^-), \\
& {\rm BR}({\rm b} \to {\rm c} \to \ell^+), \\
& {\rm BR}({\rm c} \to \ell^+), \\
& \overline{\chi},
\end{aligned}
\qquad (5.26)
$$

$f(\mathrm{D}^+)$,
$f(\mathrm{D_s})$,
$f(\mathrm{c_{baryon}})$,
$\mathrm{P}(\mathrm{c} \to \mathrm{D}^{*+}) \times \mathrm{BR}(\mathrm{D}^{*+} \to \pi^+\mathrm{D}^0)$.

In this case the forward-backward asymmetries are averaged at three different centre-of-mass energies. Alternatively, they can all be interpreted as measurements of the asymmetry at the Z-peak, $A_{\mathrm{FB}}^{\mathrm{b\overline{b}}}(\mathrm{pk})$ and $A_{\mathrm{FB}}^{\mathrm{c\overline{c}}}(\mathrm{pk})$, as described below.

Each experimental result is referred to as r_i^μ. The ith result could be a measurement of any of the parameters, R_b, ($\mu = 1$), $R_\mathrm{c}(\mu = 2)$ and so on. A group of k results could be measured simultaneously in the same analysis to give: r_i^μ, r_{i+1}^ν ... r_{i+k-1}^ρ.

The averages are given by minimising the χ^2:

$$\chi^2 = \sum_{ij} (r_i^\mu - x^\mu) \mathcal{C}_{ij}^{-1} (r_j^\nu - x^\nu)\,. \tag{5.27}$$

Almost all the complications in building the χ^2 are in calculating the $n \times n$ covariance matrix, $\mathcal{C}$, relating the $i = 1, n$ measurements. This matrix must take into account statistical and systematic correlations. Statistical errors arise from overlap of samples within an experiment, and for groups of measurements of closely related parameters in the same fit. Some systematic errors only lead to correlations between measurements made by the same experiment, for example errors due to the modelling of track resolutions in a particular detector. Others are potentially common to all the measurements. The experiments provide their measurements in the form of input tables, which list the central values, the statistical errors, any correlations between statistical errors and a detailed breakdown of the systematic errors. This breakdown is used to calculate the systematic error contribution to the covariance matrix by assuming that any particular systematic uncertainty, for example the uncertainty due to the lifetime of the B^0-meson, is fully correlated for all measurements [173]. This assumption is legitimate since common values and uncertainties are used for those quantities taken from external experimental measurements. If necessary, older results are corrected to use the latest agreed set. The input parameters are discussed in section 5.6. In summary, the covariance matrix has the form:

$$\mathcal{C}_{ij} = \mathcal{C}_{ij}^{\mathrm{stat}} + \sum_k \sigma_i^k \sigma_j^k\,, \tag{5.28}$$

where $\mathcal{C}_{ij}^{\mathrm{stat}}$ is the covariance matrix of statistical errors and σ_i^k is the systematic error in measurement i, due to the source of systematic uncertainty k. Some errors, such as the error from Monte Carlo statistics, are uncorrelated for all results and therefore contribute only to the diagonal elements of $\mathcal{C}$. Others, such as those connected with lepton identification or tracking efficiency, are correlated for any measurements made by the same experiment. The remaining errors, arising from the physics sources discussed in section 5.6, are assumed to be fully correlated for all measurements.

It is also important to take into account that even when two electroweak parameters are not measured in the same fit, the measured value of one will depend on the value assumed for another. For example, a measurement of R_b often depends on the fraction of charm contamination in the sample, and therefore on the value of R_c that was assumed. The explicit first order dependence of the value of R_b, $r_i^{R_\mathrm{b}}$, on the average value of R_c, x^{R_c}, is included as follows:

$$r_i^{R_\mathrm{b}} = R_\mathrm{b}^{\mathrm{meas}} + a_i^{R_\mathrm{c}} \frac{(x^{R_\mathrm{c}} - R_\mathrm{c}^{\mathrm{used}})}{x^{R_\mathrm{c}}}\,. \tag{5.29}$$

Here $R_{\rm b}^{\rm meas}$ is the central value of $R_{\rm b}$ measured by the experiment, assuming a value for $R_{\rm c} = R_{\rm c}^{\rm used}$. The constant $a_i^{R_{\rm c}}$ is given by

$$\frac{a_i^{R_{\rm c}}}{x^{R_{\rm c}}} = \left.\frac{{\rm d}r_i^{R_{\rm b}}}{{\rm d}x^{R_{\rm c}}}\right|_{x^{R_{\rm c}}=R_{\rm c}^{\rm used}} . \tag{5.30}$$

The dependence of any measurement on any of the other fitted parameters can be expressed in the same way.

The system of including measurements by input tables has proved to be very flexible. Different subsets of results can be combined together in cross checks, to verify that the results are robust.

As an example Table 5.7 shows the measurements of $R_{\rm b}^0$ used in the fit. The line labelled "$R_{\rm b}^0$(published)" shows the value published by the collaborations while in the line "$R_{\rm b}^0$(used)" the values corrected for the agreed input parameters are given. The errors labelled "uncorrelated" are either internal to the analysis or to the experiment while the ones labelled "correlated" are potentially in common with other experiments. Also the dependencies of the $R_{\rm b}^0$ measurements on the other input parameters are given.

	ALEPH	DELPHI	L3	OPAL	SLD
	92-95 [117]	92-95 [118]	94-95 [119]	92-95 [113]	93-98† [114]
$R_{\rm b}^0$(published)	0.2159	0.2163	0.2174	0.2178	0.2171
$R_{\rm b}^0$(input)	0.2157	0.2163	0.2174	0.2174	0.2171
Statistical	0.0009	0.0007	0.0015	0.0011	0.0009
Uncorrelated	0.0007	0.0004	0.0015	0.0009	0.0005
Correlated	0.0007	0.0004	0.0018	0.0008	0.0005
Total Systematic	0.0009	0.0006	0.0023	0.0012	0.0008
$a(R_{\rm c})$	-0.0033	-0.0041	-0.0376	-0.0122	-0.0057
$R_{\rm c}^{\rm used}$	0.1720	0.1720	0.1734	0.1720	0.1710
$a({\rm BR}({\rm c}\to\ell^+))$			-0.0133	-0.0067	
${\rm BR}({\rm c}\to\ell^+)^{\rm used}$			9.80	9.80	
$a(f({\rm D}^+))$	-0.0010	-0.0010	-0.0086	-0.0029	-0.0008
$f({\rm D}^+)^{\rm used}$	0.2330	0.2330	0.2330	0.2380	0.2370
$a(f({\rm D_s}))$	-0.0001	0.0001	-0.0005	-0.0001	-0.0003
$f({\rm D_s})^{\rm used}$	0.1020	0.1030	0.1030	0.1020	0.1140
$a(f(\Lambda_{\rm c}))$	0.0002	0.0003	0.0008	0.0003	-0.0003
$f(\Lambda_{\rm c})^{\rm used}$	0.0650	0.0630	0.0630	0.0650	0.0730

Table 5.7: The measurements of $R_{\rm b}^0$. All measurements use a lifetime tag enhanced by other features like invariant mass cuts or high p_T leptons. The lines $a(X)$ and $x^{\rm used}$ refer to the dependencies defined in equation 5.30

Since the uncertainties on the branching fractions of some of the decay modes used in the charm counting $R_{\rm c}$ analyses are rather large, two refinements are added to the fit to correct for non linear effects. The products $R_{\rm c}{\rm P}({\rm c}\to{\rm D}^{*+})\times{\rm BR}({\rm D}^{*+}\to\pi^+{\rm D}^0)$, $R_{\rm c}f({\rm D}^+)$, $R_{\rm c}f({\rm D}^0)$, $R_{\rm c}f({\rm D_s})$ and $R_{\rm c}f({\rm c_{baryon}})$ are given as experimental results r_i^μ and are compared to the product of the relevant fit parameters in the χ^2 calculation. In addition the errors on these parameters,

again mainly the branching fraction errors, are more Gaussian if they are treated as relative errors. For this reason the logarithm of the products is fitted instead of the products themselves.

It has been verified that the fit results depend on whether the logarithms or the values themselves are used only for $R_c f(D_s)$ and $R_c f(c_{baryon})$. However these two measurements are completely dominated by the branching fraction error for which it is clear that the logarithmic treatment is the better one.

5.9 Results

This section contains the results of the summer01 conferences, they are not final!

The results used in this combination have been described in sections 5.3, 5.4 and 5.5 and are summarised in tables A.1 - A.20 in Appendix A. Figures 5.13 – 5.15 compare the main electroweak results of the different experiments.

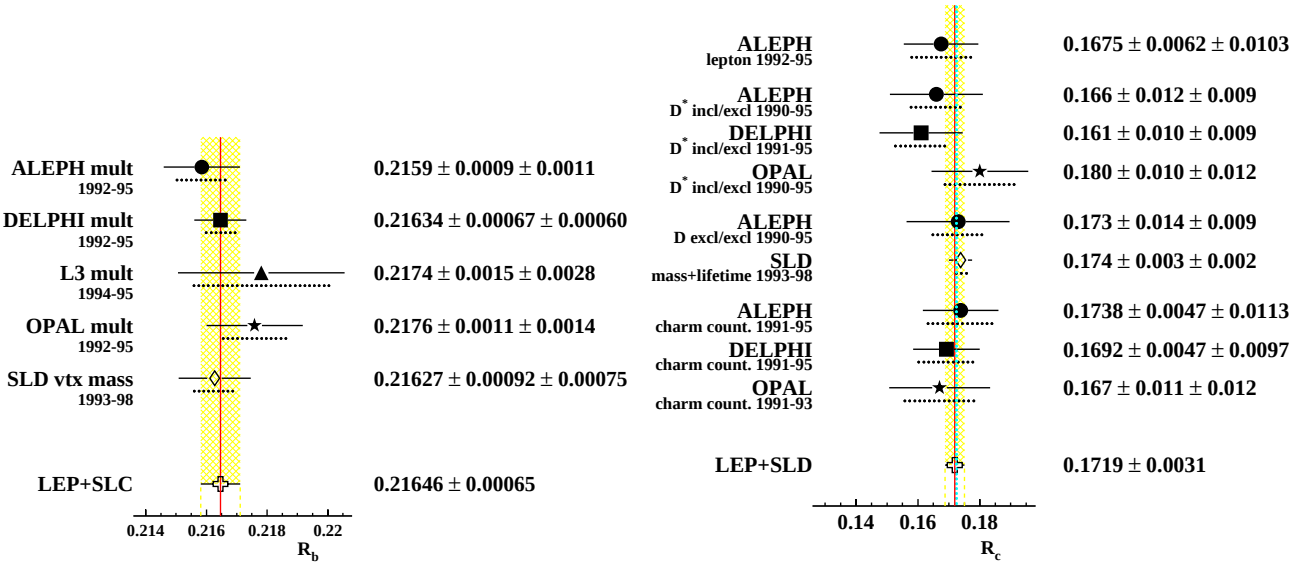

Figure 5.13: R_b^0 and R_c^0 measurements used in the heavy flavour combination. The dotted lines indicate the size of the systematic error.

In a first fit the different analyses have been combined with the asymmetries kept at the three different energies, yielding in total 18 free parameters. The results of this fit for the asymmetries are:

$$\begin{aligned} A_{FB}^{b\bar{b}}(-2) &= 0.0508 \pm 0.0068 \\ A_{FB}^{c\bar{c}}(-2) &= -0.035 \pm 0.017 \\ A_{FB}^{b\bar{b}}(\mathrm{pk}) &= 0.0975 \pm 0.0018 \\ A_{FB}^{c\bar{c}}(\mathrm{pk}) &= 0.0620 \pm 0.0036 \\ A_{FB}^{b\bar{b}}(+2) &= 0.1150 \pm 0.0057 \\ A_{FB}^{c\bar{c}}(+2) &= 0.130 \pm 0.013 \end{aligned} \tag{5.31}$$

with a χ^2/d.o.f. of $43/(99-18)$. All correlations between the asymmetries are below 20%.

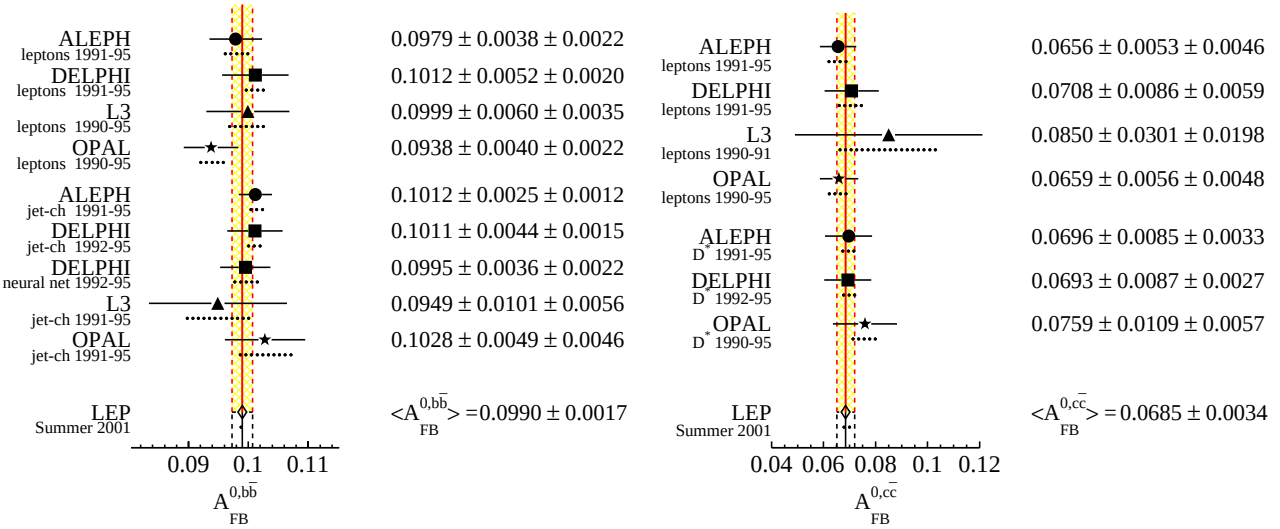

Figure 5.14: $A_{\mathrm{FB}}^{0,\mathrm{b}}$ and $A_{\mathrm{FB}}^{0,\mathrm{c}}$ measurements used in the heavy flavour combination. The $A_{\mathrm{FB}}^{0,\mathrm{b}}$ measurements with D-mesons contribute only very little weight and are not shown in the plots.

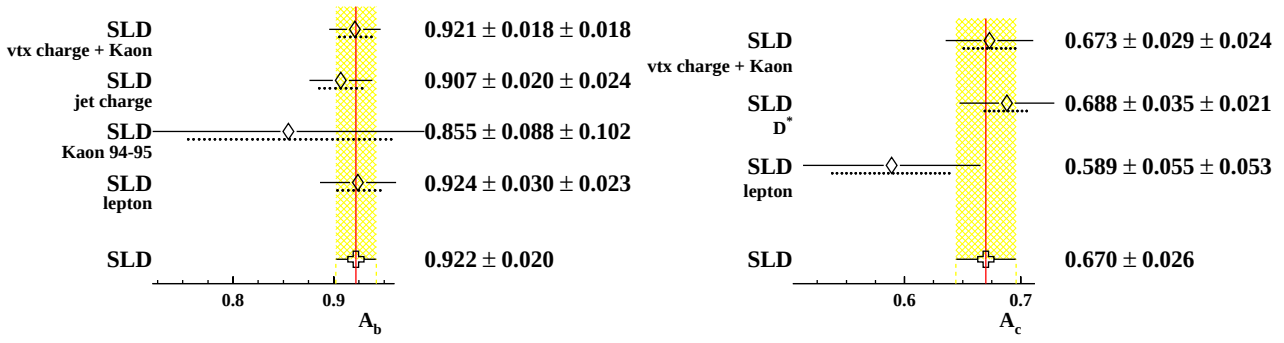

Figure 5.15: $\mathcal{A}_{\mathrm{b}}$ and $\mathcal{A}_{\mathrm{c}}$ measurements used in the heavy flavour combination. The $A_{\mathrm{FB}}^{0,\mathrm{b}}$ measurements with D-mesons contribute only very little weight and are not shown in the plots.

Figure 5.16 shows the energy dependence of $A_{\rm FB}^{\rm b,c}$ compared to the Standard Model prediction. Since the model describes the energy dependence well, in a second fit all asymmetries are corrected to the peak energy before fitting, resulting in 14 free parameters. The results of this fit are:

$$\begin{aligned}
R_{\rm b}^0 &= 0.21646 \pm 0.00065\,, \qquad (5.32)\\
R_{\rm c}^0 &= 0.1719 \pm 0.0031\,,\\
A_{\rm FB}^{0,\,\rm b} &= 0.0990 \pm 0.0017\,,\\
A_{\rm FB}^{0,\,\rm c} &= 0.0685 \pm 0.0034\,,\\
\mathcal{A}_{\rm b} &= 0.922 \pm 0.020\,,\\
\mathcal{A}_{\rm c} &= 0.670 \pm 0.026\,,\\
{\rm BR}({\rm b} \to \ell^-) &= 0.1062 \pm 0.0021\,,\\
{\rm BR}({\rm b} \to {\rm c} \to \ell^+) &= 0.0807 \pm 0.0017\,,\\
{\rm BR}({\rm c} \to \ell^+) &= 0.0979 \pm 0.0031\,,\\
\overline{\chi} &= 0.1197 \pm 0.0040\,,\\
f({\rm D}^+) &= 0.234 \pm 0.016\,,\\
f({\rm D_s}) &= 0.125 \pm 0.026\,,\\
f({\rm c_{baryon}}) &= 0.096 \pm 0.023\,,\\
{\rm P}({\rm c} \to {\rm D}^{*+}) \times {\rm BR}({\rm D}^{*+} \to \pi^+{\rm D}^0) &= 0.1620 \pm 0.0048\,,
\end{aligned}$$

with a χ^2/d.o.f. of $47/(99-14)$. The corresponding correlation matrix is given in Table 5.8. Note that here the values of $A_{\rm FB}^{\rm q\overline{q}}({\rm pk})$ actually found in the fit have been corrected to pole asymmetries, as described in Table 5.6.[§] The fit χ^2 is in all cases smaller than expected. As a cross check the fit has been repeated using statistical errors only. In this case the χ^2/d.o.f. is $87/(99-14)$. A large contribution to the χ^2 comes from ${\rm BR}({\rm b} \to \ell^-)$ measurements, which is sharply reduced when detector systematics are included. Subtracting the ${\rm BR}({\rm b} \to \ell^-)$ contribution one gets $\chi^2/{\rm d.o.f.} = 60/(93-13)$. The low χ^2 for the main fit can be explained largely by conservatively estimated systematic errors. Many error sources are evaluated by comparing test quantities between data and simulation. The statistical errors of these tests are taken as systematic uncertainties but no correction is applied, since one has good reasons to believe that the Monte Carlo describes the truth better than suggested by the test. Also in some cases, such as for the ${\rm b} \to \ell^-$ model fairly conservative assumptions are used for the error evaluation which are extreme enough to be clearly incompatible with the data.

Table 5.9 summarises the dominant errors for the electroweak parameters. In all cases the two largest error sources are statistics and systematics internal to the experiments. The internal systematics consist mainly of errors due to Monte Carlo statistics, data statistics for cross checks and the knowledge of detector resolutions and efficiencies. The error labelled "QCD effects" is due to hemisphere correlation for $R_{\rm b}^0$ and $R_{\rm c}^0$ (section 5.6.7) and due to the theoretical uncertainty in the QCD corrections for the asymmetries (section 5.7.2). For the asymmetries on average about 50% of the QCD corrections are seen. The uncertainties due the knowledge of the beam energy are negligible in all cases.

Figure 5.17 compares $R_{\rm b}^0, R_{\rm c}^0$, $A_{\rm FB}^{\rm c\overline{c}}, A_{\rm FB}^{\rm b\overline{b}}$ and $\mathcal{A}_{\rm b}, \mathcal{A}_{\rm c}$ with the Standard Model prediction. A good agreement is found everywhere, where the quark asymmetries require a Higgs-mass of a

[§]To correct the pole peak asymmetries to the pole asymmetries only an error free number is added. All errors and correlations thus remain unchanged.

	1) R_{b}	2) R_{c}	3) $A_{\mathrm{FB}}^{0,\,\mathrm{b}}$	4) $A_{\mathrm{FB}}^{0,\,\mathrm{c}}$	5) $\mathcal{A}_{\mathrm{b}}$	6) $\mathcal{A}_{\mathrm{c}}$	7) BR(1)	8) BR(2)	9) BR(3)	10) $\overline{\chi}$	11) $f(\mathrm{D}^+)$	12) $f(\mathrm{D_s})$	13) $f(c_{bar.})$	14) PcDst
1)	1.00	−0.14	−0.08	0.01	−0.08	0.04	−0.09	−0.02	−0.01	−0.03	−0.16	−0.04	0.13	0.10
2)	−0.14	1.00	0.04	−0.01	0.03	−0.05	0.06	−0.03	−0.30	0.04	−0.13	0.17	0.16	−0.44
3)	−0.08	0.04	1.00	0.15	0.02	0.00	0.05	−0.08	0.00	0.14	0.01	0.02	0.00	−0.03
4)	0.01	−0.01	0.15	1.00	0.00	0.01	0.13	−0.14	−0.08	0.14	0.00	0.00	−0.01	0.01
5)	−0.08	0.03	0.02	0.00	1.00	0.13	−0.02	0.01	0.03	0.06	0.00	0.00	0.00	−0.02
6)	0.04	−0.05	0.00	0.01	0.13	1.00	0.02	−0.04	−0.02	0.01	0.00	0.00	0.00	0.02
7)	−0.09	0.06	0.05	0.13	−0.02	0.02	1.00	−0.21	0.01	0.37	0.03	0.01	−0.01	−0.01
8)	−0.02	−0.03	−0.08	−0.14	0.01	−0.04	−0.21	1.00	0.08	−0.31	0.02	−0.01	−0.01	0.01
9)	−0.01	−0.30	0.00	−0.08	0.03	−0.02	0.01	0.08	1.00	0.14	0.01	−0.03	−0.02	0.13
10)	−0.03	0.04	0.14	0.14	0.06	0.01	0.37	−0.31	0.14	1.00	0.01	0.01	0.00	−0.03
11)	−0.16	−0.13	0.01	0.00	0.00	0.00	0.03	0.02	0.01	0.01	1.00	−0.39	−0.26	0.10
12)	−0.04	0.17	0.02	0.00	0.00	0.00	0.01	−0.01	−0.03	0.01	−0.39	1.00	−0.50	−0.08
13)	0.13	0.16	0.00	−0.01	0.00	0.00	−0.01	−0.01	−0.02	0.00	−0.26	−0.50	1.00	−0.14
14)	0.10	−0.44	−0.03	0.01	−0.02	0.02	−0.01	0.01	0.13	−0.03	0.10	−0.08	−0.14	1.00

Table 5.8: The correlation matrix for the set of the 14 heavy flavour parameters. BR(1), BR(2) and BR(3) denote BR($\mathrm{b} \to \ell^-$), BR($\mathrm{b} \to \mathrm{c} \to \ell^+$) and BR($\mathrm{c} \to \ell^+$) respectively, PcDst denotes P($\mathrm{c} \to \mathrm{D}^{*+}$) $\times$ BR($\mathrm{D}^{*+} \to \pi^+\mathrm{D}^0$).

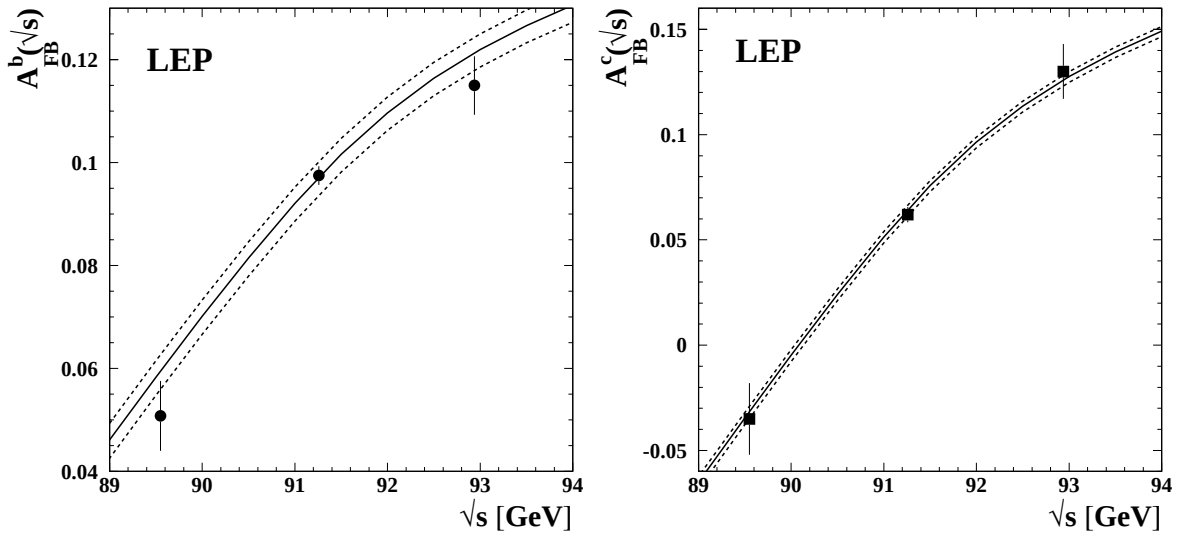

Figure 5.16: Energy dependence of $A_{\rm FB}^b$ and $A_{\rm FB}^c$. The solid line represents the Standard Model prediction for $m_{\rm t} = 175$GeV, $m_{\rm H} = 300$GeV the upper (lower) dashed line is the prediction for $m_{\rm H} = 100\,(1000)$ GeV.

	$R_{\rm b}^0$ $\cdot 10^{-3}$	$R_{\rm c}^0$ $\cdot 10^{-3}$	$A_{\rm FB}^{0,\rm b}$ $\cdot 10^{-3}$	$A_{\rm FB}^{0,\rm c}$ $\cdot 10^{-3}$	$\mathcal{A}_{\rm b}$ $\cdot 10^{-2}$	$\mathcal{A}_{\rm c}$ $\cdot 10^{-2}$
statistics	0.43	2.3	1.6	3.0	1.5	2.1
internal systematics	0.29	1.4	0.6	1.4	1.2	1.5
QCD effects	0.18	0.1	0.3	0.1	0.3	0.2
BR(D $\rightarrow$ neut.)	0.14	0.3	0	0	0	0
D decay multiplicity	0.13	0.3	0	0	0	0
BR($\rm D^+ \rightarrow K^-\pi^+\pi^+$)	0.09	0.2	0	0	0	0
BR($\rm D_s \rightarrow \phi\pi^+$)	0.03	0.5	0	0	0	0
BR($\Lambda_{\rm c} \rightarrow$p $\rm K^-\pi^+$)	0.06	0.5	0	0.1	0	0
D lifetimes	0.06	0.1	0	0.1	0	0
gluon splitting	0.22	0.1	0.1	0.1	0.1	0.1
c fragmentation	0.10	0.2	0.1	0.2	0.1	0.1
light quarks	0.07	0.2	0.1	0.1	0	0
beam polarisation	0	0	0	0	0.5	0.4
total	0.65	3.1	1.7	3.5	2.0	2.6

Table 5.9: The dominant error sources for the electroweak parameters from the 14-parameter fit.

few hundred GeV. The data are interpreted further, together with the leptonic observables in section 10.

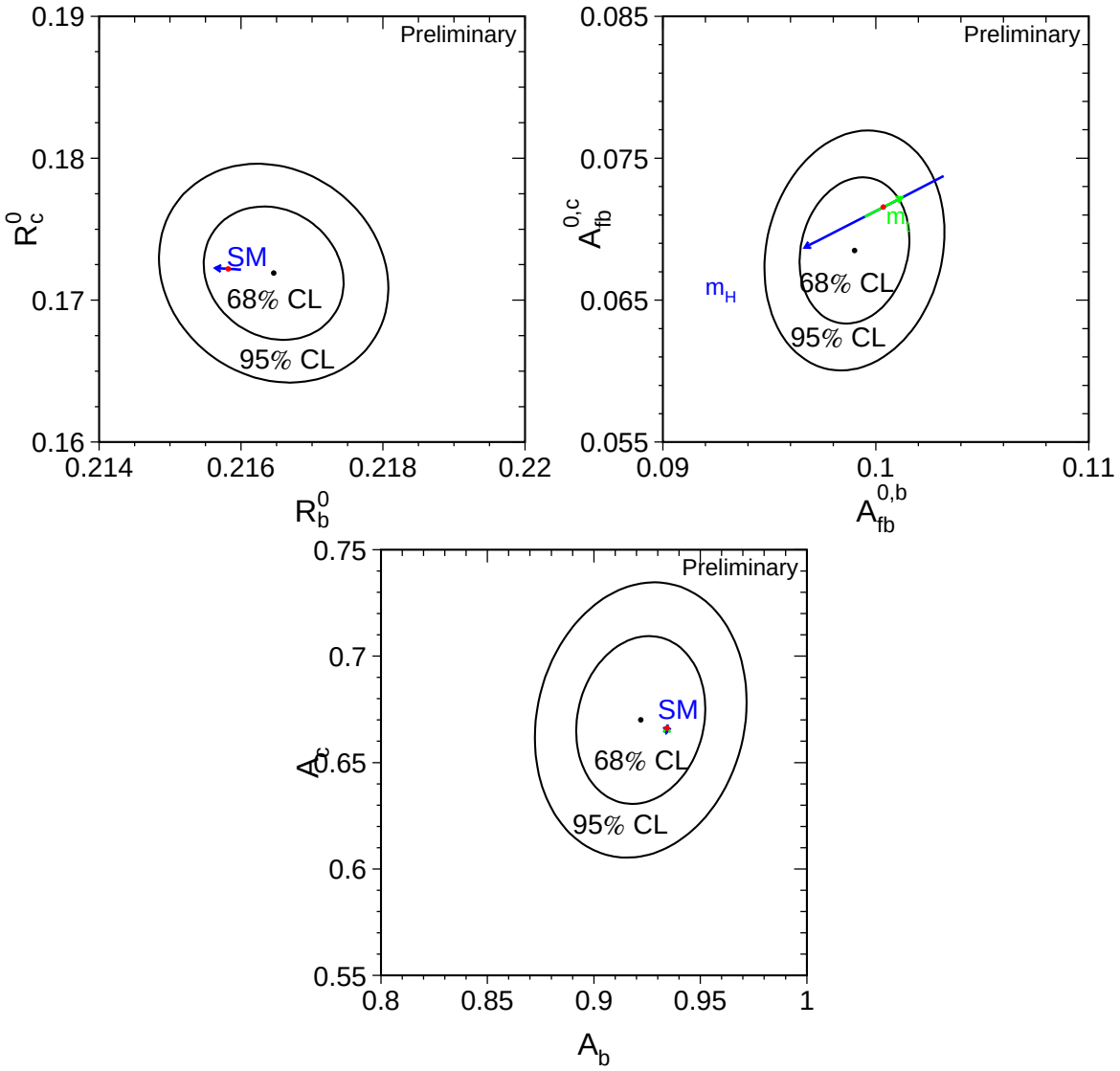

Figure 5.17: Contours in the R_c^0-R_b^0, $A_{FB}^{c\bar{c}}$-$A_{FB}^{b\bar{b}}$ and $\mathcal{A}_c$-$\mathcal{A}_b$ planes from the LEP and SLD data, corresponding to 68% confidence levels assuming Gaussian systematic errors. The Standard Model prediction for $m_t = 174.1 \pm 5.4$GeV and $m_H = 300^{+700}_{-240}$GeV is also shown.

Amongst the non-electroweak observables the B semileptonic branching fraction ($BR(b \to \ell^-) = 0.1062 \pm 0.0021$) is of special interest. The dominant error source on this quantity is the dependences on the semileptonic decay model $b \to \ell^-$ with

$$\Delta BR(b \to \ell^-)(b \to \ell^- \text{ modelling}) = 0.0011. \tag{5.33}$$

Extensive studies have been made to understand the size of this error. Amongst the electroweak quantities, the quark asymmetries measured with leptons depend on the assumptions on the decay model while the asymmetries using other methods usually do not. The fit implicitly requires that the different methods give consistent results. This effectively constrains the decay model and thus reduces the error from this source in the fit result for $BR(b \to \ell^-)$.

To get a conservative estimate of the modelling error in $\mathrm{BR}(\mathrm{b} \to \ell^-)$ the fit has been repeated removing all asymmetry measurements. The result of this fit was

$$\mathrm{BR}(\mathrm{b} \to \ell^-) \;=\; 0.1065 \pm 0.0023 \tag{5.34}$$

with

$$\Delta\mathrm{BR}(\mathrm{b} \to \ell^-)(\mathrm{b} \to \ell^- \,\mathrm{modelling}) = 0.0014. \tag{5.35}$$

Chapter 6

Results from inclusive and light flavour hadronic events

This chapter groups together several additional results for hadronic samples which have not been discussed up to now. The measurement of the total hadronic partial width of the Z described in Chapter 2 makes no attempt to distinguish different quark flavours. Similarly an inclusive forward-backward asymmetry measurement can be made using the samples of all hadronic events, taking advantage of the high statistics. However, because the up-type (charge 2/3) and down-type (charge $-1/3$) quarks contribute to the average forward-backward charge asymmetry with opposite sign, the interpretation of these measurements depends on external knowledge of the flavour ratios in the sample, and is therefore strongly dependent on the assumptions of the Standard Model, which is used to predict these ratios. The systematic errors are also much more significant than for the high efficiency and purity heavy flavour samples already discussed in Chapter 5.

Tagging methods to enhance the fraction of specific light flavour quarks (up, down or strange) have also been developed, and used to measure forward-backward asymmetries and partial widths. Although the results from these samples are rather less precise than those from heavy flavour or inclusive measurements, they do allow some explicit checks of the light quark couplings to the Z. Lastly, by exploiting the fact that the probability of photon radiation from final-state quarks is proportional to the quark charge, information on the partial widths of the Z to up-type and down-type quarks in hadronic Z decays has been inferred from the observed rate of direct photon production.

6.1 Inclusive flavour hadronic events

Many of the ideas developed in Chapter 5 can be extended and applied to an inclusive sample of $\mathrm{Z} \to \mathrm{q\overline{q}}$ decays. In particular, the mean difference in jet charge measured in the forward and backward event hemispheres has been measured by all four LEP experiments [133, 183–185]. This quantity is denoted $\langle Q_{\mathrm{FB}} \rangle$, or forward-backward charge flow, and may be expressed as:

$$\langle Q_{\mathrm{FB}} \rangle = \sum_{\mathrm{q}} R^0_{\mathrm{q}} A^{\mathrm{q\overline{q}}}_{\mathrm{FB}} \delta_{\mathrm{q}} C_{\mathrm{q}} \,, \tag{6.1}$$

where the sum runs over the 5 primary quark flavours, the charge separation, $\delta_{\mathrm{q}} = \langle Q_{\mathrm{q}} - Q_{\overline{\mathrm{q}}} \rangle$, is the mean jet charge difference between the hemispheres containing quark and the anti-quark, and the coefficients C_{q} account for the acceptance of each flavour subsample. The charge

separation can also be expressed in terms of the jet charges in the hemispheres containing the negatively charged parton, Q_-, and the positively charged parton, Q_+:

$$\delta_{\mathrm{q}} = s_{\mathrm{q}} \langle Q_- - Q_+ \rangle \,, \tag{6.2}$$

where $s_{\mathrm{q}} = +1$ for down-type quarks and -1 for up-type quarks. This notation is used by some of the experiments, and makes explicit the fact that the contributions to $\langle Q_{\mathrm{FB}} \rangle$ from the different quark types are of opposite sign. An example showing the separation between Q_+ and Q_- is given in Figure 6.1.

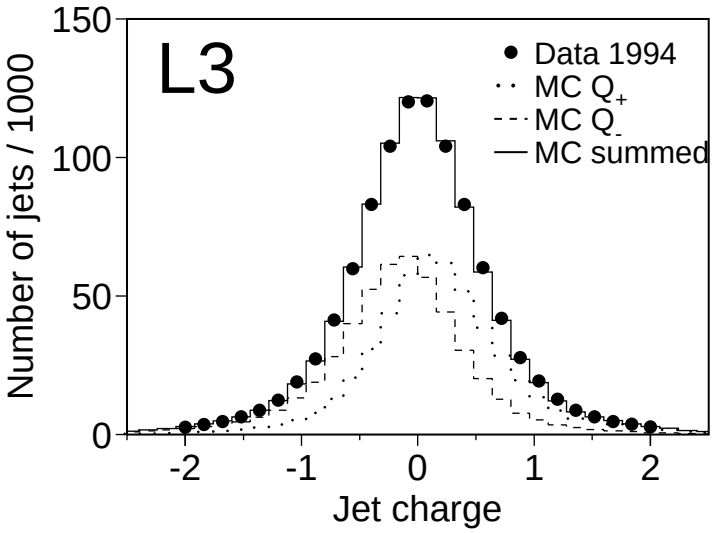

Figure 6.1: The Q_+ and Q_- distributions obtained from Monte Carlo simulation by L3. Their sum is compared to the sum of the Q_{F} and Q_{B} distributions for 1994 data.

Experimentally, the crux of the measurement is to determine the mean charge separations for each flavour. As described in Chapter 5 when discussing measurements of the forward-backward asymmetry in $\mathrm{Z} \to \mathrm{b\overline{b}}$ events using jet charges, the mean charge separation for $\mathrm{Z} \to \mathrm{b\overline{b}}$ events may be determined directly from the data, in a sample of b-tagged events (see Equation 5.14). In a similar way, charm tagging may be used to determine the mean charge separation in $\mathrm{Z} \to \mathrm{c\overline{c}}$ events. However, in both cases the bias due to the tagging method employed must be evaluated, as these biases are absent in the inclusive measurement. The reduction in systematic errors from assessing the charge separation from data outweights the uncertainties introduced by the bias correction. For the charge separation in light-quark events, Monte Carlo models must be used. This is the largest source of systematic uncertainty in the analyses. The mean charge separation for the inclusive sample may also be determined from the data, and while not directly applicable to the charge flow, it may be used as an additional constraint on the light-quark mean charge separations.

The parameters R_{q}^0 and $A_{\mathrm{FB}}^{\mathrm{q\overline{q}}}$ can all be expressed in the Standard Model as a function of the effective weak mixing angle, $\sin^2\theta_{\mathrm{eff}}^{\mathrm{lept}}$. Once the charge separations δ_{q} are known, the the measurement of $\langle Q_{\mathrm{FB}} \rangle$ can then be interpreted as a measurement of $\sin^2\theta_{\mathrm{eff}}^{\mathrm{lept}}$. Since the observed values of $\langle Q_{\mathrm{FB}} \rangle$ reflect the experimental acceptance and resolution, they cannot be

combined directly. The results are therefore combined at the level of these derived $\sin^2\theta^{\rm lept}_{\rm eff}$ values.

It must be emphasised that because the $\langle Q_{\rm FB}\rangle$ measurements in this section are interpreted as $\sin^2\theta^{\rm lept}_{\rm eff}$ measurements entirely within the context of the Standard Model they must be used with care when comparing with alternative models. This is in contrast with, results such as $A^{\rm b\overline{b}}_{\rm FB}$ and $R_{\rm b} = \Gamma_{\rm b\overline{b}}/\Gamma_{\rm q\bar{q}}$. For example, the value of $\sin^2\theta^{\rm lept}_{\rm eff}$ discussed here can only legitimately be used to test a model that does not change the relative fractions of each flavour.

6.1.1 Systematic Uncertainties

Due to the lack of high-purity and high-efficiency tags for specific light flavours, by far the dominant systematic uncertainties in these results arise from the model input required to describe the light quark properties. All experiments use the JETSET Monte Carlo as a reference fragmentation model, while the HERWIG model is used for systematic comparisons. The parameter set within JETSET is also often varied as part of the assessment of the fragmentation model uncertainties. However, neither the parameter set used for the central values nor the method for parameter variation is common to the experiments, with different experimental measurements being used by the experiments to constrain the model parameters. In addition, there are typically code changes made to the Monte Carlo programs to improve the overall description in each experiment. Thus, there is far from 100% correlation between the quoted uncertainties due to fragmentation and hadronisation modelling.

Apart from systematic uncertainties due to modelling of fragmentation and hadronisation, the remaining significant uncertainties are all specific to a given experiment, for example due to the modelling of detector resolution, or due to the evaluation of the charge bias of the apparatus.

The QCD correction required to the forward-backward asymmetries for each flavour is another potentially common uncertainty. These corrections are all essentially taken from JETSET, and a modified correction would introduce shifts in the derived value of $\sin^2\theta^{\rm lept}_{\rm eff}$. However, the QCD correction uncertainties are all much smaller than the quoted fragmentation uncertainties and other experimental errors, and so have little effect on the conclusions.

6.1.2 Combination Procedure

The derived values of the effective weak mixing angle, $\sin^2\theta^{\rm lept}_{\rm eff}$, are combined by first forming a full covariance matrix for the uncertainties, assuming that the errors associated with quark fragmentation and hadronisation are the only source of correlation. As explained above, these dominant systematic uncertainties are not fully correlated because they are not evaluated in the same way for each experiment. The off-diagonal terms are therefore taken to be the smaller of the two quoted fragmentation uncertainties for each pair of measurements (so-called "minimum-overlap" estimate). The matrix is then inverted, and a χ^2 minimisation performed as for the heavy flavour results, although here there is only one free parameter. In order to assess the sensitivity of the combined result to the assumptions in building the covariance matrix, different approaches have also been considered. The resulting weights for each input result and the final combined $\sin^2\theta^{\rm lept}_{\rm eff}$ are little changed by the assumptions made. For example, taking as the off-diagonal elements only the smallest error common to all the inputs only changes the central value by 0.00005. However, if the common systematic errors are considered to be fully correlated, the system is badly behaved. There is an excessive pull towards the low-precision

DELPHI result giving negative effective weights to the ALEPH and L3 contributions.

6.1.3 Combined Results and Interpretation

The results from the four LEP experiments have been combined using the procedure described above. The inputs and the combination are given in Table 6.1; the correlation matrix for the total errors assumed for the averages is given in Table 6.2. The results and average are presented graphically in Figure 6.2.

Experiment		$\sin^2\theta^{\rm lept}_{\rm eff}$
ALEPH	(90-94)	$0.2322 \pm 0.0008 \pm 0.0011$
DELPHI	(90-91)	$0.2345 \pm 0.0030 \pm 0.0027$
L3	(91-95)	$0.2327 \pm 0.0012 \pm 0.0013$
OPAL	(90-91)	$0.2321 \pm 0.0017 \pm 0.0029$
LEP Average		0.2324 ± 0.0012

Table 6.1: Summary of the determination of $\sin^2\theta^{\rm lept}_{\rm eff}$ from inclusive hadronic charge asymmetries at LEP. For each experiment, the first error is statistical and the second systematic. The latter is dominated by fragmentation and decay modelling uncertainties.

Experiment				
ALEPH	1.0	0.12	0.27	0.14
DELPHI	0.12	1.0	0.13	0.37
L3	0.27	0.13	1.0	0.15
OPAL	0.14	0.37	0.15	1.0

Table 6.2: The 'minimum overlap' correlation matrix for the total errors used in the final average of $\langle Q_{\rm FB}\rangle$ results.

The derived value of $\sin^2\theta^{\rm lept}_{\rm eff}$ has some correlation with that implicit in the corresponding measurement of $A^{\rm b\overline{b}}_{\rm FB}$ using jet charges in the same experiment, the latter using similar techniques and a subset of the same data. This degree of correlation has been estimated in specific cases, and the typical degree of correlation is 20% to 25%. In addition, the jet charge results contribute only half of the information to the combined $A^{\rm b\overline{b}}_{\rm FB}$ result, further diluting the correlation. This leads to a negligible change in the relative weights of the $A^{\rm b\overline{b}}_{\rm FB}$ and $\langle Q_{\rm FB}\rangle$ results in a combined determination of a global $\sin^2\theta^{\rm lept}_{\rm eff}$ value and the Standard Model fits.

6.2 Light flavour tagging

6.2.1 Asymmetry measurements

The first measurement of the strange quark forward-backward asymmetry was made by DELPHI [186], using 1992 data, and identifying strange quark events from kaons in the Ring Imaging Čerenkov detectors (RICH). The measurement was then updated with the full 1992-1995 data

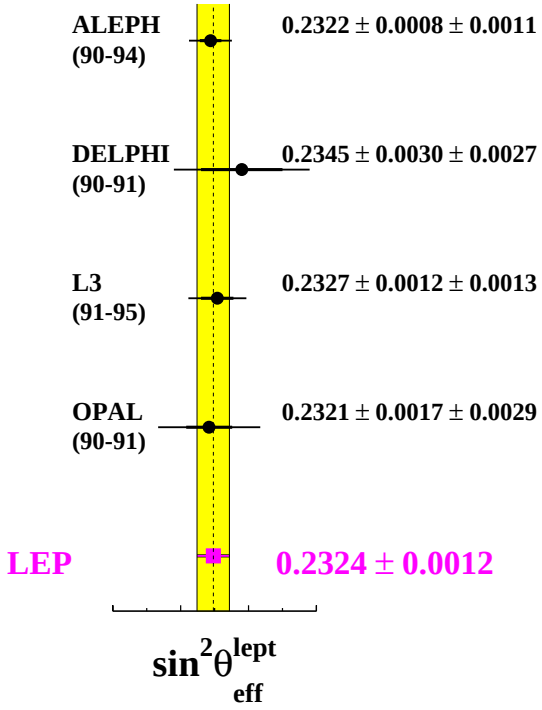

Figure 6.2: The input values and derived average of $\sin^2\theta^{\rm lept}_{\rm eff}$ from $\langle Q_{\rm FB}\rangle$ measurements.

set [187]. The Barrel RICH covers $40^\circ < \theta < 140^\circ$, and was used for the full dataset. The Forward RICH covers $15^\circ < \theta < 35^\circ$ plus $145^\circ < \theta < 165^\circ$, and was used for the 1994–1995 data. Kaons with momenta between 10 and 24 GeV/c are selected in the RICH detectors, with an average identification efficiency of 53% (42%) in the Barrel (Forward) region. At least two photoelectrons had to be identified in the ring, and the angle of the ring w.r.t. the track direction had to be consistent with the theoretical expectation for kaons within 2.5 standard deviations, and at least 2 standard deviations away from the pion expectation. The distribution of Čerenkov angle as a function of momentum is shown in Figure 6.3. The quark direction is taken to be the event thrust axis, signed according to the charge of the identified kaon. The strange fraction of the sample selected by the kaon tag is 43%. For events in the barrel region, which overlap with the micro-vertex acceptance, bottom and charm quark events are removed by a requirement on the event b-tagging probability, which increases the strange fraction to 55% and reduces the dependence of the result on modelling kaon production in heavy quark decays.

The asymmetry of the selected event sample is a linear combination of five quark forward-backward asymmetries, weighted by the fraction of that flavour and a flavour dependent charge dilution factor, as in Equation 5.9. The asymmetry of the selected sample is estimated by a χ^2 fit to the asymmetry in bins of $\cos\theta$ of the event thrust axis, signed by the charge of the kaon. The sample asymmetry is corrected for background, dominated by misidentified pions. This correction depends on the polar angle of the kaon candidate. The s-quark asymmetry is then evaluated, taking into account the fraction of each quark flavour in the kaon-tagged sample, and the probability that the charge is correctly tagged for each flavour. Corrections for QED radiation and QCD effects are also made. The analysis is somewhat model dependent, in that it assumes the Standard Model prediction for production fractions for each flavour, and for non-strange asymmetries, taken either from ZFITTER [24] or from LEP combined measurements. The analysis also relies on the Monte Carlo simulation to compute the efficiencies and dilutions for each flavour. However, the explicit dependence on the other flavour asymmetries can be

Place holder for DELPHI RICH plot

Figure 6.3: For DELPHI 1994 data, the reconstructed average Čerenkov angle in the gaseous radiator of (left) the barrel RICH and (right) the forward RICH as a function of the particle momentum. The two solid lines show the Čerenkov angle for the pion and kaon hypotheses.

included in the result, which is:

$$
\begin{aligned}
A_{\mathrm{FB}}^{0,\mathrm{s}} &= 0.1008 \pm 0.0113 \pm 0.0036 && (6.3)\\
&+ 0.0292 \frac{A_{\mathrm{FB}}^{0,\mathrm{c}} - 0.0709}{0.0709} && (6.4)\\
&+ 0.0121 \frac{A_{\mathrm{FB}}^{0,\mathrm{d}} - 0.1031}{0.1031} && (6.5)\\
&+ 0.0115 \frac{A_{\mathrm{FB}}^{0,\mathrm{u}} - 0.0736}{0.0736} \,. && (6.6)
\end{aligned}
$$

The dependence on the b-quark forward-backward asymmetry is a factor 10 smaller and has been neglected.

OPAL [188] has also measured light quark asymmetries, using the full 1990-1995 data-set, and high-momentum stable particles as a tag for light flavour events. Their approach is quite different from that of DELPHI, aiming for the minimum model dependence. The tag method uses the fact that the leading particle in a jet tends to carry the quantum numbers of

the primary quark, and that the decay of c- and b-hadrons does not usually yield very high momentum stable particles. Identified $\pi^{\pm}$, $\mathrm{K}^{\pm}$, $\mathrm{p}(\overline{\mathrm{p}})$, ${\mathrm{K_s}}^0$ or $\Lambda(\overline{\Lambda})$ hadrons with momentum, p_h, satisfying $2p_h/\sqrt{s} > 0.5$ are selected. Charged protons, pions and kaons are identified from the $\mathrm{d}E/\mathrm{d}x$ measured in the OPAL jet chamber, while ${\mathrm{K_s}}^0$ and $\Lambda(\overline{\Lambda})$ are selected by reconstructing their decay vertex and mass cuts. Only events where the polar angle of the thrust axis satisfies $|\cos\theta| < 0.8$ are considered, and after all selection cuts about 110 thousand tagged hemispheres are retained out of 4.3 million events. The purities range from 89.5% for pions to 59% for protons.

With the 5 different tags, the analysis uses a system of 5 single and 15 double tag equations to derive the light flavour composition of the tagged hemispheres directly from data (see section 5 for a description of the double tag method). The unknowns are the 15 η_q^h, the fractions of hemispheres of flavour q tagged by hadron h, and the three light flavour partial widths R_q, plus one correlation coefficient which is assumed to be the same for all tagging hadrons and flavours. The small heavy quark fractions are measured from data from a b-tagged sample for b-quarks, and from Monte Carlo simulation using measured uncertainties on their properties for c-quark events. To solve the system of equations, it is then also assumed that $R_{\mathrm{d}} = R_{\mathrm{s}} \equiv R_{\mathrm{d,s}}$, and that a few hadronisation symmetries are valid, for example $\eta_d^{\pi^{\pm}} = \eta_u^{\pi^{\pm}}$. In order to measure the forward-backward asymmetry, the charge tagging probabilities are also measured from the double tagged events, and it is assumed that $A_{\mathrm{FB}}^{0,\mathrm{d}} = A_{\mathrm{FB}}^{0,\mathrm{s}} \equiv A_{\mathrm{FB}}^{0,\mathrm{d,s}}$.

The OPAL results are

$$A_{\mathrm{FB}}^{0,\mathrm{d,s}} = 0.072 \pm 0.035 \pm 0.011 \tag{6.7}$$

$$- \; 0.0119 \frac{A_{\mathrm{FB}}^{0,\mathrm{c}} - 0.0722}{0.0722}\,, \tag{6.8}$$

$$A_{\mathrm{FB}}^{0,\mathrm{u}} = 0.044 \pm 0.067 \pm 0.018 \tag{6.9}$$

$$- \; 0.0334 \frac{A_{\mathrm{FB}}^{0,\mathrm{c}} - 0.0722}{0.0722}\,. \tag{6.10}$$

The correlation between the two results is more than 90%, so only $A_{\mathrm{FB}}^{0,\mathrm{d,s}}$ should be used for studying quark couplings. These pole asymmetries include corrections of +0.004 which have been applied to the measured $A_{\mathrm{FB}}^{\mathrm{s\overline{s}},\mathrm{d\overline{d}}}$ and $A_{\mathrm{FB}}^{\mathrm{u\overline{u}}}$ to account for QCD and ISR effects. The dependence on the c-quark forward-backward asymmetry has been quoted explicitly, and the results have negligible dependence on other Standard Model parameters. Correlated systematic uncertainties with other measurements are also very small.

SLD have published a measurement of the strange quark coupling parameter, $\mathcal{A}_{\mathrm{s}}$, from the left-right forward-backward asymmetry of events tagged by the presence in each hemisphere of a high momentum $\mathrm{K}^{\pm}$ or ${\mathrm{K_s}}^0$ [189]. The measurement uses the full sample of 550,000 Z decays recorded in 1993–1998. Charged kaons with momentum above 9 GeV/c are identified by the Čerenkov Ring Imaging Detector (CRID), with efficiency (purity) of 48% (91.5%). Background from kaons from heavy flavour events is suppressed by identifying B and D decay vertices. Requiring a strange tag in both hemispheres further suppresses the $\mathrm{u\overline{u}} + \mathrm{d\overline{d}}$ events. The thrust axis is used to estimate the s-quark production angle, with the charge identified from a $\mathrm{K}^{\pm}$ in one hemisphere, which must be opposite to either a $\mathrm{K}^{\mp}$ or a $\mathrm{K_s^0}$. For the two tagging cases, 1290 and 1580 events are selected, with $\mathrm{s\overline{s}}$ purities of 73% and 60% respectively. The corresponding analysing powers are 0.95 and 0.70, where analysing power is defined as $(N_r - N_w)/(N_r + N_w)$, and N_r (N_w) is the number of events where the thrust axis was signed correctly (incorrectly). The asymmetry is derived from a simultaneous maximum likelihood fit to the distributions shown in Figure 6.4, taking into account contributions from each flavour. As in the case of the

OPAL measurement, this analysis is designed to be self-calibrating as much as possible. The analysing powers and the $u\overline{u} + d\overline{d}$ backgrounds are constrained from the data, by examining the relative rates of single and multi-tagged hemispheres.

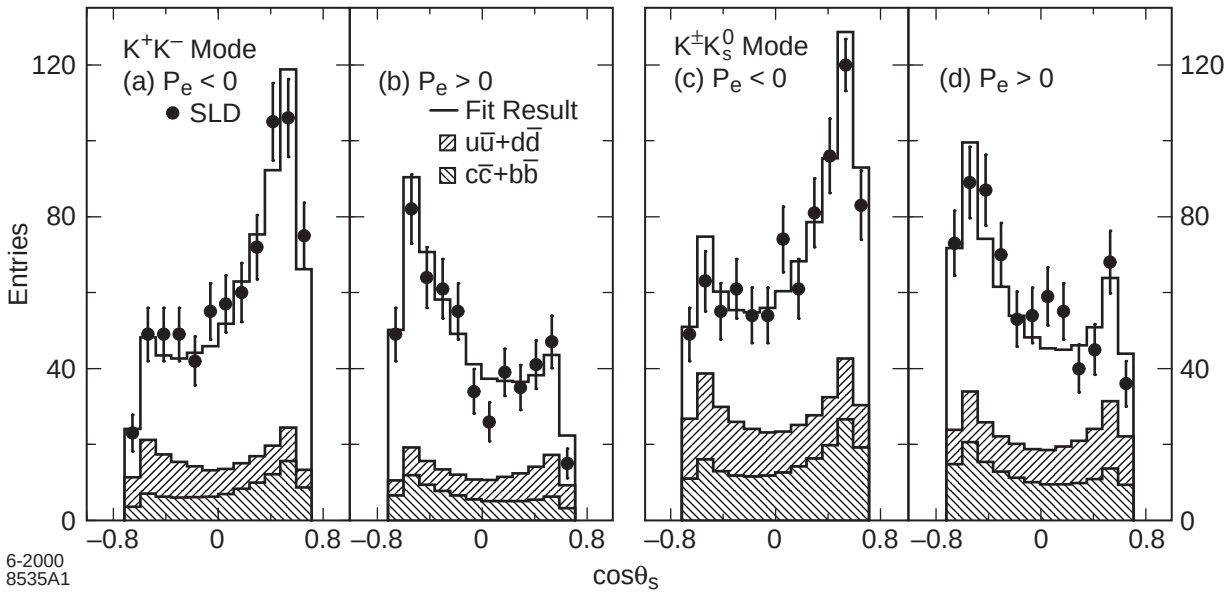

Figure 6.4: Measured s-quark polar angle distributions (dots) for selected SLD events in the a,b) K^+K^- modes, produced with a,c) left- and b,d) right-polarised electron beams. The histograms represent the result of a simultaneous fit to the four distributions, and the upper (lower) hatched areas indicate the estimated $u\overline{u} + d\overline{d}(c\overline{c} + b\overline{b})$ backgrounds.

The result of the fit is

$$\begin{aligned}
\mathcal{A}_s &= 0.895 \pm 0.066 \pm 0.062 \\
&- 0.02(R_b - 0.21656) - 0.01(\mathcal{A}_b - 0.881) \\
&+ 0.06(R_c - 0.1735\ ) - 0.20(\mathcal{A}_c - 0.641) \\
&+ 0.66(R_d - 0.21940) - 0.06(\mathcal{A}_d - 0.93528) \\
&+ 0.85(R_u - 0.17114) - 0.05(\mathcal{A}_u - 0.66619) \\
&- 1.31(R_s - 0.21940)\,,
\end{aligned} \tag{6.11}$$

where the the dependence on other electroweak parameters is given explicitly.

Common systematic uncertainties between any of these light quark results and the measurements in the heavy flavour sector, for example from QCD corrections, or the SLC electron beam polarisation, can safely be neglected for all these results, since the total statistical and systematic errors are relatively much larger. Correlations between the light-quark results are also small, in particular because the OPAL and SLD results rely on data to constrain systematic uncertainties.

6.2.2 Partial width measurements

The OPAL analysis described above [188], using 1990-1995 data, and high-momentum stable particles as a light-flavour tag, also gives measurements of the ratios of partial widths:

$$\frac{R_{\mathrm{d,s}}}{R_{\mathrm{d}}+R_{\mathrm{u}}+R_{\mathrm{s}}} = 0.371 \pm 0.016 \pm 0.016 \tag{6.12}$$

$$\frac{R_{\mathrm{u}}}{R_{\mathrm{d}}+R_{\mathrm{u}}+R_{\mathrm{s}}} = 0.258 \pm 0.031 \pm 0.032\,, \tag{6.13}$$

where $R_{\mathrm{d,s}} = R_{\mathrm{d}} = R_{\mathrm{s}}$. These two results are completely negatively correlated, so only one should be used to investigate quark couplings.

In addition, DELPHI [190], L3 [191] and OPAL [192] have used the rate of hadronic events with identified direct photons, interpreted as final state radiation from quarks, to access effective couplings defined as:

$$c_{\mathrm{u}} = (g^2_{\mathrm{Vu}} + g^2_{\mathrm{Au}} + g^2_{\mathrm{Vc}} + g^2_{\mathrm{Ac}})/2 \tag{6.14}$$

$$c_{\mathrm{d}} = (g^2_{\mathrm{Vd}} + g^2_{\mathrm{Ad}} + g^2_{\mathrm{Vs}} + g^2_{\mathrm{As}} + g^2_{\mathrm{Vb}} + g^2_{\mathrm{Ab}})/3\,, \tag{6.15}$$

which are proportional to the up-type or down-type partial widths. The measured quantity is the fraction of hadronic events with an isolated photon, which is given by

$$\Gamma(\mathrm{Z} \to \gamma + \mathrm{jets})(y_{\mathrm{cut}}) = \frac{h}{9}\frac{\alpha}{2\pi}F(y_{\mathrm{cut}})S_{\mathrm{qq}\gamma}\,, \tag{6.16}$$

where $h = 3G_{\mathrm{F}}m_{\mathrm{Z}}^3/24\pi\sqrt{2}$, $F(y_{\mathrm{cut}})$ expresses the theoretical matrix element calculation for the rate of qqγ events as a function of the jet resolution parameter y_{cut}, and $S_{\mathrm{qq}\gamma}$ is a function of the effective couplings given by:

$$S_{\mathrm{qq}\gamma} = 8c_{\mathrm{u}} + (3-\epsilon)c_{\mathrm{d}}\,. \tag{6.17}$$

This reflects the relative strengths of the up and down-type quark couplings to the photon. The quantity ϵ takes into account the b-quark mass, and is also expected to depend on the jet resolution as discussed below. The total hadronic width of the Z can be expressed as

$$\Gamma_{\mathrm{had}} = h\left[1 + \frac{\alpha_{\mathrm{S}}^{(2)}}{\pi} + 1.41\left(\frac{\alpha_{\mathrm{S}}^{(2)}}{\pi}\right)^2\right]S_{\mathrm{qq}}\,, \tag{6.18}$$

where $\alpha_{\mathrm{S}}^{(2)} = 0.1220 \pm 0.0055$ is the strong coupling constant in second order and

$$S_{\mathrm{qq}} = 2c_{\mathrm{u}} + 3c_{\mathrm{d}}\,. \tag{6.19}$$

The two Equations 6.17 and 6.19 can be solved to give the effective couplings, c_{u} and c_{d}. Although ALEPH have also investigated prompt photon production [193], the collaboration chose not to interpret these QCD studies in terms of electroweak couplings.

Experimentally, the photon is identified in hadronic events as an isolated calorimeter cluster, with no associated track. DELPHI and OPAL use shower shape variables to reduce the background from light neutral meson decays such as $\pi^0 \to \gamma\gamma$. The other dominant background is from initial state radiation. This is reduced by restricting the analysis to the central region of the detector. The event samples and the photon selection criteria are outlined in Table 6.3.

The particles in the event excluding the photon are grouped into jets. The photon is then merged with the jets using the same jet resolution parameter (DELPHI, OPAL) or the angle

	DELPHI	L3	OPAL
Data set:			
Years	91–93	90–91	90–91
Multihadron events	1.5 M	320 k	350 k
Photon selection:			
θ_γ in range	$25 - 155°$	$45 - 135°$	$\lvert\cos\theta_\gamma\rvert < 0.72$
E_γ satisfies	> 5.5 GeV	> 5.0 GeV	> 7.5 GeV
Isolation half angle	$20°, E > 400$ MeV	$15°, E > 500$ MeV	$15°, E > 250$ MeV
Jet scheme:	Durham, $y_{\rm cut} = 0.02$	JADE, $y_{\rm cut} = 0.05$	JADE, $y_{\rm cut} = 0.06$
Photon–jet	same	same	γ $20°$ from jet

Table 6.3: Comparison of direct photon analyses. The jet finding schemes and resolution parameters are those chosen for the central value of the electroweak couplings by each experiment.

between the photon and the jet (L3). The rate of isolated photons therefore depends on the jet resolution parameter that has been chosen. The rate as a function of $y_{\rm cut}$ is used in various QCD studies, but one working point is chosen for the calculation of electroweak parameters of relevance here. The rates are corrected for detector and fragmentation effects, and for the geometric acceptance. When compared with the predictions of matrix element calculations they yield a measurement of $S_{\rm qq\gamma}$.

The correction to account for the b-quark mass was estimated by L3 to be $\epsilon = 0.2 \pm 0.1$. However this correction should depend on the effective mass of the photon-jet system. No correction was used by OPAL, while DELPHI adopted the same correction as L3, but in both cases the effective mass of the photon-jet system is constrained to be about an order of magnitude larger than for L3, where the relative impact of the b-quark mass should be much smaller. For this reason, the correction has been used here for the L3 result only.

The published values for $S_{\rm qq\gamma}$ with the error categories chosen by the three experiments are as follows: for DELPHI,

$$S_{\rm qq\gamma} = 11.71 \pm 0.43 \pm 0.78 \pm 0.50 \pm 0.25^{+1.07}_{-1.78}\,, \tag{6.20}$$

where the errors account for statistics, experimental effects, theory, α_s and the y_{cut} range respectively; for L3

$$S_{\rm qq\gamma} = 11.88 \pm 1.17 \pm 0.09 \pm 0.63\,, \tag{6.21}$$

where the errors represent statistical and experimental effects, hadronisation and variations of the photon-jet collinearity cut; and for OPAL,

$$S_{\rm qq\gamma} = 12.36 \pm 0.78 \pm 0.64 \pm 0.29\,, \tag{6.22}$$

where the the first error is statistical plus experimental, the second covers photon energy and isolation requirements, and the third variations in $\alpha_{\rm S}$ and theory.

In order to derive the effective couplings, $c_{\rm u}$ and $c_{\rm d}$, common uncertainties in $S_{\rm qq\gamma}$ have been assumed of 3% relative for possible common experimental effects (for example in the η and π^0 background to the photon sample), and 5% relative for theoretical matrix element calculations, $\alpha_{\rm S}$ variations and hadronisation uncertainties. These are used to calculate the off-diagonal

terms in the covariance matrix relating the three measurements of $S_{\mathrm{qq}\gamma}$. From Equation 6.18, the value of S_{qq} is calculated to be

$$S_{\mathrm{qq}} = 6.740 \pm 0.027\,. \tag{6.23}$$

From a χ^2 fit based on the heavy-flavour averaging procedure, the derived values of the couplings are

$$c_{\mathrm{u}} = 0.89 \pm 0.14 \tag{6.24}$$

$$c_{\mathrm{d}} = 1.65 \pm 0.10\,. \tag{6.25}$$

These values are more than 99% anti-correlated, which be understood from the structure of Equations 6.17 and 6.19, and noting that the relative uncertainties on S_{qq} and $S_{\mathrm{qq}\gamma}$ are very different. The quoted errors on c_{u} and c_{d} include uncertainties due to the variation of $\Gamma_{\mathrm{Z}} = 1.7458 \pm 0.0027$ of $\delta c_{\mathrm{u}} = \mp 0.0017$ and $\delta c_{\mathrm{d}} = \pm 0.0046$, and due to the variation of $\alpha_{\mathrm{S}} = 0.1220 \pm 0.0055$ of $\delta c_{\mathrm{u}} = \pm 0.0021$ and $\delta c_{\mathrm{d}} = \mp 0.0056$. The uncertainty due to the variation of $m_{\mathrm{Z}} = 91.1875 \pm 0.0021$ GeV is negligible.

Chapter 7

Summary of Z-Pole Results

$Id: physrep_coupling.tex,v 1.76 2001/12/18 13:01:25 kellogg Exp $

7.1 Overview

The final combined Z-pole results as derived from the SLD and LEP-1 measurements, including their correlations, constitute the main result of this report. They are presented at the following locations:

- Chapter 2: Z lineshape and leptonic forward-backward asymmetries from LEP in Table 2.13;
- Chapter 3: Polarised leptonic asymmetries from SLD in Equation 3.11 and Table 3.6;
- Chapter 4: Tau polarisation from LEP in Table 4.3;
- Chapter 5: Heavy quark flavour results from SLD and LEP in Equation 5.32 and Table 5.8;
- Chapter 6: Inclusive quark flavour results from LEP in Table 6.1.

Grouping the measurement according to closely related experimental analyses, all correlations within each set of Z-pole observables extracted from the corresponding group of measurements are easily incorporated. In addition, however, correlations also exist between results extracted from different groups of measurements, arising due to common uncertainties on:

- the centre-of-mass energy:
  shared between all LEP results; shared between all SLC results;
- the beam polarisation:
  shared between all SLC results;
- the QCD correction for quark-pair final state asymmetries:
  shared between all results on quarks;

The resulting uncertainties on the individual Z-pole observables due to these sources is discussed in the corresponding chapters. Non-negligible correlations between groups of measurements are caused only by the uncertainty on the SLC beam polarisation. Thus the following additional correlations coefficients $C(\mathcal{A}_\ell, \mathcal{A}_\mathrm{q})$ between the combined results on $\mathcal{A}_\ell$ from SLD (Chapter 3)

and on $\mathcal{A}_{\mathrm{q}}$, as this quantity is measured by SLD only (Chapter 5), must be taken into account in any joint analysis of all results, namely:

$$C(\mathcal{A}_\ell, \mathcal{A}_{\mathrm{b}}) = +0.10 \tag{7.1}$$
$$C(\mathcal{A}_\ell, \mathcal{A}_{\mathrm{c}}) = +0.06\,. \tag{7.2}$$

In addition, correlations between the jet-charge based heavy-flavour asymmetries (Chapter 5) and the inclusive hadronic charge asymmetries (Section 6.1) could appear for the LEP-1 measurements. They are due to overlapping event samples and common systematic errors arising from the use of similar analysis techniques. However, this is the case only for some of the measurements from some experiments. Therefore, the resulting correlations between the overall averages on these quantities are negligible.

Even though the various sets of parameters representing the Z-pole measurements are constructed in such a way as to minimise correlations between sets and inside sets of parameters, the correlations still need to be taken into account for any precision analysis using these final Z-pole results. Also the additional correlations quantified in the above two equations are taken into account in all analyses presented in the following chapters, as they modify values of quantities derived from these combined averages at the level of several % of the respective total uncertainty.

7.2 Further Analysis

As an example, the following chapters present physics analyses based on the combined results presented previously, showing clearly their high precision and resulting predictive power. In Chapter 8, simple parameter transformations are performed in order to obtain the partial decay widths and the decay branching fractions of the Z boson, while in Chapter 9, largely model-independent analyses are presented, which express the results in various effective neutral weak current couplings, such as the asymmetry parameters, the effective coupling constants, or the effective electroweak mixing angle. Tests of lepton universality and comparisons with expectations in the framework of the Standard Model are presented. In Chapter 10, analyses and tests within the constraining framework of the Minimal Standard Model are presented, allowing the indirect determination of Standard-Model parameters such as the mass of the top quark, not directly measured at the Z pole, and the mass of the Higgs boson, not directly observed so far.

Chapter 8

Z-Boson Decay Widths and Branching Fractions

$Id: physrep_coupling.tex,v 1.76 2001/12/18 13:01:25 kellogg Exp $

As discussed above, the electroweak measurements are quoted in terms of experimentally motivated pseudo-observables defined such that correlations between them are reduced. More familiar pseudo-observables, such as Z-boson partial decay widths and branching fractions, are then obtained through simple parameter transformations.

8.1 Z-Boson Decay Parameters

The partial Z decay widths are summarised in Table 8.1. Note that they have larger correlations than the original set of results. If lepton universality is imposed, a more precise value of $\Gamma_{\rm had}$ is obtained, because $\Gamma_{\rm ee}$ in the relation between the hadronic pole cross-section and the partial widths is replaced by the more precise value of $\Gamma_{\ell\ell}$. The invisible width, $\Gamma_{\rm inv} = \Gamma_{\rm Z} - \Gamma_{\rm had} - \Gamma_{\rm ee} - \Gamma_{\mu\mu} - \Gamma_{\tau\tau}$, is also shown in the table. The Z branching fractions, *i.e.*, the ratios between each partial decay width and the total width of the Z, are shown in Table 8.2. The branching fraction to invisible particles is derived by constraining the sum of all branching fractions to one and therefore does not constitute an independent measurement.

In order to test lepton universality in Z decays quantitatively, the ratios of the leptonic partial widths or equivalently the ratios of the leptonic branching fractions is calculated. The results are:

$$\frac{\Gamma_{\mu\mu}}{\Gamma_{\rm ee}} = \frac{B(\mathrm{Z}\to\mu^+\mu^-)}{B(\mathrm{Z}\to\mathrm{e}^+\mathrm{e}^-)} = 1.0009 \pm 0.0028 \tag{8.1}$$

$$\frac{\Gamma_{\tau\tau}}{\Gamma_{\rm ee}} = \frac{B(\mathrm{Z}\to\tau^+\tau^-)}{B(\mathrm{Z}\to\mathrm{e}^+\mathrm{e}^-)} = 1.0019 \pm 0.0032 \tag{8.2}$$

with a correlation of -0.63. In both cases, good agreement with unity is observed.

Assuming lepton universality, the leptonic pole cross-section σ^0_ℓ, defined in analogy to the hadronic pole cross section, is measured to be:

$$\sigma^0_\ell \equiv \frac{12\pi}{m_{\rm Z}^2}\frac{\Gamma^2_{\ell\ell}}{\Gamma^2_{\rm Z}} = \frac{\sigma^0_{\rm h}}{R^0_\ell} = 2.0003 \pm 0.0027 \text{ nb}\,. \tag{8.3}$$

Note that this quantity has a higher sensitivity to α_s than any of the other hadronic Z-pole observables $\Gamma_{\rm Z}$, $\sigma^0_{\rm h}$ or $R^0_{\rm f}$.

Parameter	Average [MeV]	Correlations
Without Lepton Universality		
$\Gamma_{\rm had}$	1745.8 ± 2.7	
$\Gamma_{\rm ee}$	83.92 ± 0.12	−0.29
$\Gamma_{\mu\mu}$	83.99 ± 0.18	0.66 −0.20
$\Gamma_{\tau\tau}$	84.08 ± 0.22	0.54 −0.17 0.39
$\Gamma_{\rm b\overline{b}}$	377.9 ± 1.3	0.45 −0.13 0.30 0.25
$\Gamma_{\rm c\overline{c}}$	300.1 ± 5.4	0.09 −0.02 0.06 0.05 −0.09
$\Gamma_{\rm inv}$	497.4 ± 2.5	−0.67 0.78 −0.45 −0.40 −0.30 −0.06
With Lepton Universality		
$\Gamma_{\rm had}$	1744.4 ± 2.0	
$\Gamma_{\ell\ell}$	83.984 ± 0.086	0.38
$\Gamma_{\rm b\overline{b}}$	377.6 ± 1.2	0.35 0.13
$\Gamma_{\rm c\overline{c}}$	299.8 ± 5.4	0.06 0.02 −0.11
$\Gamma_{\rm inv}$	499.0 ± 1.5	−0.30 0.49 −0.10 −0.02

Table 8.1: Partial Z decay widths in MeV and error correlation coefficients, derived from the combined results of Table 2.13.

Parameter	Average [%]	Correlations
Without Lepton Universality		
$\rm B(Z \to q\overline{q})$	69.967 ± 0.093	
$\rm B(Z \to e^+e^-)$	3.3632 ± 0.0042	−0.76
$\rm B(Z \to \mu^+\mu^-)$	3.3662 ± 0.0066	0.59 −0.50
$\rm B(Z \to \tau^+\tau^-)$	3.3696 ± 0.0083	0.48 −0.40 0.33
$\rm B(Z \to b\overline{b})$	15.145 ± 0.050	0.40 −0.31 0.24 0.19
$\rm B(Z \to c\overline{c})$	12.03 ± 0.22	0.73 −0.06 0.04 0.04 −0.10
$\rm B(Z \to inv)$	19.934 ± 0.098	−0.99 0.75 −0.63 −0.54 −0.40 −0.07
With Lepton Universality		
$\rm B(Z \to q\overline{q})$	69.911 ± 0.056	
$\rm B(Z \to e^+e^-, \mu^+\mu^-, \tau^+\tau^-)$	10.0898 ± 0.0069	−0.30
$\rm B(Z \to b\overline{b})$	15.131 ± 0.047	0.26 −0.08
$\rm B(Z \to c\overline{c})$	12.02 ± 0.22	0.05 −0.01 −0.12
$\rm B(Z \to inv)$	20.000 ± 0.055	−0.99 0.18 −0.26 −0.05

Table 8.2: Z branching fractions in %, derived from the combined results of Table 2.13. Note that the branching fraction to invisible particles is fully correlated with the sum of the branching fractions to the visible final states.

8.2 Number of Light Neutrino Species

Assuming only standard particles, the invisible Z-decay width determines the number N_ν of light neutrinos species: $\Gamma_{\rm inv} = N_\nu \, \Gamma_{\nu\nu}$. Since the ratio $\Gamma_{\rm inv}/\Gamma_{\ell\ell}$ is experimentally determined with higher precision, and the Standard-Model prediction of $\Gamma_{\nu\nu}/\Gamma_{\ell\ell}$ shows a reduced dependence on the unknown Standard-Model parameters, the number of neutrinos derived from:

$$R^0_{\rm inv} \equiv \frac{\Gamma_{\rm inv}}{\Gamma_{\ell\ell}} = N_\nu \left(\frac{\Gamma_{\nu\nu}}{\Gamma_{\ell\ell}}\right)_{\rm SM} . \tag{8.4}$$

The Standard Model value for the ratio of the partial widths to neutrinos and to charged leptons is 1.9912±0.0012, where the uncertainty arises from variations of the top quark mass within its experimental error and of the Higgs mass within 100 GeV $< m_{\rm H} <$ 1000 GeV. Assuming lepton universality, the measured value of $R^0_{\rm inv}$ is:

$$R^0_{\rm inv} = 5.942 \pm 0.0016 \, , \tag{8.5}$$

and the corresponding number of light neutrino species is determined to be:

$$N_\nu = 2.9841 \pm 0.0083 \, . \tag{8.6}$$

This result fixes the number of fermion families with light neutrinos to the observed three.

8.3 Limits On Non-Standard Z Decays

Limits on non-Standard Model contributions to Z decays are obtained by taking the difference of the widths in Table 8.1 or the branching fractions of Table 8.2 with the corresponding Standard Model predictions. In order to calculate the upper limit for such contributions, parametric errors on the Standard Model prediction are added in quadrature to the experimental errors. The unknown value of the Higgs boson mass is taken into account by choosing its value within the allowed range of 114 GeV [194] to 1000 GeV such that the Standard-Model prediction is minimal, *i.e.*, either $m_{\rm H} = 114$ GeV or $m_{\rm H} = 1000$ GeV. The 95 % CL limits and the Standard Model predictions are shown in Table 8.3; these limits are Bayesian assuming zero probability below the Standard Model prediction and a uniform prior probability above.

	$\Delta\Gamma_x$ [MeV]	min. $\Gamma_{\rm SM}$ [MeV]	ΔB_x	min. $B_{\rm SM}$
Without Lepton Universality				
$Z \to q\overline{q}$	15.1	1735.6±1.4	0.0035	0.69773 ±0.00014
$Z \to e^+e^-$	0.36	83.780±0.047	0.00007	0.033662±0.000015
$Z \to \mu^+\mu^-$	0.54	83.779±0.047	0.00013	0.033662±0.000015
$Z \to \tau^+\tau^-$	0.85	83.590±0.047	0.00025	0.033586±0.000015
$Z \to b\overline{b}$		±		±
$Z \to c\overline{c}$		±		±
$Z \to$ inv		±		±
With Lepton Universality				
$Z \to q\overline{q}$	12.7	1735.6±1.4	0.0023	0.69773 ±0.00014
$Z \to e^+e^-, \mu^+\mu^-, \tau^+\tau^-$	1.10	251.15±0.14	0.00015	0.100910±0.000045
$Z \to b\overline{b}$		±		±
$Z \to b\overline{b}$		±		±
$Z \to$ inv	2.1	500.7±0.2	0.00061	0.20105 ±0.00009

Table 8.3: Limits on non-Standard Model contributions to the Z widhts and branching fractions, derived from the results of Tables 8.1 and 8.2. The values assumed for $m_{\rm t}$, $\alpha(m_{\rm Z}^2)$ and $\alpha_{\rm S}(m_{\rm Z}^2)$ are those of Table 10.6 in Chapter 10; the Higgs mass was chosen to be 114 GeV for the leptonic branching fractions and 1000 GeV for all others, since this gives the smallest value of the Standard Model prediction; the minimal Standard Model predictions for the widths and branching fractions are shown with their parametric errors. Note that there are correlations among the experimental and theoretical errors, and therefore the limits must not be used simultaneously.

Chapter 9

Effective Couplings of the Neutral Weak Current

$Id: physrep_coupling.tex,v 1.76 2001/12/18 13:01:25 kellogg Exp $

The experimental measurements and results on electroweak Z-pole observables are presented in the previous chapters. These measurements are now used to derive best values for various effective couplings of the neutral weak current at the Z pole, namely: the asymmetry parameters $\mathcal{A}_{\rm f}$ in Section 9.1, the effective vector- and axial-vector coupling constants $g_{\rm Vf}$ and $g_{\rm Af}$ in Section 9.2, the $\rho_{\rm f}$ parameters and the effective electroweak mixing angles $\sin^2\theta^{\rm f}_{\rm eff}$ in Section 9.3, and the leptonic effective electroweak mixing angle $\sin^2\theta^{\rm lept}_{\rm eff}$ in Section 9.4. The results of these model-independent analyses are compared to the expectations within the framework of the Minimal Standard Model, thereby testing its validity. A concluding discussion of these analyses is given in Section 9.5.

The inputs consist of the results presented in the previous chapters, not assuming lepton universality when deriving results for the different charged lepton species separately; otherwise the results assuming lepton universality are used. The newly derived couplings are determined in a fit to these input results, based on the simple expressions, listed Section 1.4, of the input variables in terms of the couplings to be determined. Those input results which cannot be expressed by the couplings to be determined, *e.g.*, $m_{\rm Z}$, $\Gamma_{\rm Z}$, $\sigma^0_{\rm h}$, are left floating in the fit as well.

For the determination of only leptonic couplings, including tests of lepton universality, the results of Chapters 2, 3 and 4 are taken as input. For the determination of quark couplings, the results presented in Chapter 5 are included as well and lepton universality is assumed. In the analysis for the effective electroweak mixing angle, its determination based on the hadronic charge asymmetry, Chapter 6, is also used.

9.1 The Asymmetry Parameters $\mathcal{A}_{\rm f}$

Owing to polarised electron beams at SLC, the asymmetry parameters $\mathcal{A}_{\rm f}$ are measured directly by the SLD collaboration: $A_{\rm LR} = \mathcal{A}_{\rm e}$ and $A^{\rm f}_{\rm FBLR} = (3/4)\mathcal{A}_{\rm f}$. The analyses of tau polarisation at LEP determine $\mathcal{A}_{\rm e}$ and $\mathcal{A}_\tau$ separately. The forward-backward pole asymmetries, $A^{0,{\rm f}}_{\rm FB} = (3/4)\mathcal{A}_{\rm e}\mathcal{A}_{\rm f}$, constrain the product of two asymmetry parameters. The measurements are performed separately for all three charged lepton species as well as the quarks flavours b and c (and s?) The results on the leptonic asymmetry parameters derived from measurements independent of quark asymmetry parameters are reported in Table 9.1.

Parameter	Average	Correlations		
		$\mathcal{A}_e$	$\mathcal{A}_\mu$	$\mathcal{A}_\tau$
$\mathcal{A}_e$	0.1514±0.0019	+1.00	−0.10	−0.02
$\mathcal{A}_\mu$	0.1456±0.0091	−0.10	+1.00	+0.01
$\mathcal{A}_\tau$	0.1449±0.0040	−0.02	+0.01	+1.00

Table 9.1: Results on the leptonic asymmetry parameters $\mathcal{A}_\ell$ not assuming neutral-current lepton universality and not including quark-related measurements. The combination has a χ^2/dof of 3.6/5, corresponding to a probability of 61%.

The values of the asymmetry parameters obtained for the three lepton species agree well. Under the assumption of neutral-current lepton universality, the combined result is:

$$\mathcal{A}_\ell \;=\; 0.1501 \pm 0.0016\,. \tag{9.1}$$

This average has a χ^2/dof of 1.6/2, corresponding to a probability of 44%.

As already discussed in Section 5.9 and shown in Figure 5.17, the ratios of the forward-backward pole asymmetries $A_{\rm FB}^{0,\rm b}/A_{\rm FB}^{0,\rm c} = \mathcal{A}_{\rm b}/\mathcal{A}_{\rm c}$ agree well with the ratios of the direct measurements of the asymmetry parameters $\mathcal{A}_{\rm b}$ and $\mathcal{A}_{\rm c}$. The mutual consistency of the measurements of $\mathcal{A}_{\rm q}$, $A_{\rm FB}^{0,\rm q} = (3/4)\mathcal{A}_{\rm e}\mathcal{A}_{\rm q}$ and $\mathcal{A}_\ell$ assuming lepton universality is shown in Figure 9.1 for b and c (and s?) quarks. The comparisons are valid since the results on both $\mathcal{A}_{\rm q}$ and $A_{\rm FB}^{0,\rm q}$ have QCD corrections as expected in the Standard Model and as calculated with ZFITTER [24] removed, see Section 5.7.2.

Compared to the experimental uncertainties, the Standard Model predictions are nearly constant in $\mathcal{A}_{\rm q}$, in contrast to the situation for $\mathcal{A}_\ell$. This is a consequence of the Standard-Model values of the electric charge and of the iso-spin for quarks, Table 1.3, leading to a small dependence of $\mathcal{A}_{\rm q}$, which is a function of the ratio $g_{{\rm V}q}/g_{{\rm A}q}$ (Equation 1.44) and thus of the effective electroweak mixing angle only (Equations 1.11 and 1.12), to this parameter. Therefore, the comparison of the various determinations of the quark asymmetry parameters $\mathcal{A}_{\rm q}$, reported in Table 9.2, allows the Standard Model to be tested in a manner which is unaffected by radiative corrections or the knowledge of other Standard-Model parameters.

Flavour q	$\frac{4}{3}\frac{A_{\rm FB}^{0,\rm q}}{\mathcal{A}_\ell}$	Direct $\mathcal{A}_{\rm q}$	SM
b	0.879±0.018	0.922±0.020	0.935±0.001
c	0.608±0.031	0.670±0.026	0.668±0.002

Table 9.2: Determination of the quark asymmetry parameters $\mathcal{A}_{\rm q}$, based on the ratio $A_{\rm FB}^{0,\rm q}/\mathcal{A}_\ell$ and the direct measurement $A_{\rm FBLR}^{\rm q}$. Lepton universality for $\mathcal{A}_\ell$ is assumed. The expectation of $\mathcal{A}_{\rm q}$ in the Standard Model is listed in the last column.

Each ratio $(4/3)A_{\rm FB}^{0,\rm q}/\mathcal{A}_\ell$ also determines $\mathcal{A}_{\rm q}$, with a precision comparable to that of the direct measurements of $\mathcal{A}_{\rm q}$. The ratios are lower than the direct measurements by 1.6 and 1.5 standard deviations for b and c quarks, respectively. Compared to the Standard Model expectations, the ratios are lower by 3.1 and 1.9 standard deviations respectively, while the direct measurements agree very well with the Standard Model expectations.

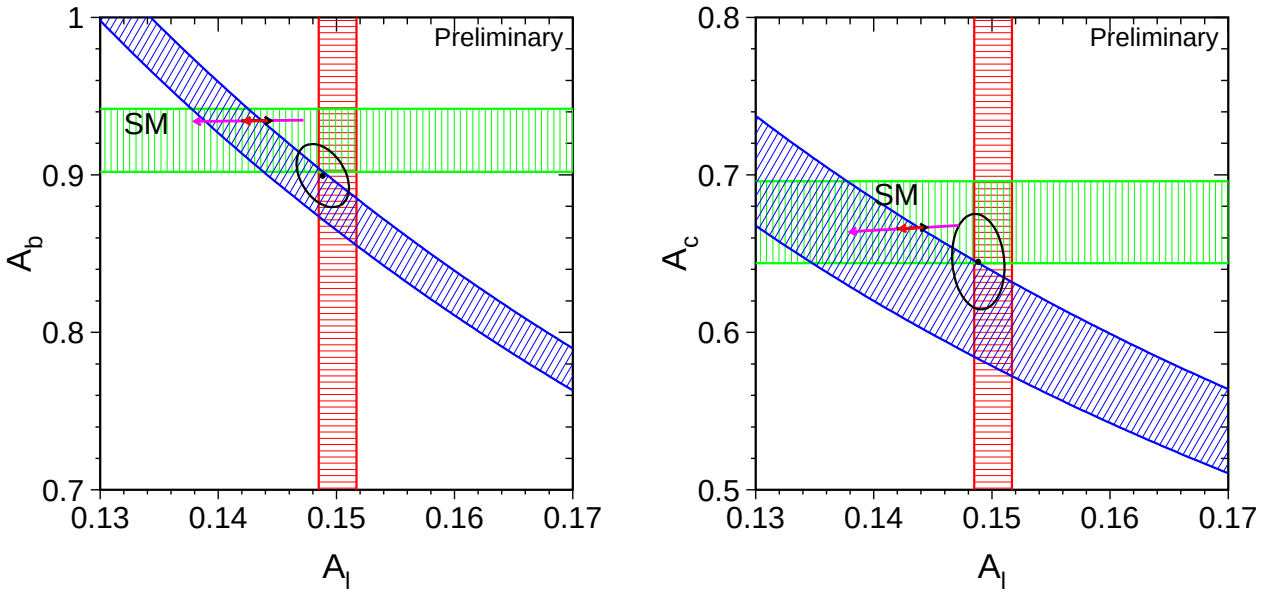

Figure 9.1: Comparison of the measurements of $\mathcal{A}_\ell$, $\mathcal{A}_\mathrm{q}$ and $A_\mathrm{FB}^{0,\mathrm{q}}$ for (left) b-quarks, (right) c-quarks, and s-quarks? assuming lepton universality. Bands of ± 1 standard deviation width in the $(\mathcal{A}_\ell, \mathcal{A}_\mathrm{q})$ plane are shown for the measurements of $\mathcal{A}_\ell$ (vertical band), $\mathcal{A}_\mathrm{q}$ (horizontal band), and $A_\mathrm{FB}^{0,\mathrm{q}} = (3/4)\mathcal{A}_\mathrm{e}\mathcal{A}_\mathrm{q}$ (diagonal band). Also shown is the 68% confidence level contour for the two asymmetry parameters resulting from the joint analysis (Table 9.3). The arrows pointing to the right and to the left show the variation in the Standard-Model prediction for varying m_t in the range 174.3 ± 5.1 GeV and m_H in the range of 300^{+700}_{-186} GeV, respectively. Varying the hadronic vacuum polarisation by $\Delta\alpha^{(5)}_\mathrm{had}(m_\mathrm{Z}^2) = 0.02761 \pm 0.00036$ yields an additional uncertainty on the Standard-Model prediction, oriented in direction of the Higgs-boson arrow and size corresponding to the top-quark arrow.

The results of the joint analysis of the leptonic and heavy-flavour measurements in terms of the asymmetry parameters $\mathcal{A}_\mathrm{f}$ are reported in Table 9.3, where the contraint of lepton universality is also imposed. Since the leptonic asymmetry parameter $\mathcal{A}_\ell$ is already well determined, the measurements of $A_\mathrm{FB}^{0,\mathrm{q}}$ improve the determination of the quark asymmetry parameters $\mathcal{A}_\mathrm{q}$. In the combined analysis, all of the resulting asymmetry parameters $\mathcal{A}_\mathrm{f}$ are decreased in value compared to their direct measurements, as shown in Figure 9.1. Compared to the Standard Model expectation, the combined extracted values for $\mathcal{A}_\mathrm{b}$ and $\mathcal{A}_\mathrm{c}$ are lower by 2.8 and 1.2 standard deviations respectively.

9.2 The Effective Vector and Axial-Vector Coupling Constants

The asymmetry parameters $\mathcal{A}_\mathrm{f}$ depend only on the ratio $g_\mathrm{Vf}/g_\mathrm{Af}$ of the effective vector and axial-vector coupling constants as shown in Equation 1.44. In contrast, the partial decay widths of the Z boson determine the sum of the squares of these two coupling constants (Equation 1.32).

Parameter	Average	Correlations			
		$\mathcal{A}_\ell$	$\mathcal{A}_\mathrm{b}$	$\mathcal{A}_\mathrm{c}$	$\mathcal{A}_\mathrm{s}$
$\mathcal{A}_\ell$	0.1488±0.0015	+1.00	−0.39	−0.11	
$\mathcal{A}_\mathrm{b}$	0.899±0.013	−0.39	+1.00	+0.17	
$\mathcal{A}_\mathrm{c}$	0.645±0.020	−0.11	+0.17	+1.00	
$\mathcal{A}_\mathrm{s}$	±				+1.00

Table 9.3: Results on the quark asymmetry parameters $\mathcal{A}_\mathrm{q}$ and the leptonic asymmetry parameter $\mathcal{A}_\ell$ assuming neutral-current lepton universality and including quark-related measurements containing also information on $\mathcal{A}_\ell$. The combination has a χ^2/dof of 5.4/4, corresponding to a probability of 25%.

It is thus possible to disentangle the effective coupling constants g_Vf and g_Af by analysing both the asymmetry measurements as well as the partial Z decay widths

For charged leptons, the results on $g_{\mathrm{V}\ell}$ and $g_{\mathrm{A}\ell}$ are reported in Table 9.4. The comparison of different lepton species in the $(g_{\mathrm{V}\ell}, g_{\mathrm{A}\ell})$ plane is also shown in Figure 9.2a. Good agreement is observed.

Parameter	Average	Correlations					
		g_Ae	$g_{\mathrm{A}\mu}$	$g_{\mathrm{A}\tau}$	g_Ve	$g_{\mathrm{V}\mu}$	$g_{\mathrm{V}\tau}$
g_Ae	−0.50111±0.00035	+1.00	−0.13	−0.12	+0.01	0.00	−0.01
$g_{\mathrm{A}\mu}$	−0.50120±0.00054	−0.13	+1.00	+0.35	−0.01	−0.30	+0.01
$g_{\mathrm{A}\tau}$	−0.50204±0.00064	−0.12	+0.35	+1.00	−0.03	+0.01	−0.07
g_Ve	−0.03816±0.00047	+0.01	−0.01	−0.03	+1.00	−0.10	−0.02
$g_{\mathrm{V}\mu}$	−0.0367±0.0023	0.00	−0.30	+0.01	−0.10	+1.00	+0.01
$g_{\mathrm{V}\tau}$	−0.0366±0.0010	−0.01	+0.01	−0.07	−0.02	+0.01	+1.00

Table 9.4: Results on the effective vector and axial-vector coupling constants for leptons not assuming neutral-current lepton universality. The combination has a χ^2/dof of 3.6/5, corresponding to a probability of 61%.

The combined result under the assumption of neutral-current lepton universality is:

$$g_{\mathrm{V}\ell} = -0.03783 \pm 0.00041 \tag{9.2}$$
$$g_{\mathrm{A}\ell} = -0.50123 \pm 0.00026\,, \tag{9.3}$$

with a correlation of −0.06. This average has a χ^2/dof of 1.6/2, corresponding to a probability of 44%. The value of $g_{\mathrm{A}\ell}$ is different from the corresponding Born-level value of $T_3^\ell = -1/2$ by 4.7 standard deviations, indicating the presence of non-trivial electroweak radiative corrections.

The effective coupling constant of the Z boson to neutrinos is derived from the partial decay width of the Z into invisible particles, attributing it solely to decays into neutrino pairs. Assuming three neutrino families with equal effective coupling constants, the result is:

$$|g_{A\nu}| = |g_{V\nu}| = 0.50068 \pm 0.00075\,. \tag{9.4}$$

Including the heavy-quark measurements and assuming lepton universality, the results are reported in Table 9.5. Note that the QCD corrections absorbed in the partial widths for quark-pair final states are taken from the Standard Model and are calculated with ZFITTER [24] when extracting effective quark couplings from partial widths. This is consistent with the treatment of the various asymmetries in quark-pair production, see Section 5.7.2, which also have final-state QCD effects as expected in the Standard Model removed.

Parameter	Average	Correlations					
		$g_{\mathrm{A}\ell}$	g_{Ab}	g_{Ac}	$g_{\mathrm{V}\ell}$	g_{Vb}	g_{Vc}
$g_{\mathrm{A}\ell}$	-0.50125 ± 0.00026	$+1.00$	-0.01	-0.02	-0.04	$+0.05$	-0.02
g_{Ab}	-0.5146 ± 0.0051	-0.01	$+1.00$	-0.02	$+0.38$	-0.97	$+0.17$
g_{Ac}	$+0.5043\pm0.0052$	-0.02	-0.02	$+1.00$	-0.06	$+0.05$	-0.27
$g_{\mathrm{V}\ell}$	-0.03751 ± 0.00037	-0.04	$+0.38$	-0.06	$+1.00$	-0.39	$+0.11$
g_{Vb}	-0.3221 ± 0.0077	$+0.05$	-0.97	$+0.05$	-0.39	$+1.00$	-0.18
g_{Vc}	$+0.1843\pm0.0067$	-0.02	$+0.17$	-0.27	$+0.11$	-0.18	$+1.00$

Table 9.5: Results on the effective coupling constants for leptons and quarks assuming neutral-current lepton universality. The combination has a χ^2/dof of 5.4/4, corresponding to a probability of 25%.

The leptonic vector coupling constant is decreased in magnitude compared to Equation 9.2 as already observed for the asymmetry parameter $\mathcal{A}_\ell$ in the previous section. For the quark flavours b and c (and s?), the results are also shown in Figure 9.2. The strong anti-correlation between the b-quark couplings arises from the tight constraint on their squares due to the measurement of R^0_{b}. The apparent deviation of the measured b-quark coupling constants from the Standard-Model expectation is a direct consequence of the combined result on $\mathcal{A}_{\mathrm{b}}$ being lower than the Standard-Model expectation as discussed in the previous section.

9.3 The ρ_{f} Parameters and the Effective Electroweak Mixing Angles

The effective vector and axial-vector coupling constants obey a simple relation with the ρ parameter and the effective electroweak mixing angle, see Equations 1.11 and 1.12. For the following analyses, the electric charge Q_{f} and the third component of the weak iso-spin I^3_{f} are assumed to be given by the Standard-Model assignments as listed in Table 1.3. Tests of fermion universality, *i.e.*, a comparison between leptons and quarks in terms of ρ_{f} and $\sin^2\theta^{\mathrm{f}}_{\mathrm{eff}}$, now become possible.

Considering the leptonic measurements alone and assuming lepton universality, the combined results on ρ_ℓ and $\sin^2\theta^{\mathrm{lept}}_{\mathrm{eff}}$ are found to be:

$$\rho_\ell = 1.0049 \pm 0.0010 \tag{9.5}$$

$$\sin^2\theta^{\mathrm{lept}}_{\mathrm{eff}} = 0.23113 \pm 0.00021\,, \tag{9.6}$$

with a correlation of +0.11. For neutrinos, based on Equation 9.4, the ρ parameter is determined

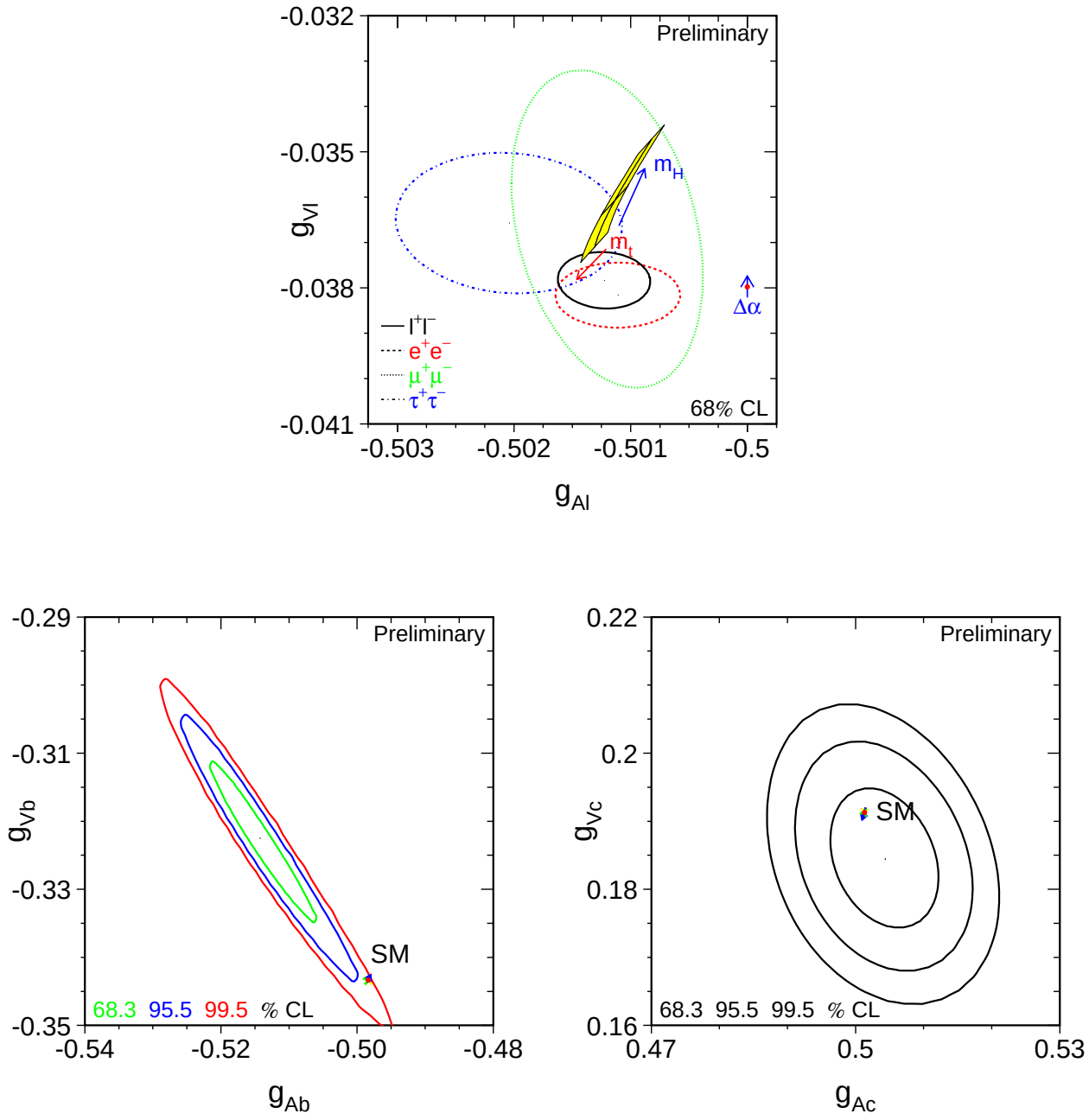

Figure 9.2: Comparison of the effective vector and axial-vector coupling constants for fermions. Top: leptons not including results on quarks (Table 9.4); bottom: quarks using results on leptons and assuming lepton universality (Table 9.5). The shaded region in (a) shows the predictions within the Standard Model for $m_{\mathrm{t}} = 174.3 \pm 5.1$ GeV and $m_{\mathrm{H}} = 300^{+700}_{-186}$ GeV; varying the hadronic vacuum polarisation by $\Delta\alpha^{(5)}_{\mathrm{had}}(m^2_{\mathrm{Z}}) = 0.02761 \pm 0.00036$ yields an additional uncertainty on the Standard-Model prediction shown by the arrow labelled $\Delta\alpha$. Compared to the experimental uncertainties, the Standard Model predictions in (b) and (c) are nearly constant for the quark coupling constants.

to be:

$$\rho_\nu \;=\; 1.0027 \pm 0.0030\,. \tag{9.7}$$

Adding the heavy-quark measurements, the results on ρ_f and the effective electroweak mixing angle for leptons and quarks are reported in Table 9.6. The measurement of $\sin^2\theta^{\mathrm{lept}}_{\mathrm{eff}}$ based on the hadronic charge asymmetry as discussed in Section 6.1 (Table 6.1) is included here. As before, neutral-current lepton universality is assumed. The value of ρ_ℓ is different from the corresponding Born-level value of unity by 5.0 standard deviations, again indicating the presence of non-trivial electroweak radiative corrections. The strong anti-correlation between ρ_b and $\sin^2\theta^{\mathrm{b}}_{\mathrm{eff}}$ arises, as for g_{Vb} and g_{Ab} above, from the tight constraint given by the measurement of R^0_b.

Parameter	Average	Correlations					
		ρ_ℓ	ρ_b	ρ_c	$\sin^2\theta^{\mathrm{lept}}_{\mathrm{eff}}$	$\sin^2\theta^{\mathrm{b}}_{\mathrm{eff}}$	$\sin^2\theta^{\mathrm{c}}_{\mathrm{eff}}$
ρ_ℓ	1.0050±0.0010	+1.00	−0.01	+0.02	+0.09	−0.04	−0.01
ρ_b	1.058±0.021	−0.01	+1.00	+0.02	−0.37	+0.99	+0.16
ρ_c	1.017±0.021	+0.02	+0.02	+1.00	−0.05	+0.04	+0.50
$\sin^2\theta^{\mathrm{lept}}_{\mathrm{eff}}$	0.23132±0.00018	+0.09	−0.37	−0.05	+1.00	−0.38	−0.11
$\sin^2\theta^{\mathrm{b}}_{\mathrm{eff}}$	0.280±0.016	−0.04	+0.99	+0.04	−0.38	+1.00	+0.17
$\sin^2\theta^{\mathrm{c}}_{\mathrm{eff}}$	0.2378±0.0056	−0.01	+0.16	+0.50	−0.11	+0.17	+1.00

Table 9.6: Results on the ρ parameter and the effective electroweak mixing angle $\sin^2\theta^{\mathrm{f}}_{\mathrm{eff}}$ assuming neutral-current lepton universality. The combination has a χ^2/dof of 6.3/5, corresponding to a probability of 28%.

The comparison between the different fermion species is shown graphically in Figure 9.3. Within the Standard Model, slightly different values for both ρ_f and $\sin^2\theta^{\mathrm{f}}_{\mathrm{eff}}$ are expected for different fermions due to non-universal flavour-specific electroweak radiative corrections. These specific corrections are largest for b quarks, $\rho_\mathrm{b} - \rho_\ell \approx -0.011$ and $\sin^2\theta^{\mathrm{b}}_{\mathrm{eff}} - \sin^2\theta^{\mathrm{lept}}_{\mathrm{eff}} \approx 0.0014$, and more than a factor of five smaller for the other quark flavours, as also shown in Figure 9.3. For all fermions the non-universal flavour-specific corrections expected in the Standard Model are small compared to the experimental errors.

9.4 The Leptonic Effective Electroweak Mixing Angle

The measurements of the various asymmetries determine $\sin^2\theta^{\mathrm{f}}_{\mathrm{eff}}$ independently of ρ_f as they depend only on the ratio of the effective coupling constants, $g_{\mathrm{Vf}}/g_{\mathrm{Af}}$. Because of the values of the electric charge Q_f and the third component of the weak iso-spin I^3_f as listed in Table 1.3, the sensitivity of the quark vector coupling $g_{\mathrm{V}q}$, and hence of $\mathcal{A}_\mathrm{q}$ and of $A^{0,\mathrm{q}}_{\mathrm{FB}}$, to $\sin^2\theta^{\mathrm{q}}_{\mathrm{eff}}$ is smaller than that for leptons. This is also visible in Figures 9.1 and 9.2, showing that for up-type quarks as well as down-type quarks both the asymmetry parameters $\mathcal{A}_\mathrm{q}$ and the effective coupling constants $g_{\mathrm{A}q}$ and $g_{\mathrm{V}q}$ are, on the scale of the experimental uncertainties, nearly constant within the Standard Model. Therefore, the heavy quark forward-backward asymmetries $A^{0,\mathrm{q}}_{\mathrm{FB}} = (3/4)\mathcal{A}_\mathrm{e}\mathcal{A}_\mathrm{q}$ as well as the hadronic charge asymmetry $\langle Q_{\mathrm{FB}}\rangle$, being sensitive

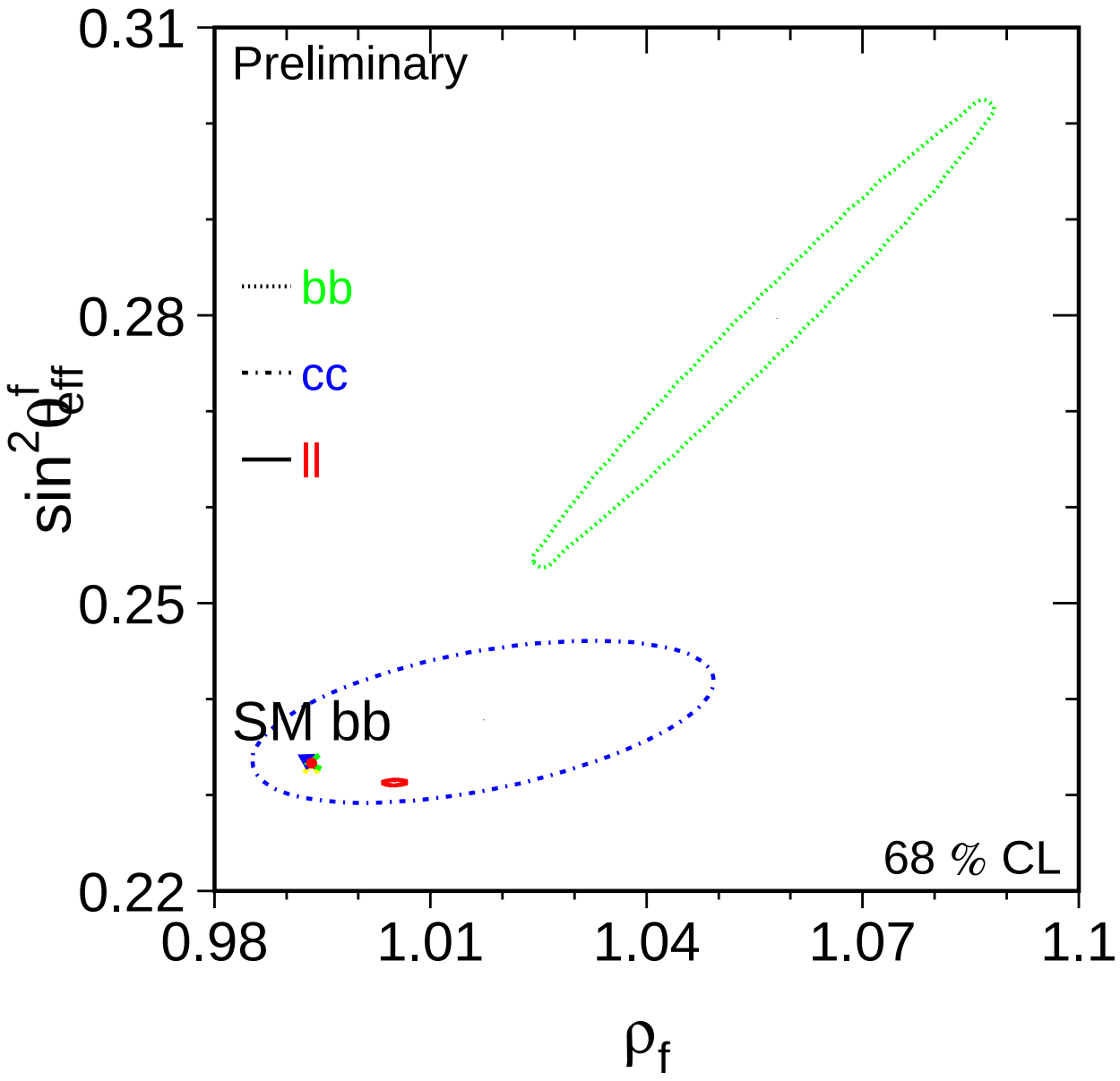

Figure 9.3: Comparison of ρ_f and the effective electroweak mixing angle $\sin^2\theta^f_{\rm eff}$ for leptons, b and c quarks. The Standard Model expectation for b quarks is shown as the dot ($\rho_b < 1$); those of c quarks and of leptons is not drawn as they lie at the same area as the experimental contour curve for leptons ($\rho_\ell > 1$). Decreasing R^0_b while keeping $A^{0,b}_{FB}$ fixed moves the b-quark contour parallel to the ρ-axis in the direction of decreasing ρ values. Decreasing $A^{0,b}_{FB}$ while keeping R^0_b fixed moves the b-quark contour along its long axis towards the Standard Model expectation.

to $\sin^2\theta^{\rm lept}_{\rm eff}$ through the factor $\mathcal{A}_{\rm e}$ rather than to $\sin^2\theta^{\rm q}_{\rm eff}$, can be interpreted as a measurement of $\sin^2\theta^{\rm lept}_{\rm eff}$.

Assuming the Standard-Model structure of the effective coupling constants in terms of $\rho_{\rm f}$ and $\sin^2\theta^{\rm f}_{\rm eff}$, the measurements of the various asymmetries are compared in terms of $\sin^2\theta^{\rm lept}_{\rm eff}$ in Figure 9.4. The measurements are grouped into two sets of three results each. In the first set, the results on $\sin^2\theta^{\rm lept}_{\rm eff}$ are derived from measurements depending on leptonic couplings only, $A^{0,\ell}_{\rm FB}$, $\mathcal{A}_\ell$(SLD) and $\mathcal{A}_\ell(P_\tau)$. In this case, only lepton universality is assumed, and no further corrections are necessary. In the second set, consisting of $A^{0,\rm b}_{\rm FB}$, $A^{0,\rm c}_{\rm FB}$ and $\langle Q_{\rm FB}\rangle$, quark couplings are involved. In this case, the small non-universal flavour-specific electroweak corrections, making $\sin^2\theta^{\rm lept}_{\rm eff}$ different from $\sin^2\theta^{\rm q}_{\rm eff}$, must be taken from the Standard Model. The effect of these corrections and their uncertainties on the extracted value of $\sin^2\theta^{\rm lept}_{\rm eff}$ is, however, negligible.

The two sets of measurements yield averages values for $\sin^2\theta^{\rm lept}_{\rm eff}$ of 0.23113 ± 0.00021 ($\chi^2/dof = 1.6/2$) and 0.23230 ± 0.00029 ($\chi^2/dof = 0.33/2$), respectively, which differ by about 3.3 standard deviations. As a consequence, the average of all six $\sin^2\theta^{\rm lept}_{\rm eff}$ determinations, yielding $\sin^2\theta^{\rm lept}_{\rm eff} = 0.23152 \pm 0.00017$, has a χ^2/dof of 12.8/5, corresponding to a probability of only 2.5%. The two most precise determinations of $\sin^2\theta^{\rm lept}_{\rm eff}$, namely those derived from the measurements of $\mathcal{A}_\ell$ by SLD, dominated by the $A_{\rm LR}$ result, and of $A^{0,\rm b}_{\rm FB}$ at LEP, yield the largest pulls and fall on opposite sides of the $\sin^2\theta^{\rm lept}_{\rm eff}$ average. This is a consequence of the same effect as discussed in the previous sections: the deviation in $\mathcal{A}_{\rm b}$ as extracted from $A^{0,\rm b}_{\rm FB}$ discussed previously is reflected in the value of $\sin^2\theta^{\rm lept}_{\rm eff}$ extracted from $A^{0,\rm b}_{\rm FB}$.

9.5 Discussion

The unexpectedly large shifts observed in the various analyses for asymmetry parameters, effective coupling constants, $\rho_{\rm f}$ and $\sin^2\theta^{\rm lept}_{\rm eff}$ all show the consequences of the same effect. It is most clearly visible in the effective couplings and $\sin^2\theta^{\rm lept}_{\rm eff}$ averages.

The results as shown in Figure 9.2 suggest that the effective couplings for b-quarks cause the main effect; both $g_{\rm Vb}$ and $g_{\rm Ab}$ deviate from the expectation. In terms of the left- and right-handed couplings $g_{\rm Lb}$ and $g_{\rm Rb}$, however, only $g_{\rm Rb}$ shows a noticeable deviation from the expectation, at the level of three standard deviations. Since for b-quarks with electric charge $-1/3$ and weak isospin $-1/2$ one has $|g_{\rm Rb}| \ll |g_{\rm Lb}|$, the effect could be explained by a change in the right-handed b-quark coupling already at Born level. This would affect $\mathcal{A}_{\rm b}$ and $A^{0,\rm b}_{\rm FB}$, both depending only on the ratio $g_{\rm Rb}/g_{\rm Lb}$, more strongly than $R^0_{\rm b} \propto g^2_{\rm Rb} + g^2_{\rm Lb}$.

From the experimental point of view, no systematic effect potentially explaining such large shifts could be identified. Within the Standard Model, flavour specific electroweak radiative corrections and their uncertainties are likewise too small to explain the difference in the extracted $\sin^2\theta^{\rm lept}_{\rm eff}$ values. All known uncertainties are investigated and are taken into account in the analyses.

Thus the effect is either a sign for new physics, invalidating the simple relations to convert between the effective parameters used in this chapter, or a fluctuation in one or more of the input measurements. In the following we assume the latter and thus neither modify nor exclude any of the measurements. As a direct consequence, the χ^2/dof in all analyses including these measurements will be rather large due to the contribution of at least 12.8 units from the six asymmetry measurements.

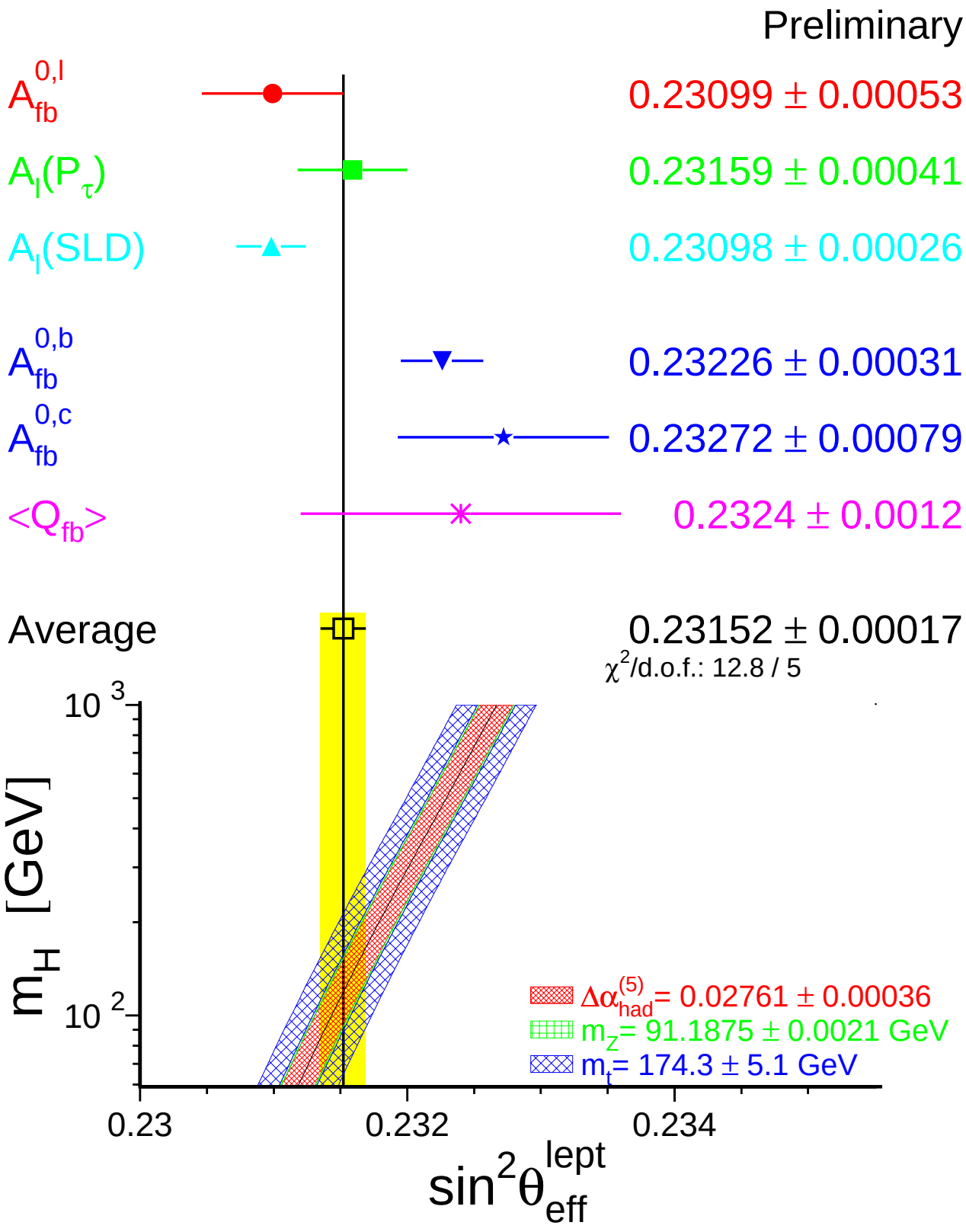

Figure 9.4: Comparison of the effective electroweak mixing angle $\sin^2\theta_{\rm eff}^{\rm lept}$ derived from measurement results depending on lepton couplings only (top) and also quark couplings (bottom). Also shown is the prediction of $\sin^2\theta_{\rm eff}^{\rm lept}$ in the Standard Model as a function of $m_{\rm H}$. The additional uncertainty of the Standard Model prediction shown is parametric and dominated by the uncertainties in $\Delta\alpha_{\rm had}^{(5)}(m_{\rm Z}^2)$ and $m_{\rm t}$, shown as the bands. The total width of the band is the linear sum of these effects.

Chapter 10

Constraints on the Standard Model

$Id: physrep_sm.tex,v 1.97 2001/12/18 15:09:43 gruenew Exp $

Numbers in this chapter not consistent concerning the final NuTeV result!

In the previous sections, several figures have already shown comparisons between the experimental results and the expectations from the Standard Model [4]. As discussed in Section 1.4, the Standard Model prediction for each Z-pole observable depends on free parameters which are not predicted by the theory, such as the coupling constants of the various interactions and the masses of the fundamental fermions (quarks and leptons) and heavy bosons (Z, W, and H). Owing to this dependence, directly at Born level or through electroweak radiative corrections, the experimental measurements of Z-pole and other observables allow us to constrain these free parameters. Most importantly it is possible to determine the mass of the top quark precisely and also the mass of the Higgs boson, albeit with less precision.

The input parameter set for Standard-Model calculations is discussed in Section 10.1. An important ingredient, the hadronic vacuum polarisation, is discussed in Section 10.2. Additional measurements from other experiments, used to increase the precision of the Standard-Model constraints, are reported in Section 10.3. Theoretical uncertainties in the calculation of Standard-Model predictions for important observables are discussed in Section 10.4. The analysis and fitting procedure used in this chapter is described in Section 10.5. The remaining sections present the results of the Standard-Model analyses. The sensitivity of the measurements to radiative corrections is discussed in Section 10.6, the complete view is given in Section 10.7. Constraints on the input parameters of the Standard Model, in particular on the masses of the heavy particles top quark, W boson and Higgs boson are reported in Section 10.8. A concluding discussion is presented in Section 10.9.

10.1 Parameters of the Minimal Standard Model

The masses of all known fundamental fermions with the exception of the top quark are small compared to the Z mass, 91 GeV, and precisely enough measured so that their influence on Z-pole observables through kinematic effects is both rather small and calculable to more than adequate precision. The only exception is the top quark with a mass of about 175 GeV, which it is too heavy to be produced directly in e^+e^- collisions at LEP1/SLC centre-of-mass energies close to the Z pole, $\sqrt{s} < 100$ GeV. However, as discussed in Section 1.4, it controls the size of the electroweak radiative corrections, because to leading order these corrections depend quadratically on the fermion mass. The top-quark mass is therefore one of the parameters of

the Standard Model which will be determined in the following, while the masses of all other fundamental fermions are fixed. The comparison of such an indirect determination of the top-quark mass with the direct measurement obtained from $t\bar{t}$ production in proton-antiproton collisions at the TEVATRON constitutes an important test of the Standard Model.

For the electromagnetic, weak and strong interactions described by the Standard Model, the corresponding three coupling constants are also not predicted, but must be inferred from measurements. Because the Standard Model gives an integrated description of the electromagnetic and the weak interaction in the form of the electroweak theory, the weak coupling is related to the electromagnetic coupling and the masses of the charged and neutral heavy gauge bosons W and Z. Therefore, just two coupling constants, those of the electromagnetic and the strong interaction, α and α_S, are considered, together with the masses of the heavy gauge bosons W and Z. The mass of the electromagnetic gauge boson, the photon, is fixed at zero as required by the theory of QED.

The mass of the Z boson is precisely measured as described in Chapter 2. When calculating radiative corrections for Z pole observables, it is advantageous to replace the mass of the W boson by the Fermi constant, $G_F = 1.16639(1) \cdot 10^{-5}$ GeV^{-2} [76], determined from the muon lifetime using recently calculated two-loop corrections [195]: To lowest order within the electroweak theory and up to a numerical factor, the Fermi constant is the squared ratio of the SU(2)$_L$ weak coupling constant to the W-boson mass. The reason for this replacement* is twofold. First, radiative corrections are smaller and more easily calculated and expressed in terms of G_F. Second, the experimental precision on G_F of 9 ppm is by far higher than that on the mass of the W boson will be in the foreseeable future. Indeed, G_F is treated as a constant in the following analyses. The mass of the W boson, m_W, is then predicted within the Standard Model as a function of G_F and the other Standard-Model parameters. Comparing this prediction with the direct measurements of m_W performed at the TEVATRON and at the LEP-2 colliders yields a second stringent test of the Standard Model.

At tree level, the Z-pole observables depend on just three of the five parameters discussed above, namely α and m_Z, and, in case of quark production, α_S, (see Equations 1.29 and 1.32). Electroweak radiative corrections such as those shown in Figure 1.9 modify this simple picture. They induce a running of the coupling constants α and α_S with momentum transfer or s. For Z-pole observables, it is a very good approximation to use a fixed $s = m_Z^2$, called Z-pole approximation, so that the relevant coupling constants are $\alpha(m_Z^2)$ and $\alpha_S(m_Z^2)$. In addition, loop corrections involving virtual top quarks and Higgs bosons introduce a dependence on the masses of these particles. To leading one-loop order these corrections are universal, showing a dependence quadratic in the top-quark mass and logarithmic in the Higgs-boson mass. Non-leading, higher-order and fermion-specific corrections allow the effects from the top quark and the Higgs boson to be disentangled.

The five parameters of the Standard Model relevant for the calculation of Z-pole observables are therefore the coupling constants of QED and QCD at the Z pole, $\alpha(m_Z^2)$ and $\alpha_S(m_Z^2)$, and the masses of the Z boson, the top quark and the Higgs boson. The measurements of electroweak observables presented in the previous chapters are used to extract and constrain each of these five parameters. Besides the mass of the Z boson, the interesting parameters of the Standard Model are the mass of the top quark and of course the mass of the Higgs Boson. The hadronic Z-pole observables will give rise to one of the most precise determinations of $\alpha_S(m_Z^2)$. The

*Note, however, that this replacement is in some sense purely technical: the constraints on the Standard-Model parameters derived from the measurements are independent of whether m_W is replaced by the measured value of G_F, or G_F is included as an additional measurement instead.

treatment of $\alpha(m_{\rm Z}^2)$ is discussed in the following section. The programs TOPAZ0 [23] and ZFITTER [24] are used to calculate all Z-pole observables including radiative corrections in the framework of the Standard Model and as a function of these Standard Model parameters. They include the equations shown in Section 1.4, supplemented by more complicated high-order expressions for improved theoretical accuracy.

10.2 Hadronic Vacuum Polarisation

The running of the electromagnetic coupling with momentum transfer, $\alpha(0) \rightarrow \alpha(s)$, caused by fermion-pair loop insertions in the photon propagator, is customarily written as:

$$\alpha(s) \;=\; \frac{\alpha(0)}{1 - \Delta\alpha_{\rm e\mu\tau}(s) - \Delta\alpha_{\rm top}(s) - \Delta\alpha^{(5)}_{\rm had}(s)}\,, \tag{10.1}$$

with $\alpha(0) = 1/137.036$ [76]. The contribution of leptons is calculated diagrammatically up to third order: $\Delta\alpha_{\rm e\mu\tau}(m_{\rm Z}^2) = 0.03150$ with negligible uncertainty [196]. Since heavy particles decouple in QED, the top-quark contribution is small: $\Delta\alpha_{\rm top}(m_{\rm Z}^2) = -0.00007(1)$; it is calculated by TOPAZ0 and ZFITTER as a function of $m_{\rm t}$. The running electromagnetic coupling is insensitive to new particles with high masses. For light-quark loops the diagrammatic calculations are not viable as at such low energy scales perturbative QCD is not applicable. Therefore, the total contribution of the five light quark flavours to the vacuum polarisation, $\Delta\alpha^{(5)}_{\rm had}(m_{\rm Z}^2)$, is more accurately obtained through a dispersion integral over the measured hadronic cross section in electron-positron annihilations at low centre-of-mass energies. In this case the uncertainty on $\Delta\alpha^{(5)}_{\rm had}(m_{\rm Z}^2)$ is given by the experimental uncertainties in the measured hadronic cross section at low centre-of-mass energies. Until recently, this uncertainty was quite large, leading to [51, 197]:

$$\Delta\alpha^{(5)}_{\rm had}(m_{\rm Z}^2) \;=\; 0.02804 \pm 0.00065\,, \tag{10.2}$$

as used in Chapter 2. Based on the same analysis technique but including recent new measurements of the hadronic cross section at low energies, in particular the precise measurements of the BES collaboration in the range 2 GeV $< \sqrt{s} <$ 5 GeV [198], the uncertainty is much reduced [199]:

$$\Delta\alpha^{(5)}_{\rm had}(m_{\rm Z}^2) \;=\; 0.02761 \pm 0.00036\,, \tag{10.3}$$

During the course of the last few years, more theory-driven determinations of $\Delta\alpha^{(5)}_{\rm had}(m_{\rm Z}^2)$ have appeared [200–208], which employ perturbative QCD to calculate the hadronic cross section in the continuum region at low $\sqrt{s}$, outside the region populated by the hadronic resonances. Since the theoretical uncertainty on the predicted cross section is assumed to be smaller than that of the experimental measurements, a reduced error on $\Delta\alpha^{(5)}_{\rm had}(m_{\rm Z}^2)$ is achieved, for example [208]:

$$\Delta\alpha^{(5)}_{\rm had}(m_{\rm Z}^2) \;=\; 0.02747 \pm 0.00012\,, \tag{10.4}$$

which also takes the new results from BES into account. All recent evaluations of $\Delta\alpha^{(5)}_{\rm had}(m_{\rm Z}^2)$ are consistent with, but lower than, the previous evaluation of Equation 10.2. In the following analyses, the experiment-driven value of $\Delta\alpha^{(5)}_{\rm had}(m_{\rm Z}^2)$ as given in Equation 10.3 will be used, on the same footing as any other experimental measurement with associated uncertainty.

10.3 Additional Measurements

Obviously, a wealth of other measurements are performed in particle physics experiments at high energies, using various particle beams and targets. The results of these experiments are crucial to explore the predictive power of the Standard Model in as large a breadth as possible. Of all these measurements, those which have a high sensitivity to the Standard Model parameters as introduced above are particularly interesting here.

For simplicity, only such additional measurements are considered here which directly or indirectly constrain fundamental parameters of the Standard-Model parameters, notably the mass of the Higgs boson. In decreasing order of importance, the additional results considered in some of the analyses presented in the following are: the mass of the top quark, the mass of the W boson, the on-shell electroweak mixing angle, and the atomic parity violation parameter.

10.3.1 Mass of the Top Quark

The top quark was discovered in proton-antiproton interactions recorded at the TEVATRON collider by the experiments CDF [209] and DØ [210]. Both experiments measure its mass directly, exploiting various decay chains. Combining the results from CDF [211] and DØ [212] obtained from data collected in Run-I, the current world average value for the pole mass of the top quark is: $m_{\mathrm{t}} = 174.3 \pm 5.1$ GeV [76].

10.3.2 Mass of the W Boson

Initially, the mass of the W boson was measured in proton-antiproton collisions, first by the experiments UA1 [213] and UA2 [214] at the SPS collider, and subsequently by CDF [215] and DØ [216] at the TEVATRON in Run-I, with a combined result of $m_{\mathrm{W}} = 80.452 \pm 0.062$ GeV [217]. Including a new *preliminary* Run-I result from DØ [218] improves this value to $m_{\mathrm{W}} = 80.454 \pm 0.060$ GeV.

Recently the LEP experiments ALEPH, DELPHI, L3 and OPAL also measure the W-boson mass directly in the process $\mathrm{e^+e^-} \to \mathrm{W^+W^-}$, made possible by more than doubling the centre-of-mass energy of the LEP accelerator (LEP-2). Combining all published [219–222] and *preliminary* LEP-2 measurements, the LEP-2 result is: $m_{\mathrm{W}} = 80.450 \pm 0.039$ GeV [223].

The results obtained at hadron and lepton colliders are in very good agreement with each other. Combining the independent results leads to a *preliminary* direct determination of the W-boson mass with an accuracy of 0.4 per-mille, $m_{\mathrm{W}} = 80.451 \pm 0.033$ GeV. As for the Z boson, the mass of the W boson quoted here is defined according to a Breit-Wigner denominator with s-dependent width, $|s - m_{\mathrm{W}}^2 + is\Gamma_{\mathrm{W}}/m_{\mathrm{W}}|$, where Γ_{W} is the total width of the W boson.

10.3.3 On-Shell Electroweak Mixing Angle

The measurement of the neutrino-nucleon neutral-to-charged current cross-section ratio also determines the electroweak mixing angle. Note that the electroweak mixing angle determined here is different from the Z-pole equivalent due to the different momentum-transfer scale in t-channel neutrino-nucleon scattering as opposed to s-channel electron-positron interactions. The result is quoted in terms of the on-shell electroweak mixing angle, adding small electroweak radiative corrections. Using both neutrino and anti-neutrino beams, the NuTeV collaboration has recently published by far the most precise result: $\sin^2\theta_{\mathrm{W}} = 1 - m_{\mathrm{W}}^2/m_{\mathrm{Z}}^2 \equiv 0.2277 \pm 0.0016 -$

$0.00022\frac{m_t^2-(175\ \mathrm{GeV})^2}{(50\ \mathrm{GeV})^2} + 0.00032 \ln\frac{m_H}{150\ \mathrm{GeV}}$ [224], where the residual dependence of this result on the Standard-Model electroweak radiative corrections is explicitly parametrised.

Using m_Z from LEP-1, Table 2.13, and ignoring the small m_t- and m_H-dependence, this result corresponds to a W-boson mass of $m_W = 80.136 \pm 0.084$ GeV. This indirect determination of m_W differs from the direct measurements of m_W discussed in the previous subsection by 3.5 standard deviations.

10.3.4 Atomic Parity Violation Parameter

The measurement of parity violation in atoms determines the weak charge of the atomic nucleus as probed by the electron, $Q_W(N,Z) = -2[(2Z+N)C_{1u} + (Z+2N)C_{1d}]$ for a nucleus with Z protons and N neutrons. The weak charges C_1 of up and down quarks as seen by the electron through the parity-violating t-channel γ/Z exchange are expressed in terms of effective vector and axial-vector coupling constants, $C_{1q} = 2 g_{Ae} g_{Vq}$. Including electroweak radiative corrections, the corresponding effective couplings are somewhat different from their Z-pole equivalents due to the momentum-transfer being nearly zero in atomic-parity violation experiments.

Precise measurements of Q_W are performed for cesium [225, 226] and thallium [227, 228]. However, certain aspects in nuclear many-body perturbation theory needed in the experimental analyses are still under discussion and only very recently addressed for cesium [229, 230], being the most precise measurement. Thus only the newly corrected experimental result for cesium, $Q_W(\mathrm{Cs}) = -72.5 \pm 0.7$ [230], will be used in the following and compared to the recent Standard-Model calculation [231].

10.4 Sensitivities and Uncertainties

Since the interesting electroweak radiative corrections involving top-quark and Higgs-boson masses are typically on the order of 1% or less at the Z pole, all other effects must be controlled at the per-mille level in order to extract quantitatively these interesting Standard-Model parameters. The uncertainties affecting the pseudo-observables as calculated within the framework of the Standard Model fall into two classes discussed in the following.

10.4.1 Parametric Uncertainties

First, there are uncertainties in the values of the five Standard-Model parameters themselves, which of course lead to uncertainties in any pseudo-observable calculated as a function of these parameters. This dependence on the five Standard-Model parameters allows their determination in the Standard-Model analysis of the measurements. As all five parameters are determined in parallel, these so-called parametric uncertainties are properly accounted for automatically by the analysis procedure discussed in Section 10.5. For the determination of the interesting parameters, namely the mass of the top-quark and the mass of the Higgs boson, a high sensitivity is advantageous, while the dependence on the other Standard-Model parameters, in particular the hadronic vacuum polarisation, should be small. Numerical results for parametric uncertainties on several pseudo-observables are reported in Table 10.1.

10.4.2 Theoretical Uncertainties

Many theorists perform the various calculations of radiative corrections. In order to make the calculations accessible to experimentalists in a consistent way, the relevant calculations are incorporated in computer programs such as TOPAZ0 [23], using the general minimal subtraction renormalisation scheme, and ZFITTER [24], using the on-mass-shell renormalisation scheme. For the realistic observables, the measured cross sections and asymmetries, the following corrections are included in TOPAZ0 and ZFITTER: up to $\mathcal{O}(\alpha^2)$ and leading $\mathcal{O}(\alpha^3)$ for initial-state QED radiation including pairs, $\mathcal{O}(\alpha)$ for final-state QED radiation and QED initial-final interference, $\mathcal{O}(\alpha_S^3)$ for final-state QCD radiation and $\mathcal{O}(\alpha\alpha_S)$ for mixed QED/QCD final-state radiation. These corrections are needed to extract the pseudo-observables discussed in this report from the realistic observables, the measured cross sections and asymmetries. For the calculation of the expectation for the extracted pseudo-observables discussed in this report, the final-state corrections listed above are also available for the Z decay widths. Furthermore, complete one-loop electroweak radiative corrections, resummed leading one-loop corrections and two-loop corrections up to $\mathcal{O}(\alpha\alpha_S, \alpha\alpha_S^2, G_F^2 m_t^4, G_F^2 m_t^2 m_Z^2, G_F m_t^2 \alpha_S, G_F m_t^2 \alpha_S^2)$ are included. Overviews and summaries of radiative corrections in Z-pole physics are given in References 21, 232, 233, which should be consulted for the references to the original calculations.

Recently, complete fermionic electroweak two-loop corrections for m_W have been calculated [234]. The effect on m_W turns out to be small compared to the current experimental uncertainty on m_W, but the naive propagation of the effect from m_W and the the on-shell electroweak mixing angle to the effective electroweak mixing angle, $\sin^2\theta_{\rm eff}^{\rm lept} = \kappa(1-m_W^2/m_Z^2)$, using the unmodified form-factor κ, causes a visible effect compared to the experimental uncertainty on $\sin^2\theta_{\rm eff}^{\rm lept}$. This calculation is thus currently used in the estimation of the theoretical uncertainty only. For a consistent analysis, the corresponding calculations of the effective electroweak mixing angle and the partial Z widths are needed.

Theoretical uncertainties in radiative corrections arise due to the fact that the perturbative expansion is known and calculated only up to a finite order. Missing higher-order electroweak, strong and mixed corrections cause the calculations of observables to be incomplete and thus approximate. Equivalently, ambiguities due to the choice of renormalisation schemes, resummation schemes, momentum-transfer scales in loop corrections, and schemes to implement the factorisation of various corrections are introduced which reflect and are of the order of the missing higher-order corrections. The uncertainty on the predicted observables due to these effects is thus estimated by comparing results obtained using different calculations performed to equivalent order [25, 233, 235]. Numerical results for theoretical uncertainties calculated with TOPAZ0 and ZFITTER are reported in Table 10.1 for several pseudo-observables.

QCD Uncertainties

The largest QCD correction on Z-pole observables arises through the final-state QCD radiation factor in quark-pair production (Equation 1.32), modifying the decay width of the Z into hadrons, $\Gamma_{\rm had}$, and thus also the Z-pole observables $\Gamma_{\rm tot}$, $\sigma_{\rm h}^0$, σ_ℓ^0, and R_ℓ^0, which depend on $\Gamma_{\rm had}$. The theoretical uncertainty in the calculation of these observables due to unknown higher-order QCD effects, and thus in the $\alpha_S(m_Z^2)$ values extracted from measurements of these quantities, is a subject of current discussion. Estimates of the corresponding theoretical uncertainty on $\alpha_S(m_Z^2)$ vary by a factor of six, from 0.0005 to 0.003 [236–238], a range which spans the uncertainty on $\alpha_S(m_Z^2)$ caused by the experimental errors on the measured hadronic Z-pole observables.

Source	δ	Γ_Z [MeV]	σ^0_h [nb]	R^0_ℓ	R^0_b	ρ_ℓ	$\sin^2\theta^{lept}_{eff}$	m_W [MeV]
$\Delta\alpha^{(5)}_{had}(m_Z^2)$	0.00036	0.3	0.001	0.002	—	—	0.00013	7
$\alpha_S(m_Z^2)$	0.002	1.1	0.011	0.013	—	—	0.00001	1
m_Z/MeV	2.1	0.2	0.002	—	—	—	0.00002	3
m_t/GeV	5.0	1.2	0.003	0.002	0.00018	0.0005	0.00016	31
$\log_{10}(m_H/\text{GeV})$	0.3	1.9	0.001	0.006	0.00002	0.0004	0.00036	44
Theory		0.3	0.001	0.002	0.00007	0.0001	0.00006	3
Experimental		2.3	0.037	0.025	0.00068	0.0010	0.00017	33

Table 10.1: Theoretical uncertainties on selected Z-pole observables and m_W. Top: parametric uncertainties, *i.e.*, sensitivities to Standard-Model parameters. For each observable, the change is shown when varying the Standard-Model parameter listed in the first column by the amount δ listed in the second column around the following central values: $\Delta\alpha^{(5)}_{had}(m_Z^2) = 0.02761$, $\alpha_S(m_Z^2) = 0.118$, $m_Z = 91.1875$ GeV, $m_t = 175$ GeV, $m_H = 150$ GeV. Where no number is listed, the effect is smaller than half a unit in the number of digits quoted. Bottom: uncertainties due to missing higher-order corrections estimated through variation of calculational schemes implemented in TOPAZ0 and ZFITTER (half of full range of values). For comparison, the uncertainties on the experimental measurements are also shown.

Virtual quark loops, with additional gluon exchange, induce propagator corrections which introduce an additional, but much smaller level of α_S dependence in the calculation of each Z-pole observable. Since these are two-loop corrections, uncertainties on α_S in the range quoted above cause only negligible further uncertainties on the prediction of any Z-pole observable.

This has several consequences: The extracted value of $\alpha_S(m_Z^2)$ is solely given by the dependence of the hadronic Z-pole observables on the final-state QCD radiation factor. As it is the very same final-state QCD correction factor entering the calculation of all hadronic Z-pole observables, the theoretical uncertainties are fully correlated and affect the extracted $\alpha_S(m_Z^2)$ value independent of which observable is used. Because of this correlation, the extracted values of the other Standard-Model parameters are not affected by the unknown theoretical uncertainty due to unknown higher-order QCD effects.[†]

10.4.3 Sensitivities

As shown in Table 10.1, the uncertainties due to missing higher-orders are in general small compared to the leading parametric uncertainties, with the exception of the effective electroweak mixing angle. For this observable it has already been shown in Figure 9.4 that the parametric uncertainty on the Standard-Model prediction arising from $\Delta\alpha^{(5)}_{had}(m_Z^2)$ is also non-negligible compared to the experimental uncertainty of the average. As a consequence, the uncertainty on the hadronic vacuum polarisation is one of the limiting factors in the extraction of the mass of

[†]Note that this theoretical uncertainty would have to be known quantitatively and included explicitly if external measurements of $\alpha_S(m_Z^2)$ were included in the analyses. For the Standard-Model analyses presented here, however, this is not necessary as external constraints on $\alpha_S(m_Z^2)$, even without any uncertainty, do not lead to reduced uncertainties on the other Standard-Model parameters.

the Higgs boson. This situation underlines the importance of further improved determinations of the hadronic vacuum polarisation through measurements of the hadronic cross section in electron-positron annihilations at low centre-of-mass energies.

The sensitivity of the observables to the mass of the Higgs boson within the framework of the Standard Model is shown in Figures 10.1 to 10.3 and quantified in Table 10.6 below. In general, the pseudo-observables fall into three groups. First, there are the pseudo-observables which are also Standard-Model input parameters, such as the mass of the Z boson, the hadronic vacuum polarisation, and the mass of the top quark. Second, there are the pseudo-observables which are highly sensitive to electroweak radiative corrections, such as partial widths as well as the forward-backward and polarised leptonic asymmetries. They determine the ρ parameter and the effective electroweak mixing angle as discussed in the previous chapter. Note in particular, that compared to the Z-pole asymmetry measurements, the W-boson mass is relatively less sensitive to $\Delta\alpha^{(5)}_{\rm had}(m^2_{\rm Z})$ than to $m_{\rm t}$ and $m_{\rm H}$, making $m_{\rm W}$, measured at the TEVATRON and at LEP-2, an ideal observable to further reduce the error on the Higgs mass prediction. Third, there are the pseudo-observables which are, compared to their experimental uncertainties, nearly constant in the Standard Model, such as $\sigma^0_{\rm h}$ or the quark forward-backward left-right asymmetries $\mathcal{A}_{\rm q}$. Nevertheless they test the Standard Model independent of radiative corrections in terms of its static properties, such as the number of fermion generations or the quantum numbers for weak iso-spin and electric charge assigned to the fundamental fermions.

10.5 Analysis Procedure

In order to determine the five relevant Standard-Model parameters a χ^2 minimisation is performed using the program MINUIT [239]. The χ^2 is calculated as usual by comparing the measurements of Z-pole and other observables, their errors and correlations including those discussed in Chapter 7, with the predictions calculated in the framework of the Standard Model. For measurements of leptonic Z-pole observables, the results combined in the previous chapters under the hypothesis of lepton universality, inherent to the Standard Model, are used. All are reported in Table 10.6. The predictions are calculated as a function of the five Standard-Model parameters by the programs TOPAZ0 and ZFITTER, which include all relevant electroweak radiative corrections. All five Standard-Model parameters are allowed to vary in the fit, so that parametric uncertainties are correctly treated and propagated.

This analysis procedure tests quantitatively how well the Standard Model is able to describe the complete set of all measurements with just one value for each of the five parameters. For this, however, the large contribution to the χ^2 arising from the asymmetry measurements as discussed in the previous chapter has to be taken into account in the interpretation.

In addition, the mass of the remaining particle of the Standard Model without significant direct experimental evidence, the mass of the Higgs boson, will be constrained. For this part, the additional measurements presented in Section 10.3, such as the direct measurements of $m_{\rm W}$ and $m_{\rm t}$ at LEP-2 and the TEVATRON, are also included, in order to obtain the best precision.

Uncertainties due to missing higher order corrections as discussed above are typically implemented by offering various choices or options in the programs TOPAZ0 and ZFITTER calculating radiative corrections. As these choices correspond to discrete options (flags), they cannot be varied during a fit. Rather, the analysis is repeated with different flag settings. The change in the extracted Standard Model parameters is taken as an estimate of the theoretical uncertainty for the option studied. Effectively, the theoretical uncertainty in the calculation of observables is propagated back to the extracted Standard Model parameters. Since this uncer-

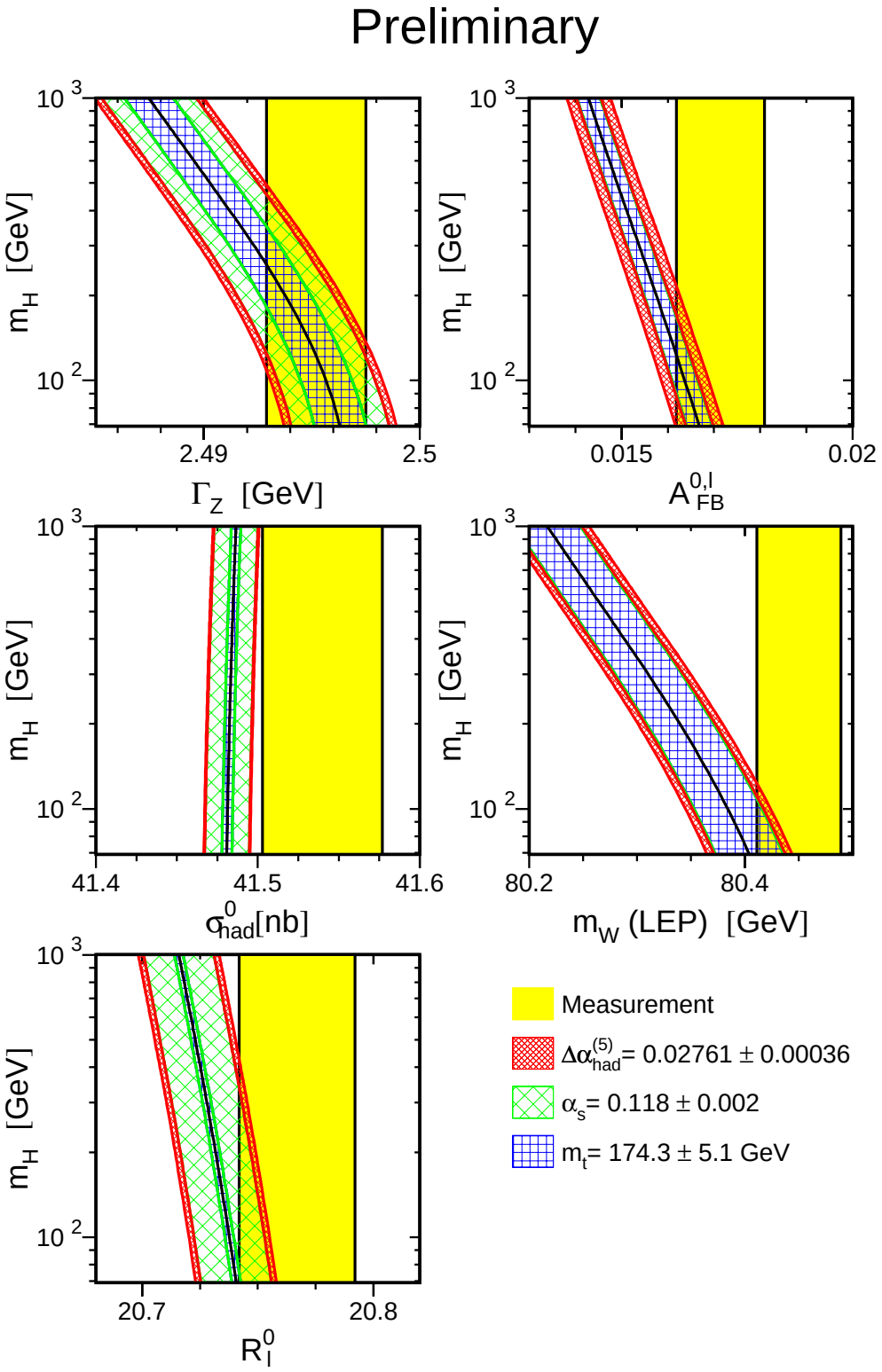

Figure 10.1: Comparison of the LEP combined measurements of Γ_Z, σ_h^0, R_ℓ^0, $A_{FB}^{0,\ell}$ and m_W(LEP-2) with the Standard-Model prediction as a function of the mass of the Higgs boson. The measurement with its uncertainty is shown as the vertical band. The width of the Standard Model band arises due to the uncertainties in $\Delta\alpha_{had}^{(5)}(m_Z^2)$, $\alpha_S(m_Z^2)$ and m_t in the ranges indicated. The total width of the band is the linear sum of these uncertainties.

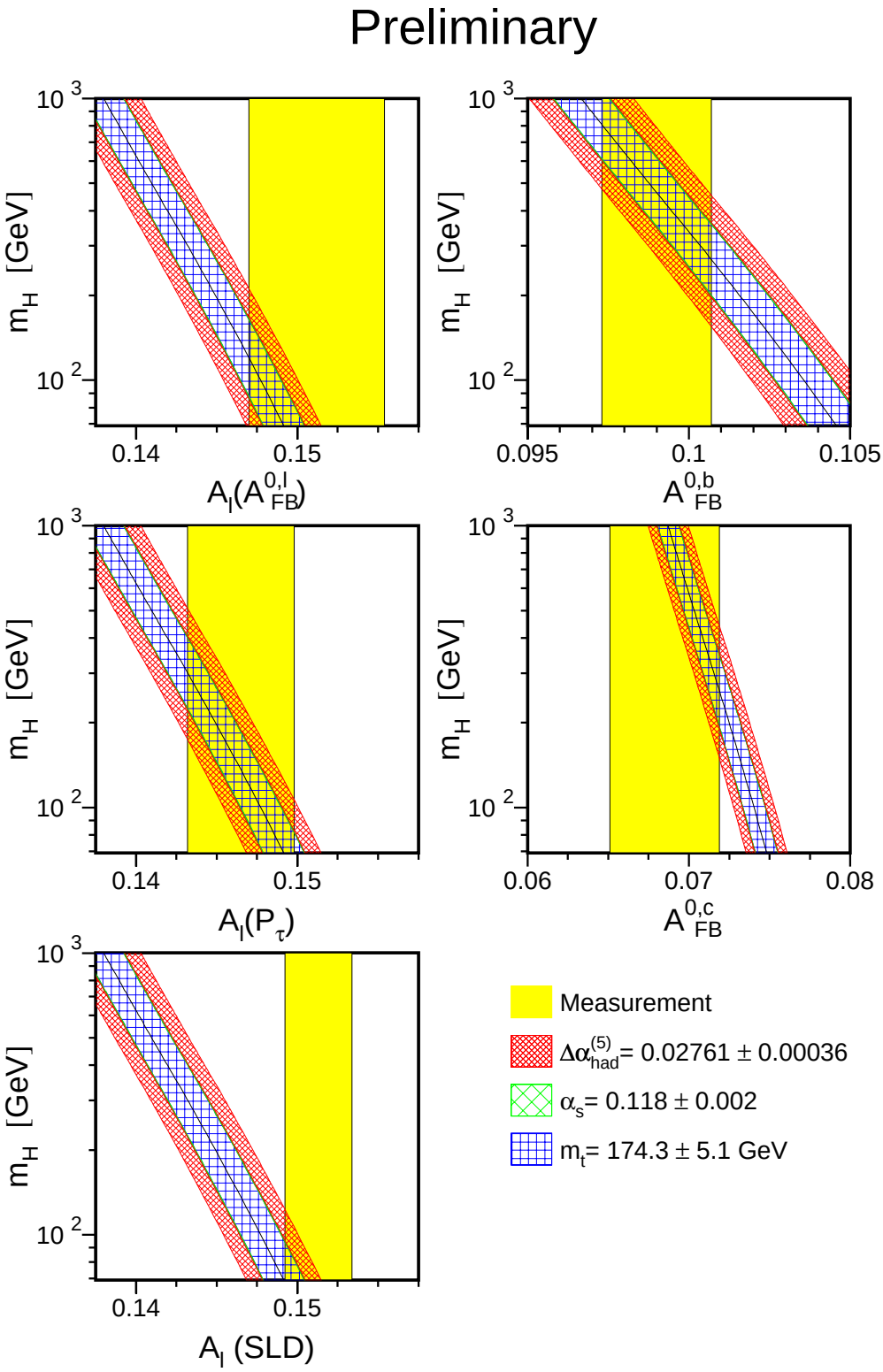

Figure 10.2: Comparison of the LEP/SLD combined measurements of $\mathcal{A}_\ell(A_{\rm FB}^{0,\ell})$, $\mathcal{A}_\ell(P_\tau)$, $\mathcal{A}_\ell$(SLD), $A_{\rm FB}^{0,\rm b}$ and $A_{\rm FB}^{0,\rm c}$ with the Standard-Model prediction as a function of the mass of the Higgs boson. The measurement with its uncertainty is shown as the vertical band. The width of the Standard Model band arises due to the uncertainties in $\Delta\alpha_{\rm had}^{(5)}(m_{\rm Z}^2)$, $\alpha_{\rm S}(m_{\rm Z}^2)$ and $m_{\rm t}$ in the ranges indicated. The total width of the band is the linear sum of these uncertainties.

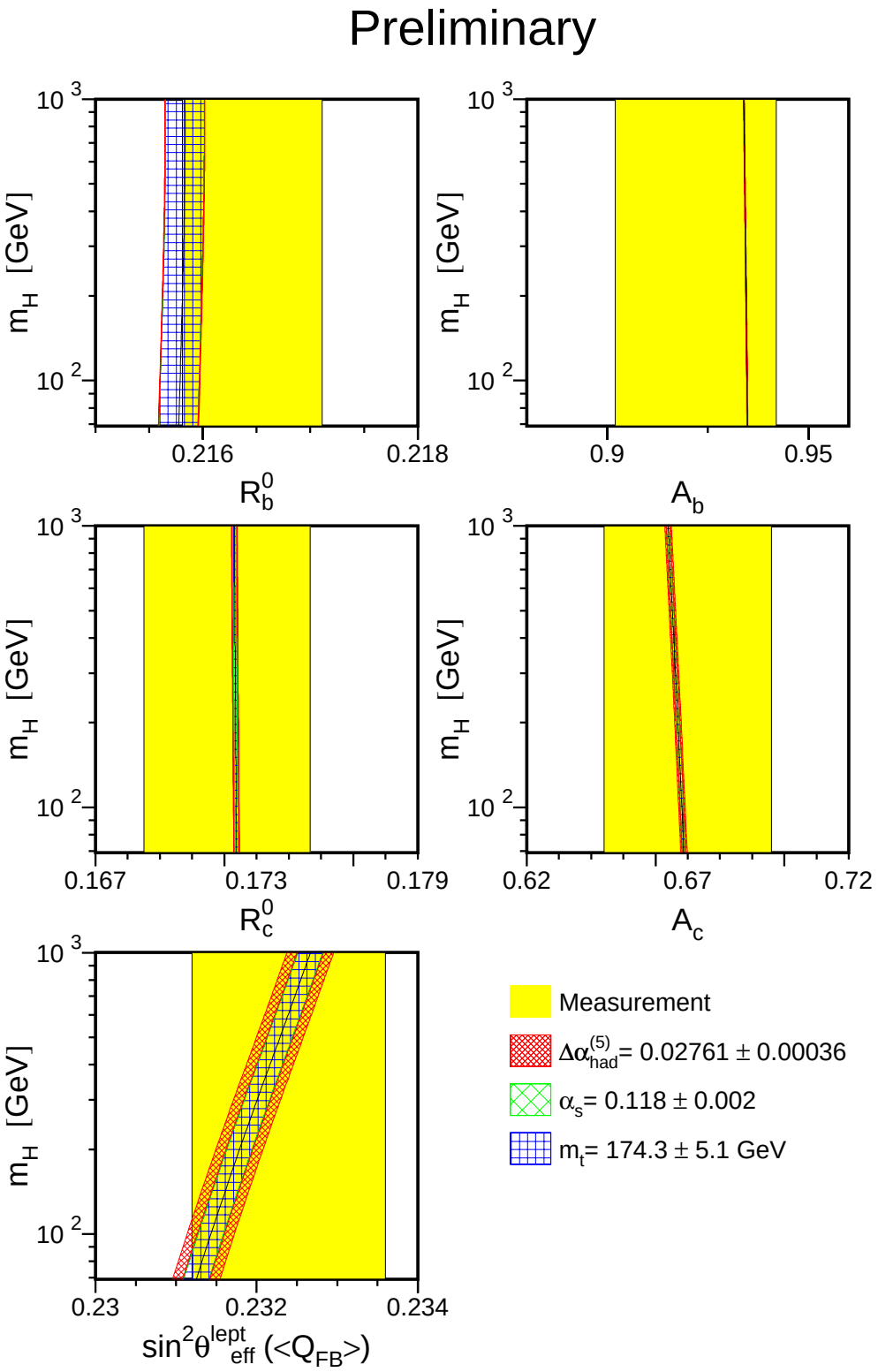

Figure 10.3: Comparison of the LEP/SLD combined measurements of R_{b}^0, R_{c}^0, $\mathcal{A}_{\mathrm{b}}$, $\mathcal{A}_{\mathrm{c}}$ and $\sin^2\theta_{\mathrm{eff}}^{\mathrm{lept}}(\langle Q_{\mathrm{FB}}\rangle)$ with the Standard-Model prediction as a function of the mass of the Higgs boson. The width of the Standard Model band arises due to the uncertainties in $\Delta\alpha_{\mathrm{had}}^{(5)}(m_{\mathrm{Z}}^2)$, $\alpha_{\mathrm{S}}(m_{\mathrm{Z}}^2)$ and m_{t} in the ranges indicated. The total width of the band is the linear sum of these uncertainties.

tainty is usually much smaller than the uncertainty arising from the experimental uncertainties in the measured Z-pole observables (Table 10.1), it is not included in the results presented in the following.

10.6 Sensitivity to Radiative Corrections Beyond QED

A fundamental question is whether the experimental Z-pole results indeed show evidence for the existence of electroweak radiative corrections beyond those solely predicted by the well known and tested theory of QED. Including only the running of α, the predictions based on Born-term expressions for the ρ parameter and the electroweak mixing angle are obtained from the equations given in Section 1.4. Setting $\Delta\rho = \Delta\kappa = \Delta r_{\mathrm{w}} = 0$, the results are:

$$\rho_0 = 1 \tag{10.5}$$

$$\sin^2\theta_0 = \frac{1}{2}\left(1 - \sqrt{1 - 4\frac{\pi\alpha(m_{\mathrm{Z}}^2)}{\sqrt{2}G_{\mathrm{F}}m_{\mathrm{Z}}^2}}\right) = 0.23101 \pm 0.00012\,, \tag{10.6}$$

where the uncertainty on $\sin^2\theta_0$ arises due to the uncertainty on $\alpha(m_{\mathrm{Z}}^2)$ mainly caused by the hadronic vacuum polarisation, see Equations 10.1 and 10.3. When these predictions are compared to the results derived from the measurement of Z-pole observables, essentially the leptonic partial decay width and the leptonic asymmetries, Table 9.6:

$$\rho_\ell = 1.0050 \pm 0.0010 \tag{10.7}$$

$$\sin^2\theta_{\mathrm{eff}}^{\mathrm{lept}} = 0.23132 \pm 0.00018\,, \tag{10.8}$$

it becomes evident in particular in the case of the ρ parameter that electroweak radiative corrections beyond QED are needed to describe the measurements. This is also shown in Figure 10.4.

In the case of the effective electroweak mixing angle, the uncertainty on the prediction of $\sin^2\theta_{\mathrm{eff}}^{\mathrm{lept}}$ within the Standard Model due to the uncertainty on $\Delta\alpha_{\mathrm{had}}^{(5)}(m_{\mathrm{Z}}^2)$ is non-negligible compared to the accuracy of experimental measurement of $\sin^2\theta_{\mathrm{eff}}^{\mathrm{lept}}$. This observation underlines the importance of a precise cross-section measurement of electron-positron annihilation into hadrons at low centre-of-mass energies. In contrast to $\sin^2\theta_{\mathrm{eff}}^{\mathrm{lept}}$, the Standard-Model prediction of the ρ parameter is not affected by the uncertainty in $\Delta\alpha_{\mathrm{had}}^{(5)}(m_{\mathrm{Z}}^2)$.

10.7 Tests of Electroweak Radiative Corrections

10.7.1 Parametrisations

As discussed above, the expected structure of electroweak radiative corrections in the Standard model shows contributions quadratic in the fermion masses and only logarithmic in the Higgs-boson mass. It has been studied how the small Higgs-mass dependence can be disentangled from the large top-quark mass dependence. For this purpose, four new effective parameters, ϵ_1, ϵ_2, ϵ_3 and ϵ_b are introduced. They are defined such that they vanish in the approximation when only effects due to pure QED and QCD are taken into account. In terms of the auxiliary quantities $\sin^2\theta_0$ defined above and $\Delta\kappa'$ relating $\sin^2\theta_{\mathrm{eff}}^{\mathrm{lept}}$ to $\sin^2\theta_0$ analogously to Equation 1.10:

$$\sin^2\theta_{\mathrm{eff}}^{\mathrm{lept}} = (1 + \Delta\kappa')\sin^2\theta_0\,, \tag{10.9}$$

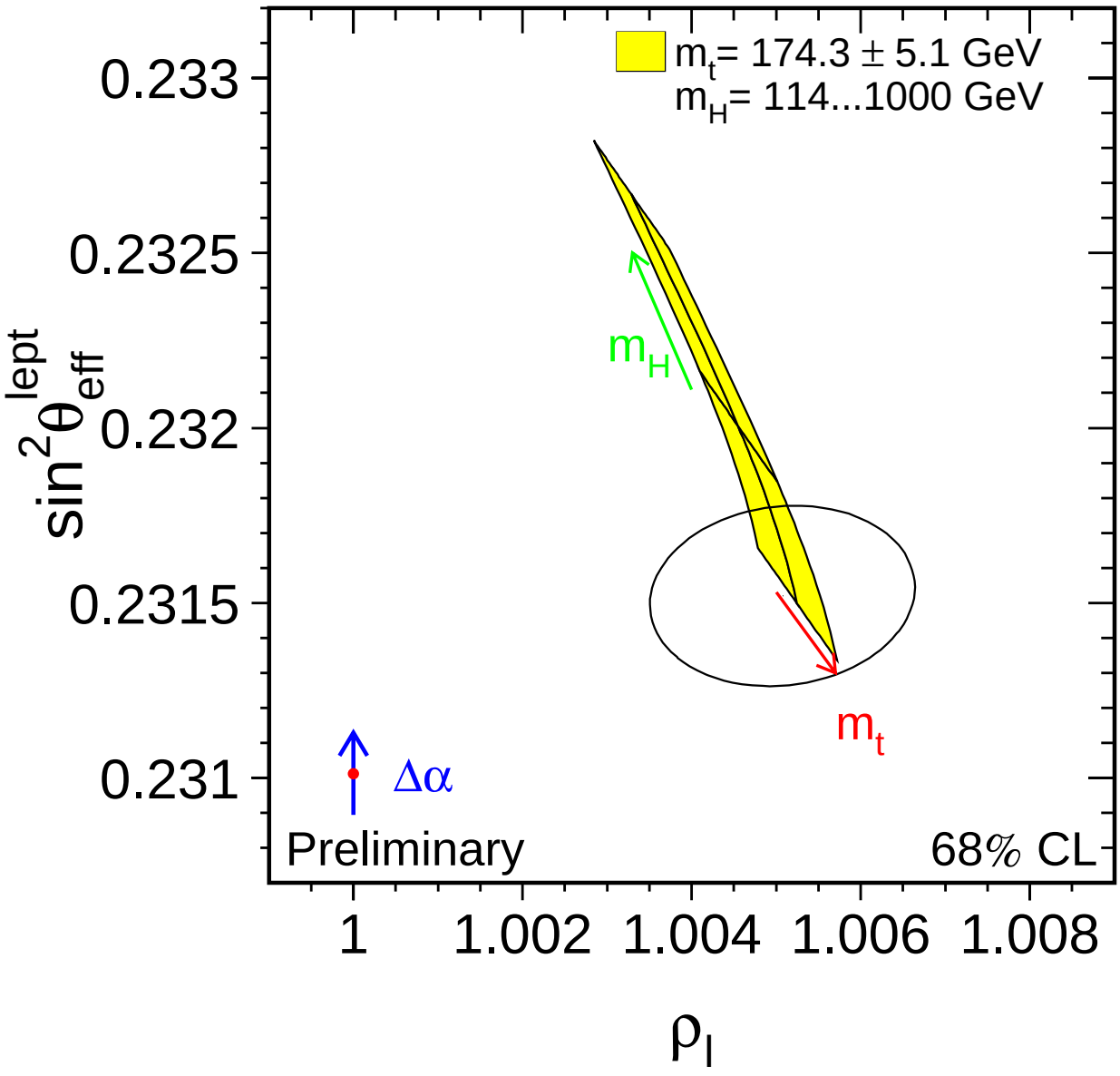

Figure 10.4: Contour curve of 68% probability in the $(\rho_\ell, \sin^2\theta^{\rm lept}_{\rm eff})$ plane. The prediction of a theory based on Born and QED with running α is shown as the dot, with the arrow representing the uncertainty due to the hadronic vacuum polarisation. The same uncertainty also affects the Standard Model prediction, shown as the shaded region drawn for a fixed $\Delta\alpha^{(5)}_{\rm had}(m_{\rm Z}^2)$ and values of $m_{\rm t}$ and $m_{\rm H}$ varied in the ranges indicated.

the ϵ parameters are given by:

$$\epsilon_1 = \Delta\rho \tag{10.10}$$

$$\epsilon_2 = \cos^2\theta_0\Delta\rho + \frac{\sin^2\theta_0}{\cos^2\theta_0 - \sin^2\theta_0}\Delta r_{\rm w} - 2\sin^2\theta_0\Delta\kappa' \tag{10.11}$$

$$\epsilon_3 = \cos^2\theta_0\Delta\rho + (\cos^2\theta_0 - \sin^2\theta_0)\Delta\kappa' \tag{10.12}$$

$$\epsilon_b = \frac{1}{2}\Delta\rho_b\,. \tag{10.13}$$

Within the Standard Model the leading contributions in terms of $m_{\rm t}$ and $m_{\rm H}$ are:

$$\epsilon_1 = \frac{3G_{\rm F}m_{\rm t}^2}{8\sqrt{2}\pi^2} - \frac{3G_{\rm F}m_{\rm W}^2}{4\sqrt{2}\pi}\tan^2\theta_{\rm W}\ln\frac{m_{\rm H}}{m_{\rm Z}} + \ldots \tag{10.14}$$

$$\epsilon_2 = -\frac{G_{\rm F}m_{\rm W}^2}{2\sqrt{2}\pi^2}\ln\frac{m_{\rm t}}{m_{\rm Z}} + \ldots \tag{10.15}$$

$$\epsilon_3 = \frac{G_{\rm F}m_{\rm W}^2}{12\sqrt{2}\pi^2}\ln\frac{m_{\rm H}}{m_{\rm Z}} - \frac{G_{\rm F}m_{\rm W}^2}{6\sqrt{2}\pi^2}\ln\frac{m_{\rm t}}{m_{\rm Z}} + \ldots \tag{10.16}$$

$$\epsilon_b = -\frac{G_{\rm F}m_{\rm t}^2}{4\sqrt{2}\pi^2} + \ldots\,. \tag{10.17}$$

Note that comparing to the equations given in Section 1.4, the argument of the natural logarithm is $m_{\rm H}/m_{\rm Z}$ rather than $m_{\rm H}/m_{\rm W}$. The difference is of subleading order.

The ϵ parameters separate electroweak radiative corrections in quadratic $m_{\rm t}$ effects and logarithmic $m_{\rm H}$ effects. Such a rearrangement is also useful in the search for new physics effects in precision measurements. Another commonly used description is based on the so-called STU parameters [240], extended by an additional parameter, γ_b, for the b-quark sector [107]. Approximate linear relations between these two sets of parameters exist:

$$S \simeq +\epsilon_3\frac{4\sin^2\theta_0}{\alpha(m_{\rm Z}^2)} - c_S \tag{10.18}$$

$$T \simeq \epsilon_1\frac{1}{\alpha(m_{\rm Z}^2)} - c_T \tag{10.19}$$

$$U \simeq -\epsilon_2\frac{4\sin^2\theta_0}{\alpha(m_{\rm Z}^2)} - c_U \tag{10.20}$$

$$\gamma_b \simeq 2\epsilon_b - c_\gamma\,. \tag{10.21}$$

In the literature, these parameters are in fact defined as shifts relative to a fixed set of Standard-Model values c_i, $i = S, T, U, \gamma$, so that $S = T = U = \gamma_b = 0$ at that point. Thus these parameters measure deviations from the electroweak radiative corrections expected in the Standard Model, in particular new physics effects in oblique electroweak corrections, *i.e.*, those entering through vacuum polarisation diagrams. For numerical results presented in the following, we use as the fixed subtraction point the values corresponding to: $\Delta\alpha^{(5)}_{\rm had}(m_{\rm Z}^2) = 0.02761$, $\alpha_{\rm S}(m_{\rm Z}^2) = 0.118$, $m_{\rm Z} = 91.1875$ GeV, $m_{\rm t} = 175$ GeV, $m_{\rm H} = 150$ GeV.

10.7.2 Results

The formulae listed above and in Chapter 1 are combined to express the measured quantities in terms of the ϵ or STU parameters, and the latter are then determined as usual in a χ^2-fit to the

measurements. In both analyses, the largest contribution to the χ^2 arises from the asymmetry measurements as discussed in Section 9.3.

The Z-pole measurements performed by SLD and at LEP-1 constrain the parameters ϵ_1 (T), ϵ_3 (S) and ϵ_b (γ_b). Given these, the measurements of the W-boson mass or of the on-shell electroweak mixing angle are solely determining ϵ_2 (U). The other additional measurements discussed in Section 10.3 are not included here as they can be expressed in terms of neither the ϵ nor the STU parameters without additional assumptions. Because of its explicit $m_{\rm t}$ and $m_{\rm H}$ dependence, also the measurement of $\sin^2\theta_{\rm W}$ by NuTeV cannot be included.

The results of the fit of all ϵ parameters to all LEP and SLD results including the measurements of the W-boson mass are reported in Table 10.2, and are shown as a contour curve in the (ϵ_3, ϵ_1) plane in Figure 10.5. All ϵ parameters are significantly different from zero, in particular the case for ϵ_2 determined by the W-boson mass, showing again that genuine electroweak radiative corrections beyond the running of α and $\alpha_{\rm S}$ are observed. The allowed region in ϵ-parameter space overlaps with the region as expected in the Standard Model for a light Higgs boson.

The results of the fit of the STU parameters to the same data set are shown in Table 10.3. The constraint $U = 0$ is imposed, as the mass of the W boson is the only measurement sensitive to U (and models with deviations in U are unlikely?). In the (T, S) plane, the overall result as well as bands corresponding to the most precise measurements are shown in Figure 10.6. The STU analyses show that there are no large unexpected electroweak radiative corrections, as the values of the STU parameters are in agreement with zero.

Parameter	Value	Correlations						
		$\Delta\alpha^{(5)}_{\rm had}(m^2_{\rm Z})$	$\alpha_{\rm S}(m^2_{\rm Z})$	$m_{\rm Z}$	ϵ_1	ϵ_2	ϵ_3	ϵ_b
$\Delta\alpha^{(5)}_{\rm had}(m^2_{\rm Z})$	0.02761±0.00036	1.00	0.00	0.00	0.00	0.06	−0.31	0.00
$\alpha_{\rm S}(m^2_{\rm Z})$	0.1178±0.0039	0.00	1.00	0.02	−0.37	−0.26	−0.27	−0.63
$m_{\rm Z}$ [GeV]	91.1873±0.0021	0.00	0.02	1.00	−0.11	−0.03	−0.06	0.00
ϵ_1	+0.0054±0.0010	0.00	−0.37	−0.11	1.00	0.61	0.86	0.00
ϵ_2	−0.0096±0.0012	0.06	−0.26	−0.03	0.61	1.00	0.40	−0.01
ϵ_3	+0.0053±0.0010	−0.31	−0.27	−0.06	0.86	0.40	1.00	0.01
ϵ_b	−0.0045±0.0016	0.00	−0.63	0.00	0.00	−0.01	0.01	1.00

Table 10.2: Results on the ϵ parameters including their correlations derived from a fit to all LEP and SLD measurements and including the measurements of the W-boson mass. The χ^2/dof has a value of 17.0/10, corresponding to a probability of 7%. See Section 10.4 for a discussion on theoretical uncertainties not included here.

Parameter	Value	Correlations					
		$\Delta\alpha^{(5)}_{\rm had}(m^2_{\rm Z})$	$\alpha_{\rm S}(m^2_{\rm Z})$	$m_{\rm Z}$	S	T	γ_b
$\Delta\alpha^{(5)}_{\rm had}(m^2_{\rm Z})$	0.02764±0.00036	1.00	0.02	0.00	−0.37	−0.05	0.00
$\alpha_{\rm S}(m^2_{\rm Z})$	0.1162±0.0038	0.02	1.00	0.01	−0.19	−0.28	−0.66
$m_{\rm Z}$ [GeV]	91.1872±0.0021	0.00	0.01	1.00	−0.05	−0.11	0.00
S	+0.07±0.10	−0.37	−0.19	−0.05	1.00	0.85	0.02
T	+0.17±0.10	−0.05	−0.28	−0.11	0.85	1.00	0.01
γ_b	+0.0028±0.0034	0.00	−0.66	0.00	0.02	0.01	1.00

Table 10.3: Results on the $STU\gamma_b$ parameters including their correlations derived from a fit to all LEP and SLD measurements and including the measurements of the W-boson mass. The parameter U is fixed to 0. The χ^2/dof has a value of 19.6/11, corresponding to a probability of 5%. See Section 10.4 for a discussion on theoretical uncertainties not included here.

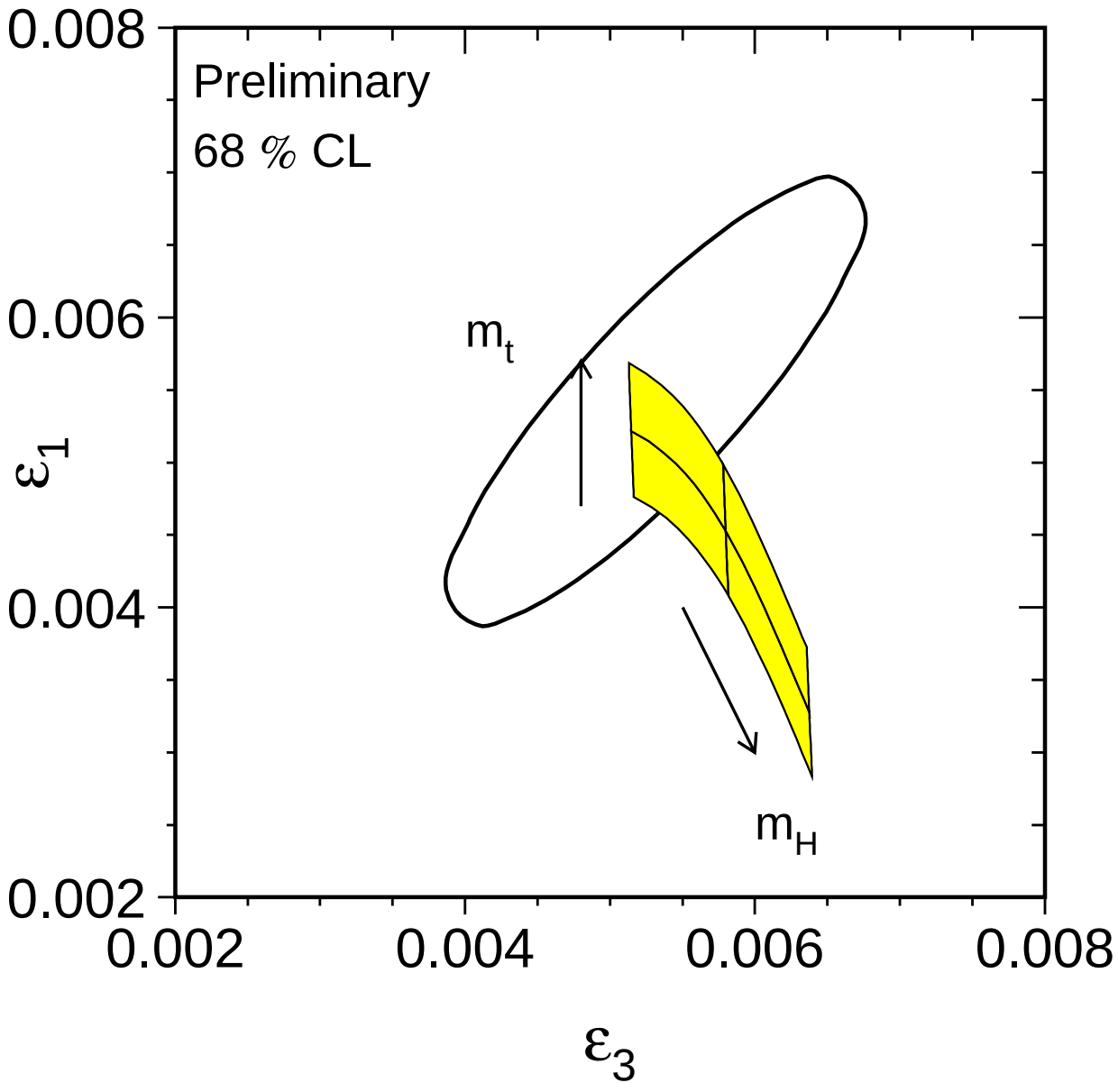

Figure 10.5: Contour curve of 68% probability in the (ϵ_3, ϵ_1) plane. The shaded region shows the predictions within the Standard Model for $m_{\rm t} = 174.3 \pm 5.1$ GeV and $m_{\rm H} = 300^{+700}_{-186}$ GeV for a fixed hadronic vacuum polarisation of $\Delta\alpha^{(5)}_{\rm had}(m^2_{\rm Z}) = 0.02761$.

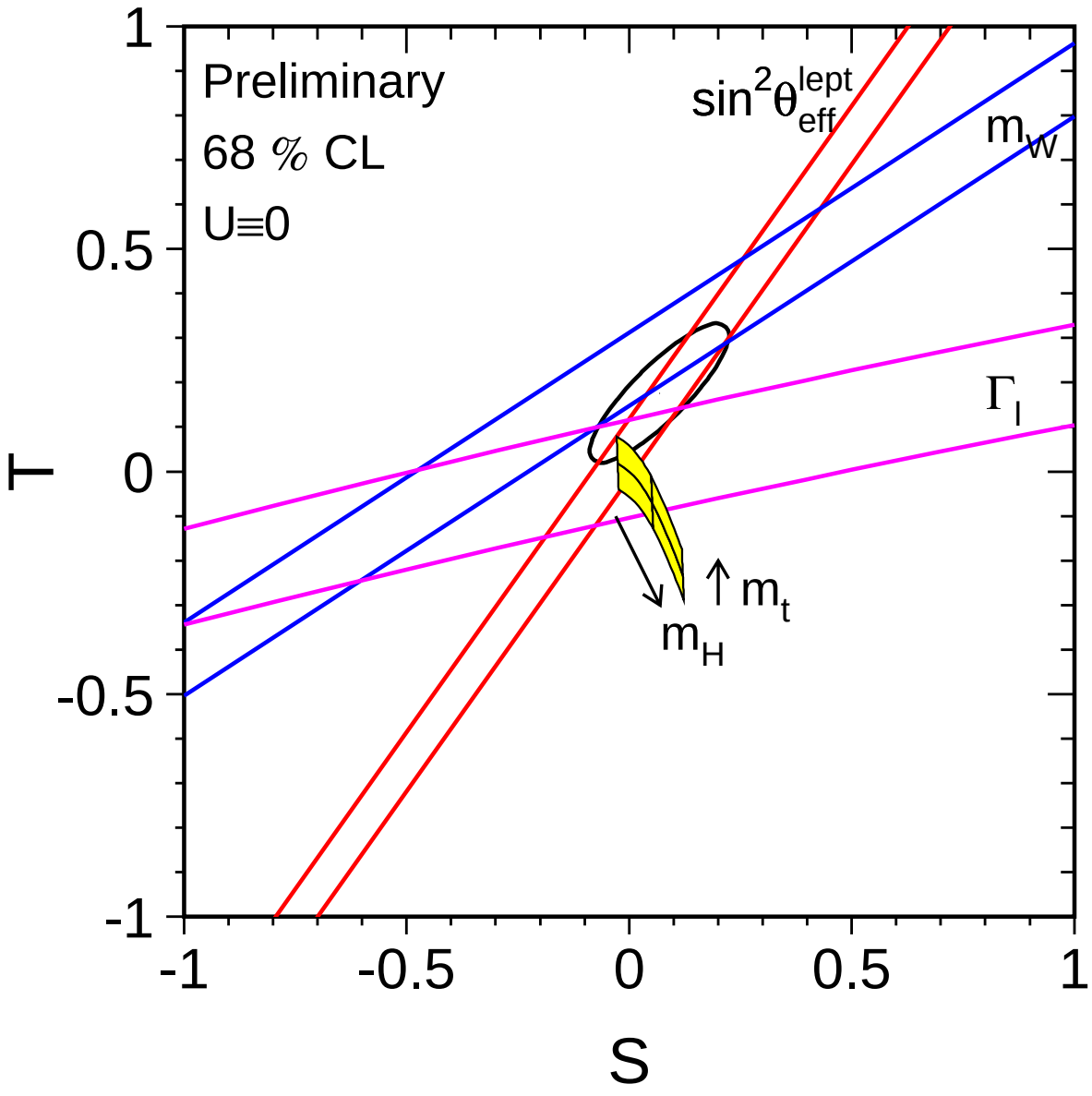

Figure 10.6: Contour curve of 68% probability in the (T, S) plane. Also shown are ± 1 standard deviation bands corresponding to the measurements of $\Gamma_{\ell\ell}$, m_{W} and $\sin^2\theta^{\mathrm{lept}}_{\mathrm{eff}}$. The shaded region shows the predictions within the Standard Model for $m_{\mathrm{t}} = 174.3 \pm 5.1$ GeV and $m_{\mathrm{H}} = 300^{+700}_{-186}$ GeV for a fixed hadronic vacuum polarisation of $\Delta\alpha^{(5)}_{\mathrm{had}}(m^2_{\mathrm{Z}}) = 0.02761$. The Standard-Model reference point at which all STU parameters vanish is chosen to be: $\Delta\alpha^{(5)}_{\mathrm{had}}(m^2_{\mathrm{Z}}) = 0.02761$, $\alpha_{\mathrm{S}}(m^2_{\mathrm{Z}}) = 0.118$, $m_{\mathrm{Z}} = 91.1875$ GeV, $m_{\mathrm{t}} = 175$ GeV, $m_{\mathrm{H}} = 150$ GeV. The constraint $U = 0$ is always applied.

10.8 Standard-Model Analyses

10.8.1 Z-Pole Results

Based on the electroweak observables measured at LEP-1 and by SLD and presented before, a fit is performed in order to determine the five parameters of the Standard Model. The result is reported in Table 10.4. A χ^2/dof of 17.5/10 is obtained, corresponding to a probability of 6%. The largest contribution to the χ^2 arises from the asymmetry measurements as discussed in Section 9.5. The Standard Model describes the complete set of measurements with a unique set of values for the free parameters. Note that the inclusion of a direct measurement of $\alpha_S(m_Z^2)$, or even fixing $\alpha_S(m_Z^2)$, introduces negligible improvements in the determination of the other Standard-Model parameters, as correlation coefficients between $\alpha_S(m_Z^2)$ and all other parameters are small.

Parameter	Value	Correlations				
		$\Delta\alpha^{(5)}_{\rm had}(m_Z^2)$	$\alpha_S(m_Z^2)$	m_Z	m_t	$\log_{10}(m_H/\mathrm{GeV})$
$\Delta\alpha^{(5)}_{\rm had}(m_Z^2)$	0.02762 ± 0.00035	$+1.00$	-0.02	0.00	$+0.01$	-0.30
$\alpha_S(m_Z^2)$	0.1188 ± 0.0027	-0.02	$+1.00$	-0.03	$+0.11$	$+0.17$
m_Z	91.1874 ± 0.0021	0.00	-0.03	$+1.00$	-0.08	-0.03
m_t	$171\pm^{12}_{9}$	$+0.01$	$+0.11$	-0.08	$+1.00$	$+0.86$
$\log_{10}(m_H/\mathrm{GeV})$	$1.95\pm^{0.37}_{0.30}$	-0.30	$+0.17$	-0.03	$+0.86$	$+1.00$
m_H	$89\pm^{121}_{45}$	-0.30	$+0.17$	-0.03	$+0.86$	$+1.00$

Table 10.4: Results on the five Standard Model parameters derived from a fit to the electroweak results obtained at LEP-1 and by SLD. The fit has a χ^2/dof of 17.5/10, corresponding to a probability of 6%. See Section 10.4 for a discussion on theoretical uncertainties not included here.

Discussion

The Z-pole data alone is not able to improve significantly on the determination of $\Delta\alpha^{(5)}_{\rm had}(m_Z^2)$ compared to the direct determination presented in Section 10.2. The strong coupling constant, $\alpha_S(m_Z^2)$, essentially determined by the leptonic pole cross section $\sigma^0_\ell = \sigma^0_h/R^0_\ell$ as discussed in Sections 8 and 10.4.2, is one of the most precise determinations of this quantity [76]. The role of the mass of the Z boson is now changed from that of a model-independent parameter, unrelated to the other pseudo-observables except for defining the pole position for the pole observables, to that of a fundamental parameter of the Standard Model affecting the calculation of all pseudo-observables. Because of its high precision with respect to the other measurements, the uncertainty on m_Z remains unchanged.

The mass of the top quark is predicted with an accuracy of about 10 GeV. This precise prediction for a fundamental particle of the Standard Model not directly accessible at the Z pole emphasizes clearly the predictive power of the Standard Model as well as the precision of the experimental results.

Despite the logarithmic dependence of the electroweak radiative corrections on the mass of the Higgs boson, its value is nevertheless predicted within an accuracy of a factor of about 2.

The value obtained shows the self-consistency of the Standard-Model analysis presented here, as such an analysis would be inconsistent and invalid for resulting Higgs masses close to or larger than 1 TeV. The large correlation coefficient of m_{H} with m_{t} shows that the precision of the m_{H} prediction will significantly improve when including the direct measurement of m_{t}, as shown in the following.

10.8.2 The mass of the top quark and of the W boson

The above indirect constraint on the mass of the top quark, Table 10.4, must be compared with the result of the direct measurement of m_{t} at the TEVATRON, $m_{\mathrm{t}} = 174.3 \pm 5.1$ GeV [76]. The indirect determination is slightly lower but in good agreement with the direct measurement. The relative accuracy of the indirect constraint on m_{t} is improved by including the direct measurements of the W boson mass at the TEVATRON and LEP-2, $m_{\mathrm{W}} = 80.451 \pm 0.033$ GeV, and the other additional measurements discussed in Section 10.3 except m_{t}, increasing the value to:

$$m_{\mathrm{t}} = 181^{+11}_{-9} \text{ GeV} . \tag{10.22}$$

It can therefore be seen that the direct measurement of the top mass is twice as accurate as this indirect determination within the framework of the Standard Model.

Having determined the five Standard Model parameters as in Table 10.4, the mass of the W boson as well as the other parameters discussed in Section 1.4 are then predicted to be:

$$\begin{aligned}
m_{\mathrm{W}} &= 80.369 \pm 0.033 \text{ GeV} && (10.23)\\
\sin^2\theta_{\mathrm{W}} &= 0.22320 \pm 0.00064 && (10.24)\\
\sin^2\theta^{\mathrm{lept}}_{\mathrm{eff}} &= 0.23149 \pm 0.00016 && (10.25)\\
\kappa &= 1.0371 \pm 0.0027 && (10.26)\\
\rho_{\ell} &= 1.00501 \pm 0.00075 && (10.27)\\
\Delta r_{\mathrm{w}} &= -0.0246 \pm 0.0022 && (10.28)\\
\Delta r &= 0.0360 \pm 0.0020 . && (10.29)
\end{aligned}$$

The prediction for the mass of the W boson is in agreement with the direct measurement. The accuracy of the m_{W} prediction is improved when the additional measurements discussed in Section 10.3 except m_{W}, in particular the direct measurement of m_{t}, is included in the fit, yielding:

$$m_{\mathrm{W}} = 80.373 \pm 0.023 \text{ GeV} . \tag{10.30}$$

The indirect Standard Model constraint on m_{W} is therefore seen to be more precise than the current direct measurements. For a stringent test of the Standard Model, the mass of the W boson should thus be measured directly to an accuracy of 20 MeV or better. The different determinations of m_{W} are compared in Figure 10.7. The indirect determinations of m_{W} are lower by nearly two standard deviations, which is mainly caused by the influence of the combined $A^{0,\mathrm{b}}_{\mathrm{FB}}$ measurement.

The many derived quantities presented here are obtained from the same data set. Thus, they cannot be used independently.

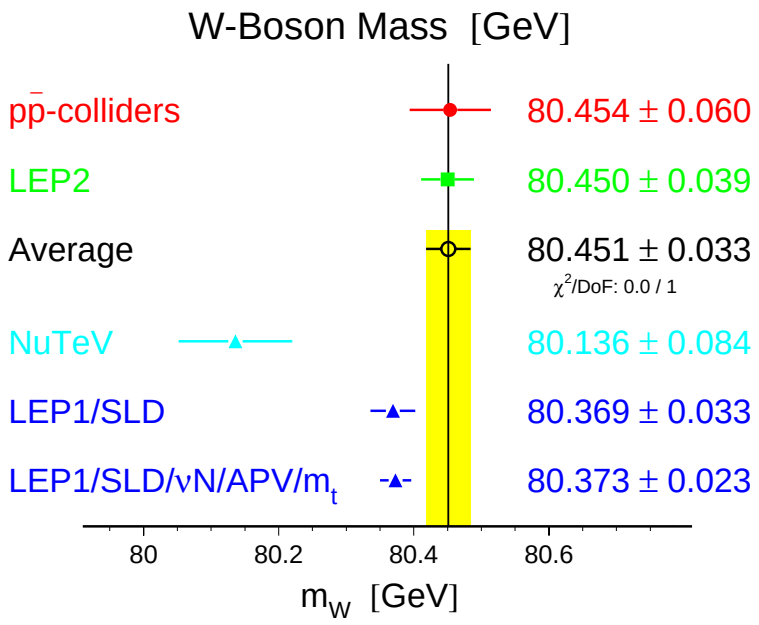

Figure 10.7: Results on the mass of the W boson, m_{W}. The direct measurements of m_{W} at the TEVATRON and at LEP-2 are compared with the indirect determinations. The **new** NuTeV result interpreted in terms of m_{W} is also shown separately.

10.8.3 The mass of the Higgs boson

The comparison between the indirect constraints and the direct measurements of m_{t} and m_{W} in the $(m_{\mathrm{t}}, m_{\mathrm{W}})$ plane is shown in Figure 10.8. The agreement is a crucial test of the Standard Model. Both contours prefer low values for the mass of the Higgs boson. As the Standard Model is so successful in predicting the values of m_{W} and m_{t}, this type of analysis is now extended to predict the mass of the Higgs Boson. The relative importance of including the direct measurements of m_{t} and m_{W} in constraining m_{H} is shown in Figure 10.9a and b. At the current level of experimental precision, the direct measurement of m_{t} is more important. A measurement of m_{W} with increased precision, however, will become very valuable.

The analysis is performed including all SLD and LEP-1 results as well as the additional measurements discussed in Section 10.3. The results are shown in Table 10.5. A χ^2/dof of 22.9/15 is obtained, corresponding to a probability of 9%. The largest contribution to the χ^2 arises from the asymmetry measurements as discussed in Section 9.5. The unchanged $\chi^2/ndof$ probability shows that also the complete set of measurements is accommodated by the Standard Model. **However, with the new NuTeV result, $\chi^2/ndof = 30.6/15$, corresponding to a probability of just 1.0%, while central values and errors of the fit parameters are nearly unchanged!** Compared to the results shown in Table 10.4, the relative uncertainty on m_{H} decreases by more than a third, mainly by including the direct measurements of m_{t} and m_{W}. The importance of the external $\Delta\alpha^{(5)}_{\mathrm{had}}(m^2_{\mathrm{Z}}) = 0.02761 \pm 0.00036$ determination for the constraint on m_{H} is shown in Figure 10.9c. Without the external $\Delta\alpha^{(5)}_{\mathrm{had}}(m^2_{\mathrm{Z}})$ constraint, the fit results are $\Delta\alpha^{(5)}_{\mathrm{had}}(m^2_{\mathrm{Z}}) = 0.02965^{+0.00091}_{-0.00119}$ and $m_{\mathrm{H}} = 25^{+35}_{-11}$ GeV.

The $\Delta\chi^2_{min}$ curve is shown in Figure 10.10. The effect of the theoretical uncertainties in the Standard-Model calculations due to missing higher-order corrections as discussed in Section 10.4 is shown by the width of the curve. Including these errors, the one-sided 95%CL upper limit

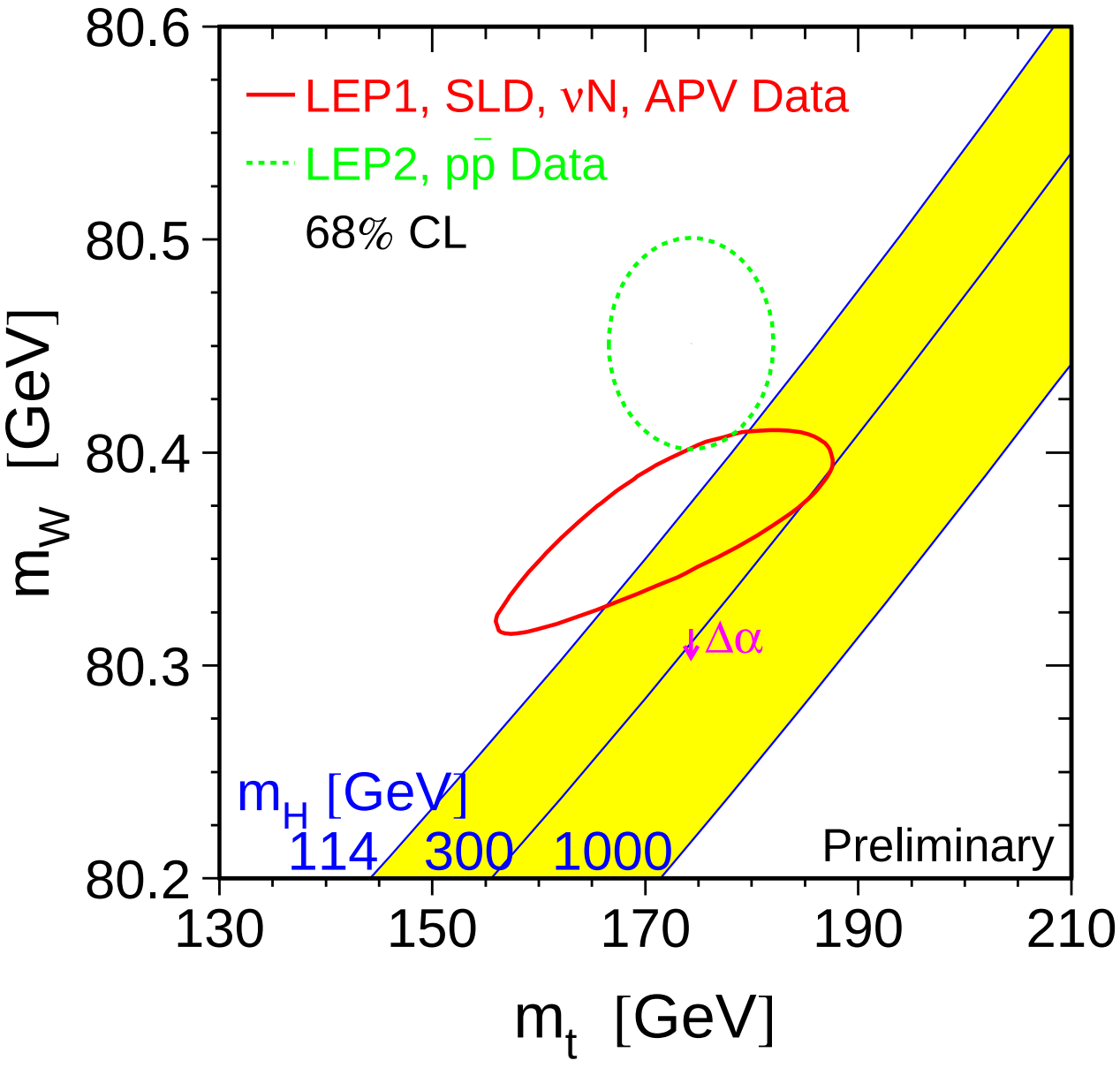

Figure 10.8: Contour curves of 68% probability in the $(m_{\rm t}, m_{\rm W})$ plane. The shaded band shows the Standard-Model prediction based on the value for $G_{\rm F}$ for various values of the Higgs mass and fixed $\Delta\alpha^{(5)}_{\rm had}(m^2_{\rm Z})$; varying the hadronic vacuum polarisation by $\Delta\alpha^{(5)}_{\rm had}(m^2_{\rm Z}) = 0.02761 \pm 0.00036$ yields an additional uncertainty on the Standard-Model prediction shown by the arrow labelled $\Delta\alpha$.

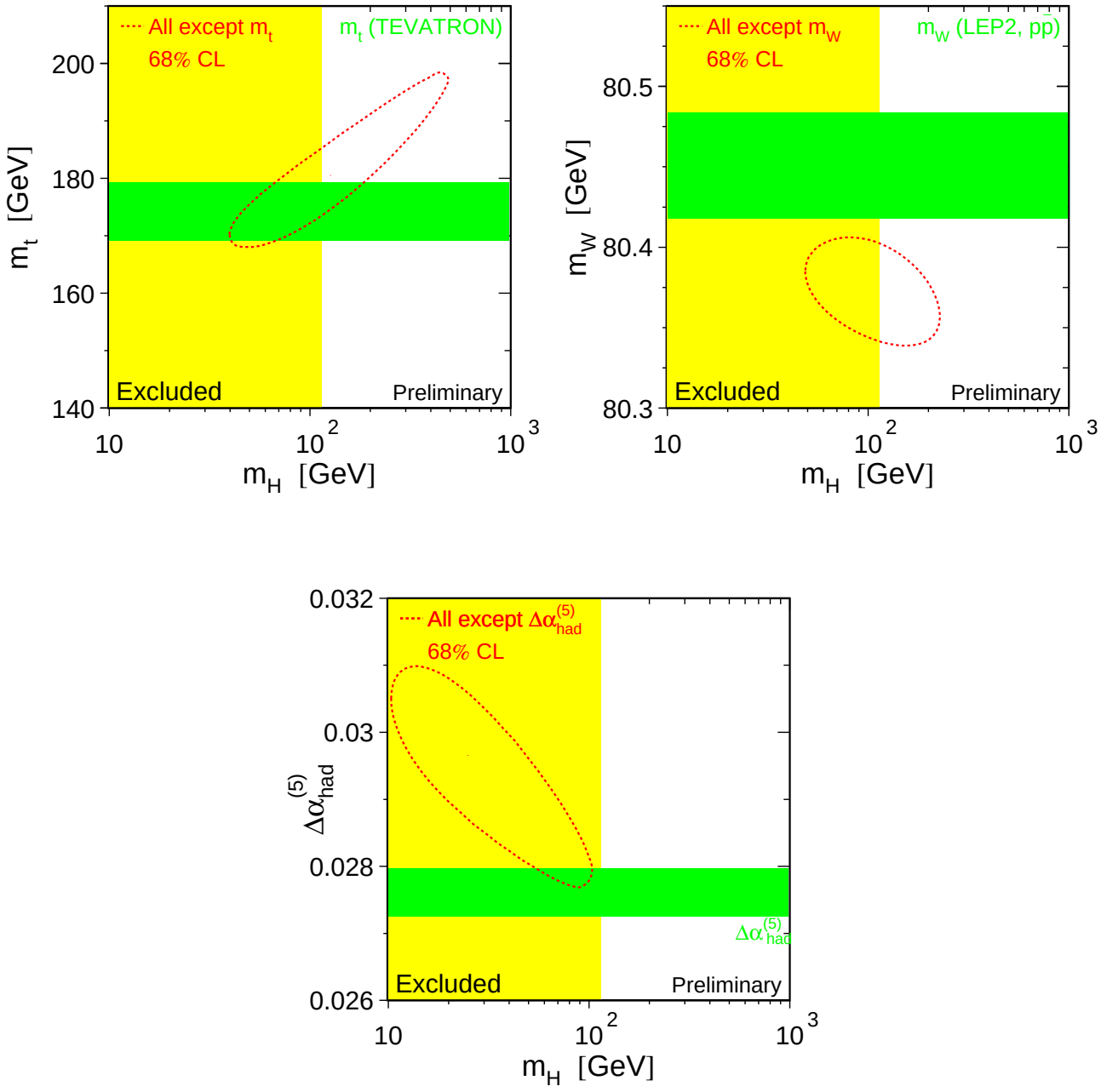

Figure 10.9: Contour curves of 68% probability in (a) the $(m_{\rm t}, m_{\rm H})$ plane, (b) the $(m_{\rm W}, m_{\rm H})$ plane, and (c) the $(\Delta\alpha^{(5)}_{\rm had}(m^2_{\rm Z}), m_{\rm H})$ plane, based on all measurements except (a) the direct measurement of $m_{\rm t}$, (b) the direct measurement of $m_{\rm W}$, and (c) the external constraint on $\Delta\alpha^{(5)}_{\rm had}(m^2_{\rm Z})$, in each case shown as the horizontal band of width ± 1 standard deviation. The vertical band shows the 95% confidence level exclusion limit on $m_{\rm H}$ of 114 GeV derived from the direct search at LEP-2 [194].

Parameter	Value	Correlations				
		$\Delta\alpha^{(5)}_{\rm had}(m^2_{\rm Z})$	$\alpha_{\rm S}(m^2_{\rm Z})$	$m_{\rm Z}$	$m_{\rm t}$	$\log_{10}(m_{\rm H}/{\rm GeV})$
$\Delta\alpha^{(5)}_{\rm had}(m^2_{\rm Z})$	0.02774±0.00035	+1.00	0.00	−0.01	−0.05	−0.46
$\alpha_{\rm S}(m^2_{\rm Z})$	0.1183±0.0026	0.00	+1.00	−0.02	+0.08	+0.12
$m_{\rm Z}$	91.1874±0.0021	−0.01	−0.02	+1.00	−0.04	+0.04
$m_{\rm t}$	175.8±4.3	−0.05	+0.08	−0.04	+1.00	+0.70
$\log_{10}(m_{\rm H}/{\rm GeV})$	1.94±0.21	−0.46	+0.12	+0.04	+0.70	+1.00
$m_{\rm H}$	$88\pm^{53}_{35}$	−0.46	+0.12	+0.04	+0.70	+1.00

Table 10.5: Results on the five Standard Model parameters derived from a fit to all electroweak results. The fit has a χ^2/dof of 22.9/15, corresponding to a probability of 9%. See Section 10.4 for a discussion on theoretical uncertainties not included here.

on the mass of the Higgs boson at $\Delta\chi^2 = 2.7$ is given by:

$$m_{\rm H} \;<\; 196 \text{ GeV}\,. \tag{10.31}$$

In case the theory-driven $\Delta\alpha^{(5)}_{\rm had}(m^2_{\rm Z})$ determination of Equation 10.4 is used, the central value of $m_{\rm H}$ increases while the uncertainty on $m_{\rm H}$ is reduced. The upper limit becomes:

$$m_{\rm H} \;<\; 222 \text{ GeV}\,. \tag{10.32}$$

Both results are in good agreement with the 95% confidence level lower limit on $m_{\rm H}$ of 114.1 GeV based on the direct search performed at LEP-2 [194].

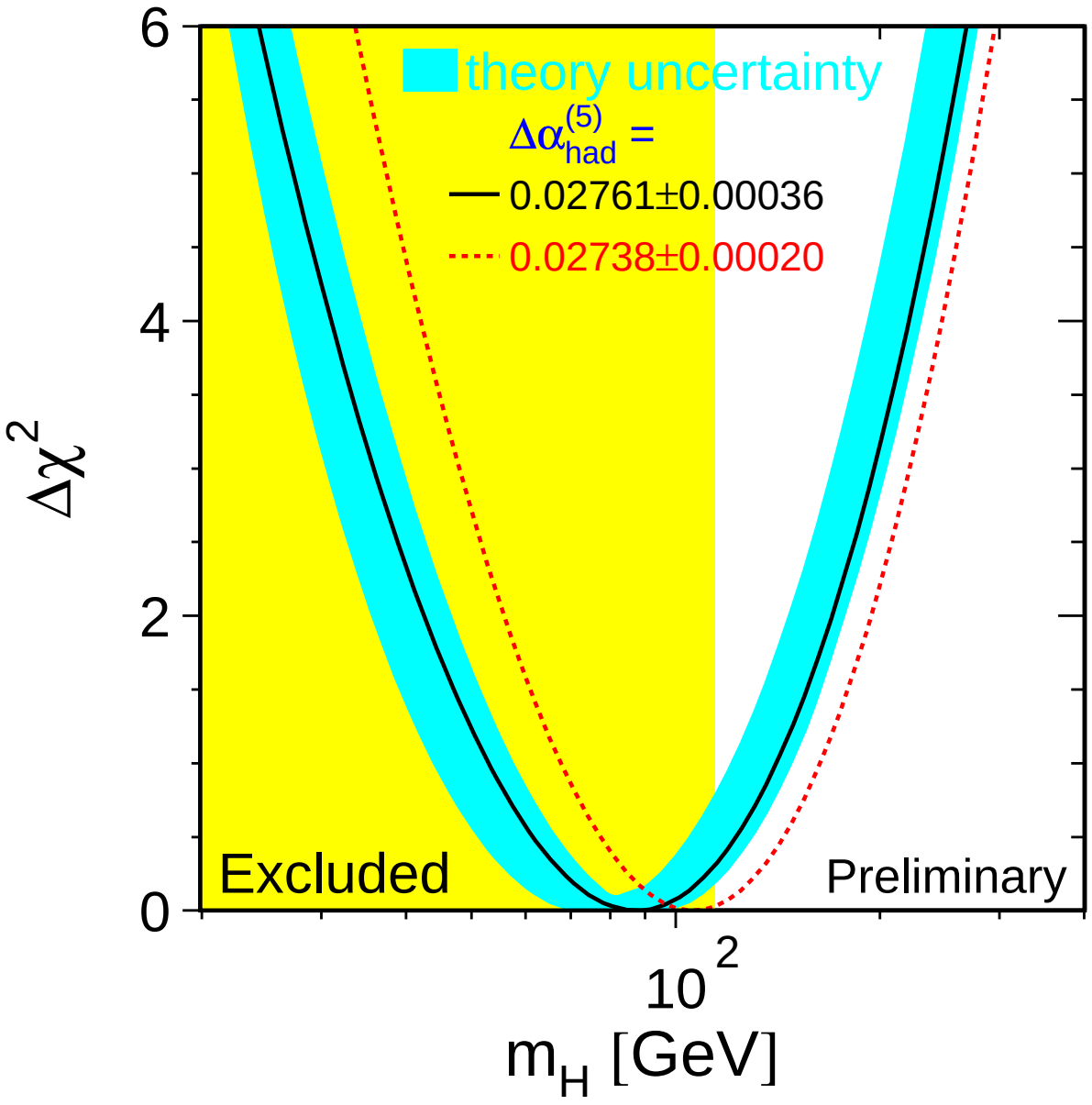

Figure 10.10: $\Delta\chi^2(m_{\rm H}) = \chi^2_{min}(m_{\rm H}) - \chi^2_{\rm min}$ as a function of $m_{\rm H}$. The line is the result of the fit using all data. The associated band represents the estimate of the theoretical uncertainty due to missing higher-order corrections as discussed in Section 10.4. The vertical band shows the 95% confidence level exclusion limit on $m_{\rm H}$ of 114 GeV derived from the direct search at LEP-2 [194]. The dashed curve is the result obtained using the theory-driven $\Delta\alpha^{(5)}_{\rm had}(m^2_{\rm Z})$ determination of Equation 10.4.

10.9 Discussion

The global χ^2/dof of the Standard-Model fit is 22.9/15, corresponding to a probability of 9%. **With the new NuTeV result, this probability reduces to 1%, while fitted values and errors are rather stable.** The contributions of the individual measurements to the global χ^2 are reported in Table 10.6 and shown in Figure 10.11 in terms of the pull of each measurement. The pull is defined as the difference between measured value and predicted value, calculated for the values of the five Standard-Model parameters corresponding to the global minimum of the χ^2, in units of the measurement uncertainty.

The by far largest contribution to the overall χ^2 has already been discussed, namely the b-quark forward-backward asymmetry measured at LEP-1. The second and third largest pulls are caused by the left-right asymmetry measured by SLD, dominating $\mathcal{A}_\ell$(SLD), and the hadronic Z pole cross section measured at LEP-1. Nearly the same pull is caused by the combined result on the direct measurement of the W-boson mass. Compared to the uncertainty of the measurement, $\sigma^0_{\rm h}$ exhibits only a weak dependence on any of the five Standard-Model parameters. This is because the principal dependence of $\sigma^0_{\rm h}$ is to the number of light neutrino generations, which is constant and equal to three in the Standard Model.

As far as the mass of the Higgs boson is concerned, both $A^{0,\,\rm b}_{\rm FB}$ and $\mathcal{A}_\ell$(SLD) exhibit a high sensitivity to it, but prefer a high and a low value, respectively, as reported also in Table 10.6. The constraint on the Higgs-boson mass arising from from each pseudo-observable is shown in Figure 10.12. The corresponding Higgs-boson mass is obtained from a five-parameter Standard-Model fit to the observable, constraining $\Delta\alpha^{(5)}_{\rm had}(m^2_{\rm Z}) = 0.02761 \pm 0.00036$, $\alpha_{\rm S}(m^2_{\rm Z}) = 0.118 \pm 0.002$, $m_{\rm Z} = 91.1875 \pm 0.0021$ GeV and $m_{\rm t} = 174.3 \pm 5.1$ GeV. Within the Standard-Model analysis, the other observables also prefer low values for $m_{\rm H}$, such as the various leptonic asymmetry measurements and in particular both measurements of the mass of the W boson. Thus the pull of the $A^{0,\,\rm b}_{\rm FB}$ measurement is enlarged compared to the $\sin^2\theta^{\rm lept}_{\rm eff}$ combination discussed in Section 9.4, while that of $\mathcal{A}_\ell$(SLD) is reduced, pointing to $A^{0,\,\rm b}_{\rm FB}$ as the deviating measurement.

Given the size of the experimental errors on the b-quark couplings compared to the size of their radiative corrections as expected in the Standard Model, a potential explanation in terms of new physics phenomena would require modifications of the b-quark couplings already at the level of the Born-term values, as also discussed in Section 9.5. Because of these considerations, it is interesting to repeat the Standard-Model analysis excluding (i) $\mathcal{A}_\ell$(SLD), (ii) $A^{0,\,\rm b}_{\rm FB}$(LEP) and (iii) the direct measurements of $m_{\rm W}$. The results are: (i) $\chi^2/dof = 19.6/14$ (14%), $m_{\rm H} = 121^{+73}_{-48}$ GeV; (ii) $\chi^2/dof = 14.4/14$ (42%), $m_{\rm H} = 51^{+39}_{-22}$ GeV; (iii) $\chi^2/dof = 19.1/13$ (12%), $m_{\rm H} = 108^{+70}_{-44}$ GeV. The largest changes in the results are observed for case (ii).

In the data collected in the year 2000, the last year of LEP-2 operation, indications for the production of the Higgs boson were found [194]. Combining all four LEP experiments, the observations, compared to the expected background, correspond to a significance of 2.1 standard deviations [194]. Attributing this excess to the production of the Standard Model Higgs boson, a mass of about 115.6 GeV is found. More data is needed to confirm or exclude this indication and its interpretation.

Such a value for $m_{\rm H}$ is in good agreement with the value predicted within the Standard Model, Table 10.5, based on the analysis of precision electroweak observables. **However, because of the low probability of 1% for the Standard-Model fit to all results, any quantitative conclusions drawn from the Standard-Model analysis have to be taken with great care.**

	Measurement with Total Error	Systematic Error	Standard Model fit	Pull	Higgs Sens.
$\Delta\alpha^{(5)}_{\rm had}(m^2_{\rm Z})$ [199]	0.02761 ± 0.00036	0.00035	0.02774	-0.3	—
$m_{\rm Z}$ [GeV]	91.1875 ± 0.0021	[a] 0.0017	91.1874	0.0	—
$\Gamma_{\rm Z}$ [GeV]	2.4952 ± 0.0023	[a] 0.0013	2.4963	-0.5	$+2.8$
$\sigma^0_{\rm h}$ [nb]	41.540 ± 0.037	[b] 0.028	41.481	1.6	$+0.11$
R^0_ℓ	20.767 ± 0.025	[b] 0.007	20.739	1.1	-0.80
$A^{0,\ell}_{\rm FB}$	0.0171 ± 0.0010	[b] 0.0003	0.0165	0.7	-2.1
$\mathcal{A}_\ell$ (SLD)	0.1513 ± 0.0021	0.0010	0.1483	1.5	-4.4
$\mathcal{A}_\ell$ (P_τ)	0.1465 ± 0.0033	0.0009	0.1483	-0.5	$+2.8$
$R^0_{\rm b}$	0.21646 ± 0.00065	0.00056	0.21573	1.1	$+0.11$
$R^0_{\rm c}$	0.1719 ± 0.0031	0.0028	0.1723	-0.1	$+0.025$
$A^{0,{\rm b}}_{\rm FB}$	0.0990 ± 0.0017	0.0010	0.1039	-2.9	$+3.9$
$A^{0,{\rm c}}_{\rm FB}$	0.0685 ± 0.0034	0.0019	0.0743	-1.7	$+1.5$
$\mathcal{A}_{\rm b}$	0.922 ± 0.020	0.017	0.935	-0.6	$+0.037$
$\mathcal{A}_{\rm c}$	0.670 ± 0.026	0.016	0.668	0.1	-0.16
$\sin^2\theta^{\rm lept}_{\rm eff}$ ($\langle Q_{\rm FB}\rangle$)	0.2324 ± 0.0012	0.0008	0.23136	0.9	$+1.0$
$m_{\rm t}$ [GeV] ($\rm p\overline{p}$ [76])	174.3 ± 5.1	4.0	175.8	-0.3	—
$m_{\rm W}$ [GeV] ($\rm p\overline{p}$ [217])	80.454 ± 0.060	0.050	80.398	0.9	-2.5
$m_{\rm W}$ [GeV] (LEP-2 [223])	80.450 ± 0.039	0.030	80.398	1.3	-3.8
$\sin^2\theta_{\rm W}$ (νN [241])	0.2255 ± 0.0021	0.0010	0.2226	1.2	$+1.4$
$Q_{\rm W}$(Cs) [230]	-72.5 ± 0.7	0.6	-72.9	0.6	-0.34

Table 10.6: Summary of measurements included in the combined analysis of Standard Model parameters. See Chapters 2 to 7 for the correlations between these results not reported in this table. The total errors in column 2 include the systematic errors listed in column 3. Although the systematic errors include both correlated and uncorrelated sources, the determination of the systematic part of each error is approximate. The Standard Model results in column 4 and the pulls (difference between measurement and fit in units of the total measurement error) in column 5 are derived from the Standard-Model analysis including all data. These analyses include all correlations between the results. The last column shows the Standard-Model Higgs sensitivity, defined as the partial derivative of the Standard-Model calculation of the observable w.r.t. $\log_{10}(m_{\rm H}/{\rm GeV})$, divided by the total measurement error. The sign tells whether the observable in question wants a higher (+) or lower (−) Higgs mass than that of the global fit.
[a] Only systematic errors arising from the uncertainties in the LEP beam energy are indicated.
[b] Only common systematic errors are indicated.

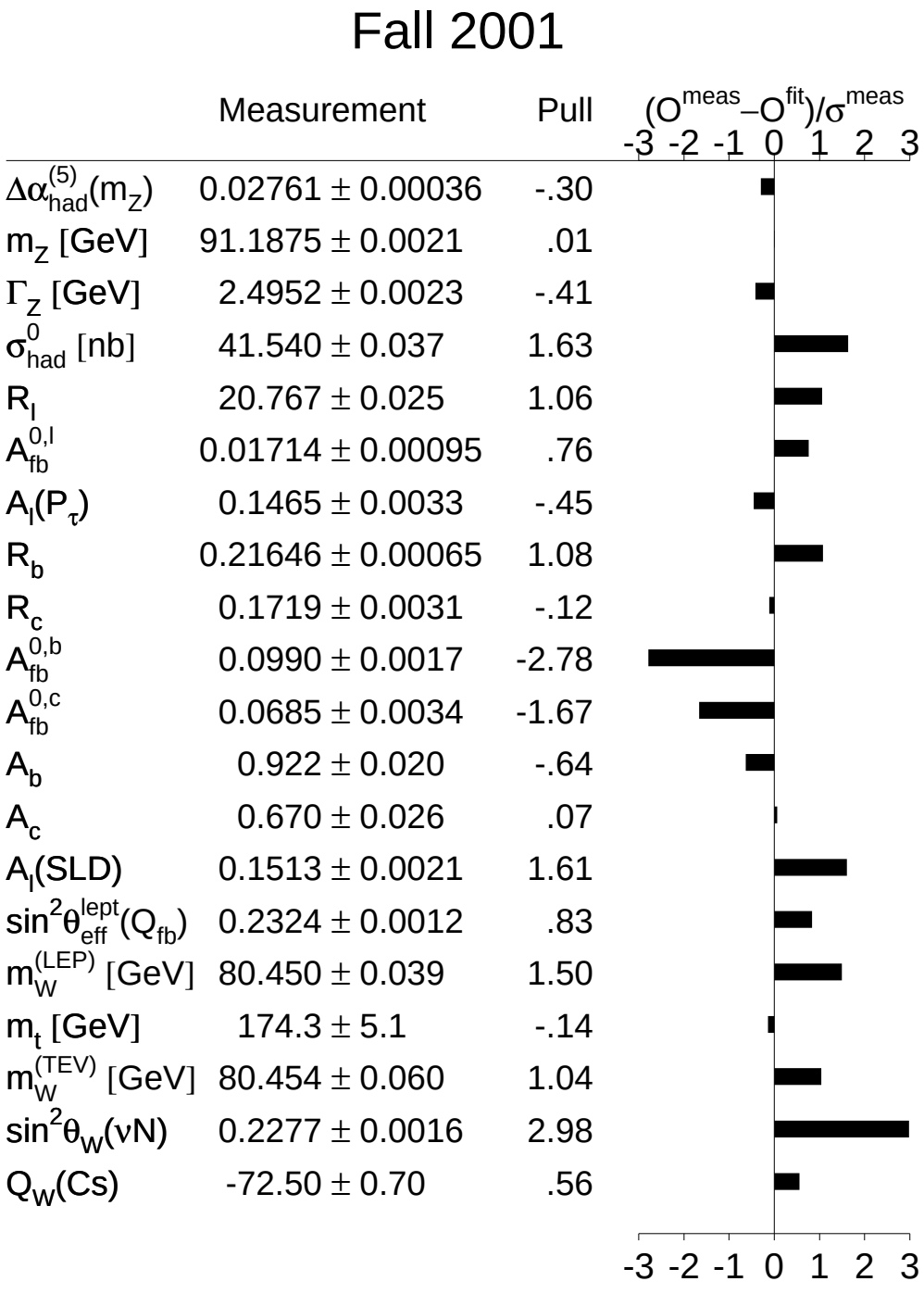

Figure 10.11: Comparison of the measurements with the expectation of the Standard Model, calculated for the Standard-Model parameter values in the minimum of the global χ^2. Also shown is the pull of each measurement, where pull is defined as the difference of measurement and expectation in units of the measurement uncertainty. **The new NuTeV result is shown!**

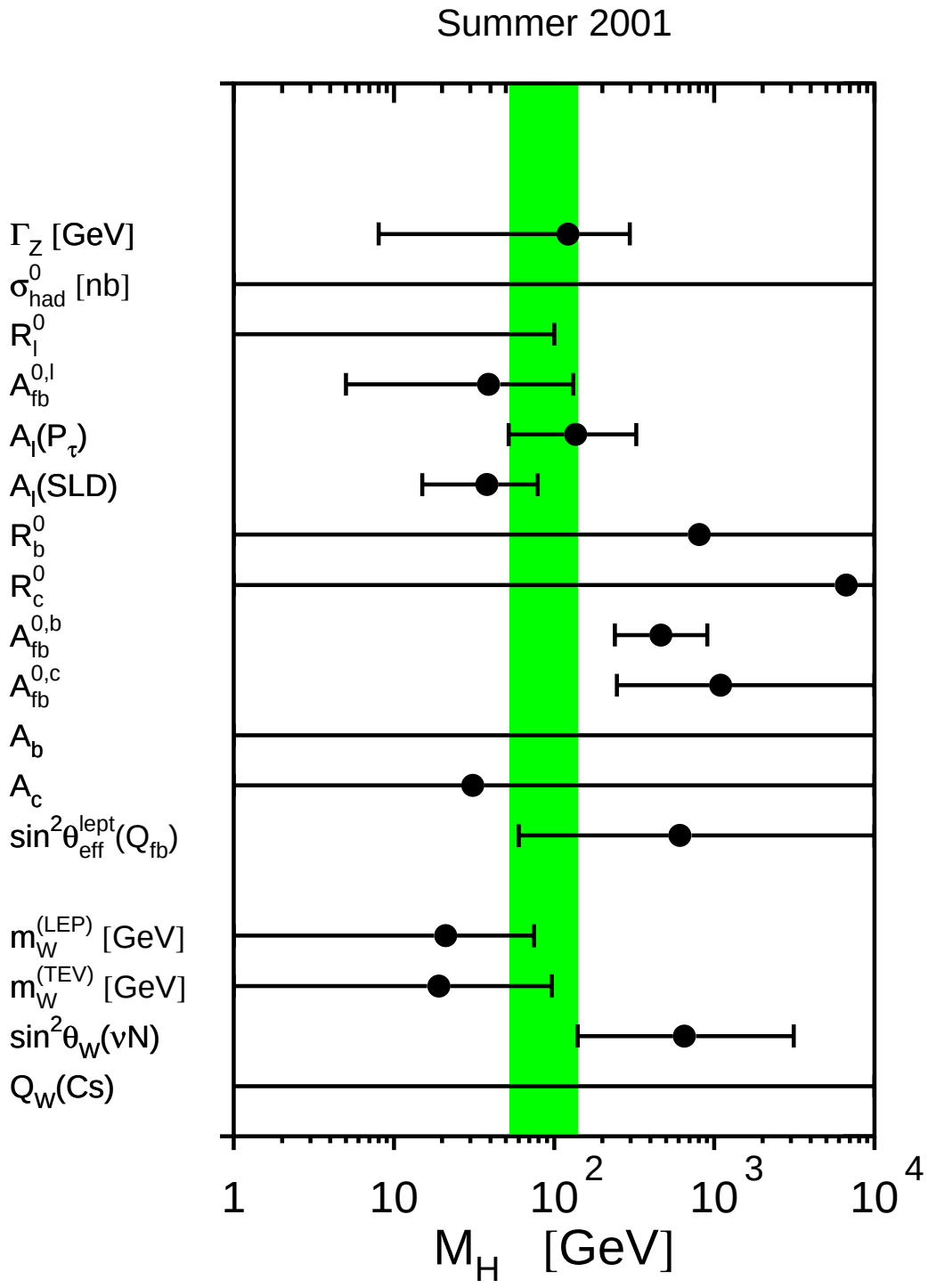

Figure 10.12: Constraints on the mass of the Higgs boson from each pseudo-observable. The Higgs-boson mass and its 68% CL uncertainty is obtained from a five-parameter Standard-Model fit to the observable, constraining $\Delta\alpha^{(5)}_{\rm had}(m_{\rm Z}^2) = 0.02761 \pm 0.00036$, $\alpha_{\rm S}(m_{\rm Z}^2) = 0.118 \pm 0.002$, $m_{\rm Z} = 91.1875 \pm 0.0021$ GeV and $m_{\rm t} = 174.3 \pm 5.1$ GeV. Because of these four common constraints the resulting Higgs-boson mass values cannot be combined. The shaded band denotes the overall constraint on the mass of the Higgs boson derived from all pseudo-observables including the above four Standard-Model parameters as reported in Table 10.5.

Chapter 11

Summary and Conclusions

$Id: physrep_summary.tex,v 1.21 2001/12/18 13:06:04 kellogg Exp $

The four LEP experiments ALEPH, DELPHI, L3 and OPAL and the SLD experiment at the SLC perform measurements in electron-positron collisions at centre-of-mass energies corresponding to the mass of the Z boson. Accumulating about 18 million Z decays with excellent detectors, the measurements are of unprecedented accuracy in high-energy particle physics. In particular, the pair-production of charged leptons and heavy quarks as well as inclusive hadron production is analysed by measuring production cross sections and various cross-section asymmetries. These measurements are presented in Chapters 2 to 6 .

The measurements are used to determine the mass of the Z boson, its decay widths and its couplings to the various fermion species:

$$\begin{aligned} m_{\mathrm{Z}} &= 91.1875 \pm 0.0021 \text{ GeV} \\ \Gamma_{\mathrm{Z}} &= 2.4952 \pm 0.0023 \text{ GeV} \\ \rho_{\ell} &= 1.0049 \pm 0.0010 \\ \sin^2\theta^{\mathrm{lept}}_{\mathrm{eff}} &= 0.23152 \pm 0.00017\,. \end{aligned}$$

The number of light neutrino species is determined to be 2.9841 ± 0.0083, in good agreement with expectations based on the three observed generations of fundamental fermions. In general, the uncertainties on the measured parameters have been reduced by two to three orders of magnitude with respect to the experimental results available before the startup of SLC and LEP.

In addition, the large and diverse set of precise measurements allows many relations inspired by the Standard Model to be stringently tested (Chapter 9) and the free parameters of the model to be tightly constrained (Chapter 10). The neutral weak current couplings for individual fermions are determined and reported in Chapter 9. Lepton universality of the neutral weak current is established at the permille level.

While most measurements are well accommodated, the various measurements of forward-backward and polarised asymmetries, when interpreted in terms of a single quantity, the leptonic effective electroweak mixing angle, show a dispersion larger than expected with a χ^2/dof of 12.8/5 (2.5%) for the average shown above. Within the Standard-Model framework, the large χ^2/dof is mainly caused by the measurement of the forward-backward asymmetry in $\mathrm{b\overline{b}}$ production, discussed in Chapter 10. This could be explained by new physics, for example, modifying the right-handed b-quark coupling, or simply by a fluctuation of one or more of the

asymmetry measurements. Further improvements on the precision of Z-pole observables could come from a linear collider taking data at the Z-pole.

Analysing all results in the framework of the Standard Model, the largest deviation w.r.t. the expectation is found for the on-shell electroweak mixing angle as measured in neutrino-nucleon scattering by the NuTeV collaboration. Note that this measurement and the forward-backward asymmetry in $\mathrm{b\overline{b}}$ production measured at LEP are completely independent experimentally, are of different precision, and are extracted from different processes involving different fermion species, at greatly differing scales of momentum transfer.

The Standard-Model fit results are rather stable when the NuTeV measurement is removed, while this is not the case when the $A_{\mathrm{FB}}^{0,\,\mathrm{b}}$ measurement is removed. In either case, the predicted masses of the top quark and of the W boson agree with the direct measurements of these quantities, successfully testing the Standard Model at the level of its radiative corrections in this respect. Based on all results, the mass of the Higgs boson is predicted with an uncertainty of about 50% and found to be less than 196 GeV at 95% confidence level, in agreement with the lower limit obtained from direct searches at LEP-2.

In the next years, improvements to three other important electroweak observables will become available, namely the masses of the top quark and of the W boson, and the hadronic vacuum polarisation. Assuming future world-average uncertainties of 2 GeV on m_{t}, 25 MeV on m_{W}, and 0.00010 on $\Delta\alpha_{\mathrm{had}}^{(5)}(m_{\mathrm{Z}}^2)$, the mass of the Higgs boson can be predicted with an uncertainty of about 30%, while the direct observation of Higgs-boson production will eventually allow its mass to be measured at the GeV level, allowing another crucial test of the Standard Model through a comparison of the direct and indirect results.

However, because some of the current results show differences from the Standard-Model expectation, the χ^2 probability of the Standard-Model fit to all results has a rather low value of 1%. Thus any quantitative conclusions drawn from the Standard-Model analysis have to be taken with great care.

Appendix A

The Measurements used in the Heavy Flavour Averages

This appendix contains the results of the summer01 conferences, they are not final!

In the following 20 tables the results used in the combination are listed. In each case an indication of the dataset used and the type of analysis is given. Preliminary results are indicated by the symbol "†". The values of centre-of-mass energy are given where relevant. In each table, the result used as input to the average procedure is given followed by the statistical error, the correlated and uncorrelated systematic errors, the total systematic error, and any dependence on other electroweak parameters. In the case of the asymmetries, the measurement moved to a common energy (89.55 GeV, 91.26 GeV and 92.94 GeV, respectively, for peak−2, peak and peak+2 results) is quoted as *corrected* asymmetry.

Contributions to the correlated systematic error quoted here are from any sources of error shared with one or more other results from different experiments in the same table, and the uncorrelated errors from the remaining sources. In the case of $\mathcal{A}_c$ and $\mathcal{A}_b$ from SLD the quoted correlated systematic error has contributions from any source shared with one or more other measurements from LEP experiments. Constants such as $a(x)$ denote the dependence on the assumed value of x^{used}, which is also given.

	ALEPH	DELPHI	L3	OPAL	SLD
	92-95 [117]	92-95 [118]	94-95 [119]	92-95 [113]	93-98† [114]
R_b^0	0.2158	0.2163	0.2173	0.2174	0.2164
Statistical	0.0009	0.0007	0.0015	0.0011	0.0009
Uncorrelated	0.0007	0.0004	0.0015	0.0009	0.0006
Correlated	0.0006	0.0004	0.0018	0.0008	0.0005
Total Systematic	0.0009	0.0005	0.0023	0.0012	0.0007
$a(R_c)$	-0.0033	-0.0041	-0.0376	-0.0122	-0.0057
R_c^{used}	0.1720	0.1720	0.1734	0.1720	0.1710
$a(\text{BR}(c \to \ell^+))$			-0.0133	-0.0067	
$\text{BR}(c \to \ell^+)^{\text{used}}$			9.80	9.80	
$a(f(D^+))$	-0.0010	-0.0010	-0.0086	-0.0029	-0.0008
$f(D^+)^{\text{used}}$	0.2330	0.2330	0.2330	0.2380	0.2370
$a(f(D_s))$	-0.0001	0.0001	-0.0005	-0.0001	-0.0003
$f(D_s)^{\text{used}}$	0.1020	0.1030	0.1030	0.1020	0.1140
$a(f(\Lambda_c))$	0.0002	0.0003	0.0008	0.0003	-0.0003
$f(\Lambda_c)^{\text{used}}$	0.0650	0.0630	0.0630	0.0650	0.0730

Table A.1: The measurements of R_b^0. All measurements use a lifetime tag enhanced by other features like invariant mass cuts or high p_T leptons.

	ALEPH			DELPHI		OPAL		SLD
	91-95 c-count [125]	91-95 D meson [121]	92-95 lepton [121]	92-95 c-count [123]	92-95 D meson [122, 123]	91-94 c-count [126]	90-95 D meson [124]	93-97† vtx-mass [120]
R_c^0	0.1735	0.1682	0.1670	0.1693	0.1610	0.1642	0.1760	0.1738
Statistical	0.0051	0.0082	0.0062	0.0050	0.0104	0.0122	0.0095	0.0031
Uncorrelated	0.0057	0.0077	0.0059	0.0050	0.0064	0.0126	0.0102	0.0019
Correlated	0.0094	0.0028	0.0009	0.0077	0.0060	0.0099	0.0062	0.0008
Total Systematic	0.0110	0.0082	0.0059	0.0092	0.0088	0.0161	0.0120	0.0021
$a(R_b)$		-0.0050						-0.0433
R_b^{used}		0.2159						0.2166
$a(\text{BR}(c \to \ell^+))$			-0.1646					
$\text{BR}(c \to \ell^+)^{\text{used}}$			9.80					

Table A.2: The measurements of R_c^0. "c-count" denotes the determination of R_c^0 from the sum of production rates of weakly decaying charmed hadrons. "D meson" denotes any single/double tag analysis using exclusive and/or inclusive D meson reconstruction.

	ALEPH				DELPHI			L3	OPAL		
	90-95 lepton [128]	90-95 lepton [128]	90-95 lepton [128]	91-95 multi [135]	93-95† lepton [129]	92-95 D-meson [137]	92-95 jet charge [132]	90-95 lepton [130]	91-95 jet charge [134]	90-95† lepton [131]	90-95 D-meso [138]
$\sqrt{s}$ (GeV)	88.380	89.380	90.210	89.470	89.433	89.434	89.550	89.500	89.440	89.490	89.490
$A_{\mathrm{FB}}^{\mathrm{b\bar{b}}}(-2)$	-3.53	5.47	9.10	4.36	5.90	5.64	6.80	6.15	4.10	3.56	-9.20
$A_{\mathrm{FB}}^{\mathrm{b\bar{b}}}(-2)$Corrected		5.87		4.55	6.18	5.92	6.80	6.27	4.36	3.70	-9.06
Statistical		1.90		1.19	2.20	7.59	1.80	2.93	2.10	1.73	10.80
Uncorrelated		0.39		0.05	0.08	0.91	0.12	0.37	0.25	0.16	2.51
Correlated		0.70		0.01	0.08	0.08	0.01	0.19	0.02	0.04	1.41
Total Systematic		0.80		0.05	0.12	0.91	0.13	0.41	0.25	0.16	2.87
$a(R_{\mathrm{b}})$		-0.3069		-9.5	-1.1543		-0.1962	-1.4467	-0.7300	-0.1000	
$R_{\mathrm{b}}^{\mathrm{used}}$		0.2192		0.2150	0.2164		0.2158	0.2170	0.2150	0.2155	
$a(R_{\mathrm{c}})$		0.0362		0.3100	1.0444		0.3200	0.3612	0.0700	0.1000	
$R_{\mathrm{c}}^{\mathrm{used}}$		0.1710		0.1725	0.1671		0.1720	0.1734	0.1730	0.1720	
$a(A_{\mathrm{FB}}^{\mathrm{c\bar{c}}}(-2))$		-0.2244		-0.2955				-0.1000	-0.3156		
$A_{\mathrm{FB}}^{\mathrm{c\bar{c}}}(-2)^{\mathrm{used}}$		-2.34		-2.87				-2.50	-2.81		
$a(\mathrm{BR}(\mathrm{b}\to\ell^-))$		-0.2486			-1.0154			-1.0290		0.3406	
$\mathrm{BR}(\mathrm{b}\to\ell^-)^{\mathrm{used}}$		11.34			10.56			10.50		10.90	
$a(\mathrm{BR}(\mathrm{b}\to\mathrm{c}\to\ell^+))$		-0.1074			-0.1424			-0.1440		-0.5298	
$\mathrm{BR}(\mathrm{b}\to\mathrm{c}\to\ell^+)^{\mathrm{used}}$		7.86			8.07			8.00		8.30	
$a(\mathrm{BR}(\mathrm{c}\to\ell^+))$		-0.0474			0.7224			0.5096		0.1960	
$\mathrm{BR}(\mathrm{c}\to\ell^+)^{\mathrm{used}}$		9.80			9.90			9.80		9.80	
$a(\overline{\chi})$		5.259			1.3054						
$\overline{\chi}^{\mathrm{used}}$		0.12460			0.11770						
$a(f(\mathrm{D}^+))$						0.5083	0.0949				
$f(\mathrm{D}^+)^{\mathrm{used}}$						0.2210	0.2330				
$a(f(\mathrm{D_s}))$						0.1742	0.0035				
$f(\mathrm{D_s})^{\mathrm{used}}$						0.1120	0.1020				
$a(f(\Lambda_{\mathrm{c}}))$						-0.0191	-0.0225				
$f(\Lambda_{\mathrm{c}})^{\mathrm{used}}$						0.0840	0.0630				
$a(\mathrm{P}(\mathrm{c}\to\mathrm{D}^{*+})\times\mathrm{BR}(\mathrm{D}^{*+}\to\pi^+\mathrm{D}^0))$				-0.1100							
$\mathrm{P}(\mathrm{c}\to\mathrm{D}^{*+})\times\mathrm{BR}(\mathrm{D}^{*+}\to\pi^+\mathrm{D}^0)^{\mathrm{used}}$				0.1830							

Table A.3: The measurements of $A_{\mathrm{FB}}^{\mathrm{b\bar{b}}}(-2)$. All numbers are given in %.

	ALEPH	DELPHI		OPAL	
	91-95 D-meson [136]	93-95† lepton [129]	92-95 D-meson [137]	90-95† lepton [131]	90-95 D-meson [138]
$\sqrt{s}$ (GeV)	89.370	89.433	89.434	89.490	89.490
$A_{\mathrm{FB}}^{\mathrm{c\bar{c}}}(-2)$	-1.10	1.12	-5.02	-6.91	3.90
$A_{\mathrm{FB}}^{\mathrm{c\bar{c}}}(-2)$Corrected	-0.02	1.82	-4.32	-6.55	4.26
Statistical	4.30	3.60	3.69	2.44	5.10
Uncorrelated	1.00	0.53	0.40	0.38	0.80
Correlated	0.09	0.16	0.09	0.23	0.30
Total Systematic	1.00	0.55	0.41	0.44	0.86
$a(R_{\mathrm{b}})$		-0.2886		-3.4000	
$R_{\mathrm{b}}^{\mathrm{used}}$		0.2164		0.2155	
$a(R_{\mathrm{c}})$		1.0096		3.2000	
$R_{\mathrm{c}}^{\mathrm{used}}$		0.1671		0.1720	
$a(A_{\mathrm{FB}}^{\mathrm{b\bar{b}}}(-2))$	-1.3365				
$A_{\mathrm{FB}}^{\mathrm{b\bar{b}}}(-2)^{\mathrm{used}}$	6.13				
$a(\mathrm{BR}(\mathrm{b} \to \ell^-))$		-1.0966		-1.7031	
$\mathrm{BR}(\mathrm{b} \to \ell^-)^{\mathrm{used}}$		10.56		10.90	
$a(\mathrm{BR}(\mathrm{b} \to \mathrm{c} \to \ell^+))$		1.1156		-1.4128	
$\mathrm{BR}(\mathrm{b} \to \mathrm{c} \to \ell^+)^{\mathrm{used}}$		8.07		8.30	
$a(\mathrm{BR}(\mathrm{c} \to \ell^+))$		1.0703		3.3320	
$\mathrm{BR}(\mathrm{c} \to \ell^+)^{\mathrm{used}}$		9.90		9.80	
$a(\overline{\chi})$		-0.0856			
$\overline{\chi}^{\mathrm{used}}$		0.11770			
$a(f(\mathrm{D}^+))$			-0.3868		
$f(\mathrm{D}^+)^{\mathrm{used}}$			0.2210		
$a(f(\mathrm{D_s}))$			-0.1742		
$f(\mathrm{D_s})^{\mathrm{used}}$			0.1120		
$a(f(\Lambda_{\mathrm{c}}))$			-0.0878		
$f(\Lambda_{\mathrm{c}})^{\mathrm{used}}$			0.0840		

Table A.4: The measurements of $A_{\mathrm{FB}}^{\mathrm{c\bar{c}}}(-2)$. All numbers are given in %.

	ALEPH		DELPHI					L3		OPAL		
	91-95† lepton [128]	91-95 multi [135]	91-92 lepton [129]	93-95† lepton [129]	92-95 D-meson [137]	92-95 jet charge [132]	92-95† multi [139]	94-95 jet charge [133]	90-95 lepton [130]	91-95 multi [134]	90-95† lepton [131]	90-95 D-meso [138]
$\sqrt{s}$ (GeV)	91.210	91.230	91.270	91.223	91.235	91.260	91.260	91.240	91.260	91.210	91.240	91.24
$A_{\rm FB}^{\rm b\overline{b}}$(pk)	9.71	10.00	10.89	9.86	7.58	9.83	9.72	9.31	9.85	10.06	9.14	9.00
$A_{\rm FB}^{\rm b\overline{b}}$(pk)Corrected	9.81	10.06	10.87	9.93	7.63	9.83	9.72	9.35	9.85	10.15	9.18	9.04
Statistical	0.40	0.27	1.30	0.64	1.97	0.47	0.35	1.01	0.67	0.52	0.44	2.70
Uncorrelated	0.16	0.11	0.33	0.15	0.76	0.13	0.21	0.51	0.27	0.41	0.14	2.14
Correlated	0.12	0.02	0.27	0.14	0.10	0.06	0.05	0.21	0.14	0.20	0.15	0.45
Total Systematic	0.20	0.11	0.43	0.20	0.77	0.15	0.22	0.55	0.31	0.46	0.20	2.19
$a(R_{\rm b})$	-0.9545	-9.5	-2.8933	-2.0201		-0.1962	0.0637	-9.1622	-2.1700	-7.6300	-0.7000	
$R_{\rm b}^{\rm used}$	0.2172	0.2158	0.2170	0.2164		0.2158	0.2164	0.2170	0.2170	0.2150	0.2155	
$a(R_{\rm c})$	0.6450	0.3100	1.0993	1.1488		0.8400	0.0595	1.0831	1.3005	0.4600	0.6000	
$R_{\rm c}^{\rm used}$	0.1720	0.1715	0.1710	0.1671		0.1720	0.1731	0.1733	0.1734	0.1730	0.1720	
$a(A_{\rm FB}^{\rm c\overline{c}}$(pk))		0.6849					0.2756	1.1603	0.9262	0.6870		
$A_{\rm FB}^{\rm c\overline{c}}(\rm pk)^{\rm used}$		6.66					6.89	6.91	7.41	6.19		
$a(\mathrm{BR}(\mathrm{b}\to\ell^-))$	-1.8480		-3.8824	-2.0308					-2.0160		-0.3406	
$\mathrm{BR}(\mathrm{b}\to\ell^-)^{\rm used}$	10.78		11.00	10.56					10.50		10.90	
$a(\mathrm{BR}(\mathrm{b}\to\mathrm{c}\to\ell^+))$	0.4233		0.4740	-0.3798					-0.1280		-0.3532	
$\mathrm{BR}(\mathrm{b}\to\mathrm{c}\to\ell^+)^{\rm used}$	8.14		7.90	8.07					8.00		8.30	
$a(\mathrm{BR}(\mathrm{c}\to\ell^+))$	0.5096		0.7840	1.0703					1.5288		0.5880	
$\mathrm{BR}(\mathrm{c}\to\ell^+)^{\rm used}$	9.80		9.80	9.90					9.80		9.80	
$a(\overline{\chi})$	2.9904		3.4467	1.6692								
$\overline{\chi}^{\rm used}$	0.12460		0.12100	0.11770								
$a(f(\mathrm{D}^+))$					0.0442	0.2761	-0.0175					
$f(\mathrm{D}^+)^{\rm used}$					0.2210	0.2330	0.2330					
$a(f(\mathrm{D_s}))$					-0.0788	0.0106	-0.0260					
$f(\mathrm{D_s})^{\rm used}$					0.1120	0.1020	0.1300					
$a(f(\Lambda_{\rm c}))$					-0.0115	-0.0495	0.0221					
$f(\Lambda_{\rm c})^{\rm used}$					0.0840	0.0630	0.0960					
$a(\mathrm{P}(\mathrm{c}\to\mathrm{D}^{*+})\times\mathrm{BR}(\mathrm{D}^{*+}\to\pi^+\mathrm{D}^0))$		-0.2500										
$\mathrm{P}(\mathrm{c}\to\mathrm{D}^{*+})\times\mathrm{BR}(\mathrm{D}^{*+}\to\pi^+\mathrm{D}^0)^{\rm used}$		0.1830										

Table A.5: The measurements of $A_{\rm FB}^{\rm b\overline{b}}$(pk). All numbers are given in %.

	ALEPH		DELPHI			L3	OPAL	
	91-95† lepton [128]	91-95 D-meson [136]	91-92 lepton [129]	93-95† lepton [129]	92-95 D-meson [137]	90-91 lepton [130]	90-95† lepton [131]	90-95 D-meson [138]
$\sqrt{s}$ (GeV)	91.210	91.220	91.270	91.223	91.235	91.240	91.240	91.240
$A_{\rm FB}^{\rm c\bar{c}}$(pk)	5.68	6.13	8.05	6.29	6.58	7.94	5.95	6.50
$A_{\rm FB}^{\rm c\bar{c}}$(pk)Corrected	5.93	6.32	8.00	6.47	6.70	8.04	6.05	6.60
Statistical	0.53	0.90	2.26	1.00	0.97	3.70	0.59	1.20
Uncorrelated	0.24	0.23	1.25	0.53	0.25	2.40	0.37	0.49
Correlated	0.36	0.17	0.49	0.27	0.04	0.49	0.32	0.23
Total Systematic	0.44	0.28	1.35	0.60	0.25	2.45	0.49	0.54
$a(R_{\rm b})$	1.4318		2.8933	-2.3087		4.3200	4.1000	
$R_{\rm b}^{\rm used}$	0.2172		0.2170	0.2164		0.2160	0.2155	
$a(R_{\rm c})$	-2.9383		-6.4736	5.4307		-6.7600	-3.8000	
$R_{\rm c}^{\rm used}$	0.1720		0.1710	0.1671		0.1690	0.1720	
$a(A_{\rm FB}^{\rm b\bar{b}}(\rm pk))$		-2.1333				6.4274		
$A_{\rm FB}^{\rm b\bar{b}}(\rm pk)^{\rm used}$		9.79				8.84		
$a(\rm BR(b \to \ell^-))$	1.8993		4.8529	-2.7618		3.5007	5.1094	
$\rm BR(b \to \ell^-)^{used}$	10.78		11.00	10.56		10.50	10.90	
$a(\rm BR(b \to c \to \ell^+))$	-1.0745		-3.9500	2.2786		-3.2917	-1.7660	
$\rm BR(b \to c \to \ell^+)^{used}$	8.14		7.90	8.07		7.90	8.30	
$a(\rm BR(c \to \ell^+))$	-3.2732		-7.2520	4.8965		-6.5327	-3.9200	
$\rm BR(c \to \ell^+)^{used}$	9.80		9.80	9.90		9.80	9.80	
$a(\overline{\chi})$	0.0453			0.3852				
$\overline{\chi}^{\rm used}$	0.12460			0.11770				
$a(f(\rm D^+))$					-0.0221			
$f(\rm D^+)^{used}$					0.2210			
$a(f(\rm D_s))$					0.0788			
$f(\rm D_s)^{used}$					0.1120			
$a(f(\Lambda_{\rm c}))$					0.0115			
$f(\Lambda_{\rm c})^{\rm used}$					0.0840			

Table A.6: The measurements of $A_{\rm FB}^{\rm c\bar{c}}$(pk). All numbers are given in %.

	ALEPH				DELPHI			L3	OPAL		
	90-95 lepton [128]	90-95 lepton [128]	90-95 lepton [128]	91-95 multi [135]	93-95† lepton [129]	92-95 D-meson [137]	92-95 jet charge [132]	90-95 lepton [130]	91-95 jet charge [134]	90-95† lepton [131]	90-95 D-meso [138]
$\sqrt{s}$ (GeV)	92.050	92.940	93.900	92.950	92.990	92.990	92.940	93.100	92.910	92.950	92.950
$A_{\mathrm{FB}}^{\mathrm{b\overline{b}}}(+2)$	3.93	10.60	9.03	11.72	10.10	8.77	12.30	13.79	14.60	10.76	-3.10
$A_{\mathrm{FB}}^{\mathrm{b\overline{b}}}(+2)$Corrected		10.03		11.71	10.05	8.72	12.30	13.63	14.63	10.75	-3.11
Statistical		1.51		0.98	1.80	6.37	1.60	2.40	1.70	1.43	9.00
Uncorrelated		0.14		0.12	0.14	0.97	0.24	0.34	0.64	0.25	2.03
Correlated		0.24		0.02	0.16	0.14	0.08	0.19	0.34	0.28	1.69
Total Systematic		0.28		0.13	0.21	0.98	0.26	0.39	0.73	0.37	2.65
$a(R_{\mathrm{b}})$		-1.964		-9.5	-2.8859		-0.1962	-3.3756	-12.9000	-0.8000	
$R_{\mathrm{b}}^{\mathrm{used}}$		0.2192		0.2156	0.2164		0.2158	0.2170	0.2150	0.2155	
$a(R_{\mathrm{c}})$		1.575		0.3100	1.3577		1.2000	1.9869	0.6900	0.8000	
$R_{\mathrm{c}}^{\mathrm{used}}$		0.1710		0.1719	0.1671		0.1720	0.1734	0.1730	0.1720	
$a(A_{\mathrm{FB}}^{\mathrm{c\overline{c}}}(+2))$		1.081		1.2793				0.5206	1.3287		
$A_{\mathrm{FB}}^{\mathrm{c\overline{c}}}(+2)^{\mathrm{used}}$		12.51		12.42				12.39	12.08		
$a(\mathrm{BR}(\mathrm{b}\to\ell^-))$		-1.762			-2.3557			-2.0790		-1.3625	
$\mathrm{BR}(\mathrm{b}\to\ell^-)^{\mathrm{used}}$		11.34			10.56			10.50		10.90	
$a(\mathrm{BR}(\mathrm{b}\to\mathrm{c}\to\ell^+))$		-0.2478			-0.7595			-1.1200		0.7064	
$\mathrm{BR}(\mathrm{b}\to\mathrm{c}\to\ell^+)^{\mathrm{used}}$		7.86			8.07			8.00		8.30	
$a(\mathrm{BR}(\mathrm{c}\to\ell^+))$		1.524			1.0703			1.9796		0.7840	
$\mathrm{BR}(\mathrm{c}\to\ell^+)^{\mathrm{used}}$		9.80			9.90			9.80		9.80	
$a(\overline{\chi})$		6.584			1.6050						
$\overline{\chi}^{\mathrm{used}}$		0.12460			0.11770						
$a(f(\mathrm{D}^+))$						0.3978	0.4229				
$f(\mathrm{D}^+)^{\mathrm{used}}$						0.2210	0.2330				
$a(f(\mathrm{D_s}))$						-0.0788	0.0211				
$f(\mathrm{D_s})^{\mathrm{used}}$						0.1120	0.1020				
$a(f(\Lambda_{\mathrm{c}}))$						0.0573	-0.0855				
$f(\Lambda_{\mathrm{c}})^{\mathrm{used}}$						0.0840	0.0630				
$a(\mathrm{P}(\mathrm{c}\to\mathrm{D}^{*+})\times\mathrm{BR}(\mathrm{D}^{*+}\to\pi^+\mathrm{D}^0))$				-0.2800							
$\mathrm{P}(\mathrm{c}\to\mathrm{D}^{*+})\times\mathrm{BR}(\mathrm{D}^{*+}\to\pi^+\mathrm{D}^0)^{\mathrm{used}}$				0.1830							

Table A.7: The measurements of $A_{\mathrm{FB}}^{\mathrm{b\overline{b}}}(+2)$. All numbers are given in %.

	ALEPH	DELPHI		OPAL	
	91-95 D-meson [136]	93-95† lepton [129]	92-95 D-meson [137]	90-95† lepton [131]	90-95 D-meson [138]
$\sqrt{s}$ (GeV)	92.960	92.990	92.990	92.950	92.950
$A_{\mathrm{FB}}^{\mathrm{c\bar{c}}}(+2)$	10.82	10.50	11.78	15.62	16.50
$A_{\mathrm{FB}}^{\mathrm{c\bar{c}}}(+2)$Corrected	10.77	10.37	11.65	15.59	16.47
Statistical	3.30	2.90	3.20	2.02	4.10
Uncorrelated	0.79	0.41	0.52	0.57	0.92
Correlated	0.18	0.28	0.07	0.62	0.43
Total Systematic	0.81	0.50	0.52	0.84	1.02
$a(R_{\mathrm{b}})$		-4.0402		9.6000	
$R_{\mathrm{b}}^{\mathrm{used}}$		0.2164		0.2155	
$a(R_{\mathrm{c}})$		7.5891		-8.9000	
$R_{\mathrm{c}}^{\mathrm{used}}$		0.1671		0.1720	
$a(A_{\mathrm{FB}}^{\mathrm{b\bar{b}}}(+2))$	-2.6333				
$A_{\mathrm{FB}}^{\mathrm{b\bar{b}}}(+2)^{\mathrm{used}}$	12.08				
$a(\mathrm{BR}(\mathrm{b} \to \ell^-))$		-3.2492		9.5375	
$\mathrm{BR}(\mathrm{b} \to \ell^-)^{\mathrm{used}}$		10.56		10.90	
$a(\mathrm{BR}(\mathrm{b} \to \mathrm{c} \to \ell^+))$		1.5191		-1.5894	
$\mathrm{BR}(\mathrm{b} \to \mathrm{c} \to \ell^+)^{\mathrm{used}}$		8.07		8.30	
$a(\mathrm{BR}(\mathrm{c} \to \ell^+))$		8.1341		-9.2120	
$\mathrm{BR}(\mathrm{c} \to \ell^+)^{\mathrm{used}}$		9.90		9.80	
$a(\overline{\chi})$		-0.2140			
$\overline{\chi}^{\mathrm{used}}$		0.11770			
$a(f(\mathrm{D}^+))$			-0.2984		
$f(\mathrm{D}^+)^{\mathrm{used}}$			0.2210		
$a(f(\mathrm{D_s}))$			0.0539		
$f(\mathrm{D_s})^{\mathrm{used}}$			0.1120		
$a(f(\Lambda_{\mathrm{c}}))$			0.0764		
$f(\Lambda_{\mathrm{c}})^{\mathrm{used}}$			0.0840		

Table A.8: The measurements of $A_{\mathrm{FB}}^{\mathrm{c\bar{c}}}(+2)$. All numbers are given in %.

	SLD			
	93-98† lepton [140]	93-98† jet charge [143]	94-95† $K^{\pm}$ [145]	96-98† multi [144]
$\sqrt{s}$ (GeV)	91.280	91.280	91.280	91.280
$\mathcal{A}_{\rm b}$	0.924	0.907	0.855	0.921
Statistical	0.030	0.020	0.088	0.018
Uncorrelated	0.018	0.023	0.102	0.018
Correlated	0.008	0.001	0.006	0.001
Total Systematic	0.020	0.023	0.102	0.018
$a(R_{\rm b})$	-0.1237		-0.0139	-0.7283
$R_{\rm b}^{\rm used}$	0.2164		0.2180	0.2158
$a(R_{\rm c})$	0.0308		0.0060	0.0359
$R_{\rm c}^{\rm used}$	0.1674		0.1710	0.1722
$a(\mathcal{A}_{\rm c})$	0.0534	0.0211	-0.0112	0.0095
$\mathcal{A}_{\rm c}^{\rm used}$	0.667	0.670	0.666	0.667
$a(\mathrm{BR}(\mathrm{b}\to\ell^-))$	-0.1999			
$\mathrm{BR}(\mathrm{b}\to\ell^-)^{\rm used}$	10.62			
$a(\mathrm{BR}(\mathrm{b}\to\mathrm{c}\to\ell^+))$	0.0968			
$\mathrm{BR}(\mathrm{b}\to\mathrm{c}\to\ell^+)^{\rm used}$	8.07			
$a(\mathrm{BR}(\mathrm{c}\to\ell^+))$	0.0369			
$\mathrm{BR}(\mathrm{c}\to\ell^+)^{\rm used}$	9.85			
$a(\overline{\chi})$	0.2951			
$\overline{\chi}^{\rm used}$	0.11860			

Table A.9: The measurements of $\mathcal{A}_{\rm b}$.

	SLD		
	93-98† lepton [141]	93-98† D-meson [142]	96-98† K+vertex [146]
$\sqrt{s}$ (GeV)	91.280	91.280	91.280
$\mathcal{A}_c$	0.589	0.688	0.673
Statistical	0.055	0.035	0.029
Uncorrelated	0.045	0.020	0.024
Correlated	0.021	0.003	0.002
Total Systematic	0.050	0.021	0.024
$a(R_b)$	0.1855		0.5395
R_b^{used}	0.2164		0.2158
$a(R_c)$	-0.4053		-0.0682
R_c^{used}	0.1674		0.1722
$a(\mathcal{A}_b)$	0.2137	-0.0673	-0.0187
$\mathcal{A}_b^{used}$	0.935	0.935	0.935
$a(\mathrm{BR}(b \to \ell^-))$	0.2874		
$\mathrm{BR}(b \to \ell^-)^{used}$	10.62		
$a(\mathrm{BR}(b \to c \to \ell^+))$	-0.1743		
$\mathrm{BR}(b \to c \to \ell^+)^{used}$	8.07		
$a(\mathrm{BR}(c \to \ell^+))$	-0.3971		
$\mathrm{BR}(c \to \ell^+)^{used}$	9.85		
$a(\overline{\chi})$	0.0717		
$\overline{\chi}^{used}$	0.11860		

Table A.10: The measurements of $\mathcal{A}_c$.

	ALEPH	DELPHI	L3		OPAL
	91-95 multi [147]	94-95 multi [148]	92 lepton [149]	94-95 multi [119]	92-95 multi [150]
$BR(b \to \ell^-)$	10.70	10.70	10.68	10.22	10.85
Statistical	0.10	0.08	0.11	0.13	0.10
Uncorrelated	0.16	0.20	0.36	0.19	0.20
Correlated	0.23	0.45	0.22	0.31	0.21
Total Systematic	0.28	0.49	0.42	0.36	0.29
$a(R_b)$			-9.2571		-0.1808
R_b^{used}			0.2160		0.2169
$a(R_c)$				1.4450	0.4867
R_c^{used}				0.1734	0.1770
$a(BR(b \to c \to \ell^+))$			-1.1700	0.1618	
$BR(b \to c \to \ell^+)^{used}$			9.00	8.09	
$a(BR(c \to \ell^+))$	-0.3078	-0.1960	-2.5480	0.9212	
$BR(c \to \ell^+)^{used}$	9.85	9.80	9.80	9.80	
$a(\overline{\chi})$	0.7683				
$\overline{\chi}^{used}$	0.1178				
$a(f(D^+))$				0.5523	0.1445
$f(D^+)^{used}$				0.2330	0.2380
$a(f(D_s))$				0.0213	0.0055
$f(D_s)^{used}$				0.1030	0.1020
$a(f(\Lambda_c))$				-0.0427	-0.0157
$f(\Lambda_c)^{used}$				0.0630	0.0650

Table A.11: The measurements of $BR(b \to \ell^-)$. All numbers are given in %.

	ALEPH	DELPHI	OPAL
	91-95† multi [147]	94-95† multi [148]	92-95 multi [150]
$BR(b \to c \to \ell^+)$	8.18	7.98	8.41
Statistical	0.15	0.22	0.16
Uncorrelated	0.19	0.21	0.19
Correlated	0.15	0.19	0.34
Total Systematic	0.24	0.28	0.39
$a(R_b)$			-0.1808
R_b^{used}			0.2169
$a(R_c)$	0.5026		0.3761
R_c^{used}	0.1709		0.1770
$a(BR(c \to \ell^+))$	0.3078		
$BR(c \to \ell^+)^{used}$	9.85		
$a(\overline{\chi})$	-1.3884		
$\overline{\chi}^{used}$	0.11940		
$a(f(D^+))$			0.1190
$f(D^+)^{used}$			0.2380
$a(f(D_s))$			0.0028
$f(D_s)^{used}$			0.1020
$a(f(\Lambda_c))$			-0.0110
$f(\Lambda_c)^{used}$			0.0660

Table A.12: The measurements of $BR(b \to c \to \ell^+)$. All numbers are given in %.

	DELPHI	OPAL
	92-95 D+lepton [122]	90-95 D+lepton [127]
$BR(c \to \ell^+)$	9.64	9.58
Statistical	0.42	0.60
Uncorrelated	0.24	0.49
Correlated	0.13	0.43
Total Systematic	0.27	0.65
$a(BR(b \to \ell^-))$	-0.5600	-1.4335
$BR(b \to \ell^-)^{used}$	11.20	10.99
$a(BR(b \to c \to \ell^+))$	-0.4100	-0.7800
$BR(b \to c \to \ell^+)^{used}$	8.20	7.80

Table A.13: The measurements of $BR(c \to \ell^+)$. All numbers are given in %.

	ALEPH	DELPHI	L3	OPAL
	90-95 multi [128]	94-95† multi [148]	90-95 lepton [130]	90-95† lepton [131]
$\overline{\chi}$	0.12446	0.12700	0.11920	0.11380
Statistical	0.00515	0.01300	0.00680	0.00540
Uncorrelated	0.00252	0.00484	0.00214	0.00306
Correlated	0.00394	0.00431	0.00252	0.00324
Total Systematic	0.00468	0.00648	0.00330	0.00445
$a(R_{\mathrm{b}})$	0.0341			
$R_{\mathrm{b}}^{\mathrm{used}}$	0.2192			
$a(R_{\mathrm{c}})$	0.0009		0.0004	
$R_{\mathrm{c}}^{\mathrm{used}}$	0.1710		0.1734	
$a(\mathrm{BR}(\mathrm{b} \to \ell^-))$	0.0524		0.0550	0.0170
$\mathrm{BR}(\mathrm{b} \to \ell^-)^{\mathrm{used}}$	11.34		10.50	10.90
$a(\mathrm{BR}(\mathrm{b} \to \mathrm{c} \to \ell^+))$	-0.0440		-0.0466	-0.0318
$\mathrm{BR}(\mathrm{b} \to \mathrm{c} \to \ell^+)^{\mathrm{used}}$	7.86		8.00	8.30
$a(\mathrm{BR}(\mathrm{c} \to \ell^+))$	0.0035	-0.0020	0.0006	0.0039
$\mathrm{BR}(\mathrm{c} \to \ell^+)^{\mathrm{used}}$	9.80	9.80	9.80	9.80

Table A.14: The measurements of $\overline{\chi}$.

	DELPHI	OPAL
	92-95 D-meson [122]	90-95 D-meson [124]
$\mathrm{P}(\mathrm{c} \to \mathrm{D}^{*+}) \times \mathrm{BR}(\mathrm{D}^{*+} \to \pi^+\mathrm{D}^0)$	0.1740	0.1514
Statistical	0.0100	0.0096
Uncorrelated	0.0040	0.0088
Correlated	0.0007	0.0011
Total Systematic	0.0041	0.0089
$a(R_{\mathrm{b}})$	0.0293	
$R_{\mathrm{b}}^{\mathrm{used}}$	0.2166	
$a(R_{\mathrm{c}})$	-0.0158	
$R_{\mathrm{c}}^{\mathrm{used}}$	0.1735	

Table A.15: The measurements of $\mathrm{P}(\mathrm{c} \to \mathrm{D}^{*+}) \times \mathrm{BR}(\mathrm{D}^{*+} \to \pi^+\mathrm{D}^0)$.

	ALEPH	DELPHI	OPAL
	91-95 D meson [125]	92-95 D meson [123]	91-94 D meson [126]
$R_c f_{D^+}$	0.0406	0.0384	0.0391
Statistical	0.0013	0.0013	0.0050
Uncorrelated	0.0014	0.0015	0.0042
Correlated	0.0032	0.0025	0.0031
Total Systematic	0.0035	0.0030	0.0052
$a(f(D^+))$		0.0008	
$f(D^+)^{used}$		0.2210	
$a(f(D_s))$		-0.0002	
$f(D_s)^{used}$		0.1120	

Table A.16: The measurements of $R_c f_{D^+}$.

	ALEPH	DELPHI	OPAL
	91-95 D meson [125]	92-95 D meson [123]	91-94 D meson [126]
$R_c f_{D_s}$	0.0207	0.0213	0.0160
Statistical	0.0033	0.0017	0.0042
Uncorrelated	0.0011	0.0010	0.0016
Correlated	0.0053	0.0054	0.0043
Total Systematic	0.0054	0.0055	0.0046
$a(f(D^+))$		0.0007	
$f(D^+)^{used}$		0.2210	
$a(f(D_s))$		-0.0009	
$f(D_s)^{used}$		0.1120	
$a(f(\Lambda_c))$		-0.0001	
$f(\Lambda_c)^{used}$		0.0840	

Table A.17: The measurements of $R_c f_{D_s}$.

	ALEPH	DELPHI	OPAL
	91-95 D meson [125]	92-95 D meson [123]	91-94 D meson [126]
$R_c f_{\Lambda_c}$	0.0157	0.0170	0.0091
Statistical	0.0016	0.0035	0.0050
Uncorrelated	0.0005	0.0016	0.0015
Correlated	0.0044	0.0045	0.0035
Total Systematic	0.0045	0.0048	0.0038
$a(f(D^+))$		0.0002	
$f(D^+)^{used}$		0.2210	
$a(f(D_s))$		-0.0001	
$f(D_s)^{used}$		0.1120	
$a(f(\Lambda_c))$		-0.0002	
$f(\Lambda_c)^{used}$		0.0840	

Table A.18: The measurements of $R_c f_{\Lambda_c}$.

	ALEPH	DELPHI	OPAL
	91-95 D meson [125]	92-95 D meson [123]	91-94 D meson [126]
$R_c f_{D^0}$	0.0965	0.0928	0.1000
Statistical	0.0029	0.0026	0.0070
Uncorrelated	0.0040	0.0038	0.0057
Correlated	0.0045	0.0023	0.0041
Total Systematic	0.0060	0.0044	0.0070
$a(f(D^+))$		0.0021	
$f(D^+)^{used}$		0.2210	
$a(f(D_s))$		-0.0004	
$f(D_s)^{used}$		0.1120	
$a(f(\Lambda_c))$		-0.0004	
$f(\Lambda_c)^{used}$		0.0840	

Table A.19: The measurements of $R_c f_{D^0}$.

	DELPHI	OPAL
	92-95 D meson [123]	90-95 D-meson [124]
$R_c P(c \to D^{*+}) \times BR(D^{*+} \to \pi^+ D^0)$	0.0282	0.0268
Statistical	0.0007	0.0005
Uncorrelated	0.0010	0.0010
Correlated	0.0007	0.0009
Total Systematic	0.0012	0.0013
$a(f(D^+))$	0.0006	
$f(D^+)^{\text{used}}$	0.2210	
$a(f(D_s))$	-0.0001	
$f(D_s)^{\text{used}}$	0.1120	
$a(f(\Lambda_c))$	-0.0004	
$f(\Lambda_c)^{\text{used}}$	0.0840	

Table A.20: The measurements of $R_c P(c \to D^{*+}) \times BR(D^{*+} \to \pi^+ D^0)$.

Bibliography

[1] Gargamelle Neutrino Collaboration, F. J. Hasert *et al.*, Phys. Lett. **B46** (1973) 138.

[2] UA1 Collaboration, G. Arnison *et al.*, Phys. Lett. **B122** (1983) 103;
UA2 Collaboration, M. Banner *et al.*, Phys. Lett. **B122** (1983) 476.

[3] UA1 Collaboration, G. Arnison *et al.*, Phys. Lett. **B126** (1983) 398;
UA2 Collaboration, P. Bagnaia *et al.*, Phys. Lett. **B129** (1983) 130.

[4] S. L. Glashow, Nucl. Phys. **22** (1961) 579;
S. Weinberg, Phys. Rev. Lett. **19** (1967) 1264;
A. Salam, Weak and Electromagnetic Interactions, p. 367, in Elementary Particle Theory, Proceedings of the 1968 Nobel Symposium, ed. N. Svartholm, (Almquist and Wiksells, Stockholm, 1968);
M. Veltman, Nucl. Phys. **B7** (1968) 637;
G. 't Hooft, Nucl. Phys. **B35** (1971) 167;
G. 't Hooft and M. Veltman, Nucl. Phys. **B44** (1972) 189;
G. 't Hooft and M. Veltman, Nucl. Phys. **B50** (1972) 318.

[5] *LEP DESIGN REPORT: VOL. 2. THE LEP MAIN RING*, Internal report, CERN, 1984, *LEP Design Report*, CERN-LEP/84-01 , June 1984;
The main features of LEP have been reviewed by:;
S. Myers and E. Picasso, Contemp. Phys. **31** (1990) 387–403;
D. Brandt *et al.*, Rept. Prog. Phys. **63** (2000) 939–1000.

[6] *SLAC LINEAR COLLIDER CONCEPTUAL DESIGN REPORT*, Internal report, SLAC, 1980, *SLAC Linear Collider Conceptual Design Report*, SLAC-R-229 , June 1980.

[7] ALEPH Collaboration, D. Decamp *et al.*, Nucl. Instrum. Meth. **A294** (1990) 121–178;
ALEPH Collaboration, D. Buskulic *et al.*, Nucl. Instrum. Meth. **A360** (1995) 481–506.

[8] DELPHI Collaboration, P. Aarnio *et al.*, Nucl. Instrum. Meth. **A303** (1991) 233–276;
DELPHI Collaboration, P. Abreu *et al.*, Nucl. Instrum. Meth. **A378** (1996) 57–100.

[9] L3 Collaboration, B. Adeva *et al.*, Nucl. Instrum. Meth. **A289** (1990) 35–102;
L3 SMD Collaboration, M. Acciarri *et al.*, Nucl. Instrum. Meth. **A351** (1994) 300–312;
M. Chemarin *et al.*, Nucl. Instrum. Meth. **A349** (1994) 345–355;
L3 F/B Muon Group Collaboration, A. Adam *et al.*, Nucl. Instrum. Meth. **A383** (1996) 342–366.

[10] OPAL Collaboration, K. Ahmet *et al.*, Nucl. Instrum. Meth. **A305** (1991) 275–319;
OPAL Collaboration, P. P. Allport *et al.*, Nucl. Instrum. Meth. **A324** (1993) 34–52;

OPAL Collaboration, P. P. Allport *et al.*, Nucl. Instrum. Meth. **A346** (1994) 476–495;
OPAL Collaboration, B. E. Anderson *et al.*, IEEE Trans. Nucl. Sci. **41** (1994) 845–852.

[11] Mark-II Collaboration, G. S. Abrams *et al.*, Phys. Rev. Lett. **63** (1989) 724.

[12] SLD Collaboration, M. J. Fero *et al.*, Nucl. Instrum. Meth. **A367** (1995) 111;
SLD Collaboration, D. Axen *et al.*, Nucl. Instrum. Meth. **A328** (1993) 472;
SLD Collaboration, K. Abe *et al.*, Nucl. Instrum. Meth. **A343** (1994) 74;
SLD Collaboration, S. C. Berridge *et al.*, IEEE Trans. Nucl. Sci. **39** (1992) 1242.

[13] SLD Collaboration, K. Abe *et al.*, Nucl. Instrum. Meth. **A400** (1997) 287.

[14] SLD Collaboration, A. C. Benvenuti *et al.*, Nucl. Instr. Meth. **A276** (1989) 94.

[15] Working Group on LEP Energy Collaboration, L. Arnaudon *et al.*, Phys. Lett. **B307** (1993) 187–193.

[16] Working group on LEP energy (L. Arnaudon *et al.*), *The Energy Calibration of LEP in 1992*, Preprint CERN SL/93-21 (DI), CERN, 1993.

[17] Working Group on LEP Energy Collaboration, R. Assmann *et al.*, Z. Phys. **C66** (1995) 567–582.

[18] R. Assmann *et al.*, Eur. Phys. J. **C6** (1999) 187–223.

[19] D. A. Ross and M. J. G. Veltman, Nucl. Phys. **B95** (1975) 135.

[20] M. J. G. Veltman, Nucl. Phys. **B123** (1977) 89.

[21] D. Bardin and G. Passarino, The standard model in the making: Precision study of the electroweak interactions, (Clarendon, Oxford, UK, 1999).

[22] F. Berends *et al.*, in Z PHYSICS AT LEP 1. PROCEEDINGS, WORKSHOP, GENEVA, SWITZERLAND, SEPTEMBER 4-5, 1989. VOL. 1: STANDARD PHYSICS, ed. G. Altarelli, R. Kleiss, and C. Verzegnassi, (CERN, Geneva, Switzerland, 1989), p. 89.

[23] G. Montagna *et al.*, Nucl. Phys. **B401** (1993) 3–66;
G. Montagna *et al.*, Comput. Phys. Commun. **76** (1993) 328–360;
G. Montagna *et al.*, Comput. Phys. Commun. **93** (1996) 120–126;
G. Montagna *et al.*, Comput. Phys. Commun. **117** (1999) 278–289, recently updated to include initial state pair radiation (G. Passarino, priv. comm.).

[24] D. Y. Bardin *et al.*, Z. Phys. **C44** (1989) 493;
D. Y. Bardin *et al.*, Comput. Phys. Commun. **59** (1990) 303–312;
D. Y. Bardin *et al.*, Nucl. Phys. **B351** (1991) 1–48;
D. Y. Bardin *et al.*, Phys. Lett. **B255** (1991) 290–296;
D. Y. Bardin *et al.*, *ZFITTER: An Analytical program for fermion pair production in e+ e- annihilation*, Preprint hep-ph/9412201, 1992;
D. Y. Bardin *et al.*, Comput. Phys. Commun. **133** (2001) 229–395, recently updated with results from [50].

[25] D. Y. Bardin, M. Grunewald, and G. Passarino, *Precision calculation project report*, Preprint hep-ph/9902452, 1999.

[26] ALEPH Collaboration, D. Decamp *et al.*, Z. Phys. **C48** (1990) 365–392;
ALEPH Collaboration, D. Decamp *et al.*, Z. Phys. **C53** (1992) 1–20;
ALEPH Collaboration, D. Buskulic *et al.*, Z. Phys. **C60** (1993) 71–82;
ALEPH Collaboration, D. Buskulic *et al.*, Z. Phys. **C62** (1994) 539–550;
ALEPH Collaboration, R. Barate *et al.*, Eur. Phys. J. **C14** (2000) 1–50.

[27] DELPHI Collaboration, P. Abreu *et al.*, Nucl. Phys. **B367** (1991) 511–574;
DELPHI Collaboration, P. Abreu *et al.*, Nucl. Phys. **B417** (1994) 3–57;
DELPHI Collaboration, P. Abreu *et al.*, Nucl. Phys. **B418** (1994) 403–427;
DELPHI Collaboration, P. Abreu *et al.*, Eur. Phys. J. **C16** (2000) 371–405.

[28] L3 Collaboration, B. Adeva *et al.*, Z. Phys. **C51** (1991) 179–204;
L3 Collaboration, O. Adriani *et al.*, Phys. Rept. **236** (1993) 1–146;
L3 Collaboration, M. Acciarri *et al.*, Z. Phys. **C62** (1994) 551–576;
L3 Collaboration, M. Acciarri *et al.*, Eur. Phys. J. **C16** (2000) 1–40.

[29] OPAL Collaboration, G. Alexander *et al.*, Z. Phys. **C52** (1991) 175–208;
OPAL Collaboration, P. D. Acton *et al.*, Z. Phys. **C58** (1993) 219–238;
OPAL Collaboration, R. Akers *et al.*, Z. Phys. **C61** (1994) 19–34;
OPAL Collaboration, G. Abbiendi *et al.*, Eur. Phys. J. **C19** (2001) 587–651.

[30] R. Brun *et al.*, *GEANT3*, Preprint CERN DD/EE/84-1, CERN, 1987, the simulations are all based on this program; details of its implementation may be found in the references on the detectors, [7–10].

[31] OPAL Collaboration, J. Allison *et al.*, Nucl. Instrum. Meth. **A317** (1992) 47–74.

[32] *DELSIM*, Internal Report 87-96/PROG 99, DELPHI, 1989;
DELSIM, Internal Report 87-98/PROG 100, DELPHI, 1989.

[33] T. Sjostrand, Comput. Phys. Commun. **82** (1994) 74–90, (JETSET).

[34] G. Marchesini *et al.*, Comput. Phys. Commun. **67** (1992) 465–508, (HERWIG).

[35] L. Lonnblad, Comput. Phys. Commun. **71** (1992) 15–31, (ARIADNE).

[36] S. Jadach, B. Ward, and Z. Wąs, Comput. Phys. Commun. **79** (1994) 503, (KORALZ 4.0).

[37] S. Jadach, B.F.L. Ward and Z. Wąs, Comput. Phys. Commun. **130** (2000) 260, (KK Monte Carlo).

[38] F.A. Berends, R. Kleiss and W. Hollik, Nucl. Phys. **B304** (1988) 712, (BABAMC).

[39] H. Anlauf *et al.*, Comput. Phys. Commun. **79** (1994) 466–486, (UNIBAB).

[40] J. H. Field and T. Riemann, Comput. Phys. Commun. **94** (1996) 53–87, (BHAGENE3).

[41] S. Jadach, W. Placzek, E. Richter-Wąs, B.F.L. Ward and Z. Wąs, Comput. Phys. Commun. **102** (1997) 229, (BHLUMI 4.04).

[42] J. Hilgart, R. Kleiss and F. Le Diberder, Comput. Phys. Commun. **75** (1993) 191, (FERMISV).

[43] J. Fujimoto *et al.*, Comput. Phys. Commun. **100** (1997) 128–156, (GRC4f).

[44] OPAL Collaboration, G. Abbiendi *et al.*, Eur. Phys. J. **C14** (2000) 373–425;
I. C. Brock *et al.*, Nucl. Instrum. Meth. **A381** (1996) 236–266;
D. Bederede *et al.*, Nucl. Instrum. Meth. **A365** (1995) 117–134.

[45] LEP Polarization Collaboration, L. Arnaudon *et al.*, Phys. Lett. **B284** (1992) 431–439.

[46] L. Arnaudon *et al.*, Z. Phys. **C66** (1995) 45–62.

[47] L. Knudsen *et al.*, Phys. Lett. **B270** (1991) 97–104.

[48] M. Placidi and R. Rossmanith, Nucl. Instr. Meth. **A274** (1989) 79.

[49] A. A. Sokolov and I. M. Ternov, Phys. Dokl. **8** (1964) 1203–1205.

[50] A. B. Arbuzov, *Light pair corrections to electron positron annihilation at LEP/SLC*, Preprint hep-ph/9907500, Turin U. and INFN, Turin, 1999.

[51] S. Eidelman and F. Jegerlehner, Z. Phys. **C67** (1995) 585–602.

[52] W. Beenakker, F.A. Berends and S.C. van der Marck, Nucl. Phys. **B349** (1991) 323–368, (ALIBABA).

[53] W. Beenakker and G. Passarino, Phys. Lett. **B425** (1998) 199.

[54] W. Beenakker and G. Passarino, private communication.

[55] B. F. L. Ward *et al.*, Phys. Lett. **B450** (1999) 262–266.

[56] G. Montagna *et al.*, Nucl. Phys. **B547** (1999) 39–59;
G. Montagna *et al.*, Phys. Lett. **B459** (1999) 649–652.

[57] F.A. Berends, W.L. van Neerven and G.J.H. Burgers, Nucl. Phys. **B297** (1988) 429, erratum: B304 (1988) 921.

[58] E. A. Kuraev and V. S. Fadin, Sov. J. Nucl. Phys. **41** (1985) 466–472.

[59] G. Montagna, O. Nicrosini and F. Piccinini, Phys. Lett. **B406** (1997) 243–248.

[60] M. Skrzypek, Acta Phys. Polon. **B23** (1992) 135.

[61] S. Jadach, M. Skrzypek and B.F.L. Ward, Phys. Lett. **B257** (1991) 173–178.

[62] D.R. Yennie, S.C. Frautschi and H. Suura, Ann. Phys. **13** (1961) 379–452.

[63] S. Jadach, M. Skrzypek and B. Pietrzyk, Phys. Lett. **B456** (1999) 77.

[64] M. Martinez *et al.*, Z. Phys. **C49** (1991) 645–656;
M. Martinez and F. Teubert, Z. Phys. **C65** (1995) 267–276, updated with results summarized in [63] and [233].

[65] S. Jadach, B. Pietrzyk, E. Tournefier, B.F.L. Ward and Z. Wąs, Phys. Lett. **B465** (1999) 254.

[66] B.A. Kniehl, M. Krawczyk, J.H. Kühn and R.G. Stuart, Phys. Lett. **B209** (1988) 337.

[67] S. Jadach, M. Skrzypek and M. Martinez, Phys. Lett. **B280** (1992) 129–136.

[68] A. Leike, T. Riemann, and J. Rose, Phys. Lett. **B273** (1991) 513–518;
T. Riemann, Phys. Lett. **B293** (1992) 451–456;
S. Kirsch and T. Riemann, Comp. Phys. Commun. **88** (1995) 89–108.

[69] L3 Collaboration, O. Adriani *et al.*, Phys. Rept. **236** (1993) 1–146;
L3 Collaboration, M. Acciarri *et al.*, Eur. Phys. J. **C16** (2000) 1–40;
OPAL Collaboration, G. Abbiendi *et al.*, Eur. Phys. J. **C19** (2001) 587–651.

[70] TOPAZ Collaboration, K. Miyabayashi *et al.*, PL **B347** (1995) 171.

[71] VENUS Collaboration, K. Yusa *et al.*, PL **B447** (1999) 167.

[72] ALEPH Collaboration, D. Busculic *et al.*, ZfP **C 71** (1996) 179.

[73] DELPHI Collaboration, P. Abreu *et al.*, Eur. Phys. J. **C11** (1999) 383–407.

[74] L3 Collaboration, O. Adriani *et al.*, Phys. Lett. **B315** (1993) 494–502;
L3 Collaboration, M. Acciarri *et al.*, Phys. Lett. **B479** (2000) 101–117;
L3 Collaboration, M. Acciarri *et al.*, Phys. Lett. **B489** (2000) 93–101.

[75] OPAL Collaboration, K. Ackerstaff *et al.*, Eur. Phys. J. **C2** (1998) 441–472.

[76] Particle Data Group Collaboration, D. E. Groom *et al.*, Eur. Phys. J. **C15** (2000) 1–878.

[77] SLD Collaboration, K. Abe *et al.*, Phys. Rev. Lett. **70** (1993) 2515–2520;
SLD Collaboration, K. Abe *et al.*, Phys. Rev. Lett. **73** (1994) 25–29;
SLD Collaboration, K. Abe *et al.*, Phys. Rev. Lett. **78** (1997) 2075–2079;
SLD Collaboration, K. Abe *et al.*, Phys. Rev. Lett. **84** (2000) 5945–5949.

[78] H. Park, A Measurement of the left-right cross-section asymmetry in Z0 production with polarized e+ e- collisions, Ph.D. thesis, Oregon Univ., Dec 1993, SLAC-435;
R. D. Elia, Measurement of the left-right asymmetry in Z boson production by electron - positron collisions, Ph.D. thesis, Stanford Univ., Apr 1993, SLAC-0429;
R. J. Ben-David, The First measurement of the left-right cross-section asymmetry in Z boson production, Ph.D. thesis, Yale Univ., May 1994, UMI-94-33702;
R. C. King, A precise measurement of the left-right asymmetry of Z boson production at the SLAC linear collider, Ph.D. thesis, Stanford Univ., Sep 1994, SLAC-0452;
A. Lath, A Precise measurement of the left-right cross-section asymmetry in Z boson production, Ph.D. thesis, Stanford Univ., Sep 1994, SLAC-0454;
E. C. Torrence, Search for anomalous couplings in the decay of polarized Z bosons to tau lepton pairs, Ph.D. thesis, Mass. Inst. of Tech., Jun 1997, SLAC-R-0509;
D. V. Onoprienko, Precise measurement of the left-right asymmetry in Z0 boson production by e+ e- collisions: Electron beam polarization measurement with the quartz fiber calorimeter, Ph.D. thesis, SLAC and Tennessee U., Aug 2000, SLAC-R-556.

[79] T. Maruyama *et al.*, Phys. Rev. **B46** (1992) 4261–4264;
Nakanishi *et al.*, Phys. Lett. **A158** (1991) xxx.

[80] T. Limberg, P. Emma, and R. Rossmanith, *The North Arc of the SLC as a spin rotator*, Internal Report SLAC-PUB-6210, SLAC, 1993, Presented at 1993 Particle Accelerator Conference (PAC 93), Washington, DC, 17-20 May 1993.

[81] A. Lath, A Precise measurement of the left-right cross-section asymmetry in Z boson production, Ph.D. thesis, Mass. Inst. of Tech., Sep 1994, SLAC-0454, pp.93-96.

[82] W. R. Nelson, H. Hirayama, and D. W. O. Rogers, *THE EGS4 CODE SYSTEM*, Internal Report SLAC-0265, SLAC, Dec 1985.

[83] E. C. Torrence, Search for anomalous couplings in the decay of polarized Z bosons to tau lepton pairs, Ph.D. thesis, Mass. Inst. of Tech., Jun 1997, SLAC-R-0509, pp.191-214.

[84] R. C. Field *et al.*, IEEE Trans. Nucl. Sci. **45** (1998) 670–675.

[85] S. C. Berridge *et al.*, *A quartz fiber / tungsten calorimeter for the Compton polarimeter at SLAC*, Internal Report SLAC-REPRINT-1998-024, SLAC, 1998, Prepared for 13th International Symposium on High-Energy Spin Physics (SPIN 98), Protvino, Russia, 8-12 Sep 1998;
D. V. Onoprienko, Precise measurement of the left-right asymmetry in Z0 boson production by e+ e- collisions: Electron beam polarization measurement with the quartz fiber calorimeter, Ph.D. thesis, SLAC and Tennessee U., Aug 2000, SLAC-R-556.

[86] M. L. Swartz, Phys. Rev. **D58** (1998) 014010.

[87] M. E. Levi *et al.*, *PRECISION SYNCHROTRON RADIATION DETECTORS*, Internal Report SLAC-PUB-4921, SLAC, 1989, Presented at IEEE Particle Accelerator Conf., Chicago, Ill., Mar 20-23, 1989;
J. Kent *et al.*, *PRECISION MEASUREMENTS OF THE SLC BEAM ENERGY*, Internal Report SLAC-PUB-4922, SLAC, 1989, Presented at IEEE Particle Accelerator Conf., Chicago, Ill., Mar 20-23, 1989.

[88] D. V. Onoprienko, Precise measurement of the left-right asymmetry in Z0 boson production by e+ e- collisions: Electron beam polarization measurement with the quartz fiber calorimeter, Ph.D. thesis, SLAC and Tennessee U., Aug 2000, SLAC-R-556.

[89] R. D. Elia, Measurement of the left-right asymmetry in Z boson production by electron - positron collisions, Ph.D. thesis, Stanford Univ., Apr 1993, SLAC-0429.

[90] M. Swartz *et al.*, Nucl. Instrum. Meth. **A363** (1995) 526–537.

[91] G. Mulhollan *et al.*, *A derivative standard for polarimeter calibration*, Internal Report SLAC-PUB-7325, SLAC, 1995, Talk given at 16th IEEE Particle Accelerator Conference (PAC 95) and International Conference on High-energy Accelerators (IUPAP), Dallas, Texas, 1-5 May 1995.

[92] P. R. H.R. Band and T. Wright, *The Positron Polarization (POSPOL) Experiments: T-419*, Internal Report SLD-note 268, SLD, 2000, http://www-sldnt.slac.stanford.edu/sldbb/SLDNotes/sld-note%20268.pdf.

[93] SLD Collaboration, K. Abe *et al.*, Phys. Rev. Lett. **86** (2001) 1162–1166.

[94] SLD Collaboration, K. Abe *et al.*, Phys. Rev. Lett. **79** (1997) 804–808.

[95] M. Martinez and R. Miquel, Z. Phys. **C53** (1992) 115–126.

[96] P. H. Eberhard *et al.*, in Z PHYSICS AT LEP 1. PROCEEDINGS, WORKSHOP, GENEVA, SWITZERLAND, SEPTEMBER 4-5, 1989. VOL. 1: STANDARD PHYSICS, ed. G. Altarelli, R. Kleiss, and C. Verzegnassi, (CERN, Geneva, Switzerland, 1989), pp. 235–265.

[97] K. Hagiwara, A. D. Martin, and D. Zeppenfeld, Phys. Lett. **B235** (1990) 198–202.

[98] M. Davier *et al.*, Phys. Lett. **B306** (1993) 411–417.

[99] ALEPH Collaboration, A. Heister *et al.*, Eur. Phys. J. **C20** (2001) 401–430;
ALEPH Collaboration, D. Buskulic *et al.*, Z. Phys. **C69** (1996) 183–194;
ALEPH Collaboration, D. Buskulic *et al.*, Z. Phys. **C59** (1993) 369–386;
ALEPH Collaboration, D. Decamp *et al.*, Phys. Lett. **B265** (1991) 430–444.

[100] DELPHI Collaboration, P. Abreu *et al.*, Eur. Phys. J. **C14** (2000) 585–611;
DELPHI Collaboration, P. Abreu *et al.*, Z. Phys. **C67** (1995) 183–202.

[101] L3 Collaboration, M. Acciarri *et al.*, Phys. Lett. **B429** (1998) 387–398;
L3 Collaboration, M. Acciarri *et al.*, Phys. Lett. **B341** (1994) 245–256;
L3 Collaboration, O. Adriani *et al.*, Phys. Lett. **B294** (1992) 466–478.

[102] OPAL Collaboration, G. Abbiendi *et al.*, Eur. Phys. J. **C21** (2001) 1–21;
OPAL Collaboration, G. Alexander *et al.*, Z. Phys. **C72** (1996) 365–375;
OPAL Collaboration, R. Akers *et al.*, Z. Phys. **C65** (1995) 1–16;
OPAL Collaboration, G. Alexander *et al.*, Phys. Lett. **B266** (1991) 201–217.

[103] S. Jadach, W. Placzek, and B. F. L. Ward, Phys. Lett. **B390** (1997) 298–308.

[104] J. Smith, J. A. M. Vermaseren, and J. G. Grammer, Phys. Rev. **D15** (1977) 3280.

[105] F. A. Berends, P. H. Daverveldt, and R. Kleiss, Phys. Lett. **B148** (1984) 489.

[106] F. A. Berends, P. H. Daverveldt, and R. Kleiss, Nucl. Phys. **B253** (1985) 441.

[107] Particle Data Group Collaboration, C. Caso *et al.*, Eur. Phys. J. **C3** (1998) 1–794.

[108] S. Jadach, J. H. Kuhn, and Z. Was, Comput. Phys. Commun. **64** (1990) 275–299, (TAUOLA);
S. Jadach *et al.*, Comput. Phys. Commun. **76** (1993) 361–380, (TAUOLA: Version 2.4).

[109] E. Barbiero, B. van Eijk, and Z. Wąs, Comput. Phys. Commun. **66** (1991) 115, CERN-TH 7033/93, (PHOTOS).

[110] R. Decker and M. Finkemeier, Phys. Rev. **D48** (1993) 4203.

[111] M. Finkemeier, Radiative corrections to the decay $\tau \to \pi\nu$, Ph.D. thesis, University of Karlsruhe, Feb 1994.

[112] D. J. Jackson, Nucl. Instrum. Meth. **A388** (1997) 247–253.

[113] OPAL Collaboration, G. Abbiendi *et al.*, Eur. Phys. J. **C8** (1999) 217–239.

[114] SLD Collaboration, K. Abe *et al.*, *A Preliminary Measurement of Rb using the Upgrade SLD Vertex Detector*, Preprint SLAC-PUB-7585, SLAC, 1997, Prepared for International Europhysics Conference on High- Energy Physics (HEP 97) 19-26 August 1997 Jerusalem, Israel;
SLD Collaboration, V.Serbo, *Electroweak measurements with heavy quarks at SLD*, Preprint XXXX, SLAC, 1998, Presented at III International conference on Hyperons, Charm and Beauty Hadrons, Genova, Italy, June/30–July/3/1998..

[115] P. Billoir *et al.*, Nucl. Instrum. Meth. **A360** (1995) 532–558.

[116] ALEPH Collaboration, R. Barate *et al.*, Phys. Lett. **B401** (1997) 150–162.

[117] ALEPH Collaboration, R. Barate *et al.*, Phys. Lett. **B401** (1997) 163–175.

[118] DELPHI Collaboration, P. Abreu *et al.*, Eur. Phys. J. **C10** (1999) 415–442.

[119] L3 Collaboration, M. Acciarri *et al.*, Eur. Phys. J. **C13** (2000) 47–61.

[120] SLD Collaboration, K. Abe *et al.*, *A Measurement of R_c with the SLD Detector*, Preprint SLAC-PUB-7880, SLAC, 1998, Prepared for XXIX International Conference on High Energy Physics (ICHEP 98) July 23-29 1998 Vancouver, B.C., Canada;
SLD Collaboration, N. de Groot, *Electroweak results from SLD*, Preprint XXXX, SLAC, 1999, Presented at XXXIVth Rencontres de Moriond, Electroweak Interactions and Unified Theories, Les Arcs, March 13-20 1999.

[121] ALEPH Collaboration, R. Barate *et al.*, Eur. Phys. J. **C4** (1998) 557–570.

[122] DELPHI Collaboration, P. Abreu *et al.*, Eur. Phys. J. **C12** (2000) 209–224.

[123] DELPHI Collaboration, P. Abreu *et al.*, Eur. Phys. J. **C12** (2000) 225–241.

[124] OPAL Collaboration, K. Ackerstaff *et al.*, Eur. Phys. J. **C1** (1998) 439–459.

[125] ALEPH Collaboration, R. Barate *et al.*, Eur. Phys. J. **C16** (2000) 597–611.

[126] OPAL Collaboration, G. Alexander *et al.*, Z. Phys. **C72** (1996) 1–16.

[127] OPAL Collaboration, G. Abbiendi *et al.*, Eur. Phys. J. **C8** (1999) 573–584.

[128] ALEPH Collaboration, D. Buskulic *et al.*, Phys. Lett. **B384** (1996) 414–426;
ALEPH Collaboration, A. Tricomi, *Measurement of the forward-backward asymmetries in Z –¿ b anti-b and Z –¿ c anti-c decays with leptons*, Preprint ALEPH-99-076, CERN, 1999, Prepared for International Europhysics Conference on High- Energy Physics (EPS-HEP 99), Tampere, Finland, 15-21 Jul 1999.

[129] DELPHI Collaboration, P. Abreu *et al.*, Z. Phys. **C65** (1995) 569–586;
DELPHI Collaboration, E. M. P. Antilogus and M. Paganoni, *Measurement of the Forward-Backward Asymmetries of $e^+e^- \to Z \to b\overline{b}$ and $e^+e^- \to Z \to c\overline{c}$ using prompt leptons*, Preprint DELPHI-98-143, DELPHI, 1998, Prepared for ICHEP'98, Vancouver, 22-29 July 1998.

[130] L3 Collaboration, O. Adriani *et al.*, Phys. Lett. **B292** (1992) 454–462;
L3 Collaboration, M. Acciarri *et al.*, Phys. Lett. **B448** (1999) 152–162.

[131] OPAL Collaboration, G. Alexander *et al.*, Z. Phys. **C70** (1996) 357–370.

[132] DELPHI Collaboration, P. Abreu *et al.*, Eur. Phys. J. **C9** (1999) 367–381.

[133] L3 Collaboration, M. Acciarri *et al.*, Phys. Lett. **B439** (1998) 225–236.

[134] OPAL Collaboration, K. Ackerstaff *et al.*, Z. Phys. **C75** (1997) 385–396.

[135] ALEPH Collaboration, A. Heister *et al.*, *Measurement of A(b)(FB) using inclusive b-hadron decays*, Preprint hep-ex/0107033, CERN, 2001.

[136] ALEPH Collaboration, R. Barate *et al.*, Phys. Lett. **B434** (1998) 415–425.

[137] DELPHI Collaboration, P. Abreu *et al.*, Eur. Phys. J. **C10** (1999) 219–237.

[138] OPAL Collaboration, G. Alexander *et al.*, Z. Phys. **C73** (1997) 379–395.

[139] K. Munich *et al.*, *Determination of $A_F B^b$ using inclusive charge reconstruction and lifetime tagging at LEP 1*, Internal report, CERN, 2001.

[140] SLD Collaboration, K. Abe *et al.*, *Direct measurement of A(b) at the Z0 pole using a lepton tag*, Preprint hep-ex/0009064, SLAC, 2000.

[141] SLD Collaboration, K. Abe *et al.*, *Measurement of Ab and Ac at the Z0 using a lepton tag*, Preprint SLAC-PUB-7637, SLAC, 1997, Prepared for International Europhysics Conference on High- Energy Physics (HEP 97) 19-26 August 1997 Jerusalem, Israel;
SLD Collaboration, S. Fahey, *Measurements of Quark Coupling Asymmetries at the Z0*, Preprint XXXX, SLAC, 1999, Presented at International Europhysics Conference on High- Energy Physics (EPS-HEP 99), Tampere, Finland, 15-21 Jul 1999.

[142] SLD Collaboration, K. Abe *et al.*, *Measurement of A(c) with charmed mesons at SLD*, Preprint hep-ex/9907039, SLAC, 1999.

[143] SLD Collaboration, K. Abe *et al.*, *Measurement of A(b) at the Z0 resonance using a jet-charged technique*, Preprint SLAC-PUB-7886, SLAC, 1998, Talk given at 29th International Conference on High-Energy Physics (ICHEP 98), Vancouver, Canada, 23-29 Jul 1998;
N. de Groot, *Electroweak results from SLD*, Preprint hep-ex/0105058, SLD, 2001.

[144] SLD Collaboration, K. Abe *et al.*, *New measurement of A(b) at the Z0 resonance using a vertex- charge technique*, Preprint hep-ex/9907050, SLAC, 1999.

[145] SLD Collaboration, K. Abe *et al.*, Phys. Rev. Lett. **83** (1999) 1902–1907;
SLD Collaboration, K. Abe *et al.*, *Direct measurement of A(b) using charged kaons at the SLD detector*, Preprint hep-ex/9907066, SLD, 1999.

[146] SLD Collaboration, K. Abe *et al.*, *Direct measurement of A(c) using inclusive charm tagging at the SLD detector*, Preprint hep-ex/9907065, SLAC, 1999.

[147] ALEPH Collaboration, A. Heister *et al.*, *Inclusive semileptonic branching ratios of b hadrons produced in Z decays*, Preprint hep-ex/0108007, CERN, 2001.

[148] DELPHI Collaboration, P. Abreu *et al.*, Eur. Phys. J. **C20** (2001) 455–478.

[149] L3 Collaboration, M. Acciarri *et al.*, Z. Phys. **C71** (1996) 379–390.

[150] OPAL Collaboration, G. Abbiendi *et al.*, Eur. Phys. J. **C13** (2000) 225–240.

[151] C. Peterson *et al.*, Phys. Rev. **D27** (1983) 105.

[152] ALEPH Collaboration, D. Buskulic *et al.*, Phys. Lett. **B357** (1995) 699–714.

[153] ALEPH Collaboration, D. Buskulic *et al.*, Z. Phys. **C62** (1994) 179–198.

[154] DELPHI Collaboration, P. Abreu *et al.*, Z. Phys. **C66** (1995) 323–340.

[155] OPAL Collaboration, G. Alexander *et al.*, Phys. Lett. **B364** (1995) 93–106.

[156] OPAL Collaboration, R. Akers *et al.*, Z. Phys. **C60** (1993) 199–216.

[157] P. D. B. Collins and T. P. Spiller, J. Phys. **G11** (1985) 1289.

[158] V. G. Kartvelishvili, A. K. Likhoded, and V. A. Petrov, Phys. Lett. **B78** (1978) 615.

[159] ALEPH Collaboration, D. Buskulic *et al.*, Z. Phys. **C62** (1994) 1–14.

[160] DELPHI Collaboration, P. Abreu *et al.*, Z. Phys. **C59** (1993) 533, erratum: Z. Phys. C65 (1995) 709.

[161] OPAL Collaboration, R. Akers *et al.*, Z. Phys. **C67** (1995) 27–44.

[162] ALEPH Collaboration, R. Barate *et al.*, Phys. Lett. **B434** (1998) 437–450;
DELPHI Collaboration, P. Abreu *et al.*, Phys. Lett. **B405** (1997) 202–214;
DELPHI Collaboration, P. Abreu *et al.*, Phys. Lett. **B462** (1999) 425–439;
OPAL Collaboration, G. Abbiendi *et al.*, Eur. Phys. J. **C18** (2001) 447–460;
SLD Collaboration, K. Abe *et al.*, Phys. Lett. **B507** (2001) 61–69.

[163] L3 Collaboration, M. Acciarri *et al.*, Phys. Lett. **B476** (2000) 243–255.

[164] OPAL Collaboration, G. Abbiendi *et al.*, Eur. Phys. J. **C13** (2000) 1–13.

[165] DELPHI Collaboration, P. Abreu *et al.*, Phys. Lett. **B425** (1998) 399–412;
L3 Collaboration, M. Acciarri *et al.*, Phys. Lett. **B416** (1998) 220–232;
OPAL Collaboration, R. Akers *et al.*, Z. Phys. **C61** (1994) 209–222.

[166] MARK-III Collaboration, D. Coffman *et al.*, Phys. Lett. **B263** (1991) 135–140.

[167] CLEO Collaboration, D. E. Jaffe *et al.*, Phys. Rev. **D62** (2000) 072005.

[168] CLEO Collaboration, S. Henderson *et al.*, Phys. Rev. **D45** (1992) 2212–2231.

[169] G. Altarelli *et al.*, Nucl. Phys. **B208** (1982) 365.

[170] N. Isgur *et al.*, Phys. Rev. **D39** (1989) 799.

[171] DELCO Collaboration, W. Bacino *et al.*, Phys. Rev. Lett. **43** (1979) 1073.

[172] MARK-III Collaboration, R. M. Baltrusaitis *et al.*, Phys. Rev. Lett. **54** (1985) 1976.

[173] ALEPH, DELPHI, L3, OPAL Collaboration, The LEP collaborations, Nucl. Instrum. Meth. **A378** (1996) 101–115.

[174] CLEO Collaboration, D. Bortoletto *et al.*, Phys. Rev. **D45** (1992) 21–35.

[175] CLEO Collaboration, T. E. Coan *et al.*, Phys. Rev. Lett. **80** (1998) 1150–1155;
CLEO Collaboration, D. Gibaut *et al.*, Phys. Rev. **D53** (1996) 4734–4746;
CLEO Collaboration, R. Ammar *et al.*, Phys. Rev. **D55** (1997) 13–18.

[176] ALEPH Collaboration, R. Barate *et al.*, Eur. Phys. J. **C4** (1998) 387–407.

[177] ALEPH Collaboration, R. Barate *et al.*, Eur. Phys. J. **C19** (2001) 213–227;
DELPHI Collaboration, P. Abreu *et al.*, Phys. Lett. **B496** (2000) 43–58;
L3 Collaboration, M. Acciarri *et al.*, Phys. Lett. **B332** (1994) 201–208;
L3 Collaboration, M. Acciarri *et al.*, Z. Phys. **C71** (1996) 379–390.

[178] P. Nason and C. Oleari, Phys. Lett. **B407** (1997) 57–60.

[179] LEP Heavy Flavor Working Group Collaboration, D. Abbaneo *et al.*, Eur. Phys. J. **C4** (1998) 185–191.

[180] G. Altarelli and B. Lampe, Nucl. Phys. **B391** (1993) 3–22.

[181] V. Ravindran and W. L. van Neerven, Phys. Lett. **B445** (1998) 206–213.

[182] S. Catani and M. H. Seymour, JHEP **9907** (1999) 023.

[183] ALEPH Collaboration, D. Buskulic *et al.*, Z. Phys. **C71** (1996) 357–378.

[184] DELPHI Collaboration, P. Abreu *et al.*, Phys. Lett. **B277** (1992) 371–382.

[185] OPAL Collaboration, P. D. Acton *et al.*, Phys. Lett. **B294** (1992) 436–450.

[186] DELPHI Collaboration, P. Abreu *et al.*, Z. Phys. **C67** (1995) 1–14.

[187] DELPHI Collaboration, P. Abreu *et al.*, Eur. Phys. J. **C14** (2000) 613–631.

[188] OPAL Collaboration, K. Ackerstaff *et al.*, Z. Phys. **C76** (1997) 387–400.

[189] SLD Collaboration, K. Abe *et al.*, Phys. Rev. Lett. **85** (2000) 5059–5063.

[190] DELPHI Collaboration, P. Abreu *et al.*, Z. Phys. **C69** (1995) 1–14.

[191] L3 Collaboration, O. Adriani *et al.*, Phys. Lett. **B301** (1993) 136–144.

[192] OPAL Collaboration, P. D. Acton *et al.*, Z. Phys. **C58** (1993) 405–418.

[193] ALEPH Collaboration, D. Buskulic *et al.*, Z. Phys. **C57** (1993) 17–36.

[194] L. H. W. Group, *Search for the standard model Higgs boson at LEP*, Eprint arXiv:hep-ex/0107029, 2001.

[195] T. van Ritbergen and R. G. Stuart, Phys. Rev. Lett. **82** (1999) 488–491;
T. van Ritbergen and R. G. Stuart, Nucl. Phys. **B564** (2000) 343–390;
M. Steinhauser and T. Seidensticker, Phys. Lett. **B467** (1999) 271–278.

[196] M. Steinhauser, Phys. Lett. **B429** (1998) 158–161.

[197] H. Burkhardt and B. Pietrzyk, Phys. Lett. **B356** (1995) 398–403.

[198] BES Collaboration, J. Z. Bai *et al.*, *Measurements of the cross section for e+ e –¿ hadrons at center-of-mass energies from 2-GeV to 5-GeV*, Preprint hep-ex/0102003, BES, 2001.

[199] H. Burkhardt and B. Pietrzyk, Phys. Lett. **B513** (2001) 46–52.

[200] M. L. Swartz, Phys. Rev. **D53** (1996) 5268–5282.

[201] A. D. Martin and D. Zeppenfeld, Phys. Lett. **B345** (1995) 558–563.

[202] R. Alemany, M. Davier, and A. Hocker, Eur. Phys. J. **C2** (1998) 123–135.

[203] M. Davier and A. Hocker, Phys. Lett. **B419** (1998) 419–431.

[204] J. H. Kuhn and M. Steinhauser, Phys. Lett. **B437** (1998) 425–431.

[205] J. Erler, Phys. Rev. **D59** (1999) 054008.

[206] A. D. Martin, J. Outhwaite, and M. G. Ryskin, Phys. Lett. **B492** (2000) 69–73.

[207] F. Jegerlehner, in Proceedings, 4th International Symposium, RADCOR'98, ed. J. Sola, (World Scientific, Singapore, Sep 1999), p. 75.

[208] J. F. d. Troconiz and F. J. Yndurain, *Precision determination of the muon g(mu)-2 and alpha-bar(QED)*, Eprint hep-ph/0111258, 2001.

[209] CDF Collaboration, F. Abe *et al.*, Phys. Rev. Lett. **73** (1994) 225–231;
CDF Collaboration, F. Abe *et al.*, Phys. Rev. Lett. **74** (1995) 2626–2631.

[210] D0 Collaboration, S. Abachi *et al.*, Phys. Rev. Lett. **74** (1995) 2632–2637.

[211] CDF Collaboration, F. Abe *et al.*, Phys. Rev. Lett. **82** (1999) 271–276;
CDF Collaboration, T. Affolder *et al.*, Phys. Rev. **D63** (2001) 032003;
CDF Collaboration, F. Abe *et al.*, Phys. Rev. Lett. **79** (1997) 1992–1997.

[212] D0 Collaboration, B. Abbott *et al.*, Phys. Rev. Lett. **80** (1998) 2063–2068;
D0 Collaboration, B. Abbott *et al.*, Phys. Rev. **D60** (1999) 052001;
D0 Collaboration, S. Abachi *et al.*, Phys. Rev. Lett. **79** (1997) 1197–1202;
D0 Collaboration, B. Abbott *et al.*, Phys. Rev. **D58** (1998) 052001.

[213] UA1 Collaboration, C. Albajar *et al.*, Z. Phys. **C44** (1989) 15.

[214] UA2 Collaboration, J. Alitti *et al.*, Phys. Lett. **B276** (1992) 354–364.

[215] CDF Collaboration, T. Affolder *et al.*, Phys. Rev. **D64** (2001) 52001–39.

[216] D0 Collaboration, B. Abbott *et al.*, Phys. Rev. Lett. **80** (1998) 3008;
D0 Collaboration, B. Abbott *et al.*, Phys. Rev. **LETT.** (2000) 84:222–227.

[217] The results on the W-boson mass from UA2 [214], CDF [215] and DØ [216] are combined assuming 25 MeV correlated uncertainty, see also `http://www-cdf.fnal.gov/physics/ewk/wmass_global.html` .

[218] D0 Collaboration, V. M. Abazov, *Improved D0 W boson mass determination*, Preprint hep-ex/0106018, FNAL, 2001.

[219] ALEPH Collaboration, R. Barate *et al.*, Eur. Phys. J. **C17** (2000) 241–261.

[220] DELPHI Collaboration, P. Abreu *et al.*, Phys. Lett. **B511** (2001) 159–177.

[221] L3 Collaboration, M. Acciarri *et al.*, Phys. Lett. **B454** (1999) 386–398.

[222] OPAL Collaboration, G. Abbiendi *et al.*, Phys. Lett. **B507** (2001) 29–46.

[223] T. four LEP Collaborations and the LEP W Working Group, *Combined Preliminary Results on the Mass and Width of the W Boson Measured by the LEP Experiments*, Preprint LEPEWWG/MASS/2001-01, CERN, Mar 2001, see also `http://www.cern.ch/LEPEWWG/lepww/mw/Winter01/` .

[224] NuTeV Collaboration, G. Zeller *et al.*, *A Precise Determination of Electroweak Parameters in Neutrino-Nucleon Scattering*, Preprint hep-ex/0110059, FNAL, 2001.

[225] C. S. Wood *et al.*, Science **275** (1997) 1759.

[226] S. C. Bennett and C. E. Wieman, Phys. Rev. Lett. **82** (1999) 2484–2487.

[227] N. H. Edwards *et al.*, Phys. Rev. Lett. **74** (1995) 2654–2657.

[228] P. A. Vetter *et al.*, Phys. Rev. Lett. **74** (1995) 2658–2661.

[229] A. Derevianko, Phys. Rev. Lett. **85** (2000) 1618–1621.

[230] M. G. Kozlov, S. G. Porsev, and I. I. Tupitsyn, Phys. Rev. Lett. **86** (2001) 3260–3263.

[231] D. Y. Bardin *et al.*, *Atomic parity-violation and precision physics*, Eprint hep-ph/0102233, 2001.

[232] Ed. G. Altarelli, R. Kleiss, and C. Verzegnassi, Z PHYSICS AT LEP 1. PROCEEDINGS, WORKSHOP, GENEVA, SWITZERLAND, SEPTEMBER 4-5, 1989. VOL. 1: STANDARD PHYSICS, (CERN, Geneva, Switzerland, 1989), Yellow Report CERN 89-08.

[233] W. H. D. Bardin and G. Passarino, *Reports of the working group on precision calculations for the Z resonance*, Internal Report CERN 95-03, CERN, 1995.

[234] A. Freitas *et al.*, Phys. Lett. **B495** (2000) 338–346.

[235] U. Baur *et al.*, *Theoretical and experimental status of the indirect Higgs boson mass determination in the standard model*, Eprint hep-ph/0111314, 2001.

[236] K. G. Chetyrkin, J. H. Kuhn, and A. Kwiatkowski, Phys. Rept. **277** (1996) 189–281.

[237] D. E. Soper and L. R. Surguladze, Phys. Rev. **D54** (1996) 4566–4577.

[238] S. Bethke, J. Phys. **G26** (2000) R27.

[239] F. James and M. Roos, Comp. Phys. Commun. **10** (1975) 343.

[240] M. E. Peskin and T. Takeuchi, Phys. Rev. Lett. **65** (1990) 964–967;
M. E. Peskin and T. Takeuchi, Phys. Rev. **D46** (1992) 381–409.

[241] NuTeV Collaboration, K. S. McFarland *et al.*, *Measurement of sin**2(Theta(W)) from neutrino nucleon scattering at NuTeV*, Preprint hep-ex/9806013, FNAL, 1998, The result quoted is a combination of the NuTeV and CCFR results.